Hybrid numerical simulations of relativistic magnetospheres

Adrien Soudais

THÈSE

Pour obtenir le grade de

DOCTEUR DE L'UNIVERSITÉ GRENOBLE ALPES

École doctorale : PHYS - Physique
Spécialité : Astrophysique et Milieux Dilués
Unité de recherche : Institut de Planetologie et d'Astrophysique de Grenoble

Simulations numériques hybrides de magnétosphères relativistes

Hybrid numerical simulations of relativistic magnetospheres

Présentée par :

Adrien SOUDAIS

Direction de thèse :

Benoît CERUTTI — Directeur de thèse
CHARGE DE RECHERCHE HDR, CNRS DELEGATION ALPES

Rapporteurs :

ARACHE DJANNATI-ATAÏ
DIRECTEUR DE RECHERCHE, CNRS ILE-DEFRANCE VILLEJUIF
JERÔME PETRI
MAITRE DE CONFERENCES HDR, UNIVERSITE DE STRASBOURG

Thèse soutenue publiquement le **8 juillet 2024**, devant le jury composé de :

ARACHE DJANNATI-ATAÏ, DIRECTEUR DE RECHERCHE, CNRS ILE-DEFRANCE VILLEJUIF	Président
JERÔME PETRI, MAITRE DE CONFERENCES HDR, UNIVERSITE DE STRASBOURG	Rapporteur
GILLES HENRI, PROFESSEUR DES UNIVERSITES, UNIVERSITE GRENOBLE ALPES	Examinateur
CLAIRE GUEPIN, CHARGEE DE RECHERCHE, CNRS DELEGATION OCCITANIE EST	Examinatrice
IOANNIS CONTOPOULOS, DIRECTEUR DE RECHERCHE, RES CTR FOR ASTRONOMY AND APPLIED MATHS	Examinateur

UNIVERSITÉ GRENOBLE ALPES

PHD THESIS

Hybrid numerical simulations of relativistic magnetospheres

-

Simulations numériques hybrides de magnétosphères relativistes

Author:
Adrien SOUDAIS

Supervisor:
Benoît CERUTTI

Abstract

Relativistic magnetospheres represent one of the most energetic environments in the Universe and may be involved in high-energy phenomena such as Active Galactic Nuclei, Gamma-ray Bursts, X-ray binaries or pulsars. They correspond to the highly magnetised plasma-filled surroundings of a compact object. Pulsars are neutron stars which were first detected via their radio pulsations. They are able to emit across the full electromagnetic spectrum and show strong high-energy signals. Black holes do not emit light but their surrounding does, from radio to gamma-ray wavelengths. The amount of observational data grew a lot in recent years for both pulsars and black holes. The *Fermi* collaboration published their third catalogue on gamma-ray pulsars, which are the ones emitting at the highest energies. Compared to the previous catalogue, the number of these pulsars more than doubled, making the conclusions on the population even more reliable. How and where this high-energy radiation is coming from is not fully constrained yet. The recent discovery by the HESS collaboration of TeV emission coming from the Vela Pulsar, only confirms a similar detection from the Crab pulsar. This emission only reaffirms the fact that pulsars are incredible particle accelerators. For black holes, the high variability observed in gamma rays is also part of a larger puzzle. Thanks to the development of the Very Long Baseline Interferometry, the Event Horizon Telescope collaboration was able to give the first image of the "shadow" of two supermassive black holes, M87* and SgrA*. In the images, the emission is probed down to the horizon scale and gives insights into the physics around black holes. In both pulsar and black hole magnetospheres, the matter is pushed into extreme physical regimes either by the magnetic field (pulsars) or the strong gravity (Lense-Thirring effect of black holes). If we want to study these magnetospheres, we have to rely on numerical simulations to consider the wide range of physical phenomena.

The modelling of magnetospheres was originally done using the force-free approach, the zero mass limit of magnetohydrodynamics. It allowed us to study the structure of the magnetosphere but was not able to capture radiation by construction. The Particle-in-cell method became the next approach used by the community, as the plasma near pulsars and black holes is mostly collisionless. This method directly uses particles to model the magnetosphere and captures particle acceleration. However, it uses microscopic particles to describe global systems. This implies a large-scale separation which is not achievable with the PIC approach, thus they are scaled down while conserving the hierarchy of scales. Consequently, PIC simulations are modelling a reduced system and cannot be used directly to explain the observations.

In this thesis, I have developed a new numerical method in the ZELTRON code. This method combines the force-free approach and the PIC approach simultaneously to describe relativistic magnetospheres. The goal behind it is to be able to push the scale separation of the simulation as far as possible. The ideal regions of the simulation are treated by the force-free method, while the non-ideal parts are described by the particles. Hiding some regions behind the force-free treatment allowed me to push the parameters of the simulation to a scale separation for the particles never reached before. As a result, I pinpointed the fact that the weakest millisecond pulsar seen by the *Fermi* collaboration can accelerate particles to TeV energies. Moreover, I highlighted the fact that the rescaling of PIC simulations was valid. With this work, I gave the first proof-of-principle that force-free-PIC methods are doable and can bridge the gap between simulations and observations.

Résumé

Les magnétosphères relativistes font partie des environnements les plus énergétiques de l'Univers et sont suspectées d'être impliquées dans les noyaux actifs de galaxie, sursauts gamma, binaires X et pulsars. Elles correspondent à la région proche des objets compacts qui est fortement aimanté et remplie de plasma. Les pulsars sont des étoiles à neutron historiquement détectés grâce à leurs pulsations radio. Ils présentent aussi une émission pulsée intense à travers tout le spectre électromagnétique. Les trous noirs quant à eux n'émettent pas de lumière, l'émission détectée provient de la matière en orbite. Au fil des années, beaucoup de données ont été recueillies sur les deux objets. La collaboration *Fermi* a récemment publié son troisième catalogue qui recense tous les pulsars connus émettant en gamma. Ils correspondent aux pulsars les plus énergétiques. Ce dernier catalogue contient deux fois plus de pulsars que le précédent, ce qui permet de tirer des conclusions sur les différentes populations. Où et comment les émissions à haute énergie sont produites est toujours une question ouverte. La découverte par la collaboration HESS d'émission au TeV pour le pulsar Vela réintroduit la question de l'accéleration de particules aux abords des pulsars. Cette détection vient confirmer une détection plus ancienne au TeV du pulsar du Crabe et indique que les pulsars sont d'incroyables accélérateurs de particules. Dans le cas des trous noirs, on trouve aussi une forte variabilité du rayonnement gamma. Les développements de la technologie VLBI ont permis à la collaboration Event Horizon Telescope d'imager pour la première fois l'ombre des trous noirs supermassifs, M87* et SgrA*. Les deux images montrent un plasma chaud en orbite et permettent de sonder la physique dans des régimes extrêmes. Pour étudier ces magnétosphères, nous devons nous appuyer sur des simulations numériques afin de prendre en compte toute leur complexité.

La modélisation des magnétosphères était d'abord faite en utilisant l'approche sans-force. Elle correspond à la limite idéale de la magnétohydrodynamique. Cette méthode nous a permis d'étudier la structure des magnétosphères mais ne permet pas, par construction, de contraindre le rayonnement. La méthode Particle-in-cell est maintenant préférée à cette dernière car elle permet d'obtenir le rayonnement en utilisant directement des particules pour modéliser la magnétosphère. Cependant, la méthode particulaire doit décrire un système à la fois micro- et macro-scopique ce qui est numériquement complexe. Cette grande séparation d'échelle est réduite dans les simulations PIC en rééchelonnant toutes les quantités, tout en conservant la hiérarchie des échelles du problème. Ainsi, les simulations PIC modélisent des systèmes de taille réduite et ne permettent pas une comparaison directe avec les observations.

Durant ma thèse, j'ai développé une nouvelle méthode numérique au sein du code ZELTRON . Cette méthode combine les approches sans-force et PIC de façon simultanée pour modéliser les magnétosphères relativistes. Le but de cette manœuvre est d'accroître la séparation d'échelle des simulations PIC actuelles. Les régions idéales sont alors modélisées par la méthode sans-force, tandis que pour les zones non idéales est employée la méthode PIC. L'utilisation de la méthode idéale permet d'augmenter la séparation d'échelle de la simulation de manière globale, ce qui impacte aussi les particules. Grâce à cette méthode, j'ai pu augmenter la séparation d'échelle à des valeurs non atteintes par le passé. J'ai démontré que le pulsar milliseconde le plus faible détecté par *Fermi* est capable d'accélérer des particules jusqu'au TeV. J'ai aussi réussi à valider le processus de rééchelonnage des simulations PIC. Avec ce travail, j'ai prouvé qu'il était possible de développer une méthode sans-force-PIC permettant de faire le pont entre les simulations et les observations.

Remerciements

Je souhaiterais tout d'abord remercier mon directeur de thèse, Benoît Cerutti. Je lui suis très reconnaissant de m'avoir permis de réaliser cette thèse, d'avoir partagé son savoir avec moi et de m'avoir initié au travail de chercheur. Je tiens aussi à le remercier pour sa confiance, sa disponibilité, pour les discussions diverses et variées à propos de la physique mais aussi d'autres sujets. Je n'aurais pas pu mener à bien ce projet sans ses précieux conseils, sa bienveillance ainsi que sa relecture attentive du manuscrit. Je n'oublierais jamais ces trois années. Je souhaiterais ensuite remercier mes deux rapporteurs, Jérôme Pétri et Arache Djannati-Ataï, pour leurs retours sur mon manuscrit. Je remercie les code monkeys, Jonah « le Breton » Mauxion et John « le Gourmand » Mehlhaff, pour la bonne humeur et l'ambiance dans le bureau pendant ces trois années. Je n'oublie pas Marc Van den Bossche d'avoir contribué à cette ambiance, de par les aller-retours constants que nous faisions entre nos deux bureaux, les questions en tout genre mais aussi pour sa ferveur dans la lutte contre le café. Merci à l'équipe SHERPAS de m'avoir accueilli à bras ouverts et de m'avoir intégrer dans cette grande famille. Je n'oublie pas la cuisine pendant les sherpiades. Il y a aussi la team ciné (Clément, Gaylor, Jonah, Lisa, Marc, Myriam, Simon) avec laquelle j'ai passé de nombreuses heures dans les salles obscures. À mes amis, Guillaume, Grégoire, Ophélie, Prune et Quentin, merci d'être présents à mes côtés depuis tout ce temps.

Naturellement, mes remerciements vont aussi à mes parents, mon frère et Olivier. Je tiens à les remercier pour leur soutien dans mes projets et tout au long de cette thèse, une aventure légèrement différente de la campagne auvergnate.

Enfin, je tiens à remercier Lisa pour son soutien durant tous les moments, bons comme difficiles, de la thèse et du quotidien. Merci d'avoir supporté mes absences pour les diverses conférences et mon indisponibilité pendant la rédaction.

Contents

List of Figures

List of Tables

Conventions and notations

Inside this manuscript, I will use two specific blocks of text. The first one appears as red boxes in which I give the derivation of a property or an expression

Demonstration: Property/Expression

▶ Beginning of derivation

⋮

End of derivation ◀

The second one corresponds to blue boxes in which I define a specific nomenclature that I will hereafter use.

Definition: Quantity $\mathcal{A}$

Nomenclature used to define the quantity, mostly used in the numerical parts of the manuscript.

Mathematical convention: $\mathbb{N}$ is the set of all natural integers *including zero*. Vectors are in boldface and the nabla operator is written as $\boldsymbol{\nabla}$. Indices appearing in both an upper and lower position are summed using the Einstein summation convention (mainly in the black holes sections). To lighten the reading, in-line math fractions are written as a/bc instead of $a/\left(bc\right)$.
Geometrical convention: I use the following notations for the different geometries,

Coordinate system	Vector basis
Cartesian	(x, y, z)
Cylindrical	(R, ϕ, z)
Spherical	(r, θ, ϕ)

Physical Constants

This thesis is written using the Gaussian CGS units.

Electron charge	$e = 4.803 \times 10^{-10}\ \mathrm{g}^{1/2} \cdot \mathrm{cm}^{3/2} \cdot \mathrm{s}^{-1}$
Electron mass	$m_e = 9.109 \times 10^{-28}\ \mathrm{g}$
Gravitational constant	$G = 6.674 \times 10^{-8}\ \mathrm{cm}^3 \cdot \mathrm{g}^{-1} \cdot \mathrm{s}^{-2}$
Parsec	$pc = 3.086 \times 10^{18}\ \mathrm{cm}$
Planck constant	$h = 6.626 \times 10^{-27}\ \mathrm{erg} \cdot \mathrm{s}^{-1}$
Proton mass	$m_p = 1.673 \times 10^{-24}\ \mathrm{g}$
Solar mass	$M_\odot = 1.988 \times 10^{33}\ \mathrm{g}$
Speed of light in vacuum	$c = 2.998 \times 10^{10}\ \mathrm{cm} \cdot \mathrm{s}^{-1}$

Conversion factors between SI and CGS units:

Energy	$1\ \mathrm{Joule} = 10^7\ \mathrm{erg}$
Length	$1\ \mathrm{meter} = 10^2\ \mathrm{cm}$
Magnetic field	$1\ \mathrm{Tesla} = 10^4\ \mathrm{Gauss\ [G]}$
Mass	$1\ \mathrm{kg} = 10^3\ \mathrm{g}$
Velocity	$1\ \mathrm{m} \cdot \mathrm{s}^{-1} = 10^2\ \mathrm{cm} \cdot \mathrm{s}^{-1}$

To the blessed memory of my grand-father, Jean-Claude Roy

Part I

Introduction: context and motivations

CHAPTER 1

Compact objects and their observational signatures

Contents

In this chapter, I introduce the nature of compact objects with a focus on the observational aspect. More precisely, I describe the observational constraints gathered by the community on gamma-ray pulsars and black holes. This section relies on Begelman and Rees (2020) and lectures notes by Eric Gourgoulhon.

1.1 The nature of compact objects

Similar to how an author describes with details the first scene of a book, we must give to the reader the background story of our main characters: neutron stars and black holes. Our protagonists belong to the astrophysical category of compact objects, which also include white dwarf stars. In astrophysics, the formation of compact objects marks the end of a standard star life, see Fig. 1.1 for the life cycle of stars. Each of the three types of compact objects are the by-product of a life-ending main sequence star. When stars are ageing, the nuclear reaction inside them goes through different stages from burning hydrogen to helium. When the star runs out of fuel, the thermonuclear reactions will stop. Consequently, the thermal pressure drops below a point where the star gravitationally collapses. Which of the three compact objects a star will become is determined by the initial mass of the star. Below $\sim 8-10M_{\odot}$, where $M_{\odot}$ is the mass of the Sun, the star will collapse into a white dwarf. This collapse is stopped by the degenerate electronic pressure, when it is strong enough to counterbalance gravity. White dwarfs typically have masses of $M \leq 1M_{\odot}$. The upper limit on the mass of a star supported by the degenerate electron pressure is known as the Chandrasekhar mass, $M_{\rm C} = 1.44M_{\odot}$ (Chandrasekhar, 1935). In the case of an initial star mass within $\sim 10-25M_{\odot}$, the degenerate electron pressure is not strong enough to counter-balance the collapse. However, the collapsing star can reach an other equilibrium, in which the degenerate neutron pressure and the repulsive nuclear forces become strong enough. The end product is a neutron star. The idea of forming neutron stars appeared shortly after the discovery of the neutron in 1932 by James Chadwick (Chadwick, 1932). A few years after, Oppenheimer and Volkoff (1939) made the first calculation of the structure of a neutron star. They used general relativity and considered that the star was fully made of neutrons acting as a degenerate Fermi gas. Regarding the origin of neutron stars, Baade and Zwicky (1934) suggested that the formation site could be via supernovae. This forming scenario has been validated since, when a neutron star was detected in the Crab Nebula. Black holes are the last class of compact objects. Their formation depends on the Tolman-Oppenheimer-Volkoff limit (TOV limit), this is the analogue of the Chandrasekhar mass for white dwarfs. If the mass of the forming neutron star is larger than the TOV limit, the star will keep on collapsing. The value of the TOV limit is not settled yet as it relies on the equation of state of neutron star, the latter being an active domain of research. However, under some assumptions, Rhoades and Ruffini (1974) showed that the mass of a neutron star cannot exceed $M = 3.2M_{\odot}$.
In this manuscript, I will only tackle the neutron star and black hole aspect of compact objects.

1.2 Pulsars: cosmic lighthouses made of neutrons

Pulsars are a specific type of neutron stars emitting a pulsed signal. The original name of these objects was pulsating radio source, shortened pulsar. The pulsed signal, observed with periodicities between milliseconds and tens of seconds, is coming from a narrow beam of light emitted by the source, sweeping the observer line of sight. This phenomenon is identical to the one produced by a lighthouse on the coast. In a sense, pulsars are cosmic lighthouses.

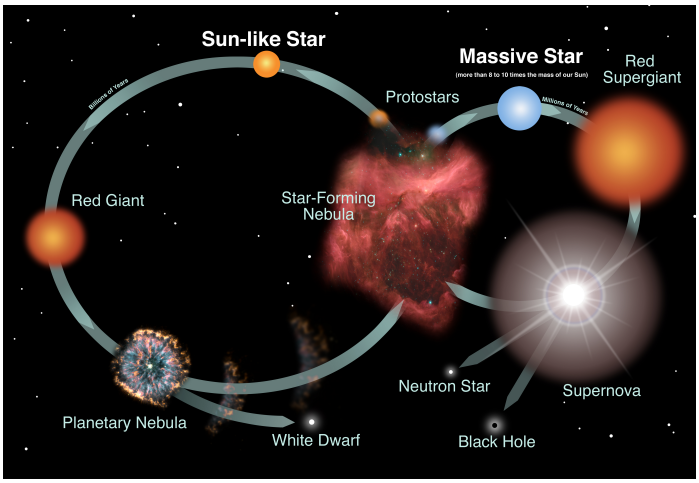

FIGURE 1.1: Life cycle of stars depending on the mass. (Credits: NASA and the Night Sky Network.)

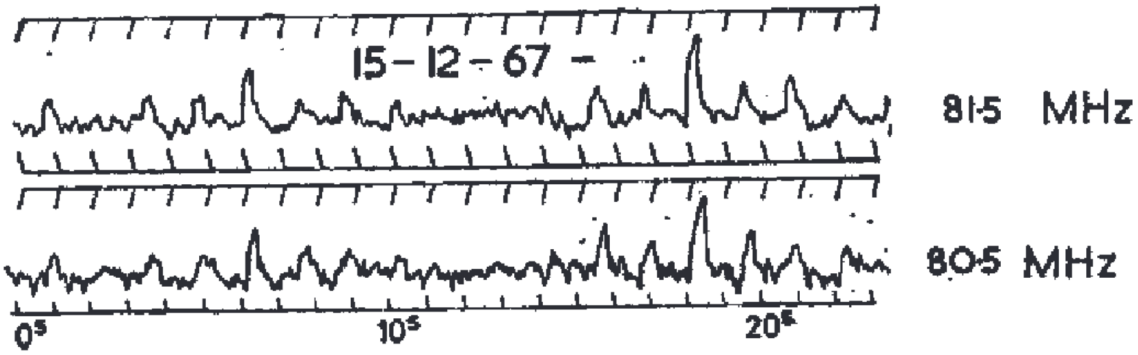

FIGURE 1.2: Recorded pulses of CP1919 for two different frequencies (Hewish et al., 1968).

1.2.1 Pulsating neutron stars

Discovery

In 1967, Jocelyn Bell discovered radio pulsations on her chart recorder paper at the Mullard Radio Astronomy Observatory, UK. The pulsations were first believed by Antony Hewish, her supervisor, to come from interference. It was the first time that such a periodic signal was observed by radio astronomers, the doubts on the signal were natural at first. However, with the repeated detections of these pulses, it became clear that a source was emitting from the sky. In their seminal paper relating the discovery, Hewish et al. (1968) indicated that the signal of CP1919 was periodic, with a periodicity of $P = 1.33733 \pm 0.00001$s. In Fig. 1.2, we show one of the recorded pulses for two different frequencies. The pulses appear as sharp features occurring during 0.3s and repeating every 1.337s. If we consider that this signal is emitted by a star, the short periodicity indicates that its size is small. The link between pulsars and neutron stars was highlighted by Gold (1968), and was validated when the community observed the supernova remnant SN 1054 and discovered a neutron star at its centre.
Since the discovery of CP1919, the number of pulsars detected has jumped to the roof with 3534 pulsars identified[1].

[1]number of detections at the date of writing (April 2024)

Representing the pulsar space

As a neutron star, pulsars have a typical radius of $r_\star = 10$km and a typical mass of $M_\star = 1.4M_\odot$. These two parameters are valid for most neutron stars with an upper limit on the radius at $r_\star \approx 13$km and $M \approx 3M_\odot$. On the contrary, the rotation period of each pulsar is an intrinsic parameter which can be precisely estimated via observations. If we assume that pulsars are rotationally powered, their rotational energy is converted into the radiation detected. Consequently, the pulsar loses energy and slows down, increasing its rotation period. The gradual slowing down of the pulsar is computed as the time derivative of the period,

$$\dot{P} = \frac{\mathrm{d}P}{\mathrm{d}t}. \tag{1.1}$$

With the period P and period derivative $\dot{P}$ of a pulsar, we can build a $P - \dot{P}$ diagram. This type of diagram is the analogue of the Hertzsprung-Russell diagram for stellar evolution, in the context of pulsars. In Fig. 1.3, we show the $P - \dot{P}$ diagram representing all the detected pulsars[2] (Manchester et al., 2005).

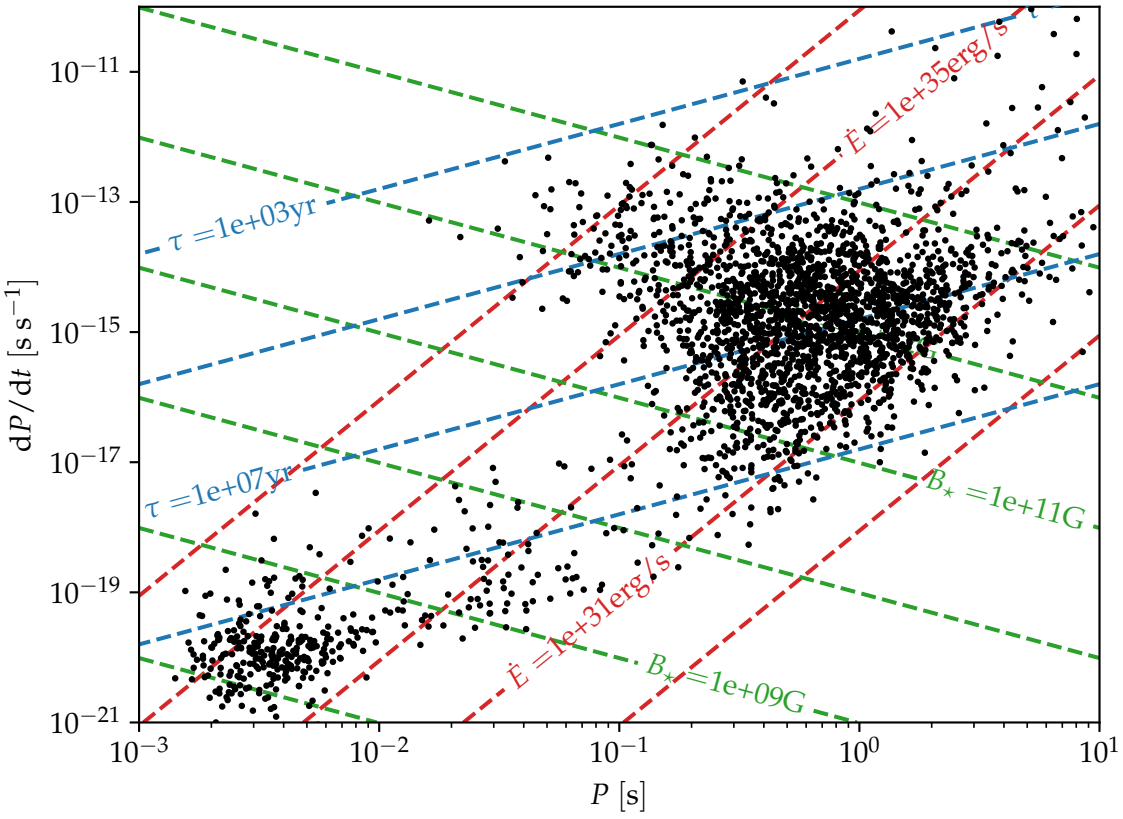

FIGURE 1.3: $P - \dot{P}$ diagram of all detected pulsars. Blue, green, and red dashed lines indicate respectively iso-levels of the age, surface magnetic field strength, and spindown power.

Several things emerge when we use this representation to show the pulsar population. The first aspect is the dichotomy in periods. The first category of pulsars is called normal pulsar as they have parameters similar to the first pulsar detected. As a bulk population, normal pulsars have a spin period $P \sim 1$s and a period derivative $\dot{P} \sim 10^{-15}$. The second

[2]Data provided by the ATNF pulsar catalogue, http://www.atnf.csiro.au/research/pulsar/psrcat/expert.html

population is located at the bottom left corner of the $P - \dot{P}$ diagram, and is referred to as the millisecond pulsar population. The latter can be defined as pulsars with $P \in]1.39, 20[$ ms and $\dot{P} < 10^{-19}$ (Özel & Freire, 2016). Another point highlighted by this representation is the absence of pulsars in the bottom right corner. This part of the diagram corresponds to the dead-zone. It is possible to derive a frontier called the "death-line", however, the position of the frontier is model dependent (Zhang et al., 2000). The reason behind this absence of pulsations is believed to be a consequence of the shortage of pair production (Sturrock, 1971; Ruderman & Sutherland, 1975) in an ageing pulsar.

The period of a pulsar and its derivative are also precious to compute three other intrinsic parameters. These new parameters are: the age τ, the surface magnetic field $B_\star$, and the spindown power $\dot{E}$ of a pulsar. Each of these parameters appear in the $P - \dot{P}$ diagram as different isolevels. The "characteristic age" is defined as

$$\tau = \frac{P}{2\dot{P}}. \tag{1.2}$$

Looking at the $P - \dot{P}$ diagram, we can see that the normal population is younger than the millisecond one, which is populated by old pulsars. When a pulsar gets older, its period increases while its period derivative decreases. Following this argument, normal pulsars move to the bottom right corner when ageing. However, we see that the millisecond population is older but still above the death-line. They have a smaller period derivative in agreement with the expected behaviour, but their spin period has decreased. The hypothesis behind this difference is that millisecond pulsars are recycled pulsars. They are believed to have be spun up by the accretion of material from a companion (Alpar et al., 1982). Millisecond pulsars are old normal pulsars which drifted to the left side of the diagram thanks to their companion.

The second isolevel we can compute is for the spindown power $\dot{E}$, which corresponds to the energy extracted from the pulsar's rotation. It is defined as

$$\dot{E} = 4\pi^2 I \frac{\dot{P}}{P^3} \tag{1.3}$$

where $I \approx M_\star r_\star^2$ is the moment of inertia of the neutron star. We mentioned the death-line of pulsars, past which pulsars turn off. In terms of power, this corresponds to a spindown power of $\dot{E} \sim 10^{29}$erg/s. The total population is less divided regarding the average spindown power. On the one hand, the milliseconds pulsars have a narrow spindown power window centred at $\dot{E} \sim 10^{34}$ erg/s. On the other hand, normal pulsars span a wider range $\dot{E} \in [10^{31}, 10^{35}]$ erg/s. Among the normal pulsars, some of the youngest show the highest spindown power observed. The Crab pulsar is one of these pulsars and is the focus of the next section.

One last important parameter to describe a pulsar is its magnetic field. Here, we assume that the rotator is an orthogonal dipole. If we consider that the spindown power $\dot{E}$ is produced by the radiation field of a magnetic dipole, i.e. $P_{\rm rad} = 2B_\star^2 r_\star^6 \Omega^4 / 3c^3$, we can compute the surface magnetic field as a function of P and $\dot{P}$. The expression of the surface magnetic field is

$$B_\star = \frac{\sqrt{1.5 I c^3 P \dot{P}}}{2\pi r_\star^3} \simeq 3.2 \times 10^{19} \sqrt{P\dot{P}}\ \text{G}, \tag{1.4}$$

where c is the speed of light. Plugging these isolevels in the $P - \dot{P}$ diagram, indicates that normal pulsars have a strong magnetic field. The bulk of the normal population sits at $B_\star \sim 10^{12}$G, while the recycled population has a much weaker field with $B_\star \leq 10^9$G.

FIGURE 1.4: Crab nebula seen by the JWST. (Credit: NASA, ESA, CSA, STScI, Tea Temim (Princeton University))

1.2.2 Crab pulsar: the Rosetta stone of pulsar observations

History

This source represents one of the most well-studied astrophysical objects after the Sun, with written traces going back to 1054 AD. At the time called "guest-stars", Chinese astronomers wrote in the *Wenxian Tongkao*, the emergence of SN 1054 in July 1054. Notes translated by Édouard Biot in 1843, state that the new star was visible during 23 consecutive days during daylight. This system is located close to Earth, at a distance $d = 2$kpc. In Fig. 1.4, we show one of the most recent picture of this system.

SN 1054[3] or the Crab nebula, is a supernova remnant located in the constellation of Taurus. The outer part of the nebula is made of the matter previously ejected by the star mixed with the interstellar medium matter. The outer region probes the material coming from the explosion of the star, thus the past history of the system. As we look closer to the centre of the nebula, we probe the youngest part of it. At the very centre of the nebula, we find the Crab pulsar or PSR J0534+2200[4] as the result of the collapse of the star. Between the outer and central part, we find the pulsar wind nebula. This region corresponds to the wind emitted by the pulsar, propagating inside the nebula. The link between neutron stars and pulsars occurred with the development of new observing technologies and multiwavelength astronomy.

[3] first object in the Messier catalogue, M1.

[4] PSR: Pulsating Source of Radio, J: equinox J2000, 0534: right ascension 05h 34 min, +2200: declination $+22^\circ$

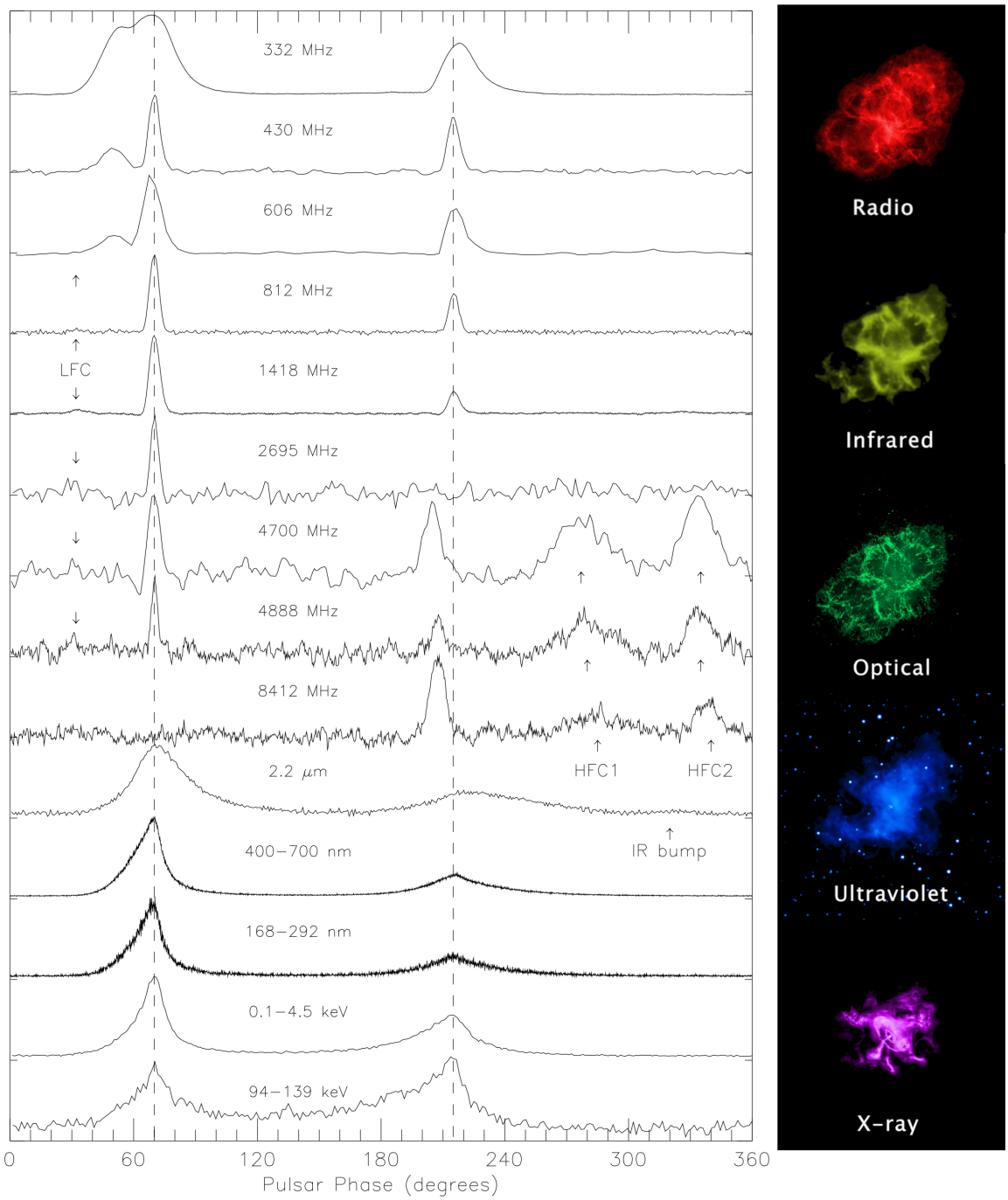

FIGURE 1.5: Observations of the Crab system across the full electromagnetic spectrum. Left: profile of the observed pulsations (Moffett & Hankins, 1996). Right: observations of the Crab nebula from radio (top) to X-rays (bottom) (Credits: NASA, ESA, and Hubble/STScI).

Multiwavelength emission

When tackling multiwavelength emission, one has to start with radio emissions. As the foundation of pulsar astronomy, radio telescope were pointed towards the Crab nebula. The detection of the pulsar was reported by Lovelace et al. (1968), Staelin and Reifenstein (1968). As a result of this observation, the pulsar spin period was constrained to $P = 33$ms.

In Fig. 1.5 (left), we show the pulsed profile of the Crab pulsar. In the figure, the radio

profiles are correctly centred after removing the dispersion delay. However, the other profiles are arbitrarily aligned with respect to the peak of the main pulse (Moffett & Hankins, 1996). We can see that two pulses, main and inter pulses, are detected in almost every wavelength, from radio to X-rays. The main pulse is present at all wavelengths with the exception at $\nu = 8412$MHz where it vanishes. The second pulse also shows this behaviour but at a different frequency, $\nu = 2695$MHz. Regarding the shape of the pulses in the different frequency windows, pulses are wider at high frequencies and get narrower with a decreasing frequency. For the amplitudes of the pulses, we see that their ratio is not constant with wavelength. The interpulse can have an amplitude as large as the main pulse in the X-rays but also only a small fraction at radio frequencies. In the latter, the pulse profile contains a precursor before the main pulse. The precursor shifts to higher pulsar phase for lower radio frequencies, eventually merging with the main pulse.
The pulsar is not the only source emitting across the full electromagnetic spectrum. In Fig. 1.5, the right panel shows the observation of the Crab nebula for different wavelengths. Starting with the radio emission, we see that the full nebula is shining with an excess at the centre where the pulsar stays. The radio emission is associated to the pulsar itself, but also to the radiation emitted by the nebula's material energised by the particles inside the pulsar wind. The next observation is in infrared. It shows the radiation emitted by the dust after absorption of optical and ultraviolet emissions. In optical, the emission is mainly coming from the matter inside the filaments of the nebula. The pulsar wind nebula is seen in the ultraviolet, where the emission is produced by the mildly energetic particles of the wind. The structure is more coherent (torus shape) and the pulsar can be seen at the centre of the pulsar wind nebula. A more detailed observation of the inner region revealed the presence of compact knots of emission close to the pulsar (Weisskopf et al., 2000). The last image is in the high-energy range, where the emission comes from accelerated energetic particles. The question of this acceleration is still open, but the community tends towards an acceleration at the pulsar wind termination shock which proceeds inside the nebula. In X-rays, the pulsar wind nebula can be divided into several sharp features. First, at the centre of the image, we observe a bright spot corresponding to the (unresolved) pulsar and its close environment. This feature indicates that significant X-ray radiations are being produced. Emerging from the pulsar, we see the development of a jet and counter-jet aligned with the pulsar spinning axis. Finally, a torus emitting X-rays is visible, centred around the pulsar. The inner-edge of the torus is well discernible, which was not the case in the ultraviolet range.

There is one other way of looking at the Crab nebula and its pulsar, or any other astrophysical objects. We can compute the spectral energy distribution associated to the object. A spectral energy distribution (SED) allows us to represent the observed power per frequency interval of a source as a function of energy. We show the SED of the Crab nebula and pulsar in Fig. 1.6. Even though the SED is a different representation of the system, we still see the emission across the full electromagnetic spectrum. For the nebula, a first steep power-law is visible from the radio up to the near IR, where a first break occurs. It evolves into a softer power-law from the near-IR to the near-UV before breaking a second time. A third power-law describes the SED from the near-UV to the hard X-ray band. The power-laws indicate that these distribution are non-thermal, such distributions can be produced for example by synchrotron and inverse Compton radiations. Moreover, the SED of the Crab nebula, possesses an extra component at the highest energies. If we look at the pulsar itself, we see a strong emission in the X-ray and gamma-ray band. The latter can outshine the nebula at the highest energies. The gamma-ray detection from the Crab system was recorded by Browning et al. (1971). The system is able to produce γ-ray emission, meaning that particles are accelerated to relativistic speeds by the pulsar itself and in the nebula. The emission at these high energies are not produced by all pulsars but only by a

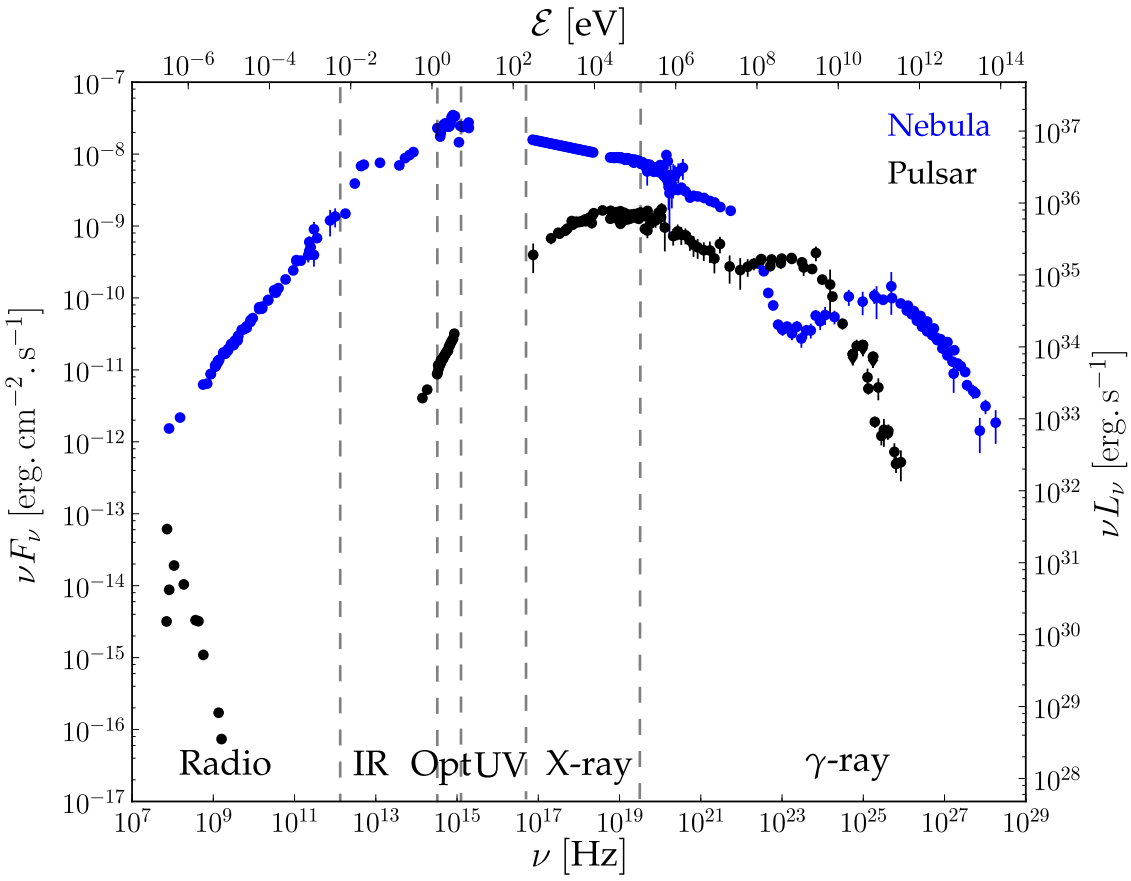

FIGURE 1.6: Observed SED of the Crab system spanning from radio to gamma-rays, adapted from Bühler and Blandford (2014). The SED of the nebula and of the pulsar are respectively in blue and black.

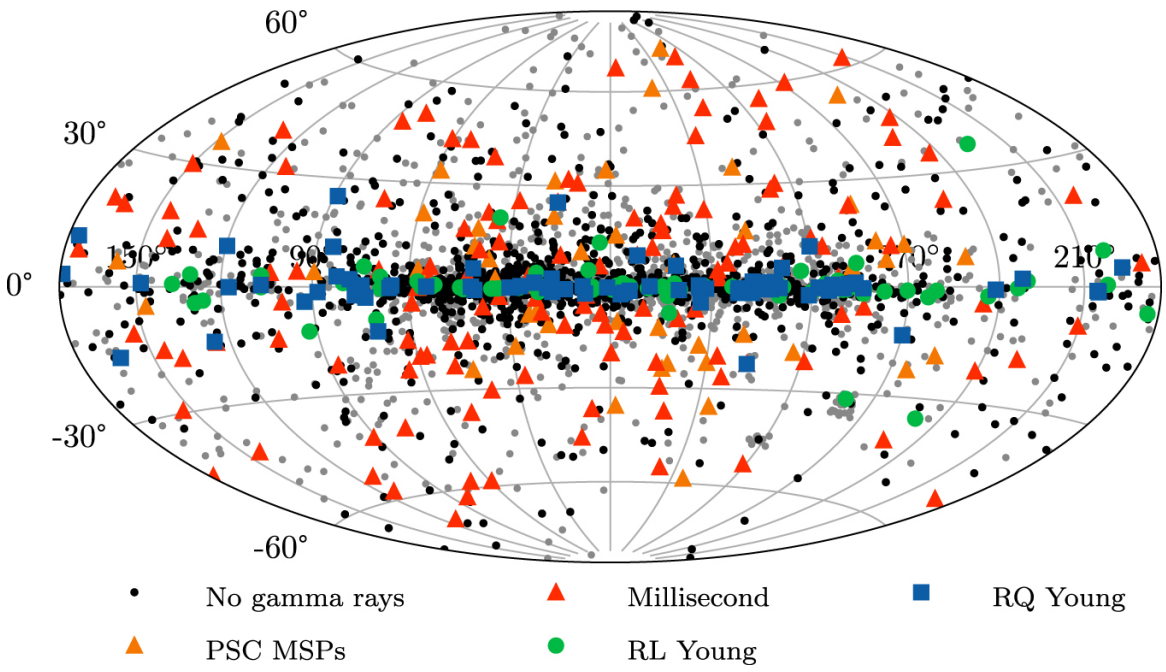

FIGURE 1.7: Sky map showing where the gamma-ray pulsars of 3PC are located, from Smith et al. (2023).

fraction of them, called gamma-ray pulsars.

1.2.3 Gamma-ray pulsars

Gamma-ray pulsars are a sub-class of pulsars and belong to both the normal and the millisecond population. This class of pulsars could not be detected with ground based telescope as the gamma-rays do not penetrate Earth's atmosphere. The detections started with the launch of the Compton Gamma-Ray Observatory (CGRO). The instrument EGRET behind the detections was on board of the CGRO, and allowed the community to discover at least 6 high-confidence gamma-ray pulsars (Thompson, 2004). This observatory was later followed in 2008 by the *Fermi* satellite, on boarding the Large Array Telescope (LAT) with an energy range of 10MeV − 300GeV. The *Fermi*-LAT opened a new sky for gamma-ray astronomy, especially for gamma-ray pulsars. The first catalogue on gamma-ray pulsars was released in 2010 (Abdo et al., 2010) with 46 detections. The pulsars reported by the collaboration were mostly located in the equatorial plane of the galaxy. In their third and latest catalogue (3PC) on gamma-ray pulsars (Smith et al., 2023), the number of detections by the *Fermi*-LAT reached 294 pulsars. This represents almost 10% of the total pulsar population. In Fig. 1.7, we show the location of all LAT detected pulsars. With almost 300 gamma-ray pulsars and more than 3000 detected pulsar, the population study from the skymap becomes relevant. We can see on the skymap that a high concentration of pulsars and gamma pulsars lies in the equatorial plane of the galaxy, close to the centre. However, a fraction of pulsars are also detected isotropically above and below the Galactic plane. We note that most of the gamma-ray pulsars detected outside of the equatorial plane are mainly millisecond pulsars.

The gamma-ray pulsars can be represented in the $P - \dot{P}$ diagram along with all other pulsars, this is shown in Fig. 1.8. Gamma-rays pulsars are still rotationally powered, and divided between millisecond pulsars and young pulsars. The split between both population is sharper than the one previously given. The young pulsar population has typical parameters slightly different than normal pulsars. The average spin period is $P \sim 0.1\,\mathrm{s}$

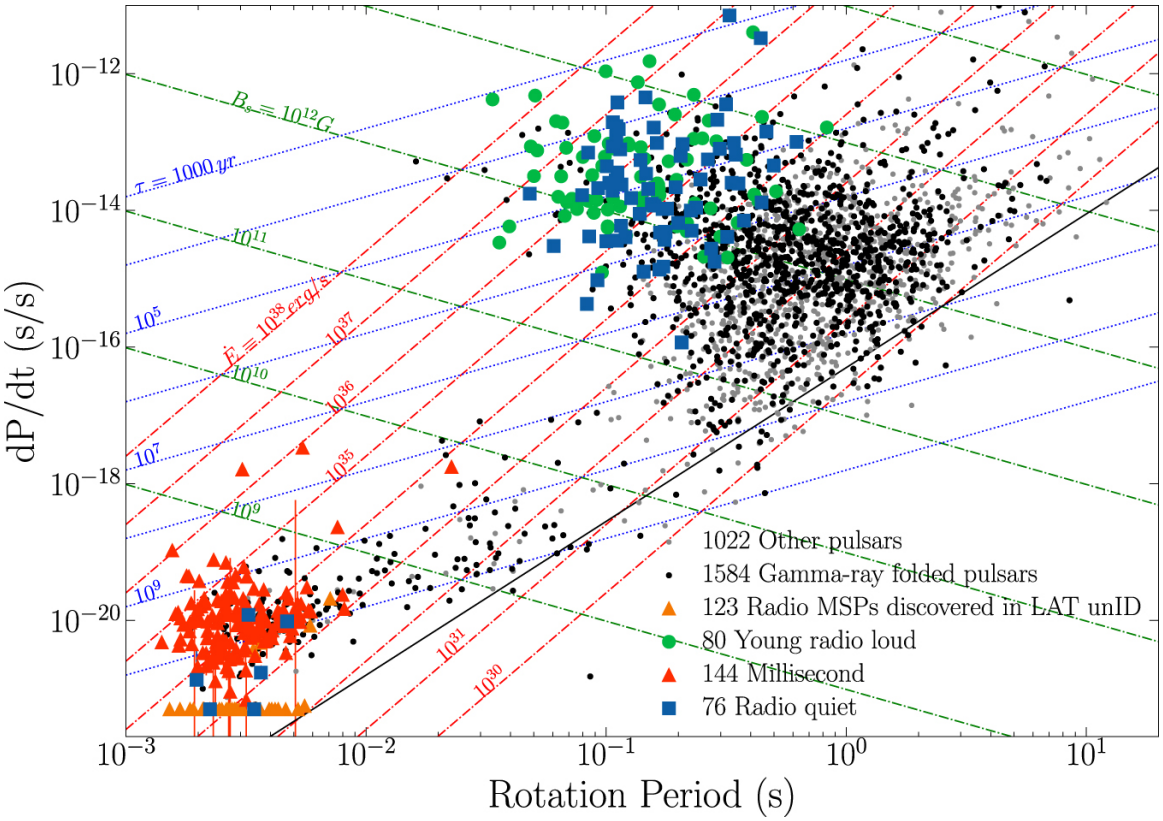

FIGURE 1.8: $P - \dot{P}$ diagram showing the gamma-ray pulsar population of 3PC, from Smith et al. (2023).

and they have a stronger surface magnetic field, slightly above $B_\star \sim 10^{12}$ G. This results in a strong spindown power with $\dot{E} \sim 10^{35-36}$erg/s. The gamma-ray millisecond population does not show differences with the other millisecond pulsars. For both gamma-ray population, a deathline can be drawn at $\dot{E} \sim 10^{33}$erg/s, which is higher than the one derived before. Among the young pulsars, two categories emerge: the radio loud and radio quiet pulsars. The radio loud pulsars are sources showing pulsations in the gamma-rays as well as in the radio, while the radio quiet ones do not show significant pulsations in the radio. Figure 1.9 shows the pulse profile in gamma-ray and radio for a millisecond and a young pulsar. In the gamma-ray profiles, two main pulses are observed along with two weaker pulses. If we compare the main peaks with the radio peaks, we see a slight shift meaning that there is a lag between the radio and gamma-ray emission. This difference seems to indicate that radio and gamma-ray emissions are not produced at the same location in the magnetosphere.

From gamma-ray observations, it is possible to derive a total gamma-ray luminosity. Noted L_γ, this luminosity is given by

$$L_\gamma = 4\pi d^2 f_\Omega G_{100} \tag{1.5}$$

where d is the distance, f_Ω is the beaming fraction, and G_{100} is the spectral energy flux integrated above 100 MeV. This luminosity can be used to establish how much spindown energy is converted into gamma-rays. Noted η, the efficiency of a pulsar is the ratio between the gamma-ray luminosity and the spindown power. This procedure was applied to the pulsars from 3PC to produce Fig. 1.10. From the figure, we can conclude that the efficiency of gamma-ray pulsars is between $1 - 10\%$ on average, some pulsars do show higher

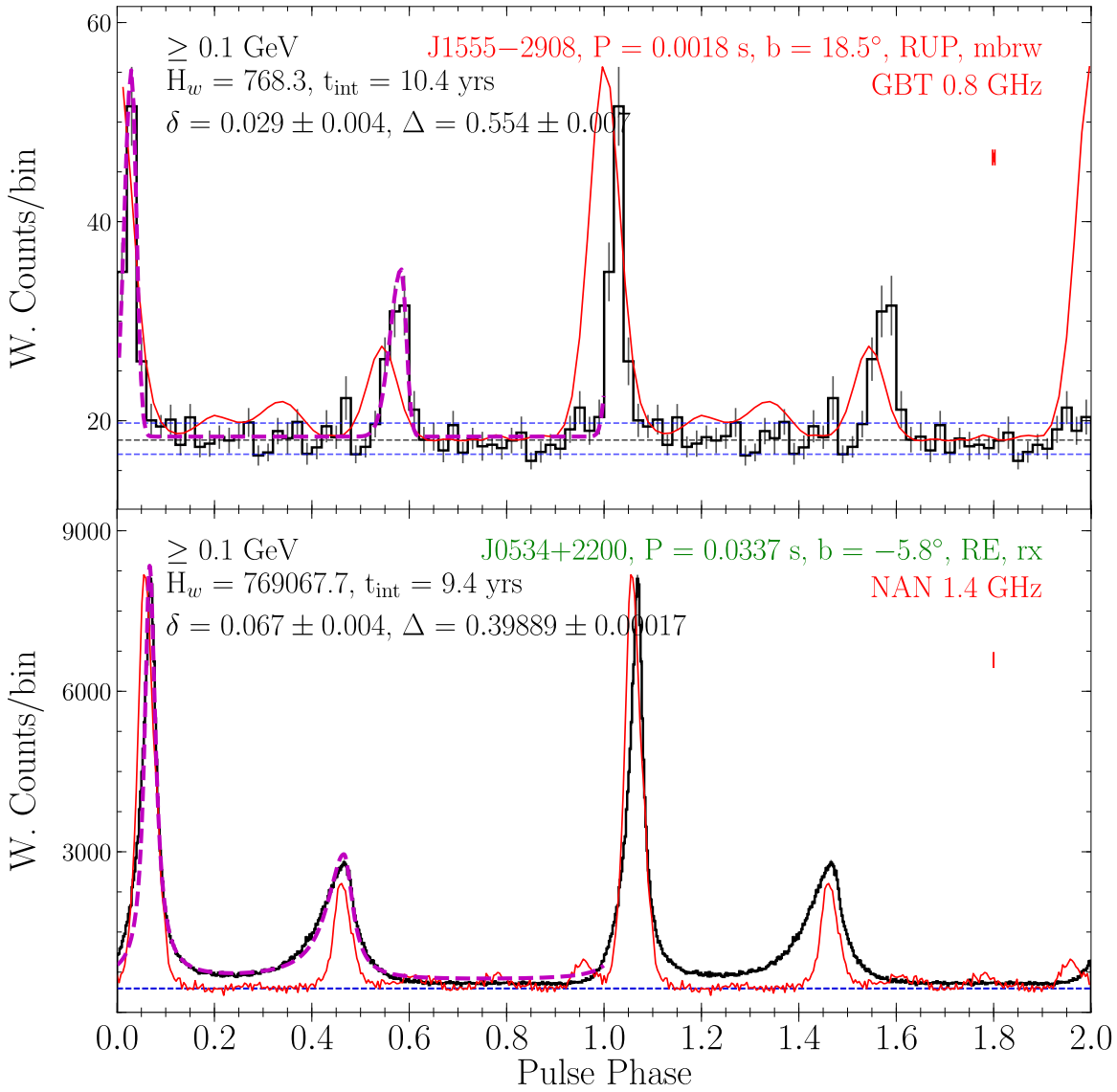

FIGURE 1.9: Pulse profile of a millisecond pulsar and a young pulsar (Crab pulsar). The gamma-ray profile is in black while the radio profile is in red.

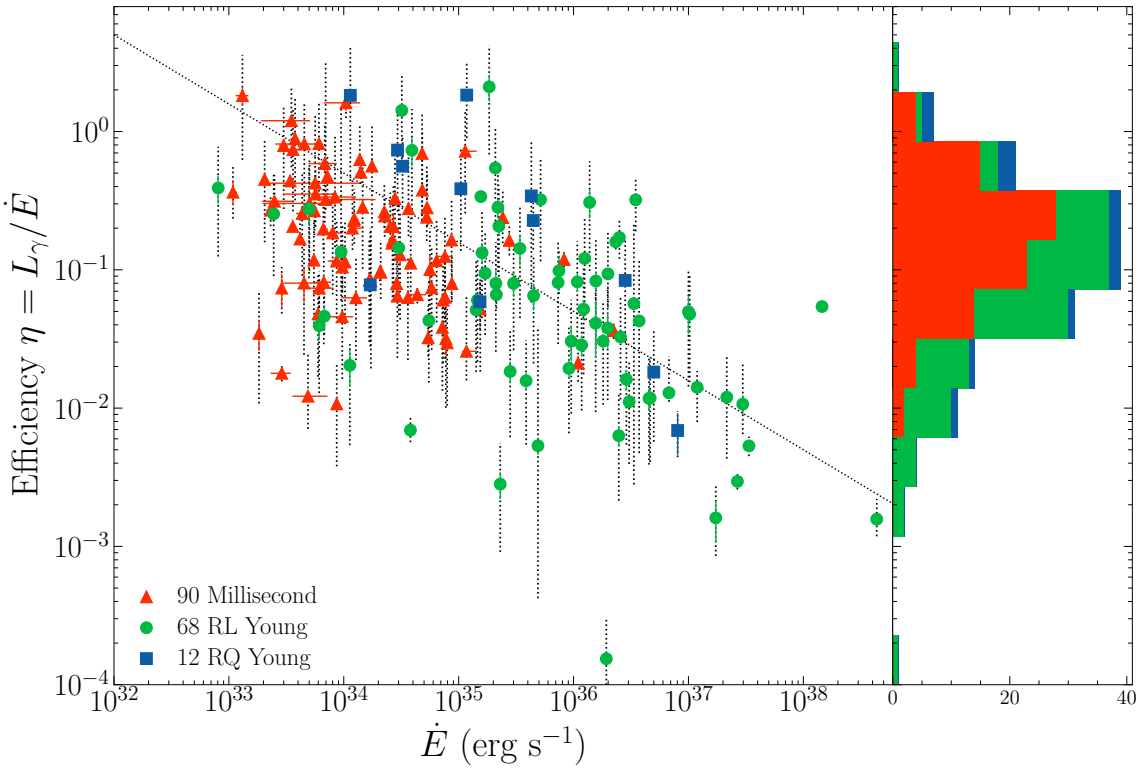

FIGURE 1.10: Gamma-ray efficiency as a function of spindown power (from Smith et al. 2023).

efficiencies. The computation of the efficiency does not come without some caveats. For example, the distance is known with some errors and the computation does not consider the inclination angle of each pulsar. However, one clear conclusion is that gamma-ray pulsars are efficient at converting their spindown power in gamma-ray radiation. This indicates that particle acceleration is occurring, thus a physical mechanism is at play. In order to produce gamma-ray photons, the accelerated particles must reach (ultra)-relativistic Lorentz factors. Consequently, theoretical models need to explain the high-energetics of pulsars but also give the mechanisms behind it.

But the puzzle of pulsars and their emission would not be complete without the recent discovery of TeV photons. Up to 2022, the only pulsar emitting TeV photons was the Crab pulsar (Ansoldi, S. et al., 2016). At these energies, ground based Cherenkov telescopes can be employed. By using the air-shower produced by the gamma-ray photons entering the atmosphere, we are able to recover the location of the source. This emission was for the moment an isolated case. However, in 2023, the HESS collaboration reported the detection of a 20 TeV emission coming from the Vela pulsar (Djannati-Ataï, 2022; H. E. S. S. Collaboration et al., 2023). The detection of both TeV emission is given in Fig. 1.11. Above 10 GeV, the SED of the Crab pulsar can be fitted with a power-law extending up to the TeV. However, this is not the case for the Vela pulsar where the SED breaks from an exponential cut-off to a power-law near TeV energies. With two different detections, the TeV emission from pulsars is confirmed. The mystery of the TeV emission from the Crab and Vela pulsars adds to the puzzle surrounding pulsars and is challenging the models. One thing is for sure: these high-energy photons are emitted by particles with very high Lorentz factors. One way of reaching this condition, is by having particles propagating in an extreme environment where the energy density is high. For pulsars, the most extreme conditions

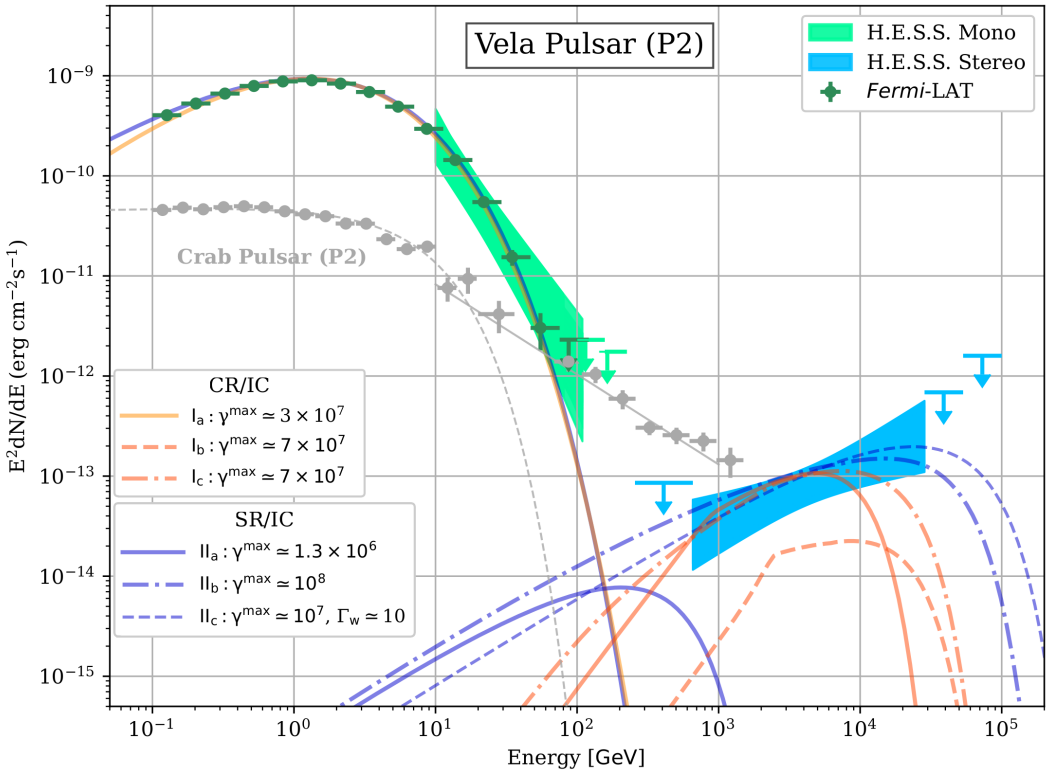

FIGURE 1.11: SED of the pulse P2 of the Vela pulsar, from H. E. S. S. Collaboration et al. (2023). The SED of the pulse P2 from the Crab pulsar is shown in grey.

are inside what is called the magnetosphere[5]. The latter corresponds to the environment close to the neutron star, filled with plasma, and where the magnetic field is the strongest. Therefore, theoretical models must explain how particles are accelerated to high Lorentz factors in the magnetosphere, in order to produce the observed gamma-ray emission. They also need to establish which mechanisms are able to convert the available energy in kinetic energy.

1.3 Black holes

1.3.1 Concept and first black holes

A black hole is defined as a region of space where gravity is so strong that nothing can escape from it, not even light. The existence of such astrophysical object was for a long time highly debated in the community. The first track of this idea goes back to 1784 when Reverend John Michell (Michell, 1784) mentioned the idea that above a given mass, even light could not have an escape velocity large enough to escape gravity. This idea was followed by a similar writing by Laplace (1799) using the same argument on the escape velocity. The proto-black holes, or "dark stars", were left aside for many time before coming back on the front scene with the theory of general relativity by Albert Einstein.
The concept of black hole was reintroduced in the physics community when Karl Schwarschild gave the first solution of Einstein's equations. In his paper, Schwarzschild (1916) derived the description of the spacetime centred around a mass assuming a spherically symmetrical sphere. Within the solution appeared a critical radius, later called the Schwarschild

[5]The magnetosphere here is defined as the environment between the surface of the neutron star and a few light-cylinders.

radius, $r_S = 2GM/c^2$ where G is the gravitational constant and M is the mass of the spherical body. It corresponds to the radius at which the escape velocity is equal to the speed of light, and acts as the boundary between the visible and the invisible. For $r > r_S$, the light suffers from the gravitational field of the mass but can still reach a distant observer. This is not the case any more for $r < r_S$, where not even light can fight against the gravitational attraction of the mass. The next important development occurred with the mathematician Roy Kerr. In 1963, Kerr published the exact derivation of the spacetime around a rotating mass (Kerr, 1963). This solution played an important role in the development of black hole's theory and still does. The current consensus among the black hole community is that black holes are simple objects which only need three fundamental parameters to be described. These parameters are the mass, the angular momentum or spin, and the electric charge. Black holes are often said to have no hair.

1.3.2 Emission from a non-emitting source

Proving the existence of black holes was not an easy task, especially when we remember that black holes do not emit light. Therefore, the community had to rely on indirect signs of the presence of black holes. Zel'dovich's first way of finding black holes was to look for binary systems in which the visible star seems to orbit around an invisible companion. With the trajectory of the secondary, it would be possible to estimate the mass of the invisible star. The second idea in the mind of Zel'dovich (1964) and Salpeter (1964) was based on the light emitted by accretion. Accretion is a physical phenomenon in which the surrounding matter (gas and dust) is set into rotation around the star. As the matter is rotating, it settles naturally in the form of a disc called an accretion disc. With differential rotation inside the disc, the material is losing angular momentum and falling inwards onto the star. The falling material will feel the gravitational field imposed by the star as it falls, thus being compressed and heated. The heated matter is able to radiate away some of its energy. In the case of a black hole, the matter radiates constantly before going dark when it crosses the event horizon. The radiation emitted by the infalling matter corresponds to a luminosity, which is finite. Known as the Eddington limit, the maximum luminosity from accretion is computed as

$$L_{\rm Edd} = \frac{4\pi G m_{\rm p} c}{\sigma_{\rm T}} = \frac{4\pi r_{\rm g} m_{\rm p} c^3}{\sigma_{\rm T}} = 1.3 \times 10^{38} \left(\frac{M}{M_\odot}\right) \mathrm{erg \cdot s^{-1}} \tag{1.6}$$

where M is the mass of the star, $m_{\rm p}$ is the mass of the proton (heaviest particle possible in the accreted material), and $\sigma_{\rm T}$ is the Thomson cross-section. This luminosity corresponds to the equilibrium luminosity between the gravitational force and the radiation pressure. Above this limit, the radiation pressure is stronger than gravity, and the radiating material close to the black hole prevents the outer material to fall in. Below the Eddington limit, the system radiates less and matter keeps falling in. $L_{\rm Edd}$ is an upper limit on the accretion powered luminosity for a spherical accretion. In reality, the accretion is not perfectly spherical and the opacity based on the Thomson scattering may not be the dominant one. Some systems can even be in the super-Eddington regime, $L > L_{\rm Edd}$.
If we assume that the accretion disc radiates as a black-body

$$L = 4\pi r^2 \sigma T^4 \tag{1.7}$$

$$\overset{(1.6)}{\Longrightarrow} T = \left(\frac{G M m_{\rm p} c}{\sigma_{\rm T} r^2 \sigma}\right)^{1/4} = \left(\frac{m_{\rm p} c^3}{\sigma_{\rm T} G M \sigma}\right)^{1/4}, \tag{1.8}$$

where σ is the Stefan-Boltzman constant and we consider $r = r_g = GM/c^2$ for a black hole. For a solar mass black hole, the temperature is

$$T \simeq 5 \times 10^7 \left(\frac{M}{M_\odot}\right)^{1/4} \text{K}. \tag{1.9}$$

Radiations with the above temperature correspond to an energy of $\mathcal{E} = 4.5$keV, which is in the X-ray band. Therefore, if a black hole is surrounded by an accretion disc emitting as a black body, the latter would be observable by an X-ray telescope. The assumption of a black-body radiation is valid if we consider that the disc is optically thick, meaning that only the surface of the disc is able to radiate photons away. In a similar way to gamma-ray observations, X-ray observations cannot be done on the ground. As the atmosphere is blocking the X-rays, the only solution was to have space telescopes. The X-ray sky became available to the community with the launch of *Uhuru* in 1970. This satellite discovered a new type of systems called X-ray binaries or microquasars.

1.3.3 Stellar mass black holes

X-ray binaries are composed of a companion star orbiting around a stellar-mass compact object (neutron star or black hole), where the accretion disc around the compact object is made from the material of the companion. The main difficulty for such systems is to distinguish if the compact object is a black hole or a neutron star. The most straightforward way to dispel any doubts is to know the mass of the compact object. If the latter is above $3M_\odot$, the neutron star scenario is directly excluded. The first candidate to pass this criterion was Cyg X-1, with a mass estimate of $M \geq 9.5M_\odot$ for a system located at 2.5kpc (Paczynski, 1974). With a more constrained distance, the compact object mass in the system is now estimated at $M \simeq 21M_\odot$ (Miller-Jones et al., 2021). This type of black hole is called a stellar mass black hole and is the direct result of the full collapse of a star. Many black holes of this kind where discovered in the past years via gravitational waves produced during merger. Very recently, a stellar mass black hole was discovered in our galaxy. Panuzzo et al. (2024) discovered a new stellar mass black hole located at a distance $d = 590$pc. This close-by black hole was found using the data from the Gaia satellite. The high precision of the astrometry gives a well-defined orbit allowing the authors to derive the mass of the black hole. The orbit of the star is given in Fig. 1.12. With the orbital constrain, the mass of the dark companion is estimated to be $M = 33M_\odot$. This estimation on the mass excludes the possibility of a neutron star companion, however it is still possible that the dark companion is a more exotic star.

Nevertheless, stellar mass black holes are not the only ones we find in the Universe. The second black hole flavour is the supermassive black holes.

1.3.4 Supermassive black holes

Active Galactic Nuclei

Supermassive black holes[6] are defined as black holes with a mass $M \geq 10^5 M_\odot$. They are believed to be at the centre of most galaxies, but their formation mechanism is not constrained yet. While many of them are in quiescence, some show large and strong jets and are called Active Galactic Nuclei (AGN). One of the first observation of a jet from a galaxy was observed by Heber D. Curtis in 1918. His report states the presence of "a curious straight ray [...] apparently connected with the nucleus by a thin line of matter", during his observation of NGC4486 (M87) in optical. The rise of radio astronomy in the 1930s,

[6] also a great song by Muse

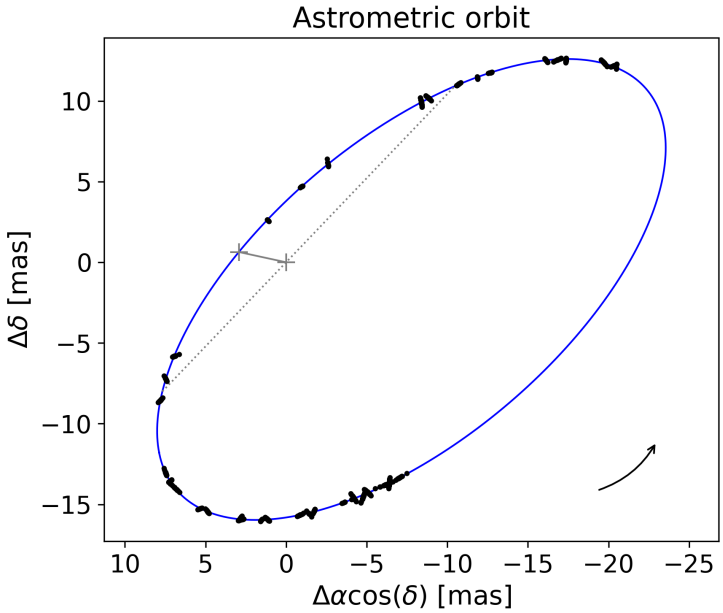

FIGURE 1.12: Astrometry measurements of a star orbiting the newly discovered stellar mass black hole, figure from Panuzzo et al. (2024).

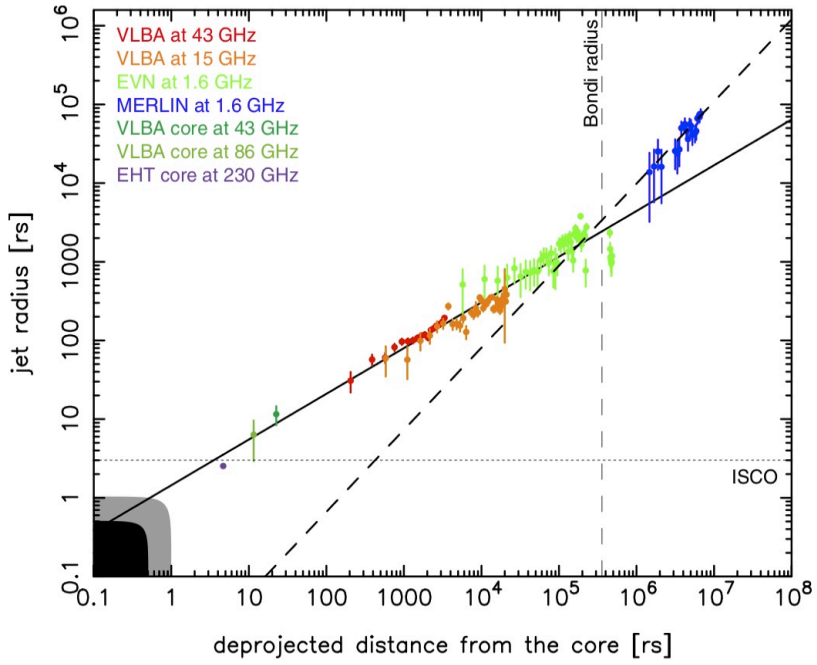

FIGURE 1.13: Relativistic jet from M87 from Blandford et al. (2019).

allowed Karl Jansky to detect radio waves originating from galaxies. The field greatly improved its observations when astronomers realised that multiple radio dishes could be combined to increase the angular resolution. Thanks to continuous improvements, Jennison and Das Gupta (1953) identified the origin of the radio emission in Cygnus A. The radio source corresponds to two lobes equally separated from the centre of the galaxy, also emitting radio waves.

As years went by, radio telescopes increased their angular resolution power and are now able to probe the full scales of jets. In Fig. 1.13, we show the jet radius from M87 as a

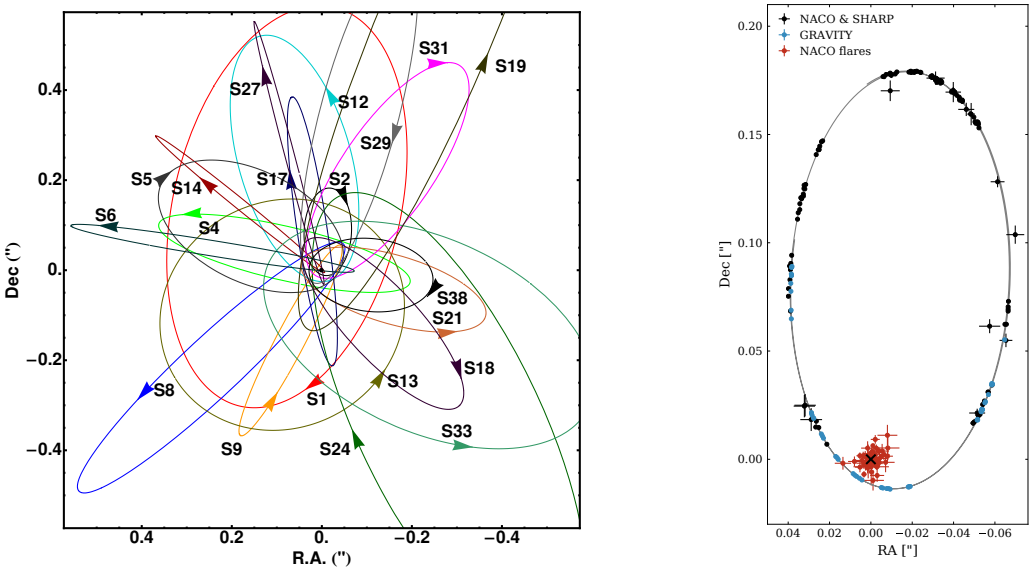

(A) (B)

FIGURE 1.14: A) S-stars orbits around the Galactic centre, from Gillessen et al. (2009). B) orbit of the star S2, from GRAVITY Collaboration et al. (2020). The black cross marks the position of the SgrA*.

function of distance from the core. We can see on the figure that it is possible to probe the very large scale $r \sim 10^7 r_S$, but also the scale close to the core up to a few Schwarzschild radii. Looking at the inner part of the jet raises questions about its origin and its potential connection to the black hole.

Proving supermassive black holes existence

Supermassive black holes are black holes with extremely high mass. In order to know the mass of the supermassive black hole, it is possible to use the exact same technique as for stellar mass black holes. In the case of a supermassive black hole, the astrometry is an even more complex task that for stellar mass black holes. Because supermassive black holes are supposed to be located at the centre of galaxies, the astrometry technique can be used on known galaxies. The "most obvious" target was the centre of the Milky Way. However, even with only a distance of 8.2kpc, this target was already a challenge. Optical and UV telescopes were of no use as the Galactic centre is darkened by the gas and dust. However, radio, infra-red, X-rays, and gamma-rays are still able to pierce through the material to probe the Galactic centre. The development of adaptive optics (Babcock, 1953) had a strong impact on the observations of the Galactic centre. These new optics lifted many issues and unveiled the trajectory of stars one by one.

In Fig. 1.14a, we show the recorded trajectories of stars at the Galactic centre. 26 trajectories are represented, they all indicate that stars are orbiting a dark companion. Within the wide range of orbits, the most interesting one is the orbit of the S2 star. A zoomed-in view of its trajectory is given in Fig. 1.14b. The star is monitored since 1992 and has a period of 15 years. This long monitoring allowed to see the full elliptic trajectory and even the precession of its orbit predicted by general relativity (GRAVITY Collaboration et al., 2020). The constrain given by the trajectory yields a dark companion mass of $M_{\mathrm{SgrA}^\star} \simeq 4.3 \times 10^6 M_\odot$. Given the mass and the compactness of the region ($\theta \simeq 20\mu$as) where the mass needs to be, the prediction of a supermassive black hole is the most reliable one.
The observations in infrared and X-rays reveal the existence of flares near SgrA*. During

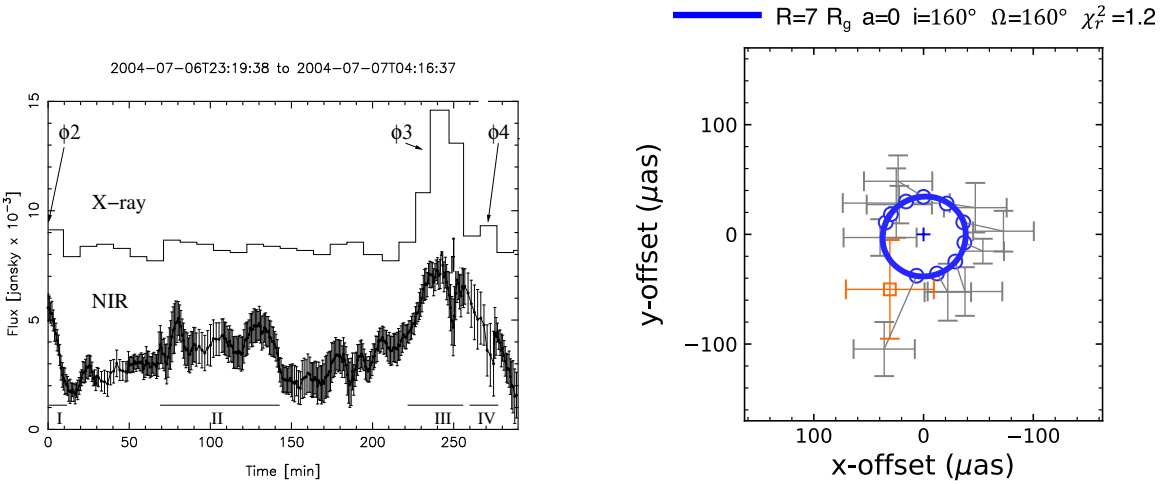

(A) (B)

FIGURE 1.15: A) Simultaneous near infrared and X-ray observations of a SgrA* flare, from Eckart et al. (2006). B) Hotspot orbit around SgrA*, from GRAVITY Collaboration et al. (2018). Data points are in grey while the best fit is in blue.

a simultaneous observations campaign, Eckart et al. (2006) revealed that when an X-ray flare is detected an infrared counterpart is observed, see Fig. 1.15a. However, the opposite is not true, infrared flares occur on average four times per day while X-ray flares are of the order of once per day.

More recently, the GRAVITY Collaboration et al. (2018) reported the orbit of a near-infrared flare, see Fig. 1.15b. The location of the flare is consistent with a hotspot orbiting at the inner-most stable orbit, $r = 7r_g$. The physical mechanism behind the flares is believed to be synchrotron radiation emitted by electrons. Flares are also observable in the gamma-ray band for the radio galaxy M87 (Aharonian et al., 2006), PKS 2155-304 (Aharonian et al., 2007) and many more. The variability and high energy flares point towards a magnetospheric origin, where the energy density is high. This origin is also supported by the timescales of the variability being close the light crossing time r_g/c.

"Bring me that horizon"

On the quest of understanding and characterising supermassive black holes and their environment, the Event Horizon Telescope (EHT) collaboration tried to produce images at the horizon scale. Thanks to the Very Long Baseline Interferometer (VLBI), the EHT collaboration was able to observe SgrA* and M87*, the radio sources at the core of SgrA and M87. One of the holy grail of black hole observations is shown in Fig. 1.16.

In the figure, we see the radiation emitted by the plasma orbiting close to the black hole. The origin of the observed emission is most likely coming from synchrotron radiation emitted by relativistic electrons. The asymmetric brightness of the ring in both images is presumably due to Doppler boosting. We note that while the global structure of the ring can be trusted, the details should be considered with a pinch of salt as they depend on the reconstruction method used. Both images do not show the black hole but the shadow (Luminet, 1979; Falcke et al., 2000) left by the event horizon. The shadow corresponds to the boundary of the emitting region and is larger than the event horizon itself. In curved spacetime, photons travel along geodesics which can cross the event horizon. When this happens, the photon is absorbed by the black hole and is not detected. The lensing of photons artificially increases the size of the black hole, leaving behind a shadow. The outer edge of this shadow is called the photon ring. The latter corresponds to the locus

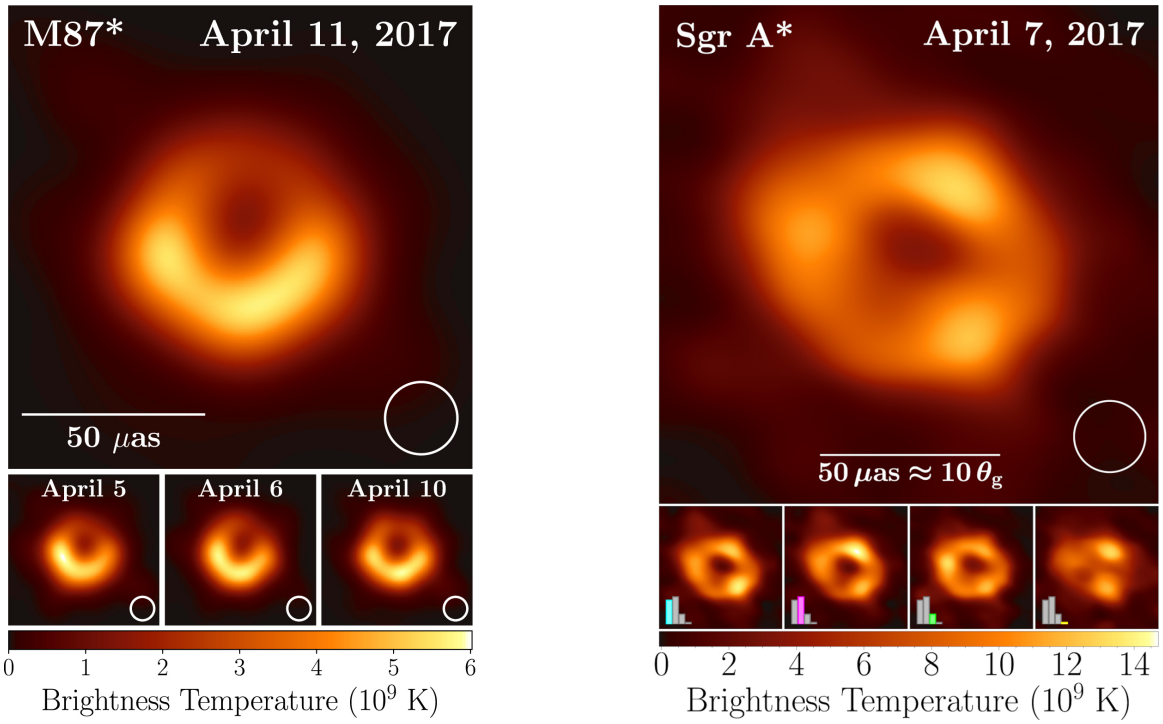

FIGURE 1.16: Event Horizon Telescope observations of the close environment of the supermassive black holes M87⋆ (left) and SgrA⋆ (right). The images are respectively from Event Horizon Telescope Collaboration et al. (2019) and The Event Horizon Telescope Collaboration (2023).

where photon orbits are not bound any more to the black hole, and can escape to a distant observer. The size of the photon ring is related to the black hole mass by

$$r_{\rm ph} = \sqrt{27} r_{\rm g} = \sqrt{27} \frac{GM}{c^2}. \tag{1.10}$$

The above equation originally assumes that the emission is coming from an optically thin disc. A recent study by Narayan et al. (2019) indicates that the photon ring does not dependent on the status of the accretion of the disc. With the shadow of both M87⋆ and SgrA⋆, we can compute the mass of each supermassive black holes. For $M87^\star$ and SgrA⋆, the photon ring yields $M_{\rm M87^\star} = 6.5 \times 10^9 M_\odot$ and $M_{\rm SgrA^\star} = 4 \times 10^6 M_\odot$. The result for SgrA⋆ is in agreement with the mass constrained by stellar dynamics. Further analysis on the polarimetry of the horizon scale plasma indicates the existence of a large-scale poloidal magnetic field. The EHT collaboration reported magnetic fields of $B \sim 1 - 30$G for M87⋆ (Event Horizon Telescope Collaboration et al., 2021), and $B \simeq 30$G for SgrA⋆ (Event Horizon Telescope Collaboration et al., 2022). The presence of this magnetic field could have a strong impact on the dynamics of the plasma in these regions, i.e. in the magnetosphere.

The results from the EHT indicate that a hot plasma orbits around black holes at the horizon scale. This plasma emits infrared radiation and presents an asymmetric brightness. It might also be responsible of the different flares and high variability observed at different energies. Understanding the behaviour of this plasma could bring a lot of potential answers for the different observed signatures. Therefore, studying the close environment, i.e. the magnetosphere of black holes, is essential if we want to explain the observations.

1.4 Concluding remarks

Stellar mass compact objects are born from extremely violent events in which a massive star collapses on itself, whereas the formation of supermassive black holes is still not clear. As a result, neutron stars and black holes are formed. Whether it is black holes or pulsars, both compact objects exhibit emissions across the full electromagnetic spectrum, even up to TeV energies. If we want to understand how this emission is produced, we need to look at the close environment of both compact objects, where the energy density is the highest. In black holes and pulsars, the highest energy density is inside the magnetosphere where the gravitational force or the magnetic field are the strongest.

1.5 [Français] Points clés du chapitre

1.5.1 Pulsars : étoiles à neutrons pulsantes

Dans ce chapitre, nous avons vu différentes observations entourant les objets compacts en nous focalisant sur les étoiles à neutrons et les trous noirs. Ces deux types d'objets compacts sont le résultat de l'effondrement d'une étoile sur elle-même à la fin de sa vie. Parmi les étoiles à neutrons, on distingue une catégorie particulière appelée pulsars. Ce terme désigne les étoiles à neutrons qui sont initialement détectés via leurs pulsations radio. Il est possible de représenter l'ensemble des pulsars dans un unique diagramme appelé diagramme P-$\dot{P}$. Grâce à la période P et sa dérivée $\dot{P}$, on peut calculer trois paramètres intrinsèques aux pulsars : l'âge τ, le champ magnétique de surface $B_\star$ et la puissance $\dot{E}$. Les pulsars détectés peuvent tout d'abord être divisés en deux catégories : les pulsars dits normaux et les pulsars millisecondes. La première catégorie correspond aux pulsars présentant des caractéristiques similaires au premier pulsar découvert. La seconde catégorie correspond à des pulsars dits recyclés qui sont des pulsars âgés où l'on suppose qu'un épisode d'accrétion de matière provenant d'une étoile compagnon a eu lieu. Parmi tous les pulsars détectés, un en a été particulièrement étudié : le pulsar du Crabe. Ce dernier est une véritable pierre de Rosette pour les observations de pulsars. Ses pulsations sont observées à toutes les longueurs d'onde, de la radio jusqu'aux rayons gamma. Les pulsars produisant ces pulsations dans la bande gamma constituent une sous-catégorie importante car elle contient les pulsars les plus énergétiques connus. Ce champ d'étude est devenu accessible grâce au satellite *Fermi*-LAT qui observe dans la bande gamma entre 10 MeV et 300 GeV. La classification précédente est toujours valide pour ce type d'objets, les pulsars gamma se divisent en pulsars gamma normaux et en pulsars gamma millisecondes. Quelle que soit la sous-catégorie de pulsars gamma, ces objets sont des sources très efficaces avec des taux de conversion entre la puissance de rotation et la luminosité gamma allant de 1 à 100%. Les modèles théoriques doivent donc expliquer comment l'émission à très haute énergie est produite et déterminer quel mécanisme en est responsable, une piste très prometteuse est la magnétosphère. Ce puzzle vient récemment d'être complété avec la validation des pulsars en tant qu'émetteurs au TeV. Après une première détection pour le pulsar du Crabe et une seconde pour le pulsar Vela, il est désormais certain que les pulsars peuvent accélérer des particules proche de la limite théorique.

1.5.2 Trous noirs

Un trou noir est défini comme une région de l'espace où la gravité est si forte que rien ne peut s'en échapper, pas même la lumière. L'existence d'un tel objet astrophysique a longtemps été un sujet de débat au sein de la communauté scientifique. Ce n'est qu'au siècle dernier que le concept de trou noir est devenu concret. Prouver l'existence d'un objet n'émettant aucune lumière n'est pas chose facile. Une méthode consiste à trouver un système binaire dans lequel une étoile semble orbiter autour d'un objet massif invisible. Une autre façon est d'observer la lumière émise par le phénomène d'accrétion. Pendant ce processus, le matériel en chute est chauffé et rayonne, ce qui permet d'associer à ce rayonnement une luminosité et une température.

Pour les trous noirs, deux catégories sont à distinguer : les trous noirs de masse stellaire et les trous noirs supermassifs. Les trous noirs de masses stellaires sont des trous noirs dont la masse varie de trois masses solaires à quelques dizaines de masses solaires. Les trous noirs sont qualifiés de supermassifs lorsque la masse de l'objet est supérieure à $10^5\,M_\odot$. Le mécanisme de formation de ces objets supermassifs reste inconnu à ce jour. On suppose que de tels objets se trouvent au centre des galaxies. Beaucoup d'entre eux

sont dans des états quiescents, mais certains possèdent des jets puissants et sont alors appelés Noyaux Actifs de Galaxies. La preuve de leur existence a été apportée par l'étude des orbites des étoiles au niveau du centre galactique. Cette étude a conclu que ces étoiles orbitent autour d'un compagnon invisible de masse $M_{\mathrm{SgrA}^\star} \simeq 4.3 \times 10^6 M_\odot$, situé dans une région très compacte. Au vu de la taille de la région et de la masse nécessaire, un trou noir supermassif est une hypothèse raisonnable.
Cette source présente également une variabilité importante avec des éruptions en infrarouge et en rayons X. Une campagne d'observation menée par la collaboration GRAVITY a indiqué que les éruptions vues en infrarouge étaient compatible avec un point chaud gravitant sur l'orbite stable la plus interne. D'autres noyaux actifs de galaxies présentent des éruptions, certaines étant même produites dans la bande gamma. L'observation des trous noirs supermassifs a pris un tournant récemment grâce à la collaboration EHT. En utilisant de l'interférométrie à très longue ligne de base, la collaboration a pu produire des images des abords des trous noirs SgrA* et M87. Ces images montrent qu'un plasma chaud orbite autour des trous noirs à l'échelle de l'horizon. Ce plasma émet un rayonnement infrarouge et présente une luminosité asymétrique. Il pourrait également être à l'origine des différentes éruptions et de la grande variabilité observée à différentes énergies. Comprendre le comportement de ce plasma pourrait apporter de nombreuses réponses aux différentes signatures observées. Par conséquent, l'étude de l'environnement proche, c'est-à-dire de la magnétosphère des trous noirs, est essentielle pour expliquer ces observations.

1.5.3 Résumé

Les objets compacts de masse stellaire naissent d'événements extrêmement violents au cours desquels une étoile massive s'effondre sur elle-même. Il en résulte la formation d'étoiles à neutrons et de trous noirs. Qu'il s'agisse de trous noirs ou de pulsars, ces deux objets compacts émettent dans tout le spectre électromagnétique, jusqu'à des énergies de l'ordre du TeV. Si nous voulons comprendre comment cette émission est produite, nous devons examiner l'environnement proche de ces objets compacts, là où la densité d'énergie est la plus élevée. Dans les trous noirs et les pulsars, cette densité d'énergie maximale se trouve à l'intérieur de la magnétosphère, là où la force gravitationnelle ou le champ magnétique sont les plus forts.

CHAPTER 2

Theoretical context

Contents

In Chap. 1, we discussed the observational signatures associated with pulsars and black holes. However, behind any signatures must exist a physical phenomenon or mechanism responsible for the emission. In this chapter, we will see the theoretical developments made by the community to try to have a better understanding of these objects. In Sect. 2.1, we will focus on pulsar theory from the very first models up to current models. We will also detail the physical mechanisms at play in relativistic magnetospheres. In Sect. 2.3, we will describe some aspects of black hole theory and we will see that it is the general relativistic analogue of pulsar theory. Some valuable reviews on pulsar theory can be found in Cerutti and Beloborodov (2017) and Philippov and Kramer (2022).

2.1 First models

In order to tackle the theory of relativistic magnetospheres, we will rely on Maxwell's equations and on plasma processes. Maxwell's set of equations is the following

$$\frac{\partial \mathbf{B}}{\partial t} = -c\,\boldsymbol{\nabla} \times \mathbf{E} \tag{2.1}$$

$$\frac{\partial \mathbf{E}}{\partial t} = c\,\boldsymbol{\nabla} \times \mathbf{B} - 4\pi \mathbf{J}, \tag{2.2}$$

$$\boldsymbol{\nabla} \cdot \mathbf{B} = 0 \tag{2.3}$$

$$\boldsymbol{\nabla} \cdot \mathbf{E} = 4\pi\rho \tag{2.4}$$

where $\mathbf{B}$ is the magnetic field, $\mathbf{E}$ is the electric field, $\mathbf{J}$ is the current density and ρ is the charge density. This set of equations describes the time evolution of an electromagnetic field in a plasma of charged particles. Knowing the behaviour of the electromagnetic field is of great interest to explain the various observational signatures. With relativistic magnetospheres being among the most extreme environments in terms of energy densities (magnetic and gravitational), Quantum Electrodynamics (QED) processes play a very important role. Therefore, they should be considered during the development of models with processes such as pair production (via Breit-Wheeler process) or photon-electron scattering (Compton and inverse Compton scattering).

2.1.1 Vacuum magnetosphere

One of the very first frameworks of pulsar theory was to consider the pulsar to be in vacuum. This assumption comes from Hoyle et al. (1964). Their argument relies on gravity and the propagation of electromagnetic waves after the formation of the neutron star. The authors state that "the strong gravitational field of the star creates a near-vacuum immediately outside itself, and the electromagnetic waves are free to travel out into space. Moreover, any residual gas outside the star would simply be swept away by the pressure of the electromagnetic waves".

The first models (Pacini, 1967; 1968; Ostriker & Gunn, 1969) were based on this assumption. Even if the vacuum assumption is not correct, it was a first useful approximation for the pulsar theory. The global picture of a pulsar is the following. A pulsar is a rotating and highly magnetised neutron star having two characteristic axes, the magnetic axis or magnetic moment $\boldsymbol{\mu}$ and the rotation axis with an angular velocity $\boldsymbol{\Omega}$. In order to have a simpler picture we will not consider an oblique rotator but an aligned one ($\boldsymbol{\mu} \parallel \boldsymbol{\Omega}$). In this picture, we lose the pulsation part of the emission as the problem is now axisymmetric with respect to the spin axis $\boldsymbol{\Omega}$. We consider the neutron star to be a perfect conductor with a magnetic field $\mathbf{B}_\star$ thus, we can write $\mathbf{E}'_\star = 0$ in the corotating frame where $\mathbf{E}'_\star$ is the electric field inside the star. This condition allows us to know the electric field $\mathbf{E}_\star$ in the lab frame with

$$\mathbf{E}'_\star = \mathbf{E}_\star + \frac{\mathbf{v} \times \mathbf{B}_\star}{c} = \mathbf{0} \tag{2.5}$$

where the velocity is $\mathbf{v} = \boldsymbol{\Omega} \times \mathbf{r}$. The analogy can be made with an unipolar inductor or Faraday disk. We consider a perfect conducting disc rotating with the angular velocity Ω immersed in a vertical magnetic field $\mathbf{B}_\mathrm{F}$. The rotation of the metallic disc forces the charges inside it into rotation. The different charges will move to balance the Lorentz force inducing an electric field inside the disc, $\mathbf{E}_\mathrm{disc} = -\mathbf{v} \times \mathbf{B}_\mathrm{F}/c$ (rotating frame). The result is a potential drop and a charge separation. For $\boldsymbol{\Omega} \cdot \mathbf{B} > 0$, negative charges are located close

to the "poles" of the disc (spin axis) while positive charges are localised on the outside of the disc. This is the same situation inside a neutron star, where the negative charges will be located at the poles and the positive ones near the equator.

The full description of a rotating dipole was derived by Deutsch (1955). The solution describes the external electric field ($r > r_\star$). To do so, we need to solve Poisson's equation in vacuum $\nabla^2\mathcal{V} = 0$. The boundary condition for this equation is set by the potential drop $\Delta\mathcal{V}$ across the neutron star surface in spherical coordinates.

$$\Delta\mathcal{V} = \int_{\mathcal{C}} \mathbf{E}\cdot\mathrm{d}\mathbf{l} = \int_0^\theta \mathbf{E}_\theta r_\star \mathrm{d}\theta' \tag{2.6}$$

where $E_\theta = -v_\phi B_r/c$. This comes from Eq. (2.5) with $B_r = 2\mu\cos\theta/r_\star^3$ the dipolar surface magnetic field and $v_\phi = \Omega r_\star \sin\theta$. The potential difference is

$$\Delta\mathcal{V} = \mathcal{V}(r_\star,\theta) - \mathcal{V}(r_\star,0) = \frac{\Omega\mu}{cr_\star}\sin^2\theta \tag{2.7}$$

This boundary condition is then used to solve for the full electric potential

$$\forall r \geq r_\star, \quad \mathcal{V}(r,\theta) = \left(\mathcal{V}_{\rm mono} + \frac{2\Omega\mu}{3cr_\star}\right)\frac{r_\star}{r} + \frac{\Omega\mu}{cr_\star}\left(\frac{r_\star}{r}\right)^3\left(\sin^2\theta - \frac{2}{3}\right) \tag{2.8}$$

where $\mathcal{V}_{\rm mono} = \mathcal{V}(r_\star,0)$ is the contribution coming from a monopole. If we assume that the star has a zero net charge at its formation then the net charge is $Q = 0$ for $\mathcal{V}_{\rm mono} = -2\Omega\mu/3cr_\star$, removing the first term on the right-hand side of Eq. (2.8). Finally, the general expression of the electric field $\mathbf{E} = -\boldsymbol{\nabla}\mathcal{V}$ is

$$E_r = \left(\mathcal{V}_{\rm mono} + \frac{2\Omega\mu}{3cr_\star}\right)\frac{r_\star}{r^2} + \frac{\Omega\mu}{c}\frac{r_\star^2}{r^4}\left(1 - 3\cos^2\theta\right) \tag{2.9}$$

$$E_\theta = -\frac{\Omega\mu}{c}\frac{r_\star^2}{r^4}\sin(2\theta) \tag{2.10}$$

$$E_\phi = 0 \tag{2.11}$$

The radial component presents a discontinuity at the stellar boundary and causes the presence of a surface charge $4\pi\Sigma = E_r - E_r^\star$. Taking $E_r^\star = v_\phi B_\theta^\star/c$ and $B_\theta^\star(r_\star,\theta) = \mu\sin\theta/r_\star^3$ for the surface dipole magnetic field,

$$Q_{int} = \frac{1}{4\pi}\iint E_r^\star r_\star^2 \sin\theta \mathrm{d}\theta\mathrm{d}\phi = \frac{2\Omega\mu}{3c} \tag{2.12}$$

where $Q_{\rm int}$ is the interior net charge of the star. For the surface net charge,

$$4\pi\Sigma = -\frac{2\Omega\mu}{cr_\star}\cos^2\theta \tag{2.13}$$

giving the total surface charge

$$Q_\star = -\frac{2\Omega\mu}{3c} = -Q_{\rm int}. \tag{2.14}$$

The star has a zero net charge due to the perfect counterbalancing of the surface charge by the interior charge (Michel & Li, 1999). The full expression of the electric and magnetic field for the vacuum solution is

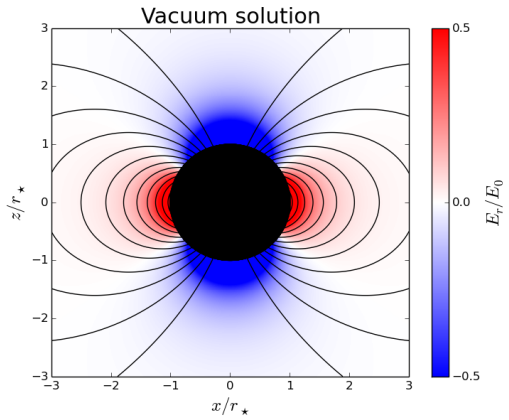

(A) Radial electric field

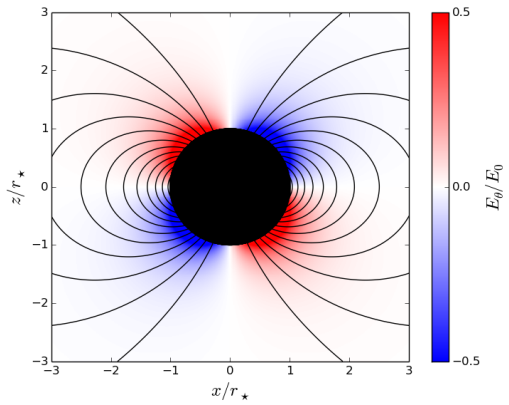

(B) Polar electric field

FIGURE 2.1: Vacuum electric field for a zero net charge of an aligned rotator along the z-axis. Figure taken from Cerutti and Beloborodov (2017).

$$B_r = 2B_\star \left(\frac{r_\star}{r}\right)^3 \cos\theta \tag{2.15}$$

$$B_\theta = B_\star \left(\frac{r_\star}{r}\right)^3 \sin\theta \tag{2.16}$$

$$B_\phi = 0 \tag{2.17}$$

$$E_r = \frac{\Omega r_\star B_\star}{c} \left(\frac{r_\star}{r}\right)^4 \left(1 - 3\cos^2\theta\right) \tag{2.18}$$

$$E_\theta = -\frac{\Omega r_\star B_\star}{c} \left(\frac{r_\star}{r}\right)^4 \sin(2\theta) \tag{2.19}$$

$$E_\phi = 0 \tag{2.20}$$

with the equatorial surface magnetic field $B_\star = \mu/r_\star^3$. This electromagnetic configuration is only valid in vacuum with a zero net charge ($Q = 0$) and gives a quadrupolar electric field (Fig. 2.1). If $Q \neq 0$, the electric field has a monopole component.

The solution can be generalised for an oblique rotator with an angle $\widehat{(\boldsymbol{\mu}, \boldsymbol{\Omega})} = \chi$. We can compute the radial Poynting flux of the generalised solution (Pacini, 1968),

$$L_{\text{vacuum}} = \iint \boldsymbol{\Pi} \cdot \mathrm{d}\mathbf{S} = \iint c \left(\frac{\mathbf{E} \times \mathbf{B}}{4\pi}\right)^r \cdot \mathrm{d}\mathbf{S} = \frac{2}{3} \frac{\mu^2 \Omega^4}{c^3} \sin^2\chi. \tag{2.21}$$

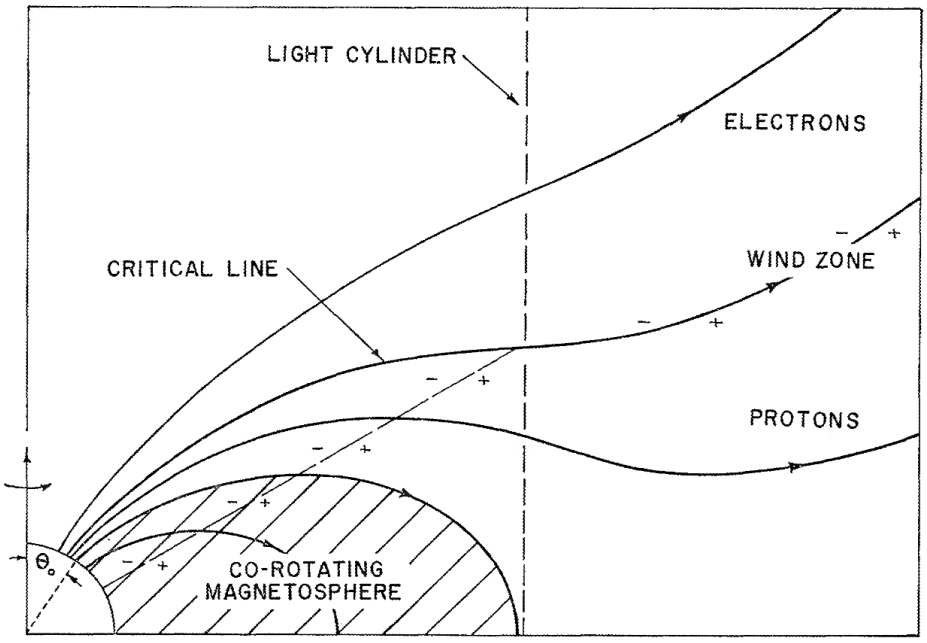

FIGURE 2.2: Sketch of the force-free magnetosphere for an aligned rotator. Figure taken from Goldreich and Julian (1969).

We can see that for the aligned case $\chi = 0$, there is no power emitted. The emission is maximum for an orthogonal rotator.

2.1.2 Beyond the vacuum approximation: Force-free magnetosphere

The main flaw of the previous solution is regarding the vacuum approximation. For a pulsar, we have a strong magnetic field, meaning that particles are magnetised and have a maximum drift velocity $\mathbf{v}_{\rm drift} = \mathbf{E} \times \mathbf{B}/B^2$. The movement of particles is thus constrained in the perpendicular direction of the magnetic field lines, but not in the direction parallel to the magnetic field. A strong parallel electric field develops at the surface of the star $E_{\parallel} = \mathbf{E} \cdot \mathbf{B} \neq 0$. This component is unscreened and is able to accelerate particles (electrons or ions) from the crust. The lifting of particles was found possible from the vacuum solution by Goldreich and Julian (1969) when they realised that the strength of the parallel electric field can easily exceed the gravitational force. In their model, Goldreich and Julian (1969) considered a magnetosphere filled with plasma for an aligned rotator. The sketch of their model is shown in Fig. 2.2. These results still represent the basis of modern pulsar theory.

For this model, we need to consider a steady-state solution. With this assumption, the electric field vanishes in the frame of the moving plasma so that, $\mathbf{E} \cdot \mathbf{B} = 0$ thus, the corotating electric field is $\mathbf{E} = \mathbf{E}_{\rm cor} = -(\mathbf{v} \times \mathbf{B})/c = -(\mathbf{\Omega} \times \mathbf{r}) \times \mathbf{B}/c$. The light-cylinder, $R_{\rm LC} = c/\Omega$, corresponds to the cylindrical radius at which the corotation velocity is $v_{\rm cor} = c$. For $r > R_{\rm LC}$, corotation cannot be sustained by the plasma as its corotation velocity would be greater than the speed of light. Regarding the magnetic field lines anchored on the surface, two configurations are possible, either they are in the corotating magnetosphere (inside the light-cylinder) and are closed, or they are crossing the light-cylinder and open up to infinity. The opened field line region is referred to as the wind zone and the closed region as the corotating magnetosphere. With the steady-state and axisymmetric assumptions, magnetic field lines are also isorotation surfaces via Ferraro's law (Ferraro, 1937), meaning that field lines have a constant angular velocity. Thanks to the corotating electric field, Goldreich and Julian (1969) derived a charge density

$$\rho_{\rm GJ} = \frac{1}{4\pi}\boldsymbol{\nabla}\cdot\mathbf{E}_{\rm cor} \simeq -\frac{\boldsymbol{\Omega}\cdot\mathbf{B}}{2\pi c} = \frac{B_\star}{2\pi c}\left(\frac{r_\star}{r}\right)^3\left(3\cos^2\theta - 1\right) \tag{2.22}$$

where $\rho_{\rm GJ}$ is often called the Goldreich-Julian charge density, derived for a dipole magnetic field. It translates into a number density $n_{\rm GJ} \sim \rho_{\rm GJ}/e$ (Goldreich-Julian density). This corresponds to the required density needed to screen the parallel electric field. This is equivalent to maintaining the corotation. In the wind region, electrons are flowing out and drive a current density $J_{\rm GJ} = c\rho_{\rm GJ}$ which induces a toroidal magnetic field. This exerts a spindown torque on the pulsar, which can be computed as the net radial Poynting flux carried outwards. Estimates of the Poynting flux were found via simulations, a long time after the seminal paper of Goldreich and Julian (1969), by Timokhin (2006) and Gruzinov (2005). The estimate is,

$$L_0 = \iint c\left(\frac{\mathbf{E}_{\rm cor}\times\mathbf{B}}{4\pi}\right)\cdot\mathrm{d}\mathbf{S} = \frac{\mu^2\Omega^4}{c^3} \tag{2.23}$$

The aligned rotator configuration radiates energy in the form of a Poynting flux, which was not the case for the vacuum solution.

We know that the magnetic field in the magnetosphere is strong, thus a reasonable question to ask is if the energy of the system is dominated by the magnetic field. To have the answer, we can compute the different ratios for the energy densities involved.

$$\frac{U_{grav}}{U_B} = \left|\frac{-GMm_{\rm p}/r_\star}{B_\star^2/8\pi}\right| \approx 10^{-21} \qquad \frac{U_{kin}}{U_B} \approx \frac{n_{\rm GJ}\gamma m_p c^2}{B_\star^2/8\pi} \approx 10^{-8} \tag{2.24}$$

with $B_\star = 10^9$ G, $M = M_\odot$, $n_{GJ} \simeq B_\star/2\pi R_{\rm LC}e \approx 10^{-11}$ cm^{-3}, $\gamma = 10$ and $P = 2\pi/R_{\rm LC} = 1$ ms. These ratios confirm the fact that the plasma is dominated by the magnetic energy in the magnetosphere. Under these assumptions, the plasma is described by the "force-free electrodynamics". The force-free electrodynamics is a limit of the relativistic magnetohydrodynamics (MHD). It corresponds to a regime where the plasma is magnetically dominated, leading to the Lorentz force being the dominant one compared to the pressure, inertia, and gravity terms (Eq. 2.24). The force-free regime is derived using the momentum equation

$$\rho\Big(\partial_t\mathbf{u} + (\mathbf{u}\cdot\boldsymbol{\nabla})\,\mathbf{u}\Big) = -\boldsymbol{\nabla}P + \frac{\mathbf{J}\times\mathbf{B}}{c} + \rho\mathbf{E} - \rho\boldsymbol{\nabla}\phi_{\rm G} \tag{2.25}$$

$$\overset{(2.24)}{\Longrightarrow} \rho\partial_t\mathbf{u} = \frac{\mathbf{J}\times\mathbf{B}}{c} + \rho\mathbf{E} = 0 \tag{2.26}$$

where $\boldsymbol{\nabla}P, \mathbf{J}\times\mathbf{B}/c + \rho\mathbf{E}, \rho\boldsymbol{\nabla}\phi_{\rm G}$ are the pressure gradient, the Lorentz, and the gravity forces. In this framework, we assume that the inertia of the plasma is small. The force-free condition is written in a more compact way as

$$F_{\mu\nu}I^\nu = 0 \tag{2.27}$$

where $F_{\mu\nu}$ is the electromagnetic tensor and I^ν is the 4-current. Two force-free conditions can be expressed from Eq. (2.27). Separating the temporal and spatial part give

$$\mathbf{E}\cdot\mathbf{J} = 0 \tag{2.28}$$

$$\rho\mathbf{E} + \frac{\mathbf{J}\times\mathbf{B}}{c} = \mathbf{0} \tag{2.29}$$

The first condition implies that there is no dissipation in virtue of the Poynting flux theorem. The plasma does not gain energy from the dissipation of the current, and particles are not accelerated. The second condition implies that the Lorentz force governs the dynamics of the plasma. From Eq. (2.29), we also have $\mathbf{E}\cdot\mathbf{B}=0$. The parallel electric field is perfectly screened in the magnetosphere, and deviations from this condition should be small and narrow in space. Thanks to these conditions and Maxwell's equations, an analytical expression of the current density can be derived (Blandford, 2002),

$$\mathbf{J}=\frac{c}{4\pi}\boldsymbol{\nabla}\cdot\mathbf{E}\left(\frac{\mathbf{E}\times\mathbf{B}}{B^2}\right)+\frac{c}{4\pi}\Big(\mathbf{B}\cdot(\boldsymbol{\nabla}\times\mathbf{B})-\mathbf{E}\cdot(\boldsymbol{\nabla}\times\mathbf{E})\Big)\frac{\mathbf{B}}{B^2} \tag{2.30}$$

The full demonstration to obtain this analytical expression is given below in Demo.1.

Demonstration 1: Current density in force-free electrodynamics

To derive the force-free current density, we will use the following set of equations, namely Maxwell's equations and the second force-free condition

$$\frac{\partial\mathbf{B}}{\partial t}=-c\,\boldsymbol{\nabla}\times\mathbf{E}\qquad\frac{\partial\mathbf{E}}{\partial t}=c\,\boldsymbol{\nabla}\times\mathbf{B}-4\pi\mathbf{J}\qquad\boldsymbol{\nabla}\cdot\mathbf{E}=4\pi\rho\qquad\rho\mathbf{E}+\frac{\mathbf{J}\times\mathbf{B}}{c}=\mathbf{0}$$

For the derivation, we start with $\mathbf{E}\cdot\mathbf{B}=0\Rightarrow\partial_t(\mathbf{E}\cdot\mathbf{B})=0$

$$\begin{aligned}\partial_t(\mathbf{E}\cdot\mathbf{B})&=\mathbf{B}\cdot\partial_t\mathbf{E}+\mathbf{E}\cdot\partial_t\mathbf{B}=0\\ &\overset{(2.1),(2.2)}{\Longleftrightarrow} c\mathbf{B}\cdot(\boldsymbol{\nabla}\times\mathbf{B}-4\pi\mathbf{J})-c\mathbf{E}\cdot(\boldsymbol{\nabla}\times\mathbf{E})=0\end{aligned} \tag{2.31}$$

Then, we extract $\mathbf{J}\cdot\mathbf{B}$ which is a crucial term for the rest of the derivation.

$$\mathbf{J}\cdot\mathbf{B}=\frac{c}{4\pi}\left(\mathbf{B}\cdot(\boldsymbol{\nabla}\times\mathbf{B})-\mathbf{E}\cdot(\boldsymbol{\nabla}\times\mathbf{E})\right) \tag{2.32}$$

The next step is to cross the second force-free condition with $\mathbf{B}$.

$$\begin{aligned}&\overset{(2.29)\times\mathbf{B}}{\Longrightarrow}\rho\mathbf{E}\times\mathbf{B}+\frac{1}{c}(\mathbf{J}\times\mathbf{B})\times\mathbf{B}=0\\ &\Longleftrightarrow\rho\mathbf{E}\times\mathbf{B}+\frac{1}{c}\left((\mathbf{J}\cdot\mathbf{B})\,\mathbf{B}-(\mathbf{B}\cdot\mathbf{B})\,\mathbf{J}\right)=0\end{aligned} \tag{2.33}$$

Finally, injecting $\mathbf{J}\cdot\mathbf{B}$ gives the full expression of the current density

$$\overset{(2.4),(2.32)}{\Longleftrightarrow}\mathbf{J}=\frac{c}{4\pi}\boldsymbol{\nabla}\cdot\mathbf{E}\left(\frac{\mathbf{E}\times\mathbf{B}}{B^2}\right)+\frac{c}{4\pi}\Big(\mathbf{B}\cdot(\boldsymbol{\nabla}\times\mathbf{B})-\mathbf{E}\cdot(\boldsymbol{\nabla}\times\mathbf{E})\Big)\frac{\mathbf{B}}{B^2} \tag{2.34}$$

The force-free current density only depends on the electric and magnetic fields, the contribution is purely electromagnetic.

The total current density is expressed in the form of an effective Ohm's law (Gruzinov, 1999; Blandford, 2002). Eq. (2.30) is composed of two terms

$$\mathbf{J}=\mathbf{J}_\perp+\mathbf{J}_\parallel \tag{2.35}$$

where

$$\mathbf{J}_{\perp} = c\frac{\boldsymbol{\nabla}\cdot\mathbf{E}}{4\pi}\left(\frac{\mathbf{E}\times\mathbf{B}}{B^2}\right) \tag{2.36}$$

$$\mathbf{J}_{\parallel} = \frac{c}{4\pi}\Big(\mathbf{B}\cdot(\boldsymbol{\nabla}\times\mathbf{B}) - \mathbf{E}\cdot(\boldsymbol{\nabla}\times\mathbf{E})\Big)\frac{\mathbf{B}}{B^2}. \tag{2.37}$$

$\mathbf{J}_{\perp}$ corresponds to the current flowing across the field lines, while $\mathbf{J}_{\parallel}$ is flowing along them. Physically speaking, the parallel term acts on $\mathbf{E}_{\parallel}$ by removing any excess of parallel electric field. For the perpendicular term, it corresponds to the current produced by the advection of the charge density with the drift velocity $\mathbf{E}\times\mathbf{B}$. The drift velocity must remain smaller than the speed of light, giving another condition

$$B^2 - E^2 > 0. \tag{2.38}$$

We previously noted that the force-free condition $\mathbf{E}\cdot\mathbf{J} = 0$ implies no dissipation. However, in general we can have a topology where the above condition can be violated, $\|\mathbf{B}\| = 0$ (Uchida, 1997). When this is the case, the force-free approximation breakdowns and we have a localised dissipation. It is possible to do an extension of the force-free regime to have a dissipation term. Lyutikov (2003) gives the resistive force-free equations. The main idea is to have a modified Ohm's law to account for the resistivity noted ξ. Under some assumptions detailed in Lyutikov (2003), the new Ohm's law and current density are

$$(\mathbf{E}\cdot\mathbf{B}) = \frac{\xi}{\gamma}(\mathbf{J}\cdot\mathbf{B}) \tag{2.39}$$

$$\mathbf{J} = \frac{c}{4\pi}\boldsymbol{\nabla}\cdot\mathbf{E}\left(\frac{\mathbf{E}\times\mathbf{B}}{B^2}\right) + \frac{1}{\xi\sqrt{1-\left(\frac{\mathbf{E}\times\mathbf{B}}{B^2}\right)^2}}(\mathbf{E}\cdot\mathbf{B})\frac{\mathbf{B}}{B^2} \tag{2.40}$$

The ideal force-free case is recovered for $\xi \longrightarrow 0$ in Ohm's law, see Lyutikov (2003) for the full derivation. With $\xi = 0$, the Ohm's law becomes $\mathbf{E}\cdot\mathbf{B} = 0$ and the ideal current is recovered via Demo. 1.

2.1.3 Michel monopole

The next step for the community of pulsar theory was to provide analytical solutions to model the force-free magnetosphere. The equation governing the electromagnetic field in this regime is known as the pulsar equation. This equation is derived in cylindrical coordinates (R,ϕ,z), under the axisymmetric and steady-state assumptions, from

$$\rho\mathbf{E} + \frac{\mathbf{J}\times\mathbf{B}}{c} = \mathbf{0}$$

which is the force-free condition. The next step is to decompose the magnetic field into a poloidal and a toroidal component,

$$\mathbf{B} = \mathbf{B}_{\mathrm{p}} + \mathbf{B}_{\phi} \tag{2.41}$$

The expressions of $\mathbf{B}_{\mathrm{p}}$ and $\mathbf{B}_{\phi}$ are derived from the magnetic flux function Ψ and the current function I. The magnetic flux function gives

$$2\pi\Psi = \iint \mathbf{B}\cdot\mathrm{d}\mathbf{S} = \oint \mathbf{A}\cdot\mathrm{d}\mathbf{l} = 2\pi R A_{\phi}. \tag{2.42}$$

Then the magnetic vector potential A_ϕ is

$$A_\phi = \frac{\Psi}{R} \tag{2.43}$$

with $R = r\sin\theta$ the cylindrical radius. From the current function, we have

$$I = \iint \mathbf{J}\cdot\mathrm{d}\mathbf{S} = \iint_\Sigma \frac{c}{4\pi}\left(\boldsymbol{\nabla}\times\mathbf{B}\right)\cdot\mathrm{d}\mathbf{S} = \frac{c}{4\pi}\oint_{\mathcal{C}}\mathbf{B}\cdot\mathrm{d}\mathbf{l} = \frac{2\pi R c}{4\pi}B_\phi \tag{2.44}$$

therefore,

$$B_\phi = \frac{I}{R}. \tag{2.45}$$

We can give the full description of $\mathbf{B}$:

$$\mathbf{B} = \boldsymbol{\nabla}\times\mathbf{A} = \begin{pmatrix} -\frac{\partial A_\phi}{\partial z} \\ \frac{\partial A_R}{\partial z} - \frac{\partial A_z}{\partial R} \\ \frac{1}{R}\frac{\partial\left(RA_\phi\right)}{\partial R} \end{pmatrix} = \begin{pmatrix} -\frac{1}{R}\frac{\partial\Psi}{\partial z} \\ \frac{\partial A_R}{\partial z} - \frac{\partial A_z}{\partial R} \\ \frac{1}{R}\frac{\partial\Psi}{\partial R} \end{pmatrix} = \mathbf{B}_\mathrm{p} + \mathbf{B}_\phi \tag{2.46}$$

written in a simpler expression

$$\mathbf{B} = \frac{1}{R}\boldsymbol{\nabla}\Psi\times\mathbf{e}_\phi + \mathbf{B}_\phi \tag{2.47}$$

The associated electric field and charge density are computed from the corotation assumption

$$\mathbf{E} = -\frac{\mathbf{v}\times\mathbf{B}}{c} = -\frac{r\sin\theta}{c}\Omega\mathbf{e}_\phi\times\mathbf{B} = -\frac{R}{R_\mathrm{LC}}\mathbf{e}_\phi\times\mathbf{B} \tag{2.48}$$

$$\rho = \frac{\boldsymbol{\nabla}\cdot\mathbf{E}}{4\pi} = -\frac{R}{4\pi R_\mathrm{LC}}\boldsymbol{\nabla}\cdot\left(\mathbf{e}_\phi\times\mathbf{B}\right) \tag{2.49}$$

The next step to derive the pulsar equation is to assume that in the rotating frame, we have a stationary vector field, $\partial_t = -\Omega\partial_\phi$. Under this hypothesis, we can express the current density

$$\begin{aligned} \partial_t\mathbf{E} = -\frac{\Omega R}{R_\mathrm{LC}}\partial_\phi\left(\mathbf{e}_\phi\times\mathbf{B}\right) &= c\boldsymbol{\nabla}\times\mathbf{B} - 4\pi\mathbf{J} \\ \iff \mathbf{J} = \frac{c}{4\pi}\boldsymbol{\nabla}\times\mathbf{B} - \frac{\Omega R}{4\pi R_\mathrm{LC}}\partial_\phi\left(\mathbf{e}_\phi\times\mathbf{B}\right) & \end{aligned} \tag{2.50}$$

We now have all the key ingredients and can inject everything in the force-free condition. Eq. (2.29) reduces to the form

$$\left(\boldsymbol{\nabla}\times\mathbf{B}'\right)\times\mathbf{B} = 0 \tag{2.51}$$

where

$$\mathbf{B}' = \left(1 - \frac{R^2}{R_\mathrm{LC}^2}\right)\frac{\boldsymbol{\nabla}\Psi\times\mathbf{e}_\phi}{R} + \frac{I}{R}\mathbf{e}_\phi \tag{2.52}$$

We can inject Eqs. (2.47) and (2.52) in $\left(\boldsymbol{\nabla}\times\mathbf{B}'\right)\times\mathbf{B} = 0$ in order to get

$$\left(1-\left(\frac{R}{R_{\rm LC}}\right)^2\right)\left(\frac{\partial^2\Psi}{\partial R^2}+\frac{\partial^2\Psi}{\partial z^2}\right)-\left(1+\left(\frac{R}{R_{\rm LC}}\right)^2\right)\frac{1}{R}\frac{\partial\Psi}{\partial R}+I\frac{\partial I}{\partial\Psi}=0 \tag{2.53}$$

This equation is the so-called pulsar equation (Michel, 1973; Scharlemann & Wagoner, 1973) and relies on two unknowns $\Psi(R,z)$ and $I(\Psi)$. The analytical solution of the pulsar equation is actually unknown, the only exception being for a rotating monopole. In this case, the analytical solution is known as the Michel monopole (Michel, 1973). In itself, the solution is surprisingly simple. We assume the following magnetic flux function

$$\Psi=\Psi_0\left(1-\cos\theta\right) \tag{2.54}$$

where $\cos\theta = z/\sqrt{R^2+z^2}$. The given flux function corresponds to the flux of $\mathbf{B}$ through a circle of radius R and at the height z. The current function is then derived by injecting Eq. (2.54) in the pulsar equation.

$$\partial_R\Psi=\frac{\Psi_0 R\cos\theta}{R^2+z^2}\qquad \partial_R^2\Psi=\frac{\Psi_0\left(z^2-2R^2\right)}{\left(R^2+z^2\right)^2}\cos\theta\qquad \partial_z^2\Psi=\frac{3\Psi_0 R^2}{\left(R^2+z^2\right)^2}\cos\theta \tag{2.55}$$

We can inject the expressions of the derivatives in Eq. (2.53),

$$-\frac{2R^2\Psi_0}{R_{\rm LC}^2\left(R^2+z^2\right)}\cos\theta=-I\frac{\partial I}{\partial\Psi}=I\frac{\partial I}{\Psi_0\partial\cos\theta} \tag{2.56}$$

written in the differential form

$$I\,{\rm d}I=-\frac{2\Psi_0^2}{R_{\rm LC}^2}\cos\theta\,{\rm dcos}\,\theta \tag{2.57}$$

The above expression can be integrated to give the current function

$$I=\pm\frac{\Psi_0}{R_{\rm LC}}\sin^2\theta \tag{2.58}$$

The current function has two possible signs depending on the orientation of the monopole, $\mathbf{\Omega}\cdot\mathbf{B}>0$ (aligned) or $\mathbf{\Omega}\cdot\mathbf{B}<0$ (anti-aligned). With the expression of I, we can finally give Michel's solution in spherical coordinates:

$$B_r=B_\star\left(\frac{r_\star}{r}\right)^2 \tag{2.59}$$
$$B_\theta=0 \tag{2.60}$$
$$B_\phi\overset{(2.45)}{=}\mp B_\star\left(\frac{r_\star}{R_{\rm LC}}\right)\left(\frac{r_\star}{r}\right)\sin\theta \tag{2.61}$$
$$E_r=0 \tag{2.62}$$
$$E_\theta=B_\phi \tag{2.63}$$
$$E_\phi=0 \tag{2.64}$$
$$\tag{2.65}$$

where Ψ_0 was replaced by the total flux $\Psi_0=B_\star r_\star^2$. Since the solution is analytic, we can compute the current density associated with this solution,

$$\mathbf{J}_{\mathrm{M}} = \frac{c}{4\pi}\left(\boldsymbol{\nabla}\times\mathbf{B}\right) = -\frac{\boldsymbol{\Omega}\cdot\mathbf{B}}{2\pi}\mathbf{e}_r = c\rho_{\mathrm{GJ}}\mathbf{e}_r. \tag{2.66}$$

The current density is purely radial and indicates that the plasma flows outwards radially, carrying out the fiducial Goldreich-Julian charge density.

Coming back to the solution, the two possible signs for I and thus of B_ϕ are convenient to produce an alternative configuration. This solution known as the split monopole now satisfies $\boldsymbol{\nabla}\cdot\mathbf{B} = 0$. We remove the forbidden magnetic monopoles by using the negative sign of B_ϕ in one hemisphere and the positive sign of B_ϕ in the other one. The current density is impacted by the reversal of $\mathbf{B}$ and becomes negative. Therefore, the jump in $\mathbf{B}$ at the equator produces a positively charged current sheet which is responsible for carrying the return current to close the electric circuit. A representation of the split-monopole solution is given in Fig. 2.3.

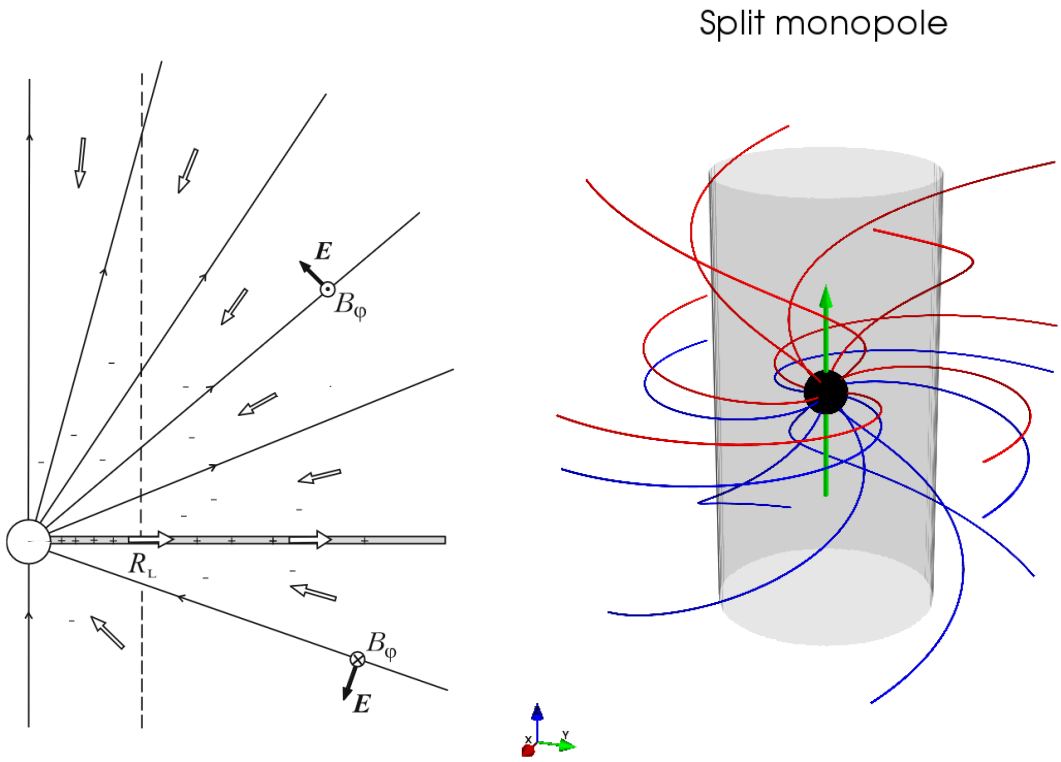

FIGURE 2.3: Exact solution of the pulsar equation known as the split-monopole. Left: 2D axisymmetric configuration, magnetic field lines are in solid black lines while the contour arrows show the flow of the current density (Figure taken from Beskin 2010). Right: 3D representation of the winding up of field lines outside the light-cylinder (Figure taken from Cerutti and Beloborodov 2017).

The solution can be decomposed into two regions with respect to the light-cylinder. If the cylindrical radius $R = r\sin\theta \ll R_{\mathrm{LC}}$, the magnetic field lines are almost radial near the star. However, if $R = r\sin\theta \gg R_{\mathrm{LC}}$, the field lines wind up with radius and the magnetic field is mainly toroidal. The spindown power of the solution can be computed and the Poynting flux is

$$L_{\rm M} = \frac{c}{4\pi}\iint (\mathbf{E}\times\mathbf{B})\cdot \mathrm{d}\mathbf{S} = \frac{c}{4\pi}\iint r^2\sin\theta\,(\mathbf{E}\times\mathbf{B})\cdot\mathbf{e}_r\,\mathrm{d}\theta\mathrm{d}\phi$$
$$= \frac{c}{2}\int_{-1}^{1} r^2 B_\phi^2\,\mathrm{d}\cos\theta = \frac{2c}{3R_{\rm LC}}B_\star^2 r_\star^4 = \frac{2c}{3R_{\rm LC}^2}\Psi_0^2 \tag{2.67}$$

The solution also has a radial Poynting flux, indicating that the star is braking. This result was generalised to the oblique rotator by Bogovalov (1999) and was found identical. The rotational losses of the split monopole do not depend on the inclination angle χ between the spin axis $\mathbf{\Omega}$ and the magnetic axis $\boldsymbol{\mu}$.

2.2 Pulsar magnetosphere

In this section, we describe the current understanding and models proposed by the community to describe pulsar magnetospheres.

2.2.1 Historical simulations

In the previous section, we derived the pulsar equation (Eq. 2.53) and gave an analytical solution. Contopoulos et al. (1999) were able to derive a numerical solution of the pulsar equation for the aligned dipole. This solution was obtained thanks to an iterative method using dipolar boundary conditions at the inner boundary (surface of the star). The solution was later reproduced by Gruzinov (2005). The solution was not continuous at the light-cylinder, and some numerical treatment was performed to have a smooth solution at the light-cylinder below a numerical error threshold. This stationary solution was improved by Timokhin (2006), giving a set of new solutions for the aligned rotator. A few months after these new solutions, Spitkovsky (2006) performed the first time-dependent force-free simulations of a pulsar magnetosphere for both the aligned and oblique configuration. This simulation marks the beginning of time-dependent pulsar modelling. Before diving into the realm of numerical simulations of pulsar magnetospheres, we remind the global picture of the magnetosphere.

Figure 2.4 shows the full axisymmetric magnetosphere. The magnetic field configuration is a dipole with magnetic field lines anchored on the stellar surface. The surface magnetic flux function is

$$\Psi(r_\star,\theta) = B_\star r_\star^2\sin^2\theta. \tag{2.68}$$

The light-cylinder radius is noted $R_{\rm LC}$, at this radius a corotating particle has a velocity equal to the speed of light. Inside the light-cylinder where the field lines are closed, the plasma is in corotation with the star (i.e. the corotating magnetosphere), and the magnetic field is poloidal $\mathbf{B}_\phi = \mathbf{J}_{\rm p} = 0$. Outside of these closed field lines, the plasma cannot maintain the corotation. The result is in an outflowing plasma along open field lines in the wind zone where the magnetic field is toroidal. If we consider $r \gg R_{\rm LC}$, this region is quasi-identical to the monopole solution with a poloidal current density and a toroidal magnetic field. One can identify a unique set of field lines closing exactly at the light cylinder, this peculiar field line is called the separatrix. The approximate location of the separatrix can be computed using the vacuum dipole solution as

$$\sin^2\theta_{\rm pc} = \frac{r_\star}{R_{\rm LC}} \tag{2.69}$$

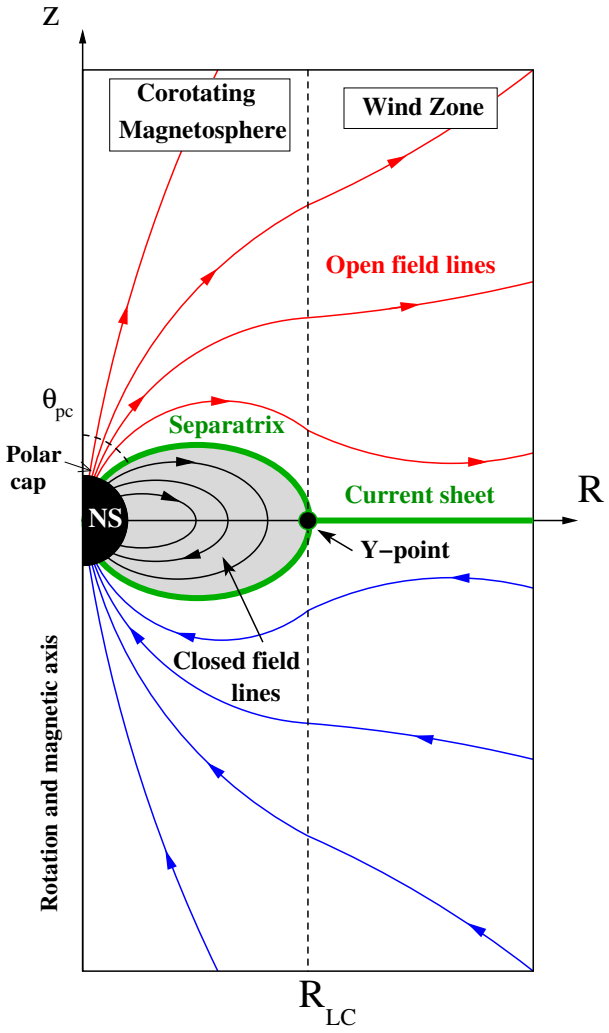

FIGURE 2.4: Schematic view of the force-free magnetosphere in the axisymmetric configuration. Figure taken from Cerutti and Beloborodov (2017).

where $\theta_{\rm pc}$ is the polar angle defined with respect to the rotation axis of the star. This angle gives the angular size of the polar cap and indicates where the footpoints of open field lines are located. In plasma-filled simulations, this angle is not equal to the vacuum one, as there is a slight inflation of the closed region. This bundle of magnetic field lines carries a magnetic flux $\Psi_{\rm pc}$ outwards. The parameter $\Psi_{\rm pc}$ will be crucial in the Sect. 5.2 and is expressed as (Eq. 2.68)

$$\Psi_{\rm pc} = B_\star r_\star^2 \sin^2\theta_{\rm pc} = \frac{r_\star^3}{R_{\rm LC}} B_\star. \tag{2.70}$$

The field lines associated with the wind zone represent the active region of the magnetosphere. The consequence of that is a torque exerted on the star which spins it down. An important aspect of the dipole configuration is at the equator where the magnetic field switches sign and thus, goes to zero. In this exact region called the current sheet, the force-free assumptions break down as $B^2 < E^2$. The physics happening in this region is not captured in force-free and can have a strong impact on the solution. However, the current sheet must exist in order to close the electric circuit, it is similar to the equatorial part of the split monopole. Lyubarskii (1990) showed that this current sheet is unique and extends up

to infinity. That author also showed that the separatrix has two branches inside the light cylinder. They merge into a single one, i.e. the current sheet, after the light cylinder. The point of connection is called the Y-point and links the two parts of the magnetosphere.

Force-free simulations do not exhibit dissipation by construction, but they are valuable for studying the global structure of the magnetosphere as well as the spin-down power. A good agreement was found between several groups with various numerical techniques on the time-dependent structure of the magnetosphere (Spitkovsky, 2006; Parfrey et al., 2012; Pétri, 2012). The theoretical picture shown in Fig. 2.4 is recovered by all studies. They also exhibit the presence of a current sheet with a strong return current. However, there is a discrepancy about the location of the Y-point. Mahlmann and Aloy (2022) studied the numerical diffusion of force-free simulations. Their experiment was looking at the impact of the electric charge reconstruction scheme. They used a charge conservation scheme (CC) and a local charge reconstruction scheme (LCR). In the CC scheme, the set of equations is

$$\partial_t \mathbf{B} = -\boldsymbol{\nabla} \times \mathbf{E} - c_\Psi^2 \boldsymbol{\nabla} \Psi \tag{2.71}$$
$$\partial_t \mathbf{E} = \boldsymbol{\nabla} \times \mathbf{B} + c_\Phi^2 \boldsymbol{\nabla} \Phi - \mathbf{J} \tag{2.72}$$
$$\partial_t \Psi = -\boldsymbol{\nabla} \cdot \mathbf{B} - \kappa_\Psi \Psi \tag{2.73}$$
$$\partial_t \Phi = \boldsymbol{\nabla} \cdot \mathbf{E} - \rho - \kappa_\Phi \Phi \tag{2.74}$$
$$\partial_t \rho = -\boldsymbol{\nabla} \cdot \mathbf{J}. \tag{2.75}$$

where Φ, Ψ are scalar potentials, c_Ψ, c_Φ are advection speeds and κ_Φ, κ_Ψ are damping constants. Φ is used to handle the errors to $\boldsymbol{\nabla} \cdot \mathbf{E} = \rho$, Ψ has the same role for $\boldsymbol{\nabla} \cdot \mathbf{B} = 0$. In the LCR scheme, Eq. (2.75) is not solved and the charge density is directly computed from $\rho = \boldsymbol{\nabla} \cdot \mathbf{E}$. A parameter α measures the advection (τ_a) and diffusion (τ_d) timescales for cleaning errors, $\alpha = \tau_d / \tau_a$. Mahlmann and Aloy (2022) found that numerical diffusion impacted the location of the Y-point. If the Y-point is inside the light-cylinder, this indicates that more field lines are opened, thus the polar cap is wider and more flux is carried out by the wind. The situation is the opposite in the case of a Y-point outside the light-cylinder.

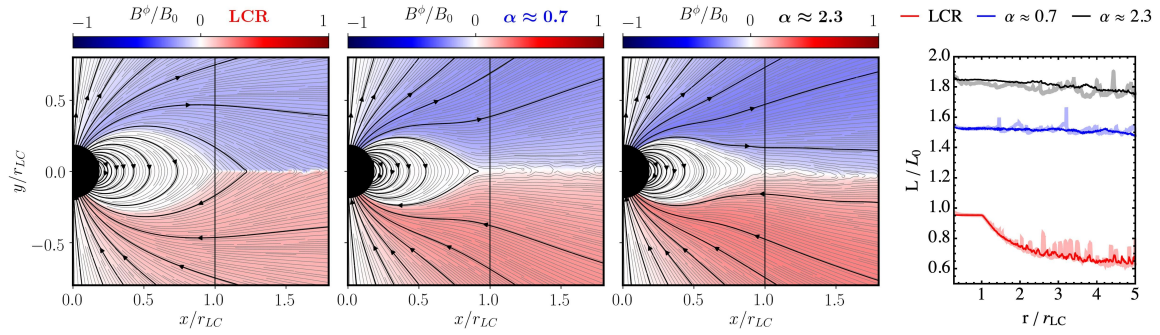

FIGURE 2.5: Left: Maps of the toroidal magnetic field for different charge reconstruction schemes. Magnetic field lines are the solid black lines, and the theoretical light-cylinder is the vertical black line. Right: Poynting flux (solid lines) of each simulation averaged over $\Delta t = 1.3P$. Figure taken from Mahlmann and Aloy (2022).

This statement is shown in Fig. 2.5 where the Poynting flux is shown in the rightmost panel. The leftmost simulation has a Y-point close to the theoretical light-cylinder, resulting in a Poynting flux equal to L_0. The right simulation has a Y-point deeper inside the light-cylinder and we see more field lines opened. Its Poynting flux is larger than for the left

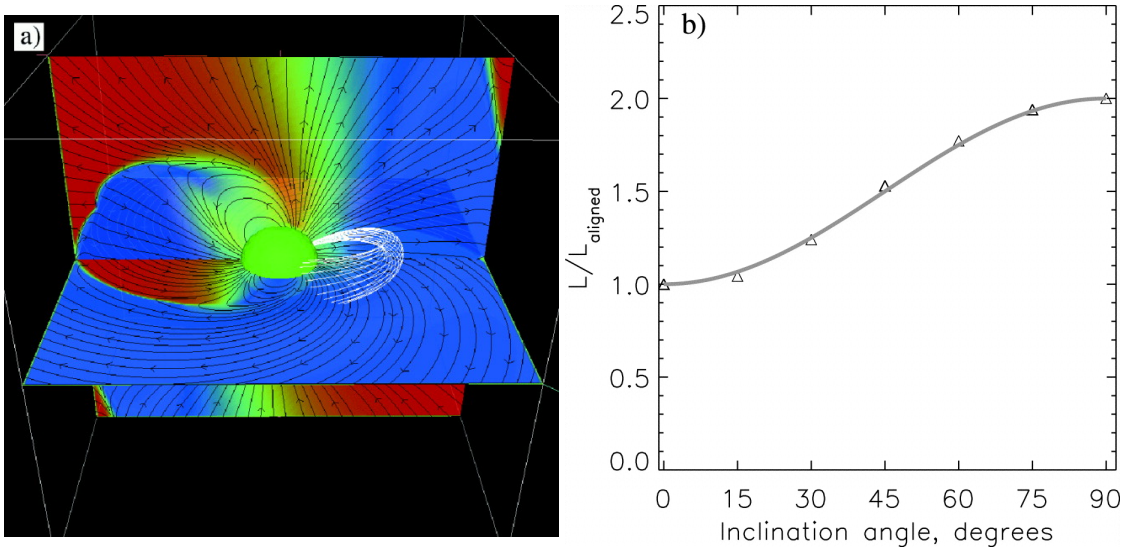

FIGURE 2.6: Results of 3*D* simulations of the oblique rotator. Left: snapshot of magnetosphere where $\chi = 60°$. Magnetic field lines are in black solid lines, a flux tube is shown in white lines, the toroidal and perpendicular magnetic fields are respectively in the horizontal and vertical plane. Right: spindown power depending on the inclination angle χ. (Figure taken from Spitkovsky, 2006).

simulation. Even if the Poynting flux is impacted by the location of the Y-point in the simulation, it represents a valuable quantity.

With 2*D* simulations of the aligned rotator, the other step was to perform 3*D* force-free simulations of the oblique rotator to model an active pulsar. From Fig. 2.6, two main results emerge from 3*D* simulations (Spitkovsky, 2006; Kalapotharakos & Contopoulos, 2009; Pétri, 2012): the current sheet is not straight and the spindown depends on the inclination angle. The current sheet has the shape of a ballerina skirt, this is reminiscent of the heliospheric current sheet but in a relativistic context. Regarding the spindown losses, Spitkovsky (2006) proposed the following relation

$$L = L_0(1 + \sin^2 \chi) \tag{2.76}$$

where $L_0 = cB^2 r_\star^6 / R_{\rm LC}^4$. It has the same dependence on the physical parameters of the pulsar as in the vacuum spindown power (Eq. 2.21). Even for the aligned case ($\chi = 0°$), the pulsar has a spin-down power. This was previously the case in the split-monopole solution.

Unfortunately, force-free simulations were not enough to unveil the great mystery behind pulsars and their emission. The main reason comes from the method being dissipation-free. No energy can be exchanged or converted from one reservoir to another, which is true everywhere in the magnetosphere except where the force-free approximation breaks down. We previously mentioned the current sheet as being the region where the force-free regime is violated. Inside it, the magnetic field goes to zero and the plasma becomes unmagnetised. Consequently, the plasma energy density overtakes the magnetic energy density, $U_{\rm kin} \gg U_B$. The plasma in this region is governed by kinetic effects, thus the simulation should consider the pressure and inertia of the plasma as well as a finite resistivity resulting in a localised dissipation of energy. The current sheet could be tearing unstable and could suffer from magnetic reconnection (Lyutikov, 2003) producing a non-thermal distribution of particles. One can add an artificial resistivity in force-free simulations (Komissarov, 2006; Li et al., 2012; Parfrey et al., 2012) or even do full MHD

simulations (Komissarov, 2006; Tchekhovskoy et al., 2013). However, it will still not be sufficient to study the acceleration and radiation of particles.

2.2.2 QED processes and radiations

Force-free simulations were incredibly useful for the pulsar theory and allowed to do the first time-dependent simulations of such an extreme environment. However, due to its limitations, the community had to use a different kind of simulations to study pulsar magnetospheres. To study the dissipation and emission produced in the magnetosphere, the community had to change strategy and look at what the plasma community was doing. The result of this is the use of Particle-In-Cell (PIC) codes. This type of simulation, widely used since the late 1950s by the plasma community, was exactly what was needed. PIC simulations allow to have an ab-initio kinetic modelling of the magnetosphere by having Lagrangian particles in an Eulerian simulation. The full description of the PIC method is given in Sect. 3.3. This switch of paradigm was encouraged by the observational side. Observations show a significant conversion of rotational energy in highly energetic photons, especially gamma-ray photons. In order to explain the production of gamma-rays, we need to know where particles are accelerated in the magnetosphere. The acceleration of particles occurs in regions where $\mathbf{E}\cdot\mathbf{B}\neq 0$, equivalent to the development of $\mathbf{E}_{\parallel}$. But also in regions where $E^2 > B^2$ through magnetic reconnection. We remind that the parallel electric field is unscreened if $\rho \ll \rho_{\rm GJ}$. The unscreened electric field at the stellar surface allows particle extraction with $\|E_{\parallel}\| \propto B_{\star}\Omega$. This extraction injects a significant density, but this mechanism is not strong enough to fill the full magnetosphere with plasma. The strong $\mathbf{E}_{\parallel}$ at the surface accelerates particles up to large Lorentz factors. The full potential drop across the polar cap can be expressed using the corotating electric field, $\mathbf{E} = -(\mathbf{\Omega}\times\mathbf{r})\times\mathbf{B}/c$, as

$$\Phi_{\rm pc} = \frac{\mu\Omega^2}{c^2}. \tag{2.77}$$

If a particle were to experience this full potential drop, the Lorentz factor it would reach is

$$\gamma_{\rm pc} = \frac{e\Phi_{\rm pc}}{m_e c^2} \approx 2.6\times 10^8 \left(\frac{B_\star}{10^7{\rm G}}\right)\left(\frac{P}{1{\rm ms}}\right)^{-2}. \tag{2.78}$$

Where the physical parameters of the pulsar correspond to the weakest pulsar detected by the *Fermi*-LAT. The result of the above computation can be seen as a lower limit of $\gamma_{\rm pc}$ for the millisecond pulsar population since it uses the weakest magnetic field observed. This value only represents an upper limit inside the magnetosphere, as part of the accelerating electric field would be screened by the plasma surrounding the star. However, quantum electrodynamics predicts that the pair production mechanism is triggered if (Erber, 1966; Harding & Lai, 2006),

$$\chi_{\rm QED} \equiv \epsilon b \geq 0.1 \tag{2.79}$$

where $\epsilon = \hbar\nu/m_{\rm e}c^2$ is the dimensionless photon energy, and $b = B_\perp/B_{\rm QED}$ is the ratio of the perpendicular magnetic field to the critical quantum field or Schwinger field, $B_{\rm QED} = m_{\rm e}^2c^3/\hbar e \approx 4.4\times 10^{13}$G. It is usually assumed that electrons radiate via synchrotron-curvature radiation (Blumenthal & Gould, 1970). If we make this assumption the critical energy of the photon is

$$\epsilon_c = \frac{3}{2}b\gamma^2. \tag{2.80}$$

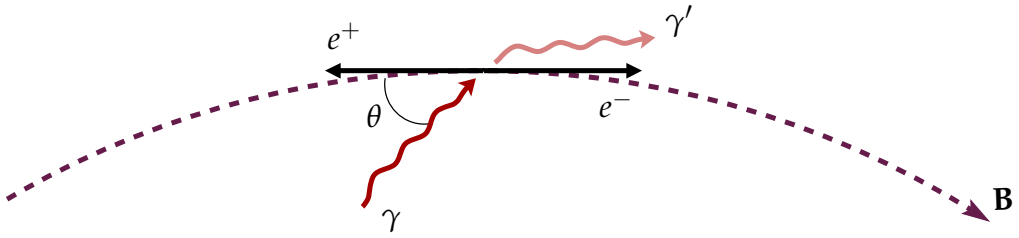

FIGURE 2.7: Magnetic conversion illustration. The energetic photon γ (in dark red) produces an electron-positron pair via magnetic conversion (magnetic field line in dashed purple line).

The threshold Lorentz factor for an electron is given by combining Eqs. (2.79) and (2.80),

$$\epsilon_c b = 0.1 \Longrightarrow \gamma_{\rm th} = \sqrt{\frac{1}{15b^2}} \approx 10^6 \left(\frac{B_\star}{10^7 \rm G}\right)^{-1}. \tag{2.81}$$

We see right away that, under our assumption of B_* and P, $\gamma_{\rm pc} \gg \gamma_{\rm th}$ meaning that pairs are produced in the magnetosphere at least close to the star. In this region, the main mechanism for pair production is believed to be via magnetic conversion. If pair production is efficient enough, the charge density will reach the Goldreich-Julian density. Once the latter is reached, the parallel electric field will be shorted out, making it inefficient at accelerating particles near the surface. The particle's Lorentz factor will drop under the threshold and pair production will stop, until the density drops below the critical density $n_{\rm GJ}$. This is the basic idea behind gap models, which are detailed further below. Nevertheless, pair production is not limited close to the stellar surface. It can happen anywhere in the magnetosphere as long as the energy threshold is reached.

We just showed that the pair production mechanism can be triggered in the magnetosphere of a pulsar. Depending on where it is in this environment, the mechanism for pair creation is different. Close to the surface, the process responsible is believed to be via magnetic conversion. Far from the surface, the Breit-Wheeler or photon-photon annihilation mechanism is expected to create the pairs. In order to have a full picture of pair production inside a pulsar magnetosphere, we briefly detail the two main mechanisms of pair creation.

Magnetic conversion: in this scenario of pair production, we consider a gamma photon with an energy ϵ travelling across a uniform magnetic field **B**. The trajectory of the photon and the orientation of the magnetic field are not parallel, and we define θ the angle between them. During the interaction, a part of the photon momentum is "absorbed" by the magnetic field to create a pair,

$$\gamma + B \longrightarrow e^- + e^+ \tag{2.82}$$

An illustration of the process is given in Fig. 2.7, and the full description of this mechanism is given by Daugherty and Harding (1983). The first relation is the energy conservation of the process

$$\epsilon = E^- + E^+ \tag{2.83}$$

where E^-, E^+ are the electron and positron energy. The second relation is the conservation of the parallel momentum

$$\epsilon \cos\theta = p_{\parallel}^{-} + p_{\parallel}^{+}. \tag{2.84}$$

The perpendicular momentum is not conserved in the magnetic conversion. It is used by the magnetic field to create the pair. In order for the mechanism to create an electron-positron pair, the photon energy must be greater than the rest mass energy of the pair, meaning

$$\epsilon \sin\theta \geq 2m_e c^2. \tag{2.85}$$

If a single photon does carry at least this amount of energy, pair production via magnetic conversion is possible.

Breit-Wheeler: this process of pair production results from the annihilation of two photons.

$$\gamma_1 + \gamma_2 \longrightarrow e^- + e^+ \tag{2.86}$$

where γ_1, γ_2 are two photons with the respective energy $\epsilon_1 m_e c^2, \epsilon_2 m_e c^2$. An illustration of the process is given in Fig. 2.8.

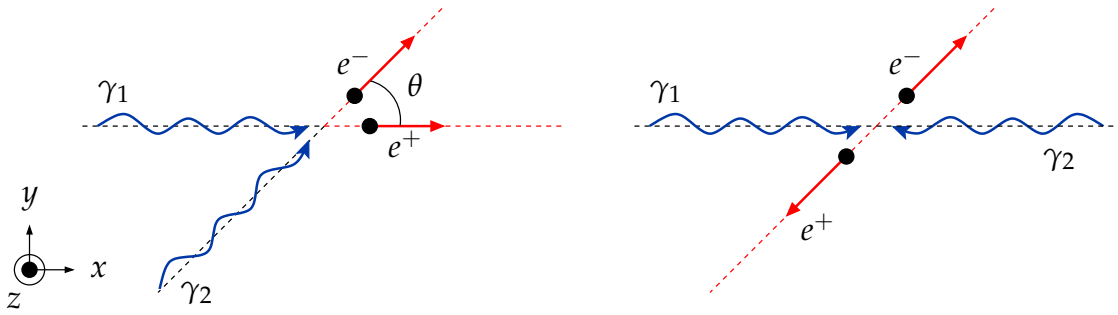

FIGURE 2.8: Breit-Wheeler mechanism or photon annihilation. Left: Lab frame. Right: Centre-of-mass frame.

To trigger the Breit-Wheeler process, the amount of energy carried by the two photons must be sufficient. In the centre-of-mass frame (starred quantities), the total energy $E^{\star}_{\text{tot}}$ of the photons must be larger than the rest-mass energy of the electron-positron pair,

$$E^{\star}_{\text{tot}} \geq 2m_e c^2. \tag{2.87}$$

To estimate the photon energies required to have pair production via photon-photon annihilation, we can use the relativistic invariant

$$c^2 P^{\mu} P_{\mu} = c^2 P^{\star\mu} P^{\star}_{\mu} \Longrightarrow (p_1 + p_2)^2 = (p_1^{\star} + p_2^{\star})^2 \tag{2.88}$$

where $P^{\mu} = (E/c, \mathbf{p})$ is the 4-momentum. Equation (2.88) can also be expressed as

$$E^{\star}_{\text{tot}}{}^2 - p^{\star}_{\text{tot}}{}^2 c^2 = E^{\star}_{\text{tot}}{}^2 = E^2_{\text{tot}} - p^2_{\text{tot}} c^2. \tag{2.89}$$

The next step is to use the angle θ in the lab frame to express p_1 and p_2. The condition for photon-photon annihilation becomes

$$s = \frac{1}{2}\epsilon_1 \epsilon_2 (1 - \cos\theta) \geq m_e^2 c^4. \tag{2.90}$$

With the above equation, we can see that pair production requires less energetic photons in the case of a head-on collision, meaning $\theta = \pi$. Using this case in Eq. (2.90) reads

$$\frac{1}{2}\epsilon_1\epsilon_2 = m_e^2c^4. \tag{2.91}$$

The conclusion of this process is the following. For pair production to occur via the Breit-Wheeler process, the energy of the photons in the centre-of-mass frame needs to be at least twice the rest mass energy of the electron. Therefore, combinations are possible. Pair production can occur by annihilation of two MeV photons, a gamma-ray photon (GeV) and an X-ray photon (keV) or a TeV photon and optical/infrared photon (eV).

Later on in this manuscript, we will mainly drag our attention into gamma-ray pulsars. Therefore, it is useful to now give the different mechanisms able to produce photons in the gamma band. These photons will be able to trigger pair production via the two processes described above. Three mechanisms producing gamma photons can occur in pulsar magnetospheres. The first one is through synchrotron radiation, the second one is via curvature radiation, and the last one is inverse Compton scattering. We will now give the details on the first two mechanisms and leave the third one on side as it will not be used inside this manuscript.

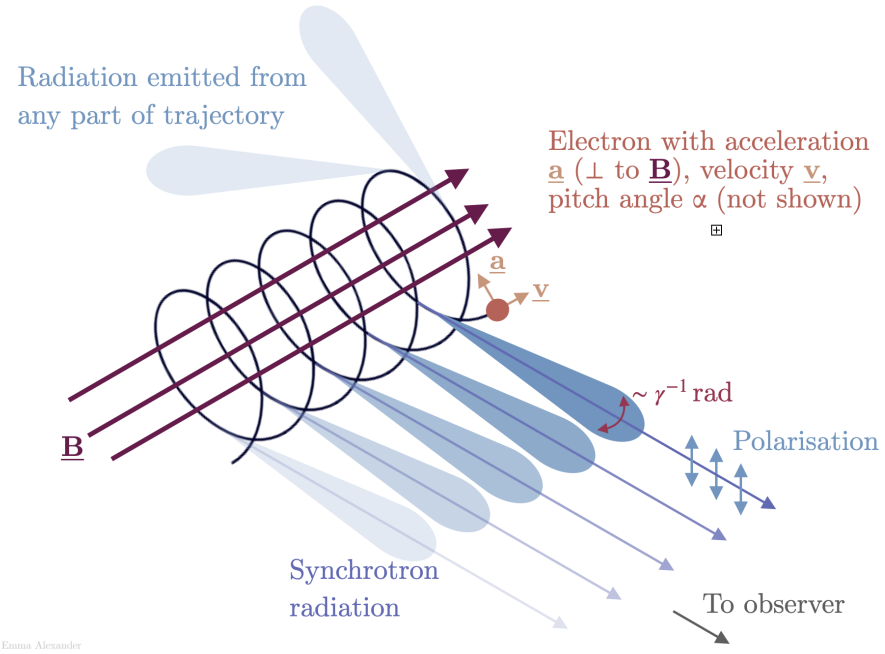

FIGURE 2.9: Sketch of the synchrotron radiation mechanism (figure from Emma Alexander).

Synchrotron radiation is an electromagnetic radiation produced by a relativistic particle. This radiation corresponds to the relativistic version of the cyclotron radiation and is represented in Fig. 2.9. If a particle is accelerated along a magnetic field line, it will radiate some of its energy away during its gyration around the field line. The radiation is emitted in a cone with an opening angle $\sim 1/\gamma$ represented by the blue shaded cones in Fig. 2.9. Any observer outside this range would not see the synchrotron emission produced by the particle.
We consider a particle of mass m_e and charge e evolving in a uniform magnetic field $\mathbf{B}$.

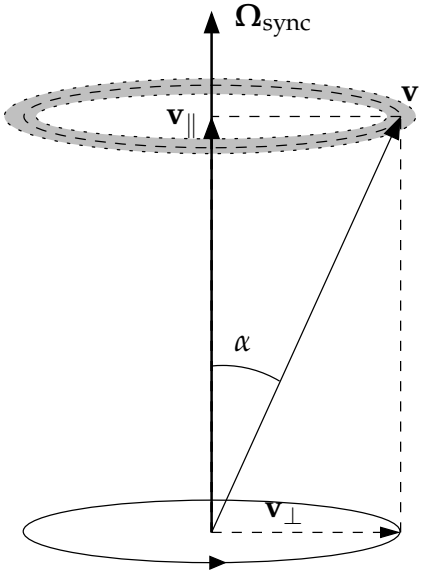

FIGURE 2.10: Synchrotron pitch-angle. The grey annulus indicates where the emission is produced as the particle gyrates.

The particle spirals around the field line with a gyrofrequency $\nu_{\rm sync}$, a Larmor frequency $\omega_{\rm L}$ and a Larmor radius $r_{\rm L}$:

$$\nu_{\rm sync} = \frac{eB}{2\pi\gamma mc} \qquad \omega_{\rm L} = \frac{\nu_{\rm sync}}{2\pi} \qquad r_{\rm L} = \frac{v_{\perp}}{\omega_{\rm L}} = \frac{\gamma m_{\rm e} c^2 \beta \sin\alpha}{eB}. \tag{2.92}$$

where γ is the Lorentz factor of the particle. We define the pitch-angle α between $\mathbf{\Omega}_{\rm sync}$ and $\mathbf{v}$ (see Fig. 2.10). We can decompose the velocity vector of the particle $\mathbf{v} = \mathbf{v}_{\perp} + \mathbf{v}_{\parallel}$ by using this pitch-angle. Furthermore, we are interested here in the power of the emitted radiation. To compute the emitted power, we can use the relativistic Larmor formula

$$\mathcal{P} = \frac{2e^2}{3m^2c^3} \frac{{\rm d}u_{\mu}}{{\rm d}\tau} \frac{{\rm d}u^{\mu}}{{\rm d}\tau} \tag{2.93}$$

where $u^{\mu} = \gamma\,(1, \mathbf{v})$ is the 4-momentum of the particle. The resulting power is

$$\mathcal{P}_{\rm sync} = \frac{2e^4}{3m^2c^3} \gamma^2 \beta^2 B^2 \sin^2\alpha. \tag{2.94}$$

If we consider an isotropic distribution of particles and of pitch-angles $\left(\langle \sin^2\alpha \rangle = 2/3\right)$, the emitted power becomes

$$\langle \mathcal{P}_{\rm sync} \rangle = \frac{4}{3}\, c\sigma_{\rm T}\, \gamma^2\, \beta^2\, U_B \tag{2.95}$$

where $\sigma_{\rm T} = 8\pi r_e^2/3 = 8\pi e^4/3m_e^2c^4$ is the Thomson cross-section and U_B is the electromagnetic energy density. With the emitted power and the energy of the particle $E = \gamma m_e c^2$, we can compute the synchrotron cooling time

$$t_{\rm sync} = \frac{E}{\mathcal{P}_{\rm sync}} = \frac{3m_{\rm e}c^2}{4\gamma c\sigma_{\rm T}\beta^2 U_B}. \tag{2.96}$$

The cooling timescale has a strong dependence on the mass of the particle $\left(m^3\right)$ and a weaker dependence on the Lorentz factor $\left(\gamma^{-1}\right)$. This indicates that the more energetic

and the lighter a particle is, the faster it will cool due to synchrotron radiation. Electrons are more efficient at cooling through synchrotron radiation than protons.

Finally, we can give the energy of the photon produced by synchrotron radiation. In the case of a single charged particle, the radiation power spectrum is centred on the critical frequency (Blumenthal & Gould, 1970)

$$\nu_c = \frac{3eB_\perp \gamma^2}{4\pi m_e c} \tag{2.97}$$

where $B_\perp = B \sin\alpha$ if we assume no external electric field. We can use this frequency to derive the energy of the photon, which reads

$$\epsilon \approx \frac{\hbar e B_\perp \gamma^2}{m_e c}. \tag{2.98}$$

Curvature radiation is also an electromagnetic radiation produced by a relativistic particle. It is a variant of synchrotron radiation for a charged particle moving along a curved field line, for which the gyromotion is neglected. If the magnetic field is strong enough, the particle is bound to the curved magnetic field line, enforcing the trajectory of the particle to be along the field line. By analogy, we can think of a bead (charged particle) on a wire (magnetic field line), see Fig. 2.11.

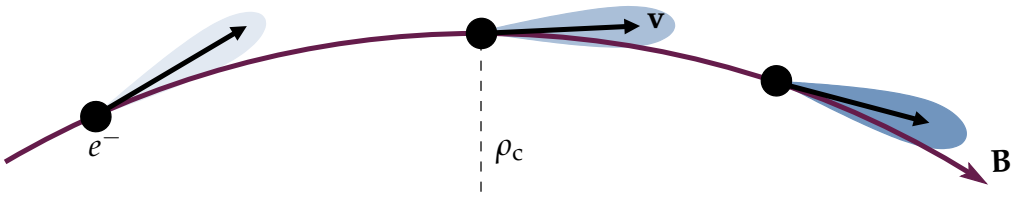

FIGURE 2.11: Sketch of the curvature radiation produced by an electron moving along a curved magnetic field line. The shaded parts correspond to the radiation emitted.

As for the synchrotron case, we can compute the power emitted by curvature radiation. For the curvature radiation, the radius that we need to consider is not the Larmor radius any more but the curvature radius of the field line. This translates into the following relation

$$\frac{v_\perp^2}{r_L} = \frac{v^2}{\rho_c} \tag{2.99}$$

where ρ_c is the curvature radius of the field line which can be expressed as $\rho_c = \left(v^2/v_\perp^2\right) r_L = r_L/\sin^2\alpha$. The amplitude of the magnetic field can be expressed as a function of the curvature radius from Eq. (2.92),

$$B = \frac{\gamma m_e c^2 \beta}{e \rho_c sin\alpha}. \tag{2.100}$$

The next step is to inject Eq. (2.100) in Eq. (2.94) to obtain the total emitted power from curvature radiation:

$$\mathcal{P}_{curv} = \frac{2}{3}\frac{e^2 c \beta^4}{\rho_c^2}\gamma^4 \tag{2.101}$$

Finally, the cooling curvature timescale is given by

$$t_{\rm curv} = \frac{E}{\mathcal{P}_{\rm curv}} = \frac{3 m_{\rm e} c \rho_{\rm c}^2}{2 e^2 \beta^4 \gamma^3} \tag{2.102}$$

Similarly to the synchrotron radiation, the cooling timescale of the curvature radiation is proportional to the mass of the particle. However, in the above equation it is proportional to γ^{-3} meaning that energetic particles radiate even more than in the synchrotron case. This aspect is also visible if we compare the total emitted power of synchrotron and curvature radiation. A particle with a Lorentz factor γ will radiate more power via curvature radiation, $\mathcal{P}_{\rm curv} \propto \gamma^4$, than via synchrotron radiation, $\mathcal{P}_{\rm sync} \propto \gamma^2$.

2.2.3 Goldreich and Julian (1969) model

Before adding complexity to the simulation with pair production, we can first simulate the model proposed by Goldreich and Julian (1969) (GJ) in a PIC simulation. The star is rotating and charges are extracted by the $E_{\parallel}$ component. Because of the rotation and the magnetic field of the star, charges at the surface of the star are decomposed into two regions: negative charges near the poles and positive charges near the equator. If we start spinning the star, the charges will order themselves and some $\mathbf{E}_{\parallel}$ will develop, leading to the extraction of charges. Electrons, the negatively charged particles, leave the stellar surface at the poles, and protons, positively charged, are extracted near the equator (similar to the Faraday disc described previously). This results in a totally different picture than the one proposed in the GJ magnetosphere. The simulation ends up in a disc-dome structure also called the electrosphere (Krause-Polstorff & Michel, 1985; Michel & Smith, 2001), see Fig. 2.12. This configuration is fully charge-separated and has a zero spin-down power. The charge separation occurs exactly at the null surface where the charge density is zero as pointed out in Fig. 2.12. This structure could not be obtained via force-free simulations because the solution is charge separated. This charge-separated aspect is an issue for force-free simulations, but not for PIC simulations.

Therefore, it is necessary to account for pair production in the theory and in simulations to fill the magnetosphere with plasma.

2.2.4 Gap models

The physics of gaps relies on the development of an unscreened electric field in the magnetosphere. The fundamental mechanism in gap models is that particles are accelerated via the unscreened electric field. Once a particle is accelerated it will radiate its energy in the form of photons. If the energy of the photon is sufficient, pair production will occur. The creation of pairs leads to an increase of the number density. If the density reaches the critical Goldreich-Julian density, the acceleration via $\mathbf{E}_{\parallel}$ will cease and pair production will stop. We define the multiplicity parameter κ as the ratio $\kappa = n/n_{\rm GJ}$. This parameter "measures" the number of pairs produced by a single accelerated particle. Once the density drops below the critical one, the accelerator will be once again able to accelerate particles to high-energy, resulting in the emission of photons able to pair produce. Several gaps were proposed in the magnetosphere such as the polar-cap gap (Sturrock, 1971; Ruderman & Sutherland, 1975; Michel, 1979), the outer gap (Cheng et al., 1986) and the slot gap (Arons, 1983; Muslimov & Harding, 2004). In these models, the gamma rays are produced either by curvature radiation (Sturrock, 1971) or inverse-Compton scattering of photons present close to the star.

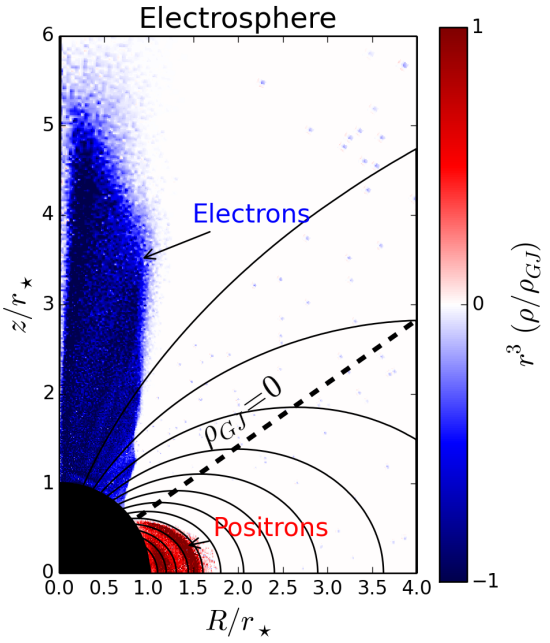

FIGURE 2.12: Electrosphere configuration for the aligned case. Figure taken from Cerutti and Beloborodov (2017).

The polar cap gap is historically the first model proposed. The polar cap is responsible for loading the open field line bundle with plasma, which flows outwards and feeds the wind zone. Two models are proposed: the vacuum gap and the space-charge-limited flow gap. The vacuum gap model introduced by Ruderman and Sutherland (1975) relies on the following main assumptions:

- the pulsar is considered as anti-aligned (opposite direction between $\boldsymbol{\mu}$ and $\boldsymbol{\Omega}$),
- ions are not extracted from the stellar surface because of their high binding energy,
- electrons are easily extracted from the surface if the electric field has the appropriate direction, giving a copious supply of electrons,
- pair cascades (sparks) can quench the gap when triggered.

The behaviour of the gap is given in Fig. 2.13. The gap in itself corresponds to the region where the electric field is unscreened, $\mathbf{E} \cdot \mathbf{B} \neq 0$. The model works as follows:

Position 0: an energetic photon is emitted via curvature radiation

Position 1: the photon is sufficiently energetic to pair produce via magnetic conversion. The positron, and the electron are respectively accelerated outwards and inwards by the electric field

Position 2: the electron emits a curvature photon towards the surface

Position 3: the photon is above the threshold for pair production, the produced pairs follow the same trajectory as in Position 1

Position 4: a curvature photon is produced by the outflowing positron

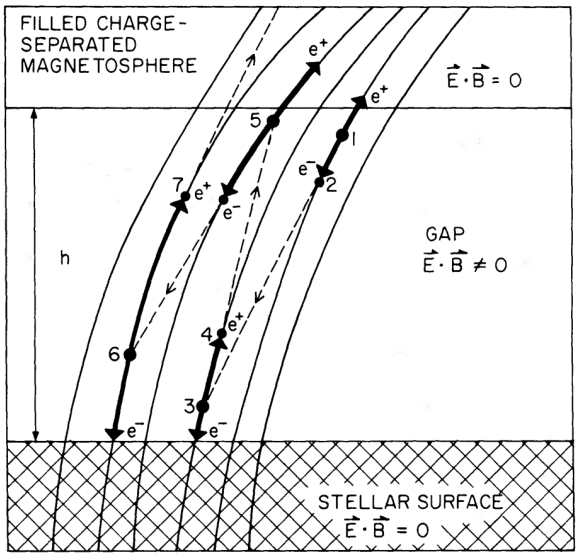

FIGURE 2.13: Polar-cap gap scheme, figure taken from Ruderman and Sutherland (1975). The gap is located where $\mathbf{E}\cdot\mathbf{B}\neq 0$.

Position 5: end of the previous cycle and beginning of the new one

The space-charge-limited flow gap is another polar cap gap model and was introduced by Arons and Scharlemann (1979). The following assumptions are made in this model

- at the surface and in the close region, the electric potential is $\Phi = 0$,
- space-charge-limited flow: the electrostatics and electron flow dynamics above the surface determine the current flowing from the crust. Particles are extracted with a zero-velocity,
- the gap ends with a pair creation front.

The first assumption implies that the star is highly conductive, which is expected from the composition of a neutron star. The second assumption implies that a current flow is able to cut the accelerating electric field at the star's surface. Finally, the pair creation front marks the height of the gap. At this location, a copious number of pairs are produced, thus starting to screen the parallel electric field. The model is schematically described in Fig. 2.14.

Outer gap model (Cheng et al., 1986) is a model based on the null surfaces ($\mathbf{\Omega}\cdot\mathbf{B} = 0$) already present in the electrosphere configuration. Compared to the previous model, the outer gap model is located at least tens of stellar radii away from the star (close to the light-cylinder). The outer gap lies between the first opened field line and the last closed field line, as shown in Fig. 2.15. However, the gap does not extend along the entire field line but starts at the null surface. If we consider that the plasma or charges are only supplied by the star, an unscreened electric field develops in the gap until the Goldreich-Julian density is reached. The acceleration of particles leads to radiation and eventually pair production, with the underlying condition that the potential drop is large enough in the gap.

Slot gap model is an extension of the polar cap gap model and a direct consequence of the space-charge-limited flow model (Arons & Scharlemann, 1979; Muslimov & Harding,

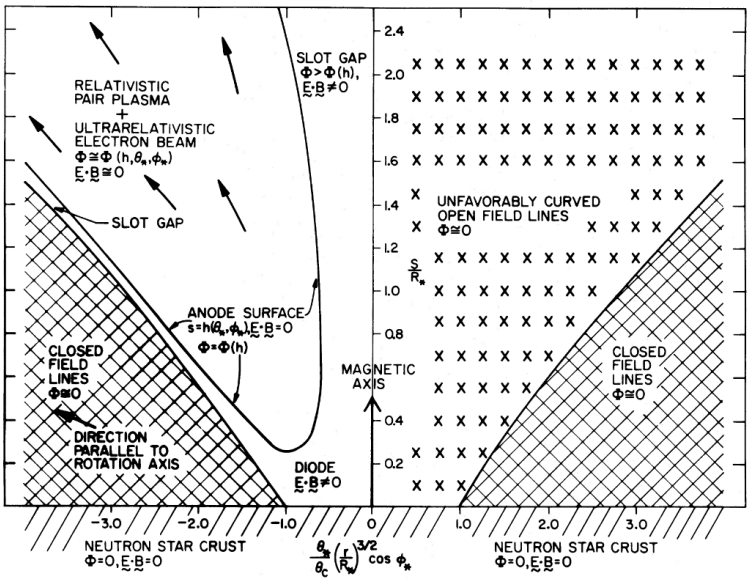

FIGURE 2.14: Space-charge-limited flow gap model, figure taken from Arons and Scharlemann (1979).

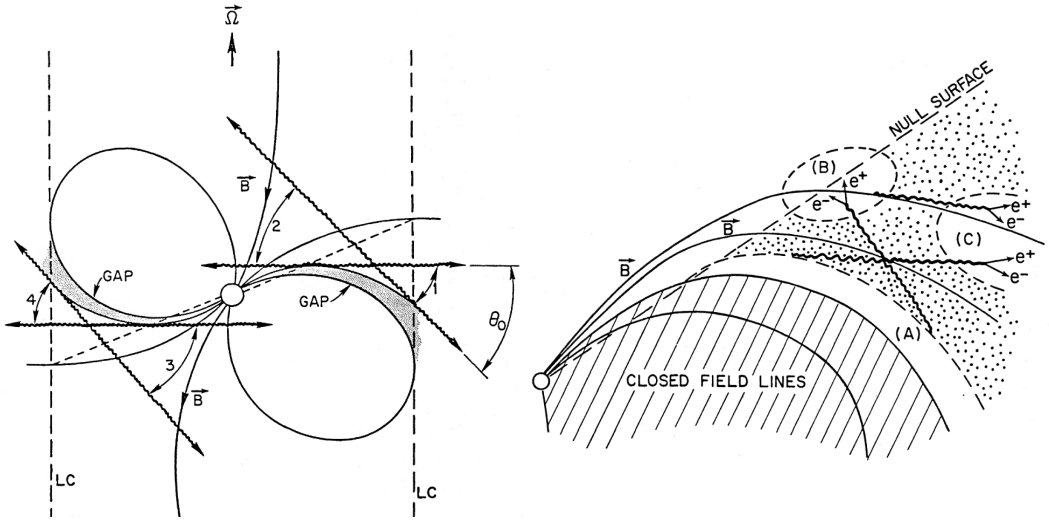

FIGURE 2.15: Outer gap model. The left panel shows the location of the gaps in the magnetosphere of an inclined rotator. The right panel shows the pair cascade occurring in such a gap. Figures taken from Cheng et al. (1986).

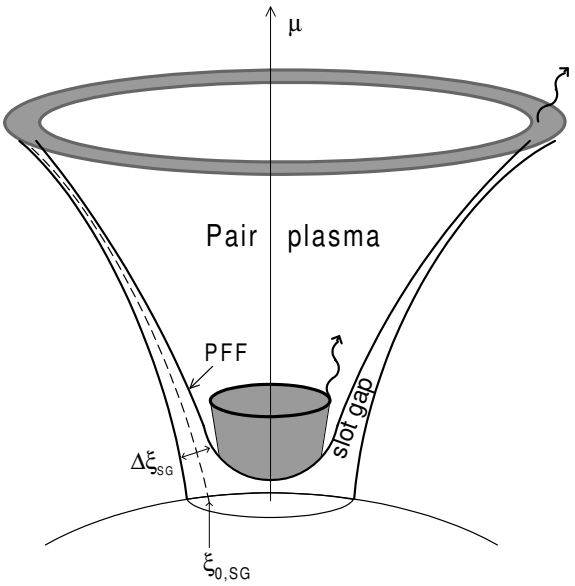

FIGURE 2.16: Slot gap model. Figure taken from Muslimov and Harding (2003)

2003). This model can be seen as a combination of the two polar cap gap models highlighted previously. For the parallel electric field to vanish in the closed region, the former should decrease when getting closer and closer to the last opened field line. If the parallel electric field is weaker on the last opened field line, the particle will need to be accelerated by $\mathbf{E}_{\parallel}$ over a longer distance to radiate a photon with enough energy to pair produce. However, as the particle accelerates thanks to the electric field, the magnetic field decreases the further the particle gets. The height of the pair production front increases as we approach the edge of the polar cap, see Fig. 2.16.

2.2.5 Reconnecting current sheet

In the global picture of the force-free magnetosphere of a pulsar, we consider a dipolar magnetic field. Outside the light-cylinder, we find a radial magnetic field very similar to the split monopole configuration. The magnetic field switches polarity when crossing the equator in the case of an aligned dipole, and magnetic field lines are facing opposite directions. This configuration represents the exact conditions required for relativistic magnetic reconnection. The latter is well known by the collisionless plasma community (solar flares, fusion). The interface between the two polarities, namely the current sheet, is tearing unstable. The current sheet is fragmented by the instability and forms magnetised structures of plasma called plasmoids. They are magnetic islands of plasma.

In a reconnecting system, the upstream plasma (reconnecting) has an inflow velocity v_{in} and the downstream plasma (reconnected) has an outflow velocity v_{out}. The relativistic condition for magnetic reconnection is based on the magnetisation of the plasma, defined as

$$\sigma = \frac{B_0^2}{4\pi\rho c^2} \tag{2.103}$$

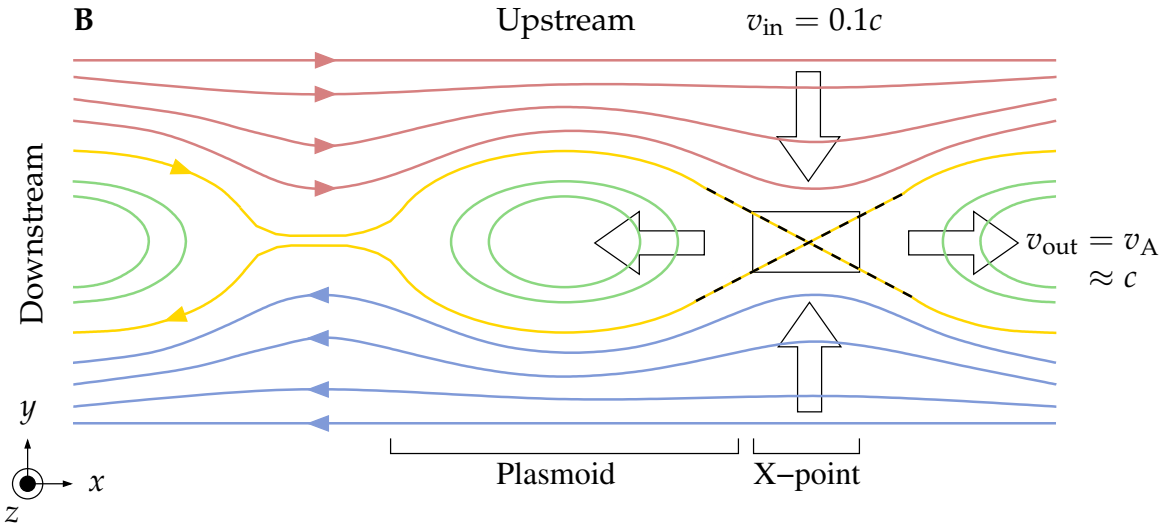

FIGURE 2.17: Scheme of a 2D relativistic magnetic reconnection. Field lines of opposite polarities are represented in red and blue, green field lines correspond to plasmoids and the gold field line is the separatrix. The dashed black line shows the X-point where magnetic reconnection occurs.

If $\sigma \gg 1$, meaning that the magnetic energy density dominates the rest-mass energy density, magnetic reconnection occurs in the relativistic regime. When this is the case, a significant fraction of the magnetic energy is transferred to the outflowing plasma. The latter becomes relativistic due to the large energy gains. The outflow velocity is the Alfvén speed $v_{\rm A}$, however, if $\sigma \gg 1$,

$$\frac{v_{\rm A}}{c} = \frac{\sigma}{1+\sigma} \approx 1 \tag{2.104}$$

and the Alfvén speed approximates the speed of light (Lyutikov & Uzdensky, 2003). Various groups studied the effect of relativistic reconnection, all leading to the same conclusion: magnetic reconnection is fast and efficient at dissipating magnetic energy, and it converts this energy into kinetic energy. Consequently, particles are strongly accelerated ($\gamma \to \sigma$) (Kirk, 2004) and produce non-thermal spectra with a hard power index. Several studies (Zenitani & Hoshino, 2001; Cerutti et al., 2012; Guo et al., 2014; Sironi & Spitkovsky, 2014; Werner et al., 2016) showed that the power index associated to magnetic reconnection is $p \in [1, 2]$ and particles are accelerated up to a Lorentz factor of $\gamma \gtrsim \sigma$.

The scenario of magnetic reconnection is shown in Fig. 2.17. The well-magnetised plasma upstream collapses towards the current sheet of thickness $\delta_{\rm c}$ bringing magnetic flux. When the plasma arrives in the current sheet, the magnetic field is zero and the plasma becomes unmagnetised. The particles of the upstream go through what is called an X-point (black dashed lines). At the X-point, magnetic field lines of opposite polarity snap (high magnetic tension) and reconnect while the slow incoming plasma is advected along the current sheet at the Alfvén speed. We can define the separatrix as the magnetic field lines currently reconnecting. The strong acceleration at the X-point comes from the non-ideal effects driven by the out-of-the-plane electric field $\mathbf{E}_{\rm rec}$. It is possible to compute the reconnection rate $\mathcal{R}$ of field lines. From the Sweet-Parker model (Parker, 1957; Sweet, 1958), the reconnection rate is

$$\mathcal{R} = \frac{v_{\rm in}}{v_{\rm A}} = \frac{\delta_{\rm c}}{L} = \frac{1}{\sqrt{S}}, \qquad S = \frac{L v_{\rm A}}{D_\eta} \tag{2.105}$$

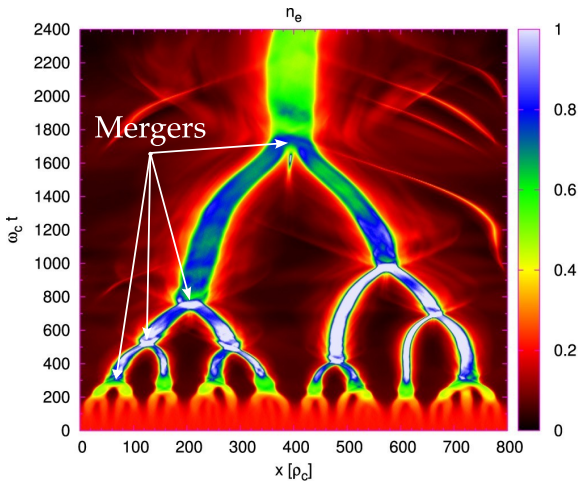

FIGURE 2.18: Hierarchy of plasmoids formation. This spacetime diagram shows the evolution of the electrons density in time inside a reconnecting current sheet. The number of plasmoids is set by the number of over-densities at each time. Figure adapted from Nalewajko et al. (2015).

where L is the macroscopic scale of the problem, S is the Lundquist number and D_η is the magnetic diffusivity or resistivity. In astrophysical systems, the Lundquist number is typically $S \simeq 10^{20}$, resulting in a very small reconnection rate. If we do the same exercise for the relativistic scenario

$$\mathcal{R} = \frac{v_{\rm in}}{v_{\rm A}} \approx \frac{v_{\rm in}}{c} \sim 0.1. \tag{2.106}$$

The reconnection rate is faster and the strength of the reconnecting electric field is around 10% of the magnetic field. This value can also be seen as a limit on the aspect ratio between the current sheet thickness and the system size, $\delta_{\rm c}/L \sim 0.1$. The condition sets the critical aspect ratio beyond which a current sheet is tearing unstable, resulting in the formation of plasmoids. The critical value of the Lundquist number for the breaking of the current sheet is $S_{\rm c} \geq 10^4$. The scenario of fast reconnection was proposed by Uzdensky et al. (2010). In this scenario, plasmoids can grow in size by merging with an adjacent one and interplasmoid current sheets can develop during the merging. This mechanism occurs until the critical layer is reached, when the current sheet becomes stable to the plasmoid instability. It exists a hierarchy in the plasmoid history illustrated in Fig. 2.18, coming from the successive mergers.

Magnetic reconnection is a powerful process for accelerating particles from a rearrangement of the magnetic topology. A fraction of the magnetic energy density is converted into particle energy. We may wonder about the application of relativistic magnetic reconnection in the context of a pulsar magnetosphere. What is the maximum energy reachable by a particle if it undergoes magnetic reconnection in the current sheet beyond the light-cylinder. If we consider that all the magnetic energy is converted into kinetic energy, we have $\gamma \approx \sigma$. We mentioned previously that the current sheet forms right at the light-cylinder. In order to have the value of the particle Lorentz factor $\gamma_{\rm LC}$ at the light-cylinder, we have to compute the magnetisation at the light-cylinder.

$$\sigma_{\rm LC} = \frac{B_{\rm LC}^2}{4\pi n^{\rm LC} m_{\rm e} c^2} \tag{2.107}$$

where $B_{\rm LC}$ and $n^{\rm LC}$ are the magnetic field strength and the number density at the light-cylinder. A dipole magnetic field decreasing as r^{-3} thus we can approximate

$B_{\rm LC} \approx B_\star (r_\star / R_{\rm LC})^3$. For the number density, we use $n^{\rm LC} = \kappa n^{\rm LC}_{\rm GJ}$, where κ is the multiplicity of the secondary pairs. We can use the full potential drop, $\Phi_{\rm pc} = B_\star r_\star^3 / R_{\rm LC}^2$, to express the magnetic field and the number density at the light-cylinder

$$B_{\rm LC} = \frac{\Phi_{\rm pc}}{R_{\rm LC}}, \qquad n^{\rm LC}_{\rm GJ} \approx \frac{\Omega B_{\rm LC}}{2\pi e c} = \frac{\Phi_{\rm pc}}{2\pi e R_{\rm LC}^2}. \tag{2.108}$$

The magnetisation finally reduces to (Cerutti et al., 2015)

$$\gamma_{\rm LC} \approx \sigma_{\rm LC} = \frac{\Phi_{\rm pc} e}{2 m_{\rm e} c^2 \kappa} \tag{2.109}$$

With the values of a canonical pulsar $B_\star = 10^{12}$G, $r_\star = 10$km, $R_{\rm LC} = cP/2\pi$ and $\kappa = 10^2$, we find

$$\sigma_{\rm LC} \approx 10^7 \left(\frac{B_\star}{10^{12}{\rm G}}\right) \left(\frac{P}{100{\rm ms}}\right)^{-2} \left(\frac{\kappa}{10^2}\right)^{-1} \tag{2.110}$$

At the light-cylinder, particles can be accelerated to the maximum Lorentz factor $\gamma_{\rm LC} \approx 10^7$. In reality, a particle will not have such a high acceleration as it will radiate its energy away. However, we can see that magnetic reconnection is able in theory to produce high-energy particles. Even pair production can be triggered after magnetic reconnection, from the radiated photons of accelerated particles. This statement was developed by Lyubarskii (1996). In pulsar current sheets, particles are accelerated and radiate synchrotron photons tangentially to field lines. If we consider that photons have an energy in the MeV range, they are able to pair produce via the Breit-Wheeler process with another photon. The current sheet represents an active site of pair production where a fresh plasma is injected. A recent study by Hakobyan et al. (2019) showed that this pair production mechanism has an impact on the mass loading of the current layer. When the mechanism is triggered, the multiplicity of the plasma increases. This directly impacts the effective magnetisation and thus could also impact the maximum particle energy scale is linked to the magnetisation. The mass loading effect could be important in the case of pulsar magnetospheres.

2.3 Black hole magnetosphere

2.3.1 3+1 electrodynamics

In order to model black hole magnetospheres, we must take into account general relativity. To this purpose, we use the 3+1 formalism (Thorne & MacDonald, 1982; Komissarov, 2004). In this approach, the spacetime is sliced between the "absolute" space and the "absolute" time. The "absolute" space corresponds to $3D$ space-like hypersurfaces to which an "absolute" time is associated. This decomposition eases the interpretation of the equations with a formulation similar to the flat spacetime equations. The physical intuition from flat spacetime can be applied to the equations of the 3+1 formalism. This formulation is also a pillar for numerical simulations, as only the absolute time needs to be accounted for.

Definition 1: Nomenclature

In this chapter, we use the following conventions:

$$\bullet\ g_{\mu\nu} \qquad \bullet\ \gamma_{ij} = g_{ij} \qquad \bullet\ \gamma = \det(\gamma_{ij}) \qquad \bullet\ g = -\alpha^2\gamma = \det\left(g_{\mu\nu}\right)$$

$$\bullet\ x^\mu = (t, x^i) \qquad \bullet\ x_\mu y^\mu = \sum_{k=0}^{3} x_k y^k$$

The metric tensor is noted $g_{\mu\nu}$, the associated metric signature is $(-,+,+,+)$. The determinant of the metric is g. The space-like part of the tensor is written γ_{ij}. The determinant of the spatial metric is γ. Regarding the coordinates, they are written as $x^\mu = (t, x^i)$ where Greek and Latin indices respectively span $\mu = 0,\dots,3$ and $i = 1,\dots,3$. Finally, we assume implicit summation over repeated indices.

The expression of the metric tensor can be derived from the spacetime interval $\mathrm{d}s^2$ using the ADM form (Arnowitt et al., 1959).

$$\mathrm{d}s^2 = \left(\beta^2 - \alpha^2\right)\mathrm{d}t^2 + 2\beta_i \mathrm{d}x^i \mathrm{d}t + \gamma_{ij}\mathrm{d}x^i\mathrm{d}x^j \tag{2.111}$$

where α is the "lapse function" and β is the "shift vector". The lapse function is used to transform the time between the absolute time coordinate t and the proper time τ_{FIDO} of a "fiducial observer" (FIDO),

$$\mathrm{d}\tau_{\mathrm{FIDO}} = \alpha \mathrm{d}t. \tag{2.112}$$

The consequence of this time transformation can be physically seen as a gravitational redshift of the FIDO with respect to an observer at infinity. The 4-velocity of the fiducial observer's time is

$$n_\mu = (-\alpha, 0, 0, 0) \tag{2.113}$$

The shift vector $\boldsymbol{\beta}$ expresses the spatial velocity of the FIDO with respect to the spatial grid associated to the spacetime. It drifts on the coordinate grid with the 4-velocity

$$n^\mu = \frac{1}{\alpha}(1, -\beta^i). \tag{2.114}$$

Finally, the spacetime interval gives the relation between time and space, and is used to determine the full metric tensor, $g_{\mu\nu}$. From Eq. (2.111), the metric tensor is expressed as

$$g_{\mu\nu} = \begin{pmatrix} \beta^2 - \alpha^2 & \beta_j \\ \beta_i & \gamma_{ij} \end{pmatrix}. \tag{2.115}$$

The metric tensor relies on the lapse function, the shift vector and the spatial metric. A useful quantity to compute is $g^{\mu\nu}$, the inverse of the metric tensor. As for any tensor, we have the identity relation $g_{\mu\sigma}g^{\sigma\nu} = \delta^\nu_\mu$. By plugging Eq. (2.115) in the identity relation, we obtain

$$g^{\mu\nu} = \begin{pmatrix} -1/\alpha^2 & \beta^j/\alpha^2 \\ \beta^i/\alpha^2 & \gamma^{ij} - \beta^i\beta^j/\alpha^2 \end{pmatrix} \tag{2.116}$$

where γ^{ij} is the inverse of the spatial metric γ_{ij}. The metric tensor will be useful to raise or lower the indices of our tensors.

With the description of the metric tensor out of the way, we can proceed to the derivation of Maxwell's equations in curved spacetime. We use the formalism described by Komissarov (2004, 2011). The covariant Maxwell's equations are

$$\nabla_\mu \star F^{\nu\mu} = 0 \tag{2.117}$$

$$\nabla_\mu F^{\nu\mu} = \frac{4\pi}{c} I^\nu \tag{2.118}$$

where $F^{\mu\nu} = g^{\mu\alpha} g^{\nu\beta} F_{\alpha\beta}$ is the electromagnetic tensor, $\star F^{\mu\nu} = (1/2)\sqrt{-g}\,\epsilon^{\mu\nu\alpha\beta} F_{\alpha\beta}$ is the Hodge dual of the electromagnetic tensor, and I^ν is the 4-vector of the electric current. The electromagnetic tensor can be expressed using the vector potential A_μ by

$$F_{\mu\nu} = \partial_\mu A_\nu - \partial_\nu A_\mu \tag{2.119}$$

Finding an analytical expression of A_μ will be at the centre of Sect. 2.3.3. Within the "3+1" approach of Komissarov (2004), we define the following quantities

$$B^i = \frac{1}{2}\sqrt{\gamma}\epsilon^{ijk} F_{jk} \tag{2.120}$$

$$E_i = F_{it} \tag{2.121}$$

$$D^i = \alpha F^{ti} \tag{2.122}$$

$$H_i = \frac{\alpha}{2}\sqrt{\gamma}\epsilon_{ijk} F^{jk} \tag{2.123}$$

$$J^i = \alpha I^i \tag{2.124}$$

$$\rho = \alpha I^t \tag{2.125}$$

Before giving Maxwell's equations, we just need to express the divergence and curl of a vector field in curved spacetime. They are expressed as

$$\boldsymbol{\nabla} \cdot \mathbf{A} = \frac{1}{\sqrt{\gamma}} \partial_i \left(\sqrt{\gamma} A^i \right) \tag{2.126}$$

$$(\boldsymbol{\nabla} \times \mathbf{A})^i = \frac{1}{\sqrt{\gamma}} \epsilon^{ijk} \partial_j A_k \tag{2.127}$$

Maxwell's equations in curved spacetime using the "3+1" formalism can be written as

$$\begin{cases} \boldsymbol{\nabla} \cdot \mathbf{D} = 4\pi\rho \\ \dfrac{1}{\sqrt{\gamma}} \dfrac{\partial \sqrt{\gamma}\,\mathbf{D}}{\partial t} = c\boldsymbol{\nabla} \times \mathbf{H} - 4\pi\mathbf{J} \\ \boldsymbol{\nabla} \cdot \mathbf{B} = 0 \\ \dfrac{1}{\sqrt{\gamma}} \dfrac{\partial \sqrt{\gamma}\,\mathbf{B}}{\partial t} = -c\boldsymbol{\nabla} \times \mathbf{E} \end{cases} \xRightarrow[\partial_t g_{\mu\nu} = 0]{\text{assuming}} \begin{cases} \boldsymbol{\nabla} \cdot \mathbf{D} = 4\pi\rho \\ \dfrac{\partial \mathbf{D}}{\partial t} = c\boldsymbol{\nabla} \times \mathbf{H} - 4\pi\mathbf{J} \\ \boldsymbol{\nabla} \cdot \mathbf{B} = 0 \\ \dfrac{\partial \mathbf{B}}{\partial t} = -c\boldsymbol{\nabla} \times \mathbf{E} \end{cases} \tag{2.128}$$

To obtain the right set of equations, we assume that the metric tensor is stationary. This set is similar to the set of Maxwell's equations for an active medium, except that here the curved spacetime is playing as the active medium. The fields $\mathbf{E}$ and $\mathbf{H}$ are defined via constitutive relations,

$$\begin{cases} \mathbf{E} = \alpha\mathbf{D} + \boldsymbol{\beta} \times \mathbf{B} \\ \mathbf{H} = \alpha\mathbf{B} - \boldsymbol{\beta} \times \mathbf{D} \end{cases} \tag{2.129}$$

The four fields can be related to two different classes of observers, the fiducial observer and the observer on the coordinate grid. The interpretation of the fields is

- **D** and **B** are the fields measured by the FIDO
- **E** and **H** are the fields attached to the coordinates grid

For a flat spacetime, the proper time τ_{FIDO} and the absolute time t are equal thus, $\alpha = 1$ and there is no shift of the observer in the spacetime, $\beta^i = 0$. In these conditions, we have $\mathbf{E} = \mathbf{D}$ and $\mathbf{H} = \mathbf{B}$ and the classical Maxwell's equations are recovered from the "3+1" set. The last unknown is the current density **J**,. This 3-vector is measured on the coordinates grid, and we have a constitutive relation

$$\mathbf{J} = \alpha\mathbf{j} + c\rho\boldsymbol{\beta} \tag{2.130}$$

where **j** is the current density measured by the FIDO. The second term corresponds to the current coming from the drifting charges relative to the FIDO.

2.3.2 Kerr metric

The first step towards the description of a black hole magnetosphere is to define the properties of the spacetime. The Kerr metric (Kerr, 1963) describes the spacetime around a rotating black hole. For convenience reasons, we use the Kerr-Schild coordinates. This set of coordinates is powerful as it removes the singularity of the Boyer-Lindquist coordinates located at the event horizon radius. The Kerr-Schild system also has a singularity but at $r = 0$, which is more convenient numerically as the singularity is inside the event horizon and thus does not need a specific treatment. In the spherical Kerr-Schild coordinates system, the Kerr metric is (Komissarov, 2004)

$$g_{\mu\nu} = \begin{pmatrix} z-1 & z & 0 & -zar_{\mathrm{g}}\sin^2\theta \\ z & 1+z & 0 & -a\sin^2\theta(1+z) \\ 0 & 0 & \rho^2 & 0 \\ -zar_{\mathrm{g}}\sin^2\theta & -a\sin^2\theta(1+z) & 0 & \Sigma\sin^2\theta/\rho^2 \end{pmatrix} \tag{2.131}$$

where

$$\rho^2 = r^2 + a^2\cos^2\theta \tag{2.132}$$

$$z = \frac{2rr_{\mathrm{g}}}{\rho^2} \tag{2.133}$$

$$\Sigma = \left(r^2 + a^2\right)^2 - a^2\Delta\sin^2\theta \tag{2.134}$$

$$\Delta = r^2 + a^2r_{\mathrm{g}}^2 - 2rr_{\mathrm{g}} \tag{2.135}$$

The parameter a is a dimensionless number characterising the spin of the black hole. This parameter ranges from $a = -1$ to $a = 1$ and corresponds respectively to a Schwarzschild black hole (non-rotating) and a maximally rotating black. From the expression of the metric, we can derive the Kerr-Schild lapse function and the shift-vector

$$\alpha = \frac{1}{\sqrt{1+z}} \qquad \beta^i = \left(\frac{z}{1+z}, 0, 0\right) \tag{2.136}$$

The shift-vector indicates that in the Kerr-Schild coordinates, a fiducial observer moves radially towards the singularity in $r = 0$. The spin of the black hole also defines the radius of the event horizon $r_{\rm H}$. This radius corresponds to the positive root found when $\Delta = 0$.

$$\begin{aligned} \Delta &= r^2 + a^2 r_{\rm g}^2 - 2 r r_{\rm g} = 0 \\ \Rightarrow r_{\rm H} &= r_g \left(1 + \sqrt{1 - a^2}\right) \end{aligned} \tag{2.137}$$

The event horizon radius gives the radial distance at which any observer, particles, or massless particles are dragged inside the black hole without any possible escape. This aspect is particularly important for numerical simulations: nothing can escape from the black hole. This means that if we see fields or particles escaping from the inside of the event horizon, they are not physical but numerical as nothing can escape once it crosses the horizon. This is a significant feature to look at when developing a General Relativistic (GR) code. Another critical radius is the radius of the ergosphere. Compared to the event horizon, it is possible to move freely inside and outside of the ergosphere. However, any observer, particles or massless particles suffer from the frame-dragging effect. They cannot be at rest and are dragged by the rotating spacetime according to the black hole rotation. The radius of the ergosphere is obtained by taking the positive root of $g_{tt} = 0$.

$$\begin{aligned} g_{tt} &= z - 1 = 0 \\ &\underset{(2.132)}{\overset{(2.133)}{\Longleftrightarrow}} r^2 + a^2 r_{\rm g}^2 \cos^2\theta - 2 r r_{\rm g} = 0 \\ &\Longrightarrow r_{\rm erg} = r_{\rm g}\left(1 + \sqrt{1 - a^2\cos^2\theta}\right) \end{aligned} \tag{2.138}$$

The radius of the ergosphere depends on the spin of the black hole but also on the azimuthal angle θ. The influence of the spin on $r_{\rm H}$ and $r_{\rm erg}$ is given in Fig. 2.19.
The slower the black hole spins, the bigger the horizon is. However, while the horizon shrinks with higher spins, the ergo-region gets bigger with spin. The maximum radial extension of the ergo-region is at the equator and is independent of the spin.

$$\forall\, a, r_{\rm erg}\left(\pi/2, a\right) = 2 r_{\rm H} \tag{2.139}$$

The final characteristic of a Kerr black hole is the light surfaces. These are the exact analogue of the light-cylinder in pulsar magnetospheres, except that here we have two surfaces. To obtain their location, we consider a point orbiting the black hole with the angular velocity Ω characterised by its worldline (Komissarov, 2004)

$$f\left(\Omega, r, \theta\right) = g_{tt} + 2 g_{t\phi}\frac{\Omega}{c} + g_{\phi\phi}\frac{\Omega^2}{c^2} \tag{2.140}$$

where $f\left(\Omega, r, \theta\right)$ is the light-surface function. Two regimes can be expressed from this equation: the subluminal and superluminal rotations. The particle can corotate if $f < 0$ with a time-like (subluminal) worldline. If $f > 0$, the particle cannot corotate and its worldline is space-like (superluminal). Instead of a particle, we can consider a rigidly rotating magnetosphere at Ω. The above conditions on f give the regions where solid rotation is possible. Light surfaces are defined as surfaces where $f = 0$. Eq. (2.140) allows

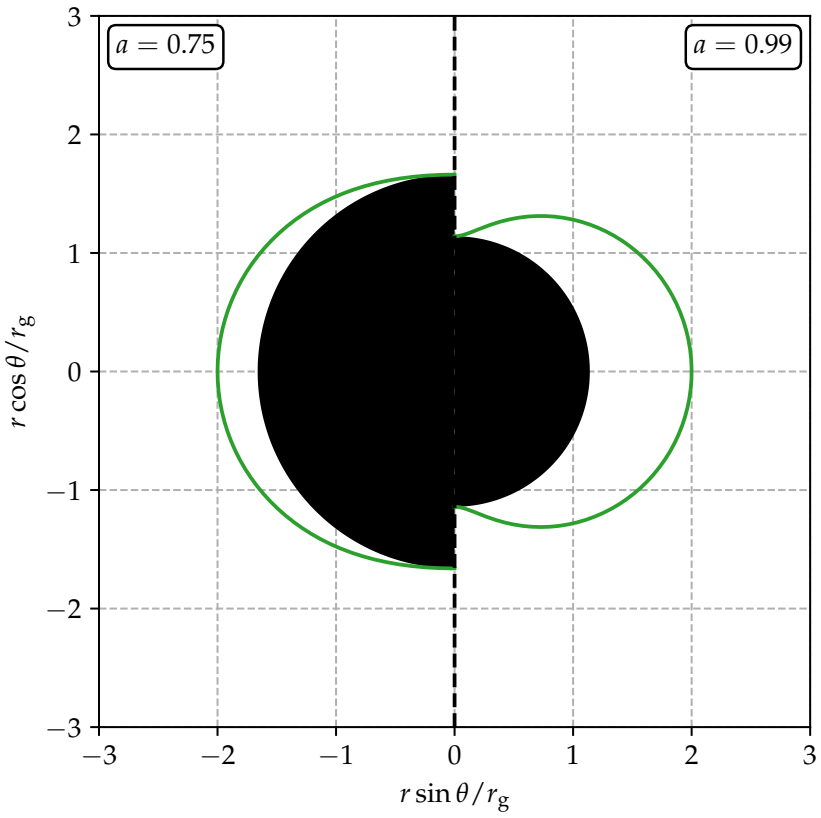

FIGURE 2.19: Figure showing the spin dependence of the event horizon and the ergosphere.

two sets of roots: one set for Ω and another one for r. First, we can the value of the angular velocity Ω satisfying $f = 0$. The roots of Eq. (2.140) for the quadratic equation in Ω are

$$\Omega_{\pm} = \Omega_{\mathrm{H}} \pm c\frac{\sqrt{g_{t\phi}^2 - g_{\phi\phi}g_{t\phi}}}{g_{\phi\phi}} \tag{2.141}$$

where $\Omega_{\mathrm{H}} = -cg_{t\phi}/g_{\phi\phi}$ is the angular velocity of the black hole. It is related to the spin of the black hole by

$$\Omega_{\mathrm{H}} = -c\frac{g_{t\phi}\left(r_{\mathrm{H}}\right)}{g_{\phi\phi}\left(r_{\mathrm{H}}\right)} = \frac{ac}{2r_{\mathrm{H}}} \tag{2.142}$$

Next, we can find the radii $r_{\mathrm{ls}}(\theta)$ for which $f = 0$. We can consider the non-rotating case and the slow-rotating one. In the case $\Omega = 0$, the light surface is given by

$$f(0,r,\theta) = g_{tt} = 0 \Longrightarrow r_{\mathrm{ls}}(\theta) = r_{\mathrm{erg}} = r_{\mathrm{g}}\left(1 + \sqrt{1 - a^2\cos^2\theta}\right) = r_{\mathrm{g}} \tag{2.143}$$

This radius corresponds to the location of the "inner light surface" which is the ergosphere for $\Omega = 0$. However, if $\Omega > 0$, the light surface is not located at the ergosphere any more but rather between the event horizon and the ergosphere. For the second light surface, we assume $0 < \Omega/\Omega_{\mathrm{H}} \ll 1$ and $r \gg r_{\mathrm{g}}$ giving

$$f(\Omega, r, \theta) = r^2 \sin^2\theta \frac{\Omega^2}{c^2} - 1 \Longrightarrow r_{\rm ls}(\theta) = \frac{c}{\Omega \sin\theta} \tag{2.144}$$

The effect of Ω on the light surfaces is shown in Fig. 2.20.

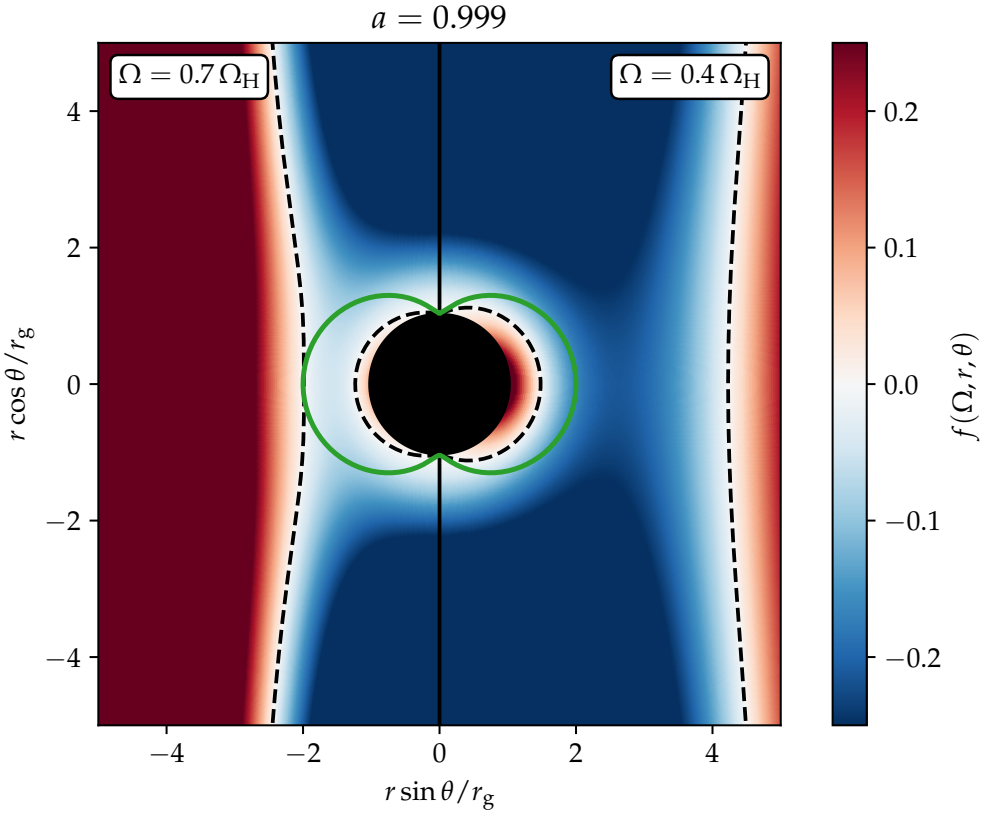

FIGURE 2.20: Light-surface function for a spin $a = 0.999$. The light-surfaces are represented by the black dashed lines. Their positions depend on the angular velocity Ω.

When Ω increases, the inner light surface gets closer to the ergosphere as expected from the $\Omega = 0$ case. For the outer light surface, it is closer for an increasing angular velocity. It also corresponds to the classical light cylinder defined in pulsar magnetosphere theory. No matter the value of Ω, both light surfaces never intersect.

2.3.3 Wald configuration

As for the pulsar theory, the first study was done in vacuum where Wald (1974) was able to derive an exact solution. This solution describes a Kerr black hole embedded in a uniform external magnetic field aligned with the black hole spin axis. Assuming stationarity and the axisymmetric geometry, Wald's 4-potential is

$$A^\mu = \frac{B_0}{2}\left(\psi^\mu + 2ar_{\rm g}\eta^\mu\right) \tag{2.145}$$

where B_0 is the amplitude of the magnetic field, ψ^μ and η^μ are the axial and timelike Killing vectors. They are expressed as

$$\eta^\mu = \partial_t = (1,0,0,0) \qquad \psi^\mu = \partial_\phi = (0,0,0,1) \tag{2.146}$$

These Killing vectors describe the two symmetries of our problem: stationarity ∂_t and axisymmetric geometry ∂_ϕ. The covariant form of the Killing vectors can be expressed by lowering the index $\left(K_\mu = g_{\mu\nu}K^\nu\right)$,

$$\eta_\mu = g_{\mu\nu}\eta^\nu = (g_{tt}, g_{rt}, 0, g_{\phi t}) \tag{2.147}$$
$$\psi_\mu = g_{\mu\nu}\psi^\nu = (g_{t\phi}, g_{r\phi}, 0, g_{\phi\phi}) \tag{2.148}$$

The full expression of the 4-potential in the contravariant and covariant form is

$$A^\mu = \frac{B_0}{2}\left(2ar_{\rm g}, 0, 0, 1\right) \tag{2.149}$$
$$A_\mu = \frac{B_0}{2}\left(g_{t\phi} + 2ar_{\rm g}g_{tt},\ g_{r\phi} + 2ar_{\rm g}g_{rt},\ 0,\ g_{\phi\phi} + 2ar_{\rm g}g_{\phi t}\right) \tag{2.150}$$
$$= \frac{B_0}{2}\begin{pmatrix} -zar_{\rm g}\,\sin^2\theta + 2ar_{\rm g}\,(z-1) \\ -a\sin^2\theta\,(1+z) + 2ar_{\rm g}z \\ 0 \\ \Sigma\frac{sin^2\theta}{\rho^2} - 2a^2r_{\rm g}^2\,z\,\sin^2\theta \end{pmatrix} \tag{2.151}$$

With the full description of the 4-potential, the electromagnetic fields are expressed as

$$B^i = \frac{1}{\sqrt{\gamma}}\epsilon^{ijk}\partial_j A_k \tag{2.152}$$
$$E_i = -\partial_i A_t - \partial_t A_i \tag{2.153}$$

The Wald solution, in vacuum for a maximally rotating black hole $(a \longrightarrow 1)$, shows that the magnetic field lines are not going through the horizon of the black hole but around it, Fig. 2.21. The field lines are expelled by the black hole or are at maximum tangent to the horizon. The effect is often called the "Meissner" effect and comes from the superconductor community. When a conductor is cooled below its critical temperature, it transitions into the superconducting state. During this transition, the magnetic field is expelled and does not enter the superconductor.

Just like in the pulsar case, we may wonder about the energetics of the vacuum solution. In general relativity, the energetics is contained in the electromagnetic-stress-energy tensor T^μ_ν, which verifies the equation

$$\nabla_\mu T^\mu{}_\nu = -F_{\nu\sigma}I^\sigma. \tag{2.154}$$

The resulting tensor reads

$$T^\mu{}_\nu = \frac{1}{4\pi}\left(F^{\mu\alpha}F_{\nu\alpha} - \frac{1}{4}\left(F_{\alpha\beta}F^{\alpha\beta}\right)\delta^\mu{}_\nu\right) \tag{2.155}$$

The electromagnetic-stress-energy tensor can also be expressed in a matrix form,

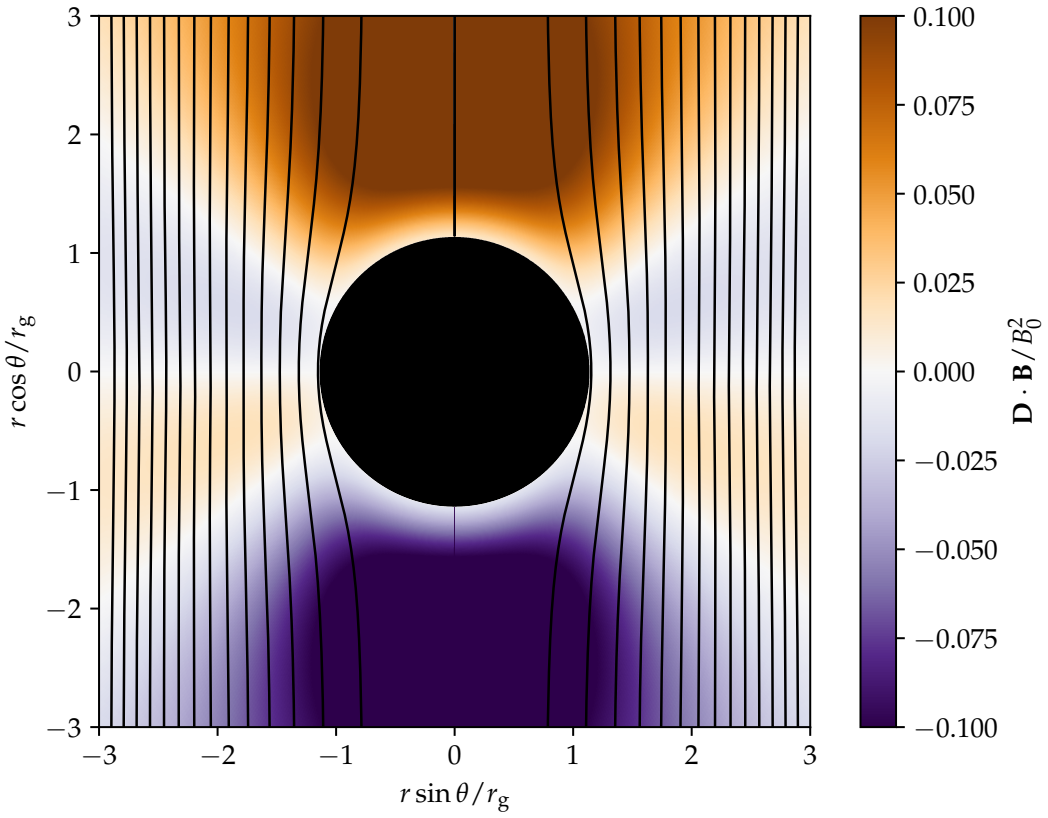

FIGURE 2.21: Map of $\mathbf{D}\cdot\mathbf{B}$ for the Wald solution in vacuum showing the Meissner effect. Magnetic field lines are represented by the solid black lines.

$$
\begin{aligned}
T^{\mu}{}_{\nu} &= \begin{pmatrix} T^{t}{}_{t} & T^{i}{}_{t} \\ T^{t}{}_{i} & T^{i}{}_{j} \end{pmatrix} \\
&= \begin{pmatrix} -\frac{1}{8\pi\alpha}\left(\mathbf{E}\cdot\mathbf{D}+\mathbf{B}\cdot\mathbf{H}\right) & -\frac{1}{4\pi\alpha}\sqrt{\gamma}\epsilon^{ijk}E_j H_k \\ \frac{1}{4\pi\alpha}\sqrt{\gamma}\epsilon_{ijk}D^j B^k & -\frac{1}{4\pi\alpha}\left(D^i E_j + B^i H_j\right) + \frac{1}{8\pi\alpha}\left(\mathbf{E}\cdot\mathbf{D}+\mathbf{B}\cdot\mathbf{H}\right)\delta^{i}{}_{j} \end{pmatrix}
\end{aligned}
\tag{2.156}
$$

The above tensor contains a lot of useful information regarding the energetics of the system. For example, the Poynting flux is expressed with the $T^{i}{}_{t}$ component as

$$
L = \iint T^{r}{}_{t}\,\alpha\sqrt{\gamma}\mathrm{d}\theta\mathrm{d}\phi = \iint \Pi^{r}\sqrt{\gamma}\mathrm{d}\theta\mathrm{d}\phi \tag{2.157}
$$

where

$$
\Pi^{r} = -c\alpha T^{r}{}_{t} = \frac{c}{4\pi}\left(\mathbf{E}\times\mathbf{H}\right)^{r} \tag{2.158}
$$

For the Wald solution, we remind the Killing vectors which are $\partial_t = \partial_\phi = 0$. If we apply these conditions to Maxwell's equations we are left with $\boldsymbol{\nabla}\times\mathbf{H} = \boldsymbol{\nabla}\times\mathbf{E} = \mathbf{0}$ which implies (via Eq. 2.153) $E_\phi = H_\phi = 0$. This leads to a zero outgoing Poynting flux, meaning that no electromagnetic energy is extracted from the black hole. The extraction of energy can only happen if charges and currents are present in the magnetosphere.

2.3.4 Beyond Wald solution in vacuum: force-free magnetosphere

The Wald solution played a crucial role in the development of black hole magnetosphere theory. However, just like in pulsar theory, the vacuum solution is not sufficient and the possibility of having plasma around the black hole needs to be discussed. In Fig. 2.21, we show a map of $\mathbf{D}\cdot\mathbf{B}$. This figure indicates the presence of a strong parallel component of the electric field $\mathbf{D}$. This is reminiscent of the unscreened electric field present in pulsar magnetospheres. We recall that this unscreened field is able to accelerate particles to high Lorentz factors, possibly above the pair creation threshold. Contrary to the case of a pulsar, a black hole is not able to inject plasma from its "surface" to start a pair cascade. This issue of the plasma supply is of high interest but at the limit of the scope of this dissertation. The plasma coming from an accretion disc or a stellar wind of a companion could be a way of supplying plasma to the magnetosphere. If such a plasma gets close to the black hole, it will experience a strong $\mathbf{D}_{\parallel}$ resulting in particle acceleration. If particles are sufficiently accelerated, they will radiate high-energy photons. The latter could interact with low-energy photons in order to produce pairs via the Breit-Wheeler mechanism ($\gamma\gamma$ process). If we consider that this mechanism is efficient enough to start a pair cascade and supply plasma to the black hole, we can end up in having a density large enough to screen the electric field. This could lead to the development of spark gaps similar to the gap models in pulsar magnetospheres (Crinquand et al., 2020).

The force-free electrodynamics was derived previously in Sect. 2.1.2. However, we now consider a curved spacetime with modified Maxwell's equations. Following the same procedure as in the flat space case, we can derive the current density in the force-free regime. We recall the set of Maxwell's equations for a stationary metric $\left(\partial_t g_{\mu\nu}=0\right)$ and the force-free condition from flat space

$$\boldsymbol{\nabla}\cdot\mathbf{D}=4\pi\rho \tag{2.159}$$

$$\frac{\partial\mathbf{D}}{\partial t}=c\boldsymbol{\nabla}\times\mathbf{H}-4\pi\mathbf{J} \tag{2.160}$$

$$\boldsymbol{\nabla}\cdot\mathbf{B}=0 \tag{2.161}$$

$$\frac{\partial\mathbf{B}}{\partial_t}=-c\boldsymbol{\nabla}\times\mathbf{E} \tag{2.162}$$

$$\rho\mathbf{E}+\frac{\mathbf{J}\times\mathbf{B}}{c}=0 \tag{2.163}$$

The recipe to derive the current density is the following (McKinney, 2006; Komissarov, 2011):

Demonstration 2: 3+1 current density recipe

1. Assume $\partial_t\left(\mathbf{D}\cdot\mathbf{B}\right)=0=\left(\partial_t\mathbf{D}\right)\cdot\mathbf{B}+\mathbf{D}\cdot\left(\partial_t\mathbf{B}\right)$
2. Derive $\mathbf{J}\cdot\mathbf{B}$ by injecting Eqs. (2.160) and (2.162) in the previous equation
3. then, take the cross product Eq. (2.163)$\times\mathbf{B}$ and inject $\mathbf{J}\cdot\mathbf{B}$

If we follow this recipe, we end up with a current density given by

$$\mathbf{J}=\frac{c}{4\pi}\boldsymbol{\nabla}\cdot\mathbf{D}\left(\frac{\mathbf{E}\times\mathbf{B}}{B^2}\right)+\frac{c}{4\pi}\Big(\mathbf{B}\cdot\left(\boldsymbol{\nabla}\times\mathbf{H}\right)-\mathbf{D}\cdot\left(\boldsymbol{\nabla}\times\mathbf{E}\right)\Big)\frac{\mathbf{B}}{B^2} \tag{2.164}$$

The expression of the current density is a combination of the fields from the FIDO $(\mathbf{D}, \mathbf{B})$ and the fields $(\mathbf{E}, \mathbf{H})$ measured on the coordinate grid. The set of equations is now closed by Eq. (2.164).

2.3.5 Blandford-Znajek solution

Similarly to what was done by the pulsar theory community, Blandford and Znajek wanted to give an analytical solution within the force-free regime. Previously, we mentioned that black hole magnetospheres are the analogue of pulsar magnetospheres in curved spacetime. Consequently, the pulsar equation appeared as a reasonable starting point. By applying a perturbation method, Blandford and Znajek (1977) were able to find an analytical solution. This solution is a monopole verifying the Znajek (1977) condition at the horizon, and the Michel monopole at infinity. If the black hole is non-rotating (i.e. $a = 0$), $\Psi = \Psi_0(1 - \cos\theta)$ is an exact solution of the "pulsar equation". Blandford and Znajek took this solution and extended it to a slowly rotating black hole for a spin $a \ll 1$. A sketch of the solution is given in Fig. 2.22. It is the GR analogue of the Michel monopole.

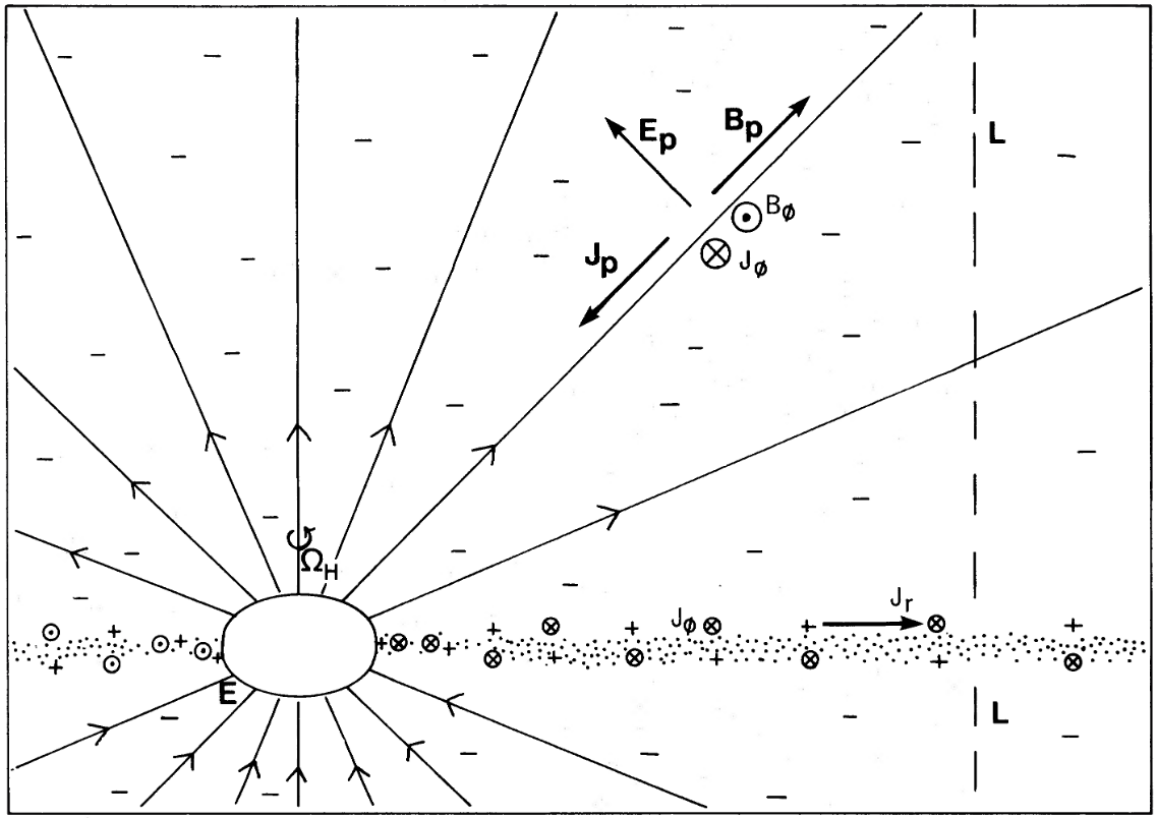

FIGURE 2.22: Sketch of the monopole solution in curved spacetime. Figure taken from Blandford and Znajek (1977).

Contrary to the Wald solution, the Blandford and Znajek (1977) solution can extract energy from the black hole. For a monopole configuration, the radially outgoing Poynting flux is

$$L_{\rm BZ} = \iint T^r_t \, \alpha \sqrt{\gamma} \mathrm{d}\theta \mathrm{d}\phi = \iint \Pi^r \sqrt{\gamma} \, \mathrm{d}\theta \mathrm{d}\phi \tag{2.165}$$

Blandford and Znajek (1977) showed that, in Boyer-Lindquist coordinates and assuming $c = r_{\rm g} = 1$,

$$T^{r}{}_{t}\,\alpha\sqrt{\gamma} = \frac{1}{4\pi}\Omega\left(\Omega_{\mathrm{H}} - \Omega\right)\left(\partial_\theta A_\phi\right)^2 \frac{r^2 + a^2}{r^2 + a^2\cos^2\theta}\sin\theta \tag{2.166}$$

Two unknowns are present in the above equation: Ω and $\partial_\theta A_\phi$. For the first unknown, we set $\Omega = \Omega_{\mathrm{H}}/2$ to maximise the expression of the radial Poynting vector. For the second unknown, the solution is a monopole where $A_\phi = B_0\left(1 - \cos\theta\right)$, this gives $\partial_\theta A_\phi = B_0 \sin\theta$. A small manipulation needs to be done on the Poynting vector before computing its flux. This manipulation consists of expanding the expression to the second order in spin a, we assume that the black hole is slowly rotating such that $a \ll 1$. We can now express the final Blandford-Znajek power as

$$L_{\mathrm{BZ}} = \frac{1}{6}\Omega_{\mathrm{H}}^2 B_0^2 \tag{2.167}$$

The radial Poynting flux is not zero, and we have energy extraction from the black hole. Similar to the pulsar case, this quantity is a constant and depends on the angular velocity of the object. A black hole with a high spin will extract more energy than one with a low spin.

2.4 Summary

In this chapter, we have introduced some aspects of the theory behind pulsars and black holes as well as some QED processes at play in their magnetosphere. In both cases, the theory started in vacuum and migrated towards a plasma-filled magnetosphere. Whether it is for pulsars or black holes, the number of analytical solutions to describe the magnetosphere is very limited. For pulsars, only one solution was found and corresponds to the Michel solution (magnetic monopole configuration). For black holes, we have the Wald solution and the Blandford-Znajek solution (the general relativistic analogue of the Michel solution). However, this lack of analytical solution did not stop the community from building complex models where QED processes are at play, to try to explain the different emissions observed. Nonetheless, because of the wide range of physical phenomena and their high non-linearity nature, the community must use numerical simulations to go further in its understanding of relativistic magnetospheres.

2.5 [Français] Points clés du chapitre

2.5.1 Pulsars

Au début de la théorie, les pulsars étaient considérés comme évoluant dans le vide. Cette hypothèse a permis de lancer la communauté mais elle fut vite remise en question. Ce type d'objet possèdant un champ magnétique intense, il est possible d'extraire de la surface de l'étoile à neutrons des particules. L'environnement proche des pulsars va donc être remplis de ces particules sous la forme d'un plasma. L'un des modèles fondateurs de la théorie des pulsars a été développé par Goldreich and Julian (1969). Ce modèle considère la magnétosphère d'un rotateur dipolaire aligné dans un régime physique dit sans-force. Dans ce régime, nous pouvons négliger toutes les forces à l'exception de la force de Lorentz. Ce régime se base sur l'hypothèse que le champ magnétique est très intense et que la force de Lorentz domine toutes les autres. Cependant, le modèle de Goldreich and Julian (1969) est purement théorique et ne possède pas de solution analytique. La première solution mathématique fut dérivée par Michel (1973). Cette solution correspond à un monopole magnétique et représente la seule solution analytique de la théorie des pulsars à ce jour. Une étape importante dans la théorie des pulsars s'est produite grâce à l'avènement des simulations numériques. Dans un premier temps, les simulations étaient des simulations sans-force reposant sur les équations de Maxwell. Ces simulations ont permis à la communauté d'obtenir de nouvelles solutions purement numérique. Elles ont permis de déterminer la structure de la magnétosphère dans le cas d'un dipole magnétique. Cette magnétosphère peut être séparée en deux régions en utilisant un critère portant sur la topologie des lignes de champs, ouverte ou fermée. Ce découpage est lié à la présence d'un cylindre de lumière dont le rayon indique la position à partir de laquelle la corotation devient superluminal. Ces simulations ont aussi permis d'étudier la puissance du pulsar en fonction de son inclinaison, la valeur de l'angle étant facilement modifiable dans une simulation car il s'agit d'un paramètre d'entrée. La théorie des pulsars a pu faire un pas en avant grâce ces simulations mais il était nécessaire d'aller encore plus loin afin de pouvoir comprendre et expliquer l'émission des pulsars. Cette méthode ne permettant pas de dissiper l'énergie contenue dans la magnétosphère, il n'était pas possible d'étudier la conversion de cette énergie en rayonnement. Une raison supplémentaire d'utiliser une autre méthode est que dans une région très spécifique de la magnétosphère les hypothèses sur lequel repose le régime sans-force sont violées. Pour palier à ce défaut des simulations sans-force et étudier le rayonnement, la communauté s'est orientée vers des simulations « Particules-in-Cell » (PIC). Ce type de simulations cinétique est ab-initio et permet de décrire la magnétosphère depuis l'échelle cinétique grâce aux particules individuelles. Elle permet aussi de prendre en compte les effets d'électrodynamique quantique (QED) et de rayonnement. L'un des effets QED principaux mis en avant par les modèles est la création de paires. Elle peut intervenir via deux processus dans les magnétosphères de pulsar : conversion magnétique et/ou processus Breit-Wheeler. Dans le cas du rayonnement, les deux principaux processus attendus sont le rayonnement synchrotron et le rayonnement de courbure. Les simulations PIC ont mis en avant le besoin d'avoir de la production de paires que ce soit pour les simulations numériques mais aussi pour la théorie. Différents scénario ont été mis au point pour la communauté pour tenter d'expliquer la création de paires ainsi que les observations. Des modèles utilisent la notion de zone de vide dans la magnétosphère dans lesquelles les particules subissent une forte accéleration causé par un champ électrique. Via cette accélération, les particules gagnent de l'énergie. Si cette dernière dépasse l'énergie seuil de la production de paires, la conséquence directe est la perte d'énergie de la particule primaire pour produire une paires. Cependant, l'accélération des particules n'est pas limitée uniquement au zone de vide, elle peut aussi être produite grâce au processus

de reconnection magnétique dans une nappe de courant. Ce mécanisme se déclenche à l'interface entre deux polarités opposées du champ magnétique. Il s'avère que ce processus est très efficace pour accélérer des particules à haute énergie et que cette configuration est exactement celle rencontrée dans une magnétosphère de pulsars.

2.5.2 Trous noirs

Pour le cas des trous noirs, il nous faut tout d'abord définir une métrique afin de décrire l'espace-temps courbé. Pour tenir compte de cette courbure, nous utilisons le formalisme « 3+1 » pour faciliter l'interprétation des équations. Grâce à ce formalisme, il est possible d'exprimer notre jeu d'équations dans une forme quasiment identique à celle des équations de Maxwell en espace plat, avec comme différence notable le nombre de champs qui passe de 2 à 4. Une autre similarité entre les trous noirs et les pulsars est la présence de surfaces de lumière au nombre de 2 pour les trous noirs contre 1 pour les pulsars. Le critère porte aussi sur la possibilité ou non d'être en corotation avec l'objet.
À l'instar de ce qui avait été fait au début de la théorie des pulsars, la première solution fut donnée pour une configuration dans le vide. Cette solution connue sous le nom de configuration de Wald (1974), s'exprime sous la forme d'un 4-potentiel totalement analytique. Suivant le même cheminement, la communauté travaillant sur les magnétosphères de trous noirs passa d'une magnétosphère vide à une magnétosphère remplie de plasma. L'origine de ce plasma est plus complexe que pour les pulsars que les trous noirs n'ont pas de surface propre d'où des particules peuvent être extraites. Le régime physique de ce type de magnétosphère est encore une fois identique au cas pulsar, elle se trouve dans un régime sans-force. Sous ces hypothèses, une seule solution analytique existe et il s'agit de la solution de Blandford and Znajek (1977). Pour obtenir cette solution, les auteurs ont utilisé la solution de Michel (monopole) et l'ont ensuite étendue au cas d'un trou noir en rotation lente. Cette solution est d'autant plus intéressante qu'elle permet d'extraire de l'énergie du trou noir.

2.5.3 Résumé

Dans ce chapitre, nous avons présenté certains aspects de la théorie des pulsars et des trous noirs, ainsi que certains processus QED à l'œuvre dans leur magnétosphère. Dans les deux cas, la théorie a commencé dans le vide et a migré vers une magnétosphère remplie de plasma. Que ce soit pour les pulsars ou les trous noirs, le nombre de solutions analytiques pour décrire la magnétosphère est très limité. Pour les pulsars, une seule solution a été trouvée et correspond à la solution Michel (configuration de monopole magnétique). Pour les trous noirs, nous disposons de la solution de Wald et de la solution de Blandford-Znajek (l'analogue relativiste général de la solution de Michel). Cependant, cette absence de solution analytique n'a pas empêché la communauté de construire des modèles complexes où des processus QED sont en jeu, pour tenter d'expliquer les différentes émissions observées. Néanmoins, en raison de la grande diversité des phénomènes physiques et de leur forte non-linéarité, la communauté doit recourir à des simulations numériques pour aller plus loin dans sa compréhension des magnétosphères relativistes.

CHAPTER 3

Numerical context

Contents

We have seen the different observational and theoretical aspects of relativistic magnetospheres. In order to understand and handle the wide variety of physical phenomena in these environments, we need to use numerical simulations. In this chapter, we will introduce some of the numerical facets behind the modelling of relativistic magnetospheres. This chapter aims at giving the required material needed for Chap. 5. In Sect. 3.1, we will describe one possible numerical method used to solve Maxwell's equations, the Finite Difference Time Domain method. In Sect. 3.2, we will detail the force-free scheme under the

FDTD method. In Sect. 3.3, we will do a similar work to the previous section but applied in the framework of Particle-in-cell simulations. Finally, we will give some limitations of both numerical methods and possible ways of overcoming them in Sect. 3.4. A great resource for numerical plasma physicists is the book by Birdsall and Langdon (1991).

3.1 Solving Maxwell's equations numerically

In order to study relativistic magnetospheres, we must do numerical simulations because of the high non-linearity of the problem. Several approaches can be used to do so. In the following, I describe the two main approaches and give the advantages and disadvantages of both.

We remind the set of equations that one must solve to model relativistic magnetospheres, i.e. Maxwell's equations:

$$\frac{\partial \mathbf{B}}{\partial t} = -c\,\boldsymbol{\nabla} \times \mathbf{E} \tag{3.1}$$

$$\frac{\partial \mathbf{E}}{\partial t} = c\,\boldsymbol{\nabla} \times \mathbf{B} - 4\pi \mathbf{J}, \tag{3.2}$$

$$\boldsymbol{\nabla} \cdot \mathbf{B} = 0 \tag{3.3}$$

$$\boldsymbol{\nabla} \cdot \mathbf{E} = 4\pi\rho \tag{3.4}$$

To numerically solve the time evolution of Eqs. (3.1, 3.2, 3.3, 3.4), we need to discretise them both in time and space. I describe in the following the numerical scheme generally used, as it is explicit and rather simple to understand and implement.

3.1.1 Finite-Difference Time Domain

The Finite-Difference Time-Domain (FDTD) method is an explicit numerical method. From here, we will only consider its second-order version. The use of higher-order methods is also possible, for example with a Runge-Kutta 4^{th}-order scheme in time, but the higher the order the more expensive the method. The FDTD allows for second-order accuracy both in time and in space. It is relatively cheap and offers good stability when solving Maxwell's equations. This algorithm described in the following sections relies on two pillars: the Yee mesh and the leapfrog scheme. It is also possible to use implicit or semi-implicit Maxwell solvers (Bacchini et al., 2019).

No matter what the explicit numerical method is and its accuracy, they are enforced to validate the *Courant-Friedrichs-Lewy* (CFL) condition (Courant et al., 1928). The latter ensures that the algorithm is numerically stable throughout the time integration of the solution (i.e. convergence condition). For a Cartesian grid, the CFL condition (Sironi & Cerutti, 2017) reads

$$1D: \quad \frac{c^2\Delta t^2}{\Delta x^2} < 1 \tag{3.5}$$

$$2D: \quad (c\Delta t)^2 \left(\frac{1}{\Delta x^2} + \frac{1}{\Delta y^2}\right) < 1 \tag{3.6}$$

$$3D: \quad (c\Delta t)^2 \left(\frac{1}{\Delta x^2} + \frac{1}{\Delta y^2} + \frac{1}{\Delta z^2}\right) < 1 \tag{3.7}$$

where Δt is the timestep, $\Delta x, \Delta y, \Delta z$ are the spatial step size in the x, y, z directions. Therefore, we can extract the condition on Δt from Eq. (3.6) depending on the grid spatial size in the $2D$ case:

$$\Delta t = \frac{1}{c}\,\mathcal{C}\,\sqrt{\frac{\Delta x^2 \Delta y^2}{\Delta x^2 + \Delta y^2}} \tag{3.8}$$

where $\mathcal{C}$ is the CFL number, which must be below 1 in order to validate Eq. (3.6). Consequently, the timestep of the simulation Δt is constrained by the grid spatial resolution. Therefore, if we consider a logarithmic grid along the x-axis, the timestep will be curtailed by the smallest cell (i.e. $\Delta x = \min(\Delta \log(x)|_{x_{\min}}^{x_{\max}})$). This condition also tells us that any timescale smaller than Δt cannot be resolved by the simulation. In practice, the most limiting frequency is the electronic plasma frequency $\omega_{\rm pe} = \sqrt{4\pi n_{\rm e} e^2/m_{\rm e}}$. This issue can be easily encountered by pushing the parameters of a simulation for a fixed resolution. For example one simulation can have a timestep Δt small enough to resolve the plasma frequency $\omega_{\rm pe}$. However, if we increase the density in the simulation, $\omega_{\rm pe}$ becomes larger and the time resolution is not sufficient to resolve it.

If we do not respect the CFL condition, numerical instabilities develop in the simulation, leading to the explosion and the crash of the simulation. To demonstrate this effect, we consider a $1D$ problem in which we evolve a plane wave in vacuum along the x-direction. This initial condition reads:

$$\begin{cases} E_z(t=0) &= E_z^{\rm ini} = E_0 \sin\left(\frac{2\pi x}{\lambda}\right) \\ B_y(t=0) &= B_y^{\rm ini} = 0 \end{cases} \tag{3.9}$$

where E_0 and B_0 are the amplitudes of the waves, λ is the wavelength. The space and time discretization are explained in detail in Sects. 3.1.3 and 3.1.2 respectively. We now solve Eqs. (3.1) and (3.2) to evolve the wave in time with an explicit integrator. To demonstrate the impact of not respecting the CFL condition, we show two different cases in Fig. 3.1. The first case validates the CFL condition with $\mathcal{C} = 0.9$ whereas the second one does not with $\mathcal{C} = 1.5$.

We see right away in Fig. 3.1 the numerical instability developing (internal oscillations of the solution) after a few iterations for $\mathcal{C} = 1.5$ whereas the case with $\mathcal{C} = 0.9$ is perfectly stable even after a long integration. The growth of the instability is exponential, and shortly the solution is overwhelmed/dominated by the instability. In practice, the grid resolution Δx and the CFL number are given by the user and the timestep Δt is defined by using Eq. (3.8) in a given geometry.

3.1.2 Space discretization

I describe in this section the space discretisation generally done when solving an electromagnetic problem with the FDTD method. From now on, we will consider a $2D$ Cartesian grid linearly spaced in the x and y directions. Each components of $\mathbf{E}$ and $\mathbf{B}$ are staggered on the numerical grid to solve Maxwell's equations. A way of staggering the fields is to use the so-called Yee mesh (Yee, 1966), see Fig. 3.2.

With this grid structure, the $\mathbf{E}$-components and $\mathbf{B}$-components are respectively edge-centred and face-centred on the numerical cell (see Fig. 3.2). This configuration allows us to solve Maxwell's equations in their integral form for a cell using the Stokes theorem

$$\frac{\partial}{\partial t}\iint \mathbf{B}\cdot \mathrm{d}\mathbf{S} = \frac{\partial}{\partial t}\iint (\boldsymbol{\nabla}\times\mathbf{E})\cdot \mathrm{d}\mathbf{S} = -c\oint_{\mathcal{C}_{\rm cell}} \mathbf{E}\cdot \mathrm{d}\mathbf{l}. \tag{3.10}$$

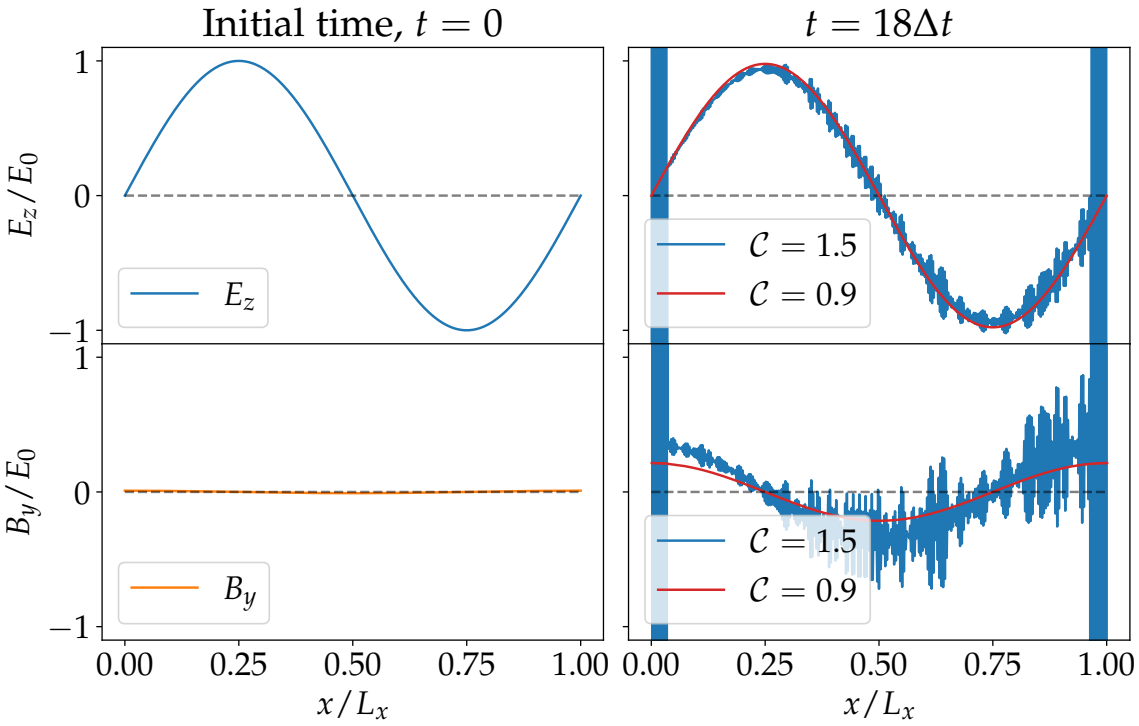

FIGURE 3.1: Impact of the CFL condition on the time evolution of a $1D$ plane wave. Left: Initial state of the wave ($t = 0$). Right: Solution after 18 iterations for two values of $\mathcal{C} = \{0.9, 1.5\}$ respectively in red and blue. The top row shows the electric field while the bottom row corresponds to the magnetic field.

The circulation of the electric field **E** on the edges of the cell gives the flux of **B** at the corresponding cell face. If we consider this configuration, we can derive Maxwell's equations by following a given nomenclature.

Definition 2: Space discretisation nomenclature

We define the position of a quantity $\mathcal{A}$ by its position on the grid by using the index i for the x-direction and the index j for the y-direction. Given this rule, we write

- $\mathcal{A}(x_i, y_j) = (\mathcal{A})_{i,j}$

Therefore, if we apply this to the components shown in Fig. 3.2, we write for example $(E_z)_{i,j}$, $(E_x)_{i+1/2,j}$, $(E_y)_{i,j+1/2}$, $(\boldsymbol{\nabla} \cdot \mathbf{B})_{i+1/2,j+1/2}$.

We can rewrite Maxwell's equation using Def. 2 and by considering derivatives (**curl, div**) to be centred finite-differences. The discretised version of Eq. (3.2)) reads:

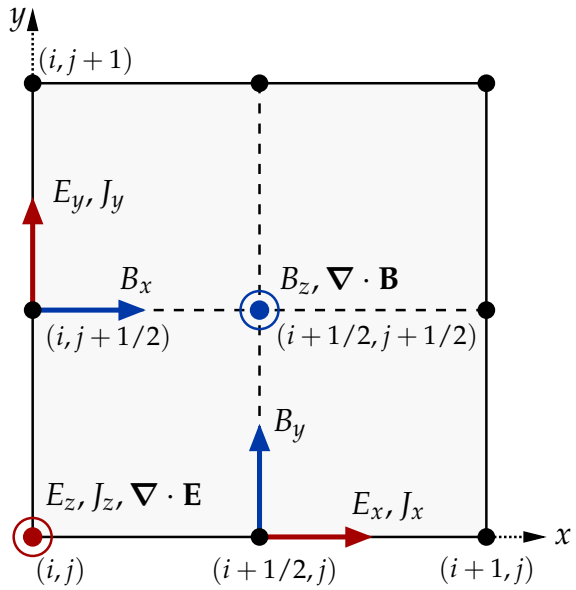

FIGURE 3.2: Yee mesh on a 2D Cartesian grid in the xy-plane. The index i corresponds to the x direction and the index j to the y direction.

$$\partial_t \left(E_x\right)_{i+1/2,j} = c \left(\frac{\left(B_z\right)_{i+1/2,j+1/2} - \left(B_z\right)_{i+1/2,j-1/2}}{\Delta y} \right) - 4\pi \left(J_x\right)_{i+1/2,j} \tag{3.11}$$

$$\partial_t \left(E_y\right)_{i,j+1/2} = -c \left(\frac{\left(B_z\right)_{i+1/2,j+1/2} - \left(B_z\right)_{i-1/2,j+1/2}}{\Delta x} \right) - 4\pi \left(J_y\right)_{i,j+1/2} \tag{3.12}$$

$$\begin{aligned} \partial_t \left(E_z\right)_{i,j} = c & \left(\frac{\left(B_y\right)_{i+1/2,j} - \left(B_y\right)_{i-1/2,j}}{\Delta x} \right) \\ - c & \left(\frac{\left(B_x\right)_{i,j+1/2} - \left(B_x\right)_{i,j-1/2}}{\Delta y} \right) - 4\pi \left(J_z\right)_{i,j} \end{aligned} \tag{3.13}$$

The most valuable benefit of using the Yee grid is that the algorithm automatically ensures the validation of Maxwell-Thomson's equation ($\boldsymbol{\nabla} \cdot \mathbf{B} = 0$) to machine precision. An underlying condition still needs to be respected which is that the initial magnetic field configuration must be divergence-free, the demonstration is done in Sect. 3.1.4.

3.1.3 Time-discretisation: Leapfrog algorithm

To constrain the time-dependence nature of the electromagnetic field, we also discretise Maxwell's equations along the time axis. A common way of doing the time discretisation is to use the **leapfrog** scheme, which is a time-centred second order scheme. If we want to use this scheme, a first procedure is mandatory because our set of equations (Eqs. 3.2 and 3.1) is coupled through $\mathbf{E}$ and $\mathbf{B}$. Therefore the procedure implies pushing one of the fields in time by half a timestep, meaning $\Delta t/2$ for the initial condition. In the following, the procedure is applied on $\mathbf{B}$ at $t = 0$. We note n the index with which time is evolved. Therefore, in our case we have $n \in \mathbb{N}$ for $\mathbf{E}$ and $n \in \frac{1}{2}\mathbb{N}$ for $\mathbf{B}$ and $\mathbf{J}$.

The leapfrog scheme is schematically described in Fig. 3.3. The main point to notice is that the electric field $\mathbf{E}$ is known at a different time than $\mathbf{B}$ and $\mathbf{J}$ which are offset by $\Delta t/2$.

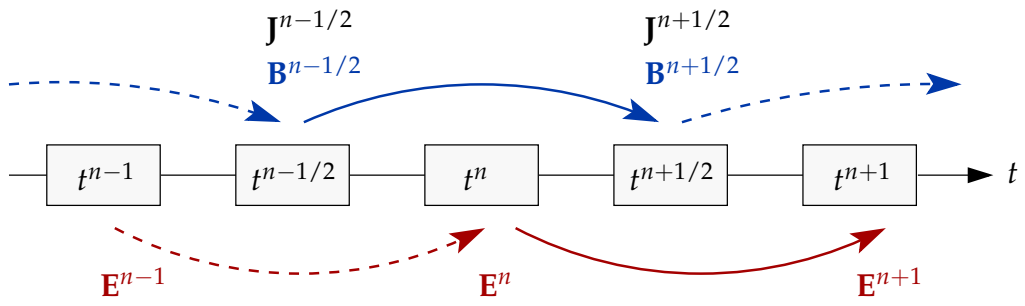

FIGURE 3.3: Sketch of the leapfrog scheme applied to the fields.

In the following, in order to simplify the expressions, we define a nomenclature for the time discretisation in the spirit of the one defined in Def. 2.

Definition 3: Time discretisation nomenclature

We note:

- $\mathbf{E}(t^n) = (\mathbf{E})^n$

where the time is $t^n = n\Delta t$ and

- $\mathbf{B}(t^{n+1/2}) = (\mathbf{B})^{n+1/2}$

where the time is $t^{n+1/2} = (n+1/2)\Delta t$

We can rewrite Maxwell's equation with this convention (Def. 3) by applying the time-centred difference on time derivatives. The time-discretised equations read:

$$\frac{(\mathbf{B})^{n+1/2} - (\mathbf{B})^{n-1/2}}{\Delta t} = -c\,(\boldsymbol{\nabla} \times \mathbf{E})^n \tag{3.14}$$

$$\frac{(\mathbf{E})^{n+1} - (\mathbf{E})^n}{\Delta t} = c\,(\boldsymbol{\nabla} \times \mathbf{B})^{n+1/2} - 4\pi\,(\mathbf{J})^{n+1/2} \tag{3.15}$$

We can compute the value of each field based on the previous timestep, thus we can update the value of each field in time. The expressions of the new updated fields are

$$(\mathbf{B})^{n+1/2} = (\mathbf{B})^{n-1/2} - c\Delta t\,(\boldsymbol{\nabla} \times \mathbf{E})^n \tag{3.16}$$

$$(\mathbf{E})^{n+1} = (\mathbf{E})^n \quad + c\Delta t\,(\boldsymbol{\nabla} \times \mathbf{B})^{n+1/2} - 4\pi\Delta t\,(\mathbf{J})^{n+1/2}\,. \tag{3.17}$$

Assuming the initial offset of $\mathbf{B}$ by half a timestep and that $(\mathbf{E})^n, (\mathbf{B})^{n-1/2}$ are known, the leapfrog steps are:

Step 1: $(\mathbf{B})^{n+1/2} \longleftarrow (\mathbf{B})^{n-1/2} - c\Delta t\,(\boldsymbol{\nabla} \times \mathbf{E})^n$

Step 2: Compute $(\mathbf{J})^{n+1/2}$

Step 3: $(\mathbf{E})^{n+1} \longleftarrow (\mathbf{E})^n + c\Delta t\,(\boldsymbol{\nabla} \times \mathbf{B})^{n+1/2} - 4\pi\Delta t\,(\mathbf{J})^{n+1/2}$

These three steps correspond to one cycle of the leapfrog scheme. The next integration cycle will use $(\mathbf{B})^{n+1/2}$ as $(\mathbf{B})^{n-1/2}$ and $(\mathbf{E})^{n+1}$ as $(\mathbf{E})^{n}$, meaning that all time indices are incremented by $+1$.

3.1.4 Fully discretised Maxwell's equations

We summarise the full set of discretised Maxwell's equations, both in time and in space by using the nomenclature defined in Def. 2 and 3. The general expressions for a $2D$ grid are

$$(E_1)^{n+1}_{i+1/2,j} = (E_1)^{n}_{i+1/2,j} - 4\pi\Delta t\,(J_1)^{n+1/2}_{i+1/2,j} + c\,\frac{\Delta t}{\sqrt{\gamma_{i+1/2,j}}}\left(\frac{(B_3)^{n+1/2}_{i+1/2,j+1/2} - (B_3)^{n+1/2}_{i+1/2,j-1/2}}{\Delta x_2}\right) \tag{3.18}$$

$$(E_2)^{n+1}_{i,j+1/2} = (E_2)^{n}_{i,j+1/2} - 4\pi\Delta t\,(J_2)^{n+1/2}_{i,j+1/2} - c\,\frac{\Delta t}{\sqrt{\gamma_{i,j+1/2}}}\left(\frac{(B_3)^{n+1/2}_{i+1/2,j+1/2} - (B_3)^{n+1/2}_{i-1/2,j+1/2}}{\Delta x_1}\right) \tag{3.19}$$

$$\begin{aligned}(E_3)^{n+1}_{i,j} = (E_3)^{n}_{i,j} &+ c\,\frac{\Delta t}{\sqrt{\gamma_{i,j}}}\left(\frac{(B_2)^{n+1/2}_{i+1/2,j} - (B_2)^{n+1/2}_{i-1/2,j}}{\Delta x_1}\right) \\ &- c\,\frac{\Delta t}{\sqrt{\gamma_{i,j}}}\left(\frac{(B_1)^{n+1/2}_{i,j+1/2} - (B_1)^{n+1/2}_{i,j-1/2}}{\Delta x_2}\right) - 4\pi\Delta t\,(J_3)^{n+1/2}_{i,j}\end{aligned} \tag{3.20}$$

$$(B_1)^{n+1/2}_{i,j+1/2} = (B_1)^{n-1/2}_{i,j+1/2} - c\,\frac{\Delta t}{\sqrt{\gamma_{i,j+1/2}}}\left(\frac{(E_3)^{n}_{i,j+1} - (E_3)^{n}_{i,j}}{\Delta x_2}\right) \tag{3.21}$$

$$(B_2)^{n+1/2}_{i+1/2,j} = (B_2)^{n-1/2}_{i+1/2,j} + c\,\frac{\Delta t}{\sqrt{\gamma_{i,j}}}\left(\frac{(E_3)^{n}_{i+1,j} - (E_3)^{n}_{i,j}}{\Delta x_1}\right) \tag{3.22}$$

$$\begin{aligned}(B_3)^{n+1/2}_{i+1/2,j+1/2} = (B_3)^{n-1/2}_{i+1/2,j+1/2} &- c\,\frac{\Delta t}{\sqrt{\gamma_{i+1/2,j+1/2}}}\left(\frac{(E_2)^{n}_{i+1,j+1/2} - (E_2)^{n}_{i,j+1/2}}{\Delta x_1}\right) \\ &+ c\,\frac{\Delta t}{\sqrt{\gamma_{i+1/2,j+1/2}}}\left(\frac{(E_1)^{n}_{i+1/2,j+1} - (E_1)^{n}_{i+1/2,j}}{\Delta x_2}\right)\end{aligned} \tag{3.23}$$

where $\gamma_{i,j}$ is the determinant of the metric at the (i,j) position of the grid, $\mathcal{A}_k$ is the k-component of the vector and Δx_i is the differential step in the x_i-direction. A more comprehensible example is to consider the geometry of the problem to be $2D$ Cartesian with

$$(E_1, E_2, E_3) = (E_x, E_y, E_z) \qquad \gamma_{i,j} = \det\begin{pmatrix}1 & 0\\ 0 & 1\end{pmatrix} = 1 \qquad (\Delta x_1, \Delta x_2) = (\Delta x, \Delta y) \tag{3.24}$$

Applying this to Eq. (3.21)

$$(B_1)^{n+1/2}_{i,j+1/2} = (B_1)^{n-1/2}_{i,j+1/2} - c\,\frac{\Delta t}{\sqrt{\gamma_{i,j+1/2}}}\left(\frac{(E_3)^{n}_{i,j+1} - (E_3)^{n}_{i,j}}{\Delta x_2}\right) \tag{3.25}$$

$$\implies (B_x)^{n+1/2}_{i,j+1/2} = (B_x)^{n-1/2}_{i,j+1/2} - c\,\Delta t\left(\frac{(E_z)^{n}_{i,j+1} - (E_z)^{n}_{i,j}}{\Delta y}\right) \tag{3.26}$$

We can show by using the Yee lattice and the leapfrog scheme that the algorithm automatically validates $\boldsymbol{\nabla} \cdot \mathbf{B} = 0$, provided that the initial magnetic configuration is divergence-free.

Demonstration 3: $\boldsymbol{\nabla} \cdot \mathbf{B} = 0$ for the leapfrog with Yee mesh scheme.

We can compute the variation over time of $\boldsymbol{\nabla} \cdot \mathbf{B}$. If we use the differential form, we obtain:

$$\frac{\partial}{\partial t}\left(\boldsymbol{\nabla} \cdot \mathbf{B}\right) = \boldsymbol{\nabla} \cdot \left(\frac{\partial \mathbf{B}}{\partial t}\right) = \boldsymbol{\nabla} \cdot \left(-c\boldsymbol{\nabla} \times \mathbf{E}\right) = -c\boldsymbol{\nabla} \cdot \left(\boldsymbol{\nabla} \times \mathbf{E}\right) = 0. \tag{3.27}$$

The discretised divergence of the magnetic field is

$$\left(\boldsymbol{\nabla} \cdot \mathbf{B}\right)^{n+1/2}_{i+1/2,j+1/2} = \frac{\left(B_x\right)^{n+1/2}_{i+1,j+1/2} - \left(B_x\right)^{n+1/2}_{i,j+1/2}}{\Delta x} + \frac{\left(B_y\right)^{n+1/2}_{i+1/2,j+1} - \left(B_y\right)^{n+1/2}_{i+1/2,j}}{\Delta y}. \tag{3.28}$$

If we look at the variation over time of $\boldsymbol{\nabla} \cdot \mathbf{B}$ but this time with the discretised version of Eq. (3.3), we have:

$$\begin{aligned}
\partial_t \left(\boldsymbol{\nabla} \cdot \mathbf{B}\right)_{i+1/2,j+1/2} &= \frac{\left(\boldsymbol{\nabla} \cdot \mathbf{B}\right)^{n+1/2}_{i+1/2,j+1/2} - \left(\boldsymbol{\nabla} \cdot \mathbf{B}\right)^{n-1/2}_{i+1/2,j+1/2}}{\Delta t} \\
&\overset{(3.28)}{=} \frac{\left(B_x\right)^{n+1/2}_{i+1,j+1/2} - \left(B_x\right)^{n+1/2}_{i,j+1/2}}{\Delta t \Delta x} + \frac{\left(B_y\right)^{n+1/2}_{i+1/2,j+1} - \left(B_y\right)^{n+1/2}_{i+1/2,j}}{\Delta t \Delta y} \\
&\quad - \left(\frac{\left(B_x\right)^{n-1/2}_{i+1,j+1/2} - \left(B_x\right)^{n-1/2}_{i,j+1/2}}{\Delta t \Delta x} + \frac{\left(B_y\right)^{n-1/2}_{i+1/2,j+1} - \left(B_y\right)^{n-1/2}_{i+1/2,j}}{\Delta t \Delta y}\right) \\
&= \frac{\left(B_x\right)^{n+1/2}_{i+1,j+1/2} - \left(B_x\right)^{n-1/2}_{i+1,j+1/2}}{\Delta t \Delta x} + \frac{\left(B_y\right)^{n+1/2}_{i+1/2,j+1} - \left(B_y\right)^{n-1/2}_{i+1/2,j+1}}{\Delta t \Delta y} \\
&\quad - \left(\frac{\left(B_x\right)^{n+1/2}_{i,j+1/2} - \left(B_x\right)^{n-1/2}_{i,j+1/2}}{\Delta t \Delta x} + \frac{\left(B_y\right)^{n+1/2}_{i+1/2,j} - \left(B_y\right)^{n-1/2}_{i+1/2,j}}{\Delta t \Delta y}\right) \\
&\overset{(3.21,3.22)}{=} \frac{c}{\Delta x \Delta y}\Big[- \left(\left(E_z\right)^n_{i+1,j+1} - \left(E_z\right)^n_{i+1,j}\right) + \left(\left(E_z\right)^n_{i+1,j+1} - \left(E_z\right)^n_{i,j+1}\right) \\
&\quad - \Big\{ - \left(\left(E_z\right)^n_{i,j+1} - \left(E_z\right)^n_{i,j}\right) + \left(\left(E_z\right)^n_{i+1,j} - \left(E_z\right)^n_{i,j}\right) \Big\} \Big] \\
&= 0
\end{aligned} \tag{3.29}$$

The scheme maintains a zero variation of $\boldsymbol{\nabla} \cdot \mathbf{B}$ over time up to machine precision.

3.1.5 Parallelisation

We have described the most common temporal and spatial schemes used, we can now perform simulations of relativistic magnetospheres, but there is a caveat. The code will only use a single Central Processing Unit (CPU), thus the simulation can take quite some time to compute the solution. To circumvent this problem, we need to parallelise the tasks. By doing so, we will be able to use multiple CPUs at once, therefore increasing the computational power. This is achieved by using an external library called *Message Passing Interface*

(MPI). With this library, the user can give directives directly to all CPUs to exchange scalars, vectors, or even arrays between different units.

The natural way of using multiple CPUs is to do a domain decomposition. Each of the subdomains are allocated to a single CPU, and it is exactly for this reason that we need communications between all CPUs. To illustrate this, we can try to compute a spatial derivative at the edge of a CPU domain. The domain belonging to this CPU ranges from $[1, NXP]$ and the derivative is

$$\frac{\partial (B_x)_{NXP}}{\partial x} = \frac{(B_x)_{NXP+1} - (B_x)_{NXP-1}}{\Delta x}. \tag{3.30}$$

The value $(B_x)_{NXP+1}$ is unknown to this CPU as it is outside of its subdomain, but it is known by its neighbour. This is exactly where we want to use communications. The basic idea is that each CPU will transfer data from their subdomain to its adjacent neighbour via a buffer. The communications needed in our example above are given in Fig. 3.4 and can be generalised easily.

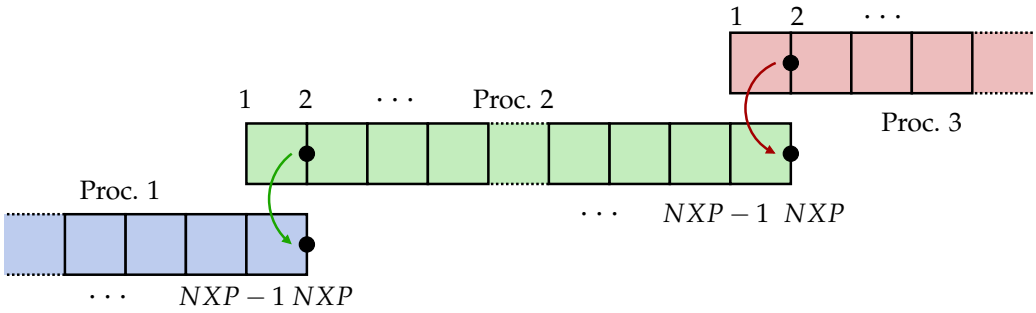

FIGURE 3.4: MPI communications. The subdomain belonging to Proc. 2 is $[1, NXP]$. The arrows correspond to the communications, meaning that the value from which the arrow originates is sent to the neighbouring Proc.

We consider a $1D$ decomposition of the domain into subdomains, each allocated to a Proc. in the figure. To know the value of the derivative at the outer-edge of its subdomain, Proc. 2 receives the value of the inner-edge of Proc. 3 and is able to compute the value of the derivative at its outer-edge. We can rewrite Eq. (3.30) in a different form:

$$\frac{\partial (B_x)^{\text{Proc. 2}}_{NXP}}{\partial x} = \frac{(B_x)^{\text{Proc. 3}}_{2} - (B_x)^{\text{Proc. 2}}_{NXP-1}}{\Delta x} \tag{3.31}$$

Once the communications are done, Proc. 2 knows the value right outside of its subdomain and the derivative can be computed.

A more efficient way of doing these communications is to build so-called "ghost cells". These cells are outside the physical domain and are only used to communicate between CPUs. This procedure is more user-friendly as all communications are usually encapsulated in a single function. Ghost-cells have become the cleanest way of doing communications inside numerical codes, an illustration of such an application is given in Fig. 3.5.
In the configuration of Fig. 3.5, the physical domain of each process is [2,N-1] with N the number of cell edges where the fields are set, for example. The darker cells are the ghost cells and are here to send and receive buffers from the neighbouring processes. In Fig. 3.5, Proc. 2 is sending and receiving buffers from both Proc. 1 and Proc. 3.

Even though communications are very powerful, they also represent a bottle-neck in terms of computing time, as they require time to be done. In practice, communications are

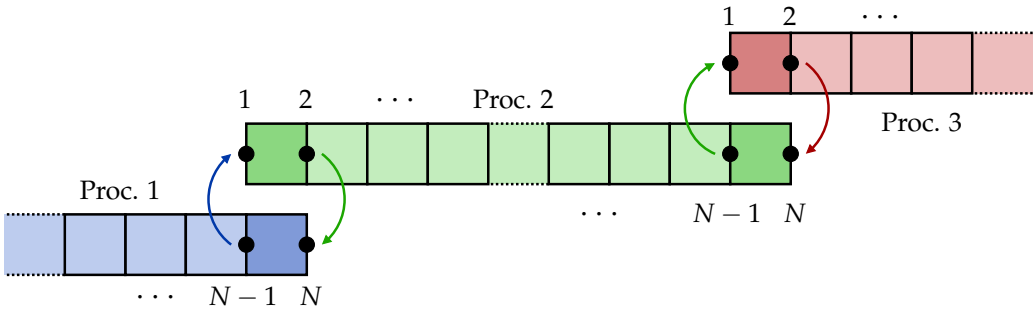

FIGURE 3.5: MPI communication in the form of ghost cells. Ghost cells are represented by the darker colours.

limited by the bandwidth of the databuses[1] connecting the different CPUs or nodes of the cluster. In High-Performance Computing (HPC), the scalability of a code is very important. It is a way of measuring the efficiency of the code and to see where improvements can be made if any are possible. The scalability can be estimated by two methods which are the strong and weak scaling. For the strong scaling, the domain size (i.e. the number of cells) is fixed and we increase the number of CPUs therefore reducing the subdomain size of each CPU. For the weak scaling, both the size of the problem and the number of CPUs vary but we keep the size of each subdomain identical. In Fig. 3.6, we show the weak scaling of the ZELTRON code. The departure from the ideal curve shows the impact of communications on the speed of the code. More CPUs require more communications, which have a strong impact on the code.

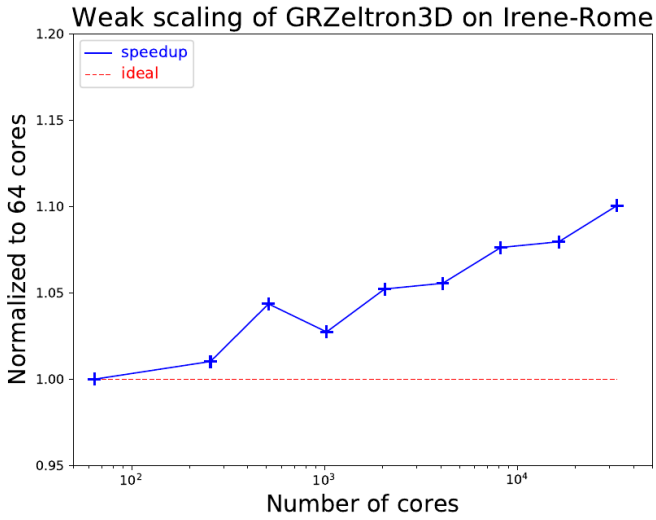

FIGURE 3.6: Weak scaling of ZELTRON to show the impact of communications on the speed-up of the code. The blue points are measurement points, while the red dashed line is the ideal scaling (Courtesy of Benoît Cerutti).

3.1.6 Other method: Pseudo-spectral method

The FDTD method is commonly used to model relativistic magnetospheres, but it is not the only one. Other methods can be used such as the pseudo-spectral method that I will briefly describe.

[1] High-performance databuses can reach up to 200Gbit/s

Parfrey et al. (2012), Pétri (2012) respectively developed pseudo-spectral codes to study relativistic magnetospheres. The strong aspect of this method is that it does not need to be spatially centred like for the FDTD method meaning that all quantities are known at the same grid points. The pseudo-spectral method can be seen as an FDTD method for which the stencil of derivatives extends to all grid points. A consequence of the pseudo-spectral method is the transformation of Partial Differential Equations in Ordinary Differential Equations easier to solve but it does come with its own limitations. The method has very low numerical dissipation in itself thus it is subject to the aliasing instability. This instability can be reduced by using spectral filters to remove the high-frequencies produced by non-linear terms. A second limitation is the difficulty of the method to handle jump discontinuities. The way this is counter-balanced is by smoothing the solution to remove those discontinuities.

As an example to illustrate the pseudo-spectral method, I describe here the decomposition in spherical harmonics used by Pétri (2012). The method is based on a decomposition of the electromagnetic field in vector spherical harmonics relying on the scalar spherical harmonic Y_{lm}.

$$Y_{lm} = \sqrt{\frac{2\,l+1}{4\pi}\,\frac{(l-m)!}{(l+m)!}}\,P_l^m(\cos\theta) \tag{3.32}$$

where P_l^m are the Legendre functions. Then we can construct the different vector spherical harmonics:

$$\mathbf{Y}_{lm} = Y_{lm}\mathbf{e}_\mathrm{r} \tag{3.33}$$

$$\mathbf{\Psi}_{lm} = \frac{r}{\sqrt{l\,(l+1)}}\boldsymbol{\nabla}Y_{lm} \tag{3.34}$$

$$\mathbf{\Phi}_{lm} = \frac{\mathbf{r}}{\sqrt{l\,(l+1)}}\times\boldsymbol{\nabla}Y_{lm} \tag{3.35}$$

Finally, we can give the vector expansions of the electric and magnetic fields which are:

$$\mathbf{E} = \sum_{l=0}^{\infty}\sum_{m=-l}^{l}\left(E^r_{lm}\mathbf{Y}_{lm} + E^{(1)}_{lm}\mathbf{\Psi}_{lm} + E^{(2)}_{lm}\mathbf{\Phi}_{lm}\right) \tag{3.36}$$

$$\mathbf{B} = \sum_{l=0}^{\infty}\sum_{m=-l}^{l}\left(B^r_{lm}\mathbf{Y}_{lm} + B^{(1)}_{lm}\mathbf{\Psi}_{lm} + B^{(2)}_{lm}\mathbf{\Phi}_{lm}\right) \tag{3.37}$$

The next step is to use for example a Runge-Kutta scheme to update the electromagnetic field.

3.2 Force-free method

Historically, the force-free method was the first used to model relativistic magnetospheres. The first simulation of a time-dependent force-free magnetosphere was performed by Spitkovsky (2006) for a pulsar. This method relies on the assumptions done in Sect. 2.1.2. I explain in the following how the force-free method works.

3.2.1 Standard force-free timestep

The force-free method usually adopts the FDTD scheme described in Sect. 3.1.1 to solve Maxwell's equations in time. The standard loop of the force-free method is described in Fig. 3.7.

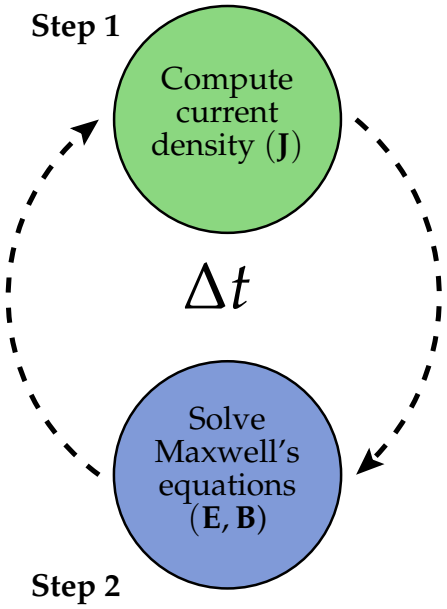

FIGURE 3.7: Timestep FFE algorithm

Of course, the stability of the force-free method is still constrained by the CFL condition (Eq. 3.6 for a $2D$ cartesian grid). For the loop in time, we assume that the electric and magnetic fields are known at time $t = 0$ from initial conditions in order to start the loop. Only two steps are actually required for the force-free loop in time. The first step is to compute the current density $\mathbf{J}$ thanks to $\mathbf{E}$ and $\mathbf{B}$. We recall the expression of the force-free current density,

$$\mathbf{J} = c\frac{\boldsymbol{\nabla}\cdot\mathbf{E}}{4\pi}\left(\frac{\mathbf{E}\times\mathbf{B}}{B^2}\right) + \frac{c}{4\pi}\Big(\mathbf{B}\cdot(\boldsymbol{\nabla}\times\mathbf{B}) - \mathbf{E}\cdot(\boldsymbol{\nabla}\times\mathbf{E})\Big)\frac{\mathbf{B}}{B^2}. \tag{3.38}$$

Once the current density is computed and known on the full grid, it is injected into Maxwell's equations. They are solved using the leapfrog scheme presented in Sect. 3.1.3. $\mathbf{E}$ and $\mathbf{B}$ are then updated in time and this closes the timestep. We iterate by following the same method for the next timestep until the desired time is reached.

3.2.2 Current density treatment

The current density computation in the force-free method represents the most technical aspect. At every steps of the computation, we must maintain the second-order accuracy of the FDTD method for stability reasons. Equation (3.38) can be divided into two terms $\mathbf{J}_\perp$ and $\mathbf{J}_\parallel$, where:

$$\mathbf{J}_\perp = c\frac{\boldsymbol{\nabla}\cdot\mathbf{E}}{4\pi}\left(\frac{\mathbf{E}\times\mathbf{B}}{B^2}\right) \tag{3.39}$$

$$\mathbf{J}_\parallel = \frac{c}{4\pi}\Big(\mathbf{B}\cdot(\boldsymbol{\nabla}\times\mathbf{B}) - \mathbf{E}\cdot(\boldsymbol{\nabla}\times\mathbf{E})\Big)\frac{\mathbf{B}}{B^2} \tag{3.40}$$

$\mathbf{J}_\perp$ and $\mathbf{J}_\parallel$ are respectively the current perpendicular and parallel to the magnetic field. In both terms, the electromagnetic field components lie at different locations within the Yee mesh and are mixed. These locations do not correspond to the position of the staggered

current density. Consequently, keeping the second-order accuracy in space is not straightforward. In practice, all field components are temporarily unstaggered and positioned at the grid nodes (i, j) using an arithmetical average:

$$\mathcal{A}_{i,j} = \frac{\mathcal{A}_{i+1/2,j} + \mathcal{A}_{i-1/2,j}}{2} \tag{3.41}$$

Once the current density is computed on the nodal grid, it is staggered back onto the Yee mesh via arithmetical averaging. Even with this manipulation, the $\mathbf{J}_\parallel$ term is still cumbersome to compute. It always involves all the field components and many derivatives. As an example, we report the expression for J_z,

$$\begin{aligned}(J_z)_{i,j} = \Bigg(\frac{c}{4\pi} \Big[& B_x \partial_y B_z - B_y \partial_x B_z + B_z \left(\partial_x B_y - \partial_y B_x \right) \\ & - E_x \partial_y E_z + E_y \partial_x E_z - E_z \left(\partial_x E_y - \partial_y E_x \right) \Big] \frac{B_z}{B_x^2 + B_y^2 + B_z^2} \Bigg)_{i,j}.\end{aligned} \tag{3.42}$$

For example, in the above equation $(B_x)_{i,j}$ and $\left(\partial_y B_z\right)_{i,j}$ are

$$(B_x)_{i,j} = \frac{(B_x)_{i,j+1/2} + (B_x)_{i,j-1/2}}{2} \tag{3.43}$$

$$\begin{aligned}\left(\partial_y B_z\right)_{i,j} = \frac{\left(\partial_y B_z\right)_{i+1/2,j} + \left(\partial_y B_z\right)_{i-1/2,j}}{2} = & \frac{1}{2} \Bigg(\frac{(B_z)_{i+1/2,j+1/2} - (B_z)_{i+1/2,j-1/2}}{\Delta y} \\ & + \frac{(B_z)_{i-1/2,j+1/2} - (B_z)_{i-1/2,j-1/2}}{\Delta y} \Bigg)\end{aligned} \tag{3.44}$$

This procedure must be done for each term of Eq. (3.42) and each component of $\mathbf{J}_\parallel$. The heavy centring of $\mathbf{J}_\parallel$ is avoided by not computing this term but only applying its consequences. The effect of $\mathbf{J}_\parallel$ is to maintain the force-free condition $\mathbf{E} \cdot \mathbf{B} = 0$ valid. Therefore, the impact of $\mathbf{J}_\parallel$ is to remove all the parallel electric field (i.e. $\mathbf{E}_\parallel = 0$). This is usually done by hand in force-free codes. To fulfil $\mathbf{E}_\parallel = 0$, we remove the component of $\mathbf{E}$ projected along $\mathbf{B}$ in the following form:

$$\mathbf{E} = \mathbf{E}' \longleftarrow \mathbf{E} - (\mathbf{E} \cdot \mathbf{B}) \frac{\mathbf{B}}{B^2}. \tag{3.45}$$

$\mathbf{E}'$ is the new electric field affected to $\mathbf{E}$ for which $\mathbf{E}' \cdot \mathbf{B} = 0$ is verified. Even in this manipulation of the electric field, we still need to conserve the second-order accuracy of the FDTD method (recentering). However, this manipulation of the electric field is not the only one done in the force-free method. A second numerical treatment needs to be applied to verify the second force-free condition $B^2 - E^2 > 0$ (see Sect. 2.1.2 for the derivation). Some configurations can lead to a violation of this second condition. A common way of avoiding this violation is to rescale the electric field whenever $E^2 > B^2$.

$$\mathbf{E} = \mathbf{E}' \longleftarrow \sqrt{\frac{B^2}{E^2}}\, \mathbf{E} \tag{3.46}$$

The treatment given by Eq. (3.46) ensures $B^2 - E'^2 = 0$ where $\mathbf{E}'$ is affected to $\mathbf{E}$. In practice, this numerical trick is applied if a current sheet is present in the simulation as the magnitude of the magnetic field drops to zero inside it. Physically speaking, this reduction

of the electric field acts as a source of dissipation that is highly localised. The energy lost because of the dissipation has no feedback on the physical domain, thus it is a straight loss for the simulation energy budget.

Generally, the numerical treatments given by Eqs. (3.45) and (3.46) are only applied at the end of the force-free timestep when all quantities have been evolved in time. This procedure assure that the next timestep will start with both force-free conditions satisfied.

3.2.3 Adding dissipation

Recently, there has been some study on the impact of dissipation in force-free simulations. Dissipation can be added to force-free simulations by modifying the expression of the current density. Several studies on resistive force-free were performed in the last decade, see Li et al. (2012), Parfrey et al. (2017), Mahlmann et al. (2021), Mahlmann and Aloy (2022). The resistive force-free current density is mainly a modification of the parallel term, which reads:

$$\mathbf{J}_{\parallel} = \frac{c}{4\pi}\Big(\mathbf{B}\cdot(\boldsymbol{\nabla}\times\mathbf{B}) - \mathbf{E}\cdot(\boldsymbol{\nabla}\times\mathbf{E}) + \kappa_I \mathbf{B}\cdot\mathbf{E}\Big)\frac{\mathbf{B}}{(1+\kappa_I\xi)B^2} \tag{3.47}$$

κ_I is the driving rate and ξ is the resistivity or dissipation coefficient. This modification is similar to an Ohm's law applied on $\mathbf{J}_{\parallel}$ and requires the computation of the $\mathbf{J}_{\parallel}$ term. We can recover the ideal force-free current density of Eq. (3.38) by setting $\kappa_I \to 0$. Taking into account this resistivity allows for a stabilisation of current sheets if any are present in the problem modelled. The other interest is to be able to control how the dissipation works and not only relying on the numerical resistivity[2]. This can be done by injecting a resistivity $\xi > \xi_{\text{grid}}$ where ξ_{grid} is the numerical resistivity associated with the grid. Even with this modification, we are still limited by the fact that the resistivity is put by hand and not driven by the physics or kinetic scales.

3.3 Particle-in-cell method

3.3.1 Theoretical framework: collisionless plasma

The Particle-in-cell method is designed to model a collisionless plasma. The point of view of the method is kinetic instead of fluid like in force-free. This theoretical framework involves that the frequency ν_C between two Coulomb collision is much smaller than the plasma frequency, $\omega_{\text{pe}} = \sqrt{4\pi n_e e^2/m_e}$ i.e. $\omega_{\text{pe}} \gg \nu_C$. If this is the case, the governing equation of such a plasma is the Vlasov equation (Vlasov, 1967):

$$\frac{\partial f}{\partial t} + \frac{\mathbf{p}}{\gamma m}\cdot\frac{\partial f}{\partial \mathbf{r}} + q\left(\mathbf{E} + \frac{\mathbf{v}\times\mathbf{B}}{c}\right)\cdot\frac{\partial f}{\partial \mathbf{p}} = 0 \tag{3.48}$$

$f(\mathbf{r},\mathbf{p},t)$ is the distribution function, $\mathbf{p} = \gamma m\mathbf{v}$ is the momentum of the particle and $\mathbf{r}$ is its position. The distribution function depends on 7 parameters: 3 parameters in space $\mathbf{r}$, 3 velocity parameters in momentum $\mathbf{p}$ and 1 parameter in time. The Vlasov equation describes the time evolution of the distribution function, taking into consideration long-range interactions. The equation is coupled to Maxwell's equations to fully describe the plasma and electromagnetic field. It is possible to solve numerically this set of equations but as mentioned above, the problem has a high dimensionality in phase space. Thus, solving for the distribution function requires a lot of computational power, memory, and

[2] related to the numerical diffusivity which is introduced when we numerically solve discretised hyperbolic systems of partial differential equations; it is also linked to the resolution

storage space. As an example, a code such as VLASIATOR (Palmroth et al., 2013) was only able to perform a $3D - 3V$ simulation of the Earth's magnetosphere very recently (see Ganse et al. 2023). A recent review of Vlasov methods (Palmroth et al., 2018) describes the different ways of solving Vlasov equation, as well as the heavy computing machinery.

In the Particle-in-cell approach, the Vlasov equation can be indirectly solved using the method of characteristics. In this method, the distribution function is

$$f(\mathbf{r}, \mathbf{p}, t) = \sum_{k=1}^{N} w_k \delta(\mathbf{r} - \mathbf{r}_k(t)) \delta(\mathbf{p} - \mathbf{p}_k(t)) \tag{3.49}$$

where N is the number of macroparticles and $w_k, \mathbf{r}_k, \mathbf{p}_k$ respectively the weight, the position and the momentum of the particle k. In PIC simulations, particles are grouped in what is called macroparticles. These are numerical particles representing a bundle of particles that would have the same trajectory in phase space. We assign a weight to each macroparticle, this weight tells us how many physical particles are modelled by each macroparticle. Even with this procedure, the number of macroparticles in the simulation needs to be large enough to have a good sampling of the distribution function.

The goal of PIC simulations is to have an ab-initio description of the plasma to study the kinetic scales. We define the kinetic scale as the scale of the plasma skin depth or near the Larmor radius. The first PIC simulations of a relativistic magnetosphere was performed by Philippov and Spitkovsky (2014).

As for the force-free method described in Sect. 3.2, the PIC approach has its own numerical scheme. It also relies on the FDTD scheme (see Sect. 3.1.1). The standard PIC-loop is described in Fig. 3.8.

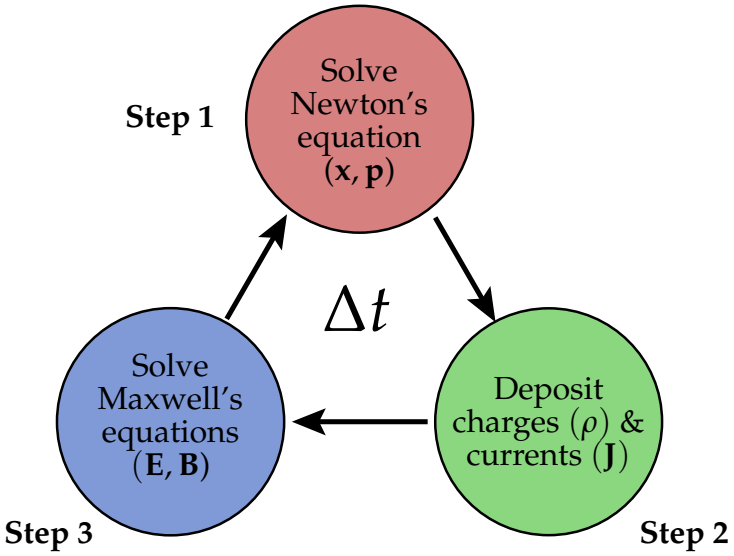

FIGURE 3.8: Standard PIC timestep.

It is divided into three different steps. Two steps are actually reminiscent of the force-free method, namely step 2 where the current density is computed and step 3 where Maxwell's equations are solved. Each step is described in detail in the following.

3.3.2 Step 1: Particle push

The first step is to push or update particles' positions and velocities according to the relativistic Newton's equation. Because of the strength of the magnetic field, the equation of

motion only contains the Lorentz force, all other forces (pressure, gravity) are negligible. Therefore, our set of equations reads:

$$\frac{\mathrm{d}\mathbf{u}}{\mathrm{d}t} = \frac{q}{m_s c}\left(\mathbf{E} + \frac{\mathbf{u}\times\mathbf{B}}{\gamma}\right) \tag{3.50}$$

$$\frac{\mathrm{d}\mathbf{r}}{\mathrm{d}t} = \mathbf{v} = \frac{c}{\gamma}\mathbf{u} \tag{3.51}$$

where $\mathbf{r}$ is the particle position, $\mathbf{u} = \gamma\mathbf{v}/c$ is the spatial component of the 4-velocity of the particle normalised by the speed of light, $\gamma = 1/\sqrt{1-(\mathbf{v}/c)^2} = \sqrt{1+\mathbf{u}^2}$ is the Lorentz factor of the particle, q is the charge of the particle and m_s is the particle's mass. The most commonly spread algorithm to solve this set of equations (Eqs. 3.50 and 3.51) is called the Boris push (Boris, 1970). It is a robust and stable algorithm widely used by the PIC community in various physical applications. The second-order accuracy is maintained, it is fast, volume-conserving in phase space as well as it conserves the particle energy (Qin et al., 2013). It has some limitations, for instance, it is not symplectic[3] and it must respect the CFL condition (Eq. 3.6). Some numerical development is currently undergoing to step away from conditionality and move to unconditionally stable time stepping (Ramachandran et al., 2023).

The Boris push algorithm can be decomposed in a similar way as the leapfrog scheme, meaning that the velocity $\mathbf{u}$ and position $\mathbf{r}$ are staggered in time. The Boris push is given in Fig. 3.9. We use the same nomenclature as the one described in Def. 3 but this time applied to the momentum $\mathbf{u}$ and position $\mathbf{r}$.

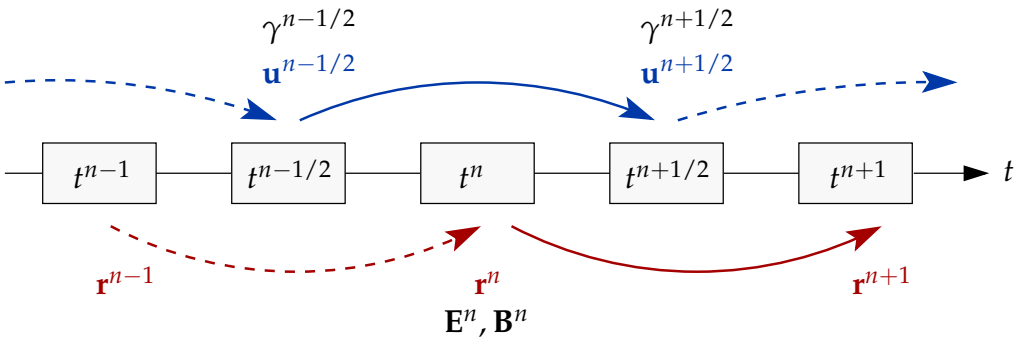

FIGURE 3.9: Boris push algorithm based on the leapfrog scheme.

Here we assume that $(\mathbf{E}^n, \mathbf{B}^n, \mathbf{r}^n)$ are initially known as well as $(\mathbf{u}^{n-1/2})$ in order to start the leapfrog scheme. The fields used in this section are not taken on the grid but at the particle position. This is done thanks to a linear interpolation, which is in most cases sufficient. If we do the same exercise as the one done with the leapfrog scheme, the time discretisation of Eqs. (3.50) and (3.51) reads:

$$\frac{\mathbf{u}^{n+1/2} - \mathbf{u}^{n-1/2}}{\Delta t} = \frac{q}{m_s c}\left(\mathbf{E}^n + \frac{\mathbf{u}^n \times \mathbf{B}^n}{\gamma^n}\right) \tag{3.52}$$

$$\frac{\mathbf{r}^{n+1} - \mathbf{r}^n}{\Delta t} = \frac{c}{\gamma^{n+1/2}}\mathbf{u}^{n+1/2} \tag{3.53}$$

[3] a symplectic integrator conserves the area in phase space

Where we define $\mathbf{u}^n = (\mathbf{u}^{n+1/2} + \mathbf{u}^{n-1/2})/2$ the arithmetic average and the same goes for $\mathbf{B}^n = (\mathbf{B}^{n+1/2} + \mathbf{B}^{n-1/2})/2$. Injecting this decomposition in Eq. (3.52) gives:

$$\frac{\mathbf{u}^{n+1/2} - \mathbf{u}^{n-1/2}}{\Delta t} = \frac{q}{m_s c}\left(\mathbf{E}^n + \frac{\left(\mathbf{u}^{n+1/2} + \mathbf{u}^{n-1/2}\right) \times \mathbf{B}^n}{2\gamma^n}\right) \tag{3.54}$$

Even with this new formulation, the time integration of the velocity is difficult because of the velocity-dependence of the $\mathbf{u} \times \mathbf{B}$ term in the Lorentz force. To overcome this difficulty, the Boris push splits the electric acceleration by defining,

$$\mathbf{u}^{n-1/2} = \mathbf{u}^- - \frac{q\Delta t}{2m_s c}\mathbf{E}^n \tag{3.55}$$

$$\mathbf{u}^{n+1/2} = \mathbf{u}^+ + \frac{q\Delta t}{2m_s c}\mathbf{E}^n \tag{3.56}$$

We substitute these in Eq. (3.54) to obtain

$$\frac{\mathbf{u}^+ - \mathbf{u}^-}{\Delta t} = \frac{q}{2m_s c\gamma^n}\left(\left(\mathbf{u}^+ + \mathbf{u}^-\right) \times \mathbf{B}^n\right) \tag{3.57}$$

The impact of such a decomposition can be seen as a three-step process. The first step is half an electric impulse that linearly accelerates the particle (Eq. 3.55), this gives $\mathbf{u}^-$. Then, a rotation is performed by the magnetic force (Eq. 3.57). Finally, the remaining half electric impulse reaccelerates the particle, leading to a full acceleration by the electric field during the timestep. The rotation can be shown by taking the scalar product of Eq. (3.57) with $(\mathbf{u}^+ + \mathbf{u}^-)$. This gives $\|\mathbf{u}^+\| = \|\mathbf{u}^-\|$ meaning a rotation of $\mathbf{u}^-$ done by the vector $\mathbf{R} = q\Delta t/(2m_s c\gamma^n)\,\mathbf{B}^n$. Nonetheless, the expression of $\mathbf{u}^+$ needed to know the time evolution is not yet explicit in $\mathbf{u}^-$. It is possible to demonstrate that after some manipulations, the component $\mathbf{u}^+$ can be expressed as

$$\mathbf{u}^+ = \mathbf{u}^- + \mathbf{u}^- \times \mathbf{s} + (\mathbf{u}^- \times \mathbf{R}) \times \mathbf{s} \tag{3.58}$$

where

$$\mathbf{s} = \frac{2\mathbf{R}}{1 + \mathbf{R}^2} \qquad \gamma^n = \sqrt{1 + (\mathbf{u}^-)^2} \tag{3.59}$$

The full demonstration is given below in Demo. 4

Demonstration 4: Isolation of $\mathbf{u}^+$ demonstration

We start from Eq. (3.57)

$$\frac{\mathbf{u}^+ - \mathbf{u}^-}{\Delta t} = \frac{q}{2m_s c\gamma^n}\left(\left(\mathbf{u}^+ + \mathbf{u}^-\right) \times \mathbf{B}^n\right) \tag{3.60}$$

We note

$$\mathbf{R} = \frac{q\Delta t}{2m_s c\gamma^n}\mathbf{B}^n \tag{3.61}$$

We can express Eq (3.60) using Eq. (3.61)

$$\mathbf{u}^+ - \mathbf{u}^- = \left(\mathbf{u}^+ + \mathbf{u}^-\right) \times \mathbf{R} \tag{3.62}$$

The next step is to estimate the dot product Eq. (3.62)$\cdot\mathbf{R}$

$$\left(\mathbf{u}^+ - \mathbf{u}^-\right) \cdot \mathbf{R} = \left(\left(\mathbf{u}^+ + \mathbf{u}^-\right) \times \mathbf{R}\right) \cdot \mathbf{R} \tag{3.63}$$
$$\iff \mathbf{u}^+ \cdot \mathbf{R} - \mathbf{u}^- \cdot \mathbf{R} = 0 \tag{3.64}$$
$$\implies \mathbf{u}^+ \cdot \mathbf{R} = \mathbf{u}^- \cdot \mathbf{R} \tag{3.65}$$

Then we estimate Eq. (3.62)$\times\mathbf{R}$

$$\left(\mathbf{u}^+ - \mathbf{u}^-\right) \times \mathbf{R} = \left(\left(\mathbf{u}^+ + \mathbf{u}^-\right) \times \mathbf{R}\right) \times \mathbf{R} \tag{3.66}$$
$$= \left(\mathbf{R} \cdot \left(\mathbf{u}^+ + \mathbf{u}^-\right)\right)\mathbf{R} - \mathbf{R}^2\left(\mathbf{u}^+ + \mathbf{u}^-\right) \tag{3.67}$$
$$\implies \mathbf{u}^+ \times \mathbf{R} = \mathbf{u}^- \times \mathbf{R} + 2\left(\mathbf{R} \cdot \mathbf{u}^-\right)\mathbf{R} - \mathbf{R}^2\left(\mathbf{u}^+ + \mathbf{u}^-\right) \tag{3.68}$$

The final step to have the expression of $\mathbf{u}^+$ is to inject Eq. (3.68)

$$\mathbf{u}^+ - \mathbf{u}^- = \mathbf{u}^+ \times \mathbf{R} + \mathbf{u}^- \times \mathbf{R} \tag{3.69}$$
$$\mathbf{u}^+ \overset{(3.68)}{=} \mathbf{u}^- + \mathbf{u}^- \times \mathbf{R} + \mathbf{u}^- \times \mathbf{R} + 2\left(\mathbf{R} \cdot \mathbf{u}^+\right)\mathbf{R} - \mathbf{R}^2\left(\mathbf{u}^- + \mathbf{u}^-\right) \tag{3.70}$$
$$\mathbf{u}^+\left(1 + \mathbf{R}^2\right) = \mathbf{u}^-\left(1 - \mathbf{R}^2\right) + 2\mathbf{u}^- \times \mathbf{R} + 2\left(\mathbf{R} \cdot \mathbf{u}^-\right)\mathbf{R} \tag{3.71}$$
$$\mathbf{u}^+ = \mathbf{u}^-\left(\frac{1 - \mathbf{R}^2}{1 + \mathbf{R}^2}\right) + \frac{2}{1 + \mathbf{R}^2}\mathbf{u}^- \times \mathbf{R} + \frac{2}{1 + \mathbf{R}^2}\left(\mathbf{R} \cdot \mathbf{u}^-\right)\mathbf{R} \tag{3.72}$$

We note

$$\mathbf{s} = \frac{2\mathbf{R}}{1 + \mathbf{R}^2} \qquad \left(\frac{1 - \mathbf{R}^2}{1 + \mathbf{R}^2}\right) = 1 - \mathbf{s} \cdot \mathbf{R} \tag{3.73}$$

The final result is

$$\mathbf{u}^+ = \mathbf{u}^- - \mathbf{u}^-\left(\mathbf{s} \cdot \mathbf{R}\right) + \mathbf{u}^- \times \mathbf{s} + \left(\mathbf{s} \cdot \mathbf{u}^-\right)\mathbf{R} \tag{3.74}$$

Using vectorial analysis, the final result is

$$\mathbf{u}^+ = \mathbf{u}^- + \mathbf{u}^- \times \mathbf{s} + \left(\mathbf{u}^- \times \mathbf{R}\right) \times \mathbf{s} \tag{3.75}$$

Expressing $\mathbf{r}^{n+1}$ from Eq. (3.53) is straightforward,

$$\mathbf{r}^{n+1} = \mathbf{r}^n + \frac{c\Delta t}{\gamma^{n+1/2}}\mathbf{u}^{n+1/2} \tag{3.76}$$

where $\gamma^{n+1/2} = \sqrt{1 + \left(\mathbf{u}^{n+1/2}\right)^2}$. In practice, the numerical workflow of the Boris push is:

Step 1: Compute $\mathbf{u}^-$ from Eq. (3.55)

Step 2: Compute the rotation $\mathbf{u}' = \mathbf{u}^- + \mathbf{u}^- \times \mathbf{R}$

Step 3: Compute $\mathbf{u}^+ = \mathbf{u}^- + \mathbf{u}' \times \mathbf{s}$

Step 4: Update $\mathbf{u}^{n+1/2}$ from Eq. (3.56)

Step 5: Update $\mathbf{r}^{n+1}$ from Eq. (3.76)

It is possible to account for continuous emission from particles by considering the radiation-reaction force in Eq. (3.50). This induces a slight modification of the Boris push (Tamburini et al., 2010).

3.3.3 Step 2: Currents and charges deposition

To be able to solve Maxwell's equation, the current and charge densities of the plasma or particles are required. Each individual particle evolves freely inside a numerical cell and thus does not bring the same amount of current or charge to each grid node. Previously the fields were interpolated at the particle position, here it is the opposite. The charge and current given by the particle within a cell are deposited at its grid nodes. What we want to do is the following: the closer the particle is to a grid node the more current and charge it will deposit on the node. To achieve this, the procedure is rather simple and consists of attributing weights to particles in the deposition scheme by computing different surfaces in $2D$.

If we consider a continuous space, we define the source terms by summing over all particles within this space.

$$\mathbf{J}(\mathbf{r}) = \sum_{k=1}^{N} q_k w_k \mathbf{v}_k \delta(\mathbf{r} - \mathbf{r}_k) \tag{3.77}$$

$$\rho(\mathbf{r}) = \sum_{k=1}^{N} q_k w_k \delta(\mathbf{r} - \mathbf{r}_k) \tag{3.78}$$

where N is the number of particles, $q_k, w_k, \mathbf{v}_k, \mathbf{r}_k$ are respectively the electric charge, the weight, the 3-velocity and the position of the particle k. In PIC, we do not have a continuous space but a grid-based space, therefore we cannot directly sum over all particles. We need to know the contribution of particles to each grid node and this is done through a deposition scheme. The general idea is to write

$$\mathbf{J}(\mathbf{r}) = \sum_{k=1}^{N} q_k w_k \mathbf{v}_k \mathbf{S}(\mathbf{r} - \mathbf{r}_k) \tag{3.79}$$

$$\rho(\mathbf{r}) = \sum_{k=1}^{N} q_k w_k \mathbf{S}(\mathbf{r} - \mathbf{r}_k). \tag{3.80}$$

The shape function $\mathbf{S}(\mathbf{r} - \mathbf{r}_k)$ replaces the Dirac function used previously. This replacement is caused by the fact that particles are not point-wise any more but have a finite size. The expression of this function depends on the deposition scheme. To illustrate how it works in practice, we illustrate a first-order linear scheme in Fig. 3.10.

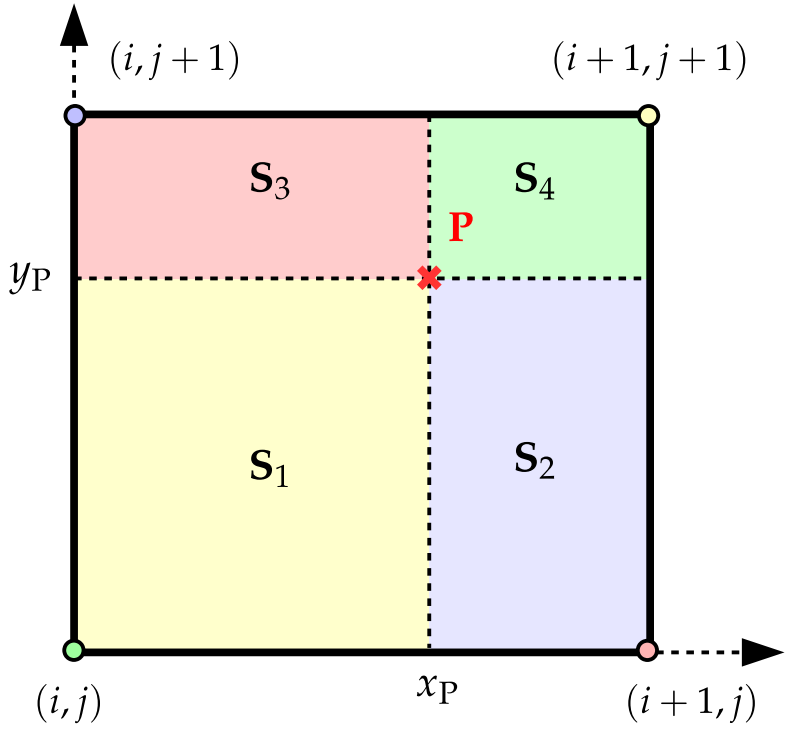

FIGURE 3.10: Charge and current deposition scheme using the area-weighting method for a single particle located at $(x_\mathrm{P}, y_\mathrm{P})$ in a $2D$ Cartesian grid. Adapted from Sironi and Cerutti (2017).

We note $(x_\mathrm{P}, y_\mathrm{P})$ the position of the particle P confined in the cell $x \in [x_i, x_{i+1}]$, $y \in [y_j, y_{j+1}]$. The contribution associated with the particle to each grid node is

$$\begin{aligned} \boxdot_{i,j+1} &= \frac{\mathbf{S}_2}{\mathbf{S}_\mathrm{tot}} = \frac{(x_{i+1} - x_\mathrm{P})\,(y_\mathrm{P} - y_j)}{(x_{i+1} - x_i)\,(y_{j+1} - y_j)}, & \boxdot_{i+1,j+1} &= \frac{\mathbf{S}_1}{\mathbf{S}_\mathrm{tot}} = \frac{(x_\mathrm{P} - x_i)\,(y_\mathrm{P} - y_j)}{(x_{i+1} - x_i)\,(y_{j+1} - y_j)} \\ \boxdot_{i,j} &= \frac{\mathbf{S}_4}{\mathbf{S}_\mathrm{tot}} = \frac{(x_{i+1} - x_\mathrm{P})\,(y_{j+1} - y_\mathrm{P})}{(x_{i+1} - x_i)\,(y_{j+1} - y_j)}, & \boxdot_{i+1,j} &= \frac{\mathbf{S}_3}{\mathbf{S}_\mathrm{tot}} = \frac{(x_\mathrm{P} - x_i)\,(y_{j+1} - y_\mathrm{P})}{(x_{i+1} - x_i)\,(y_{j+1} - y_j)}. \end{aligned} \tag{3.81}$$

The current at each grid node is computed as

$$\mathbf{J}_{i,j} = \sum_{k=1}^{N} q_k w_k \mathbf{v}_k \,(1 - p_k)\,(1 - q_k) \tag{3.82}$$

$$\mathbf{J}_{i+1,j} = \sum_{k=1}^{N} q_k w_k \mathbf{v}_k p_k \,(1 - q_k) \tag{3.83}$$

$$\mathbf{J}_{i,j+1} = \sum_{k=1}^{N} q_k w_k \mathbf{v}_k \,(1 - p_k)\, q_k \tag{3.84}$$

$$\mathbf{J}_{i+1,j+1} = \sum_{k=1}^{N} q_k w_k \mathbf{v}_k p_k q_k, \tag{3.85}$$

where $p_k = (x_k - x_i) \,/\, (x_{i+1} - x_i)$ and $q_k = (y_k - y_j) \,/\, (y_{j+1} - y_j)$ are the bilinear coefficients of the interpolation obtained from decomposing $\boxdot_{i+1,j+1}$ along the two axes.

It is worth noting that the interpolation scheme for the deposition and the Boris push (on the fields) should be the same to avoid self-forces (i.e. a particle accelerating itself). The scheme described above is the deposition scheme used in ZELTRON . It is rather simple and robust, but it is not charge-conserving. Other schemes can be used to conserve the charge (Villasenor & Buneman, 1992; Esirkepov, 2001).

3.3.4 Step 3: Field evolution

The final step of the PIC algorithm is to update $\mathbf{E}$ and $\mathbf{B}$ by solving Maxwell's equations. This step uses the leapfrog scheme and is identical to the one described in Sect. 3.1.1. The only difference being the current density which is coming from the particles instead of the fields. However, there is a new procedure that needs to be done. This procedure corresponds to a divergence cleaning, which is required by the deposition scheme used. As mentioned previously, the deposition scheme is not charge-conserving, meaning that $\boldsymbol{\nabla} \cdot \mathbf{E} = 4\pi\rho$ is not enforced to machine precision. This results in small errors accumulating, leading to unphysical charge densities. Usually, the divergence cleaning is applied periodically at the end of a timestep after the update of the electric field. We note $\mathbf{E}'$ the updated electric field and ρ the charge density. The true electric field is $\mathbf{E} = \mathbf{E}' + \delta\mathbf{E}$, with the small error $\delta\mathbf{E} = -\boldsymbol{\nabla}\phi$ where ϕ is the electric potential. We can derive Poisson's equation for ϕ

$$\boldsymbol{\nabla} \cdot \mathbf{E} = \boldsymbol{\nabla} \cdot \mathbf{E}' + \boldsymbol{\nabla} \cdot (\delta\mathbf{E}) = 4\pi\rho \tag{3.86}$$

$$\Leftrightarrow \nabla^2\phi = \boldsymbol{\nabla} \cdot \mathbf{E}' - 4\pi\rho. \tag{3.87}$$

The next step is to discretise the above equation on the grid.

$$\frac{\phi_{i+1,j} + \phi_{i-1,j} - 2\phi_{i,j}}{\Delta x^2} + \frac{\phi_{i,j+1} + \phi_{i,j-1} - 2\phi_{i,j}}{\Delta y^2} = \left(\boldsymbol{\nabla} \cdot \mathbf{E}' - 4\pi\rho\right)_{i,j} \tag{3.88}$$

Then, isolating $\phi_{i,j}$ gives

$$\phi_{i,j} = \frac{\left(\phi_{i+1,j} + \phi_{i-1,j}\right)\Delta y^2 + \left(\phi_{i,j+1} + \phi_{i,j-1}\right)\Delta x^2}{2\left(\Delta x^2 + \Delta y^2\right)} - \frac{\Delta x^2 \Delta y^2 \left(\boldsymbol{\nabla} \cdot \mathbf{E}' - 4\pi\rho\right)_{i,j}}{2\left(\Delta x^2 + \Delta y^2\right)}. \tag{3.89}$$

The standard way of solving for $\phi_{i,j}$ is to use an iterative method. This kind of method can rapidly be very expansive, depending on the accuracy wanted for the solution. After an initial guess, the chosen algorithm will iterate and converge towards a value of $\phi_{i,j}$ satisfying Eq. (3.89) up to the wanted error. Many algorithms exist for this procedure such as the Jacobi method, the Gauss-Seidel method or the Successive Overrelaxation method (see Press et al. 2007 for in-depth analysis of the different methods). In ZELTRON , we use the Gauss-Seidel method which is faster than the Jacobi method but still quite expansive.

3.3.5 Radiation-reaction force

We mentioned in Sect. 3.3.2 the fact that the Boris push could be slightly modified, to account for other forces. The pusher can handle the implementation of the radiation-reaction force, noted g^μ. This force, also called radiation dumping or Lorentz frictional force, models the radiation emitted by a moving charged particle (see Fig. 3.11). If this force is the only one in the system, the particle will continuously slow down as the radiation is emitted. There is a continuous feedback between the particle and the radiation emitted. To consider the radiation-reaction force, we need to modify the equation of motion while still

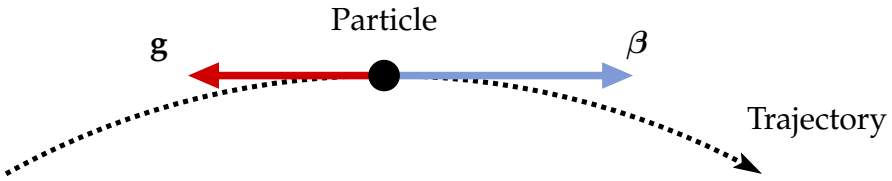

FIGURE 3.11: Radiation-reaction force acting as a friction force slowing the particle.

considering the Lorentz force. The new equation of motion, in full covariant formulation, is called the Lorentz-Abraham-Dirac equation.

$$mc\frac{\mathrm{d}u^\mu}{\mathrm{d}s} = \frac{e}{c}F^{\mu\nu}u_\nu + g^\mu \tag{3.90}$$

where u^μ is the 4-velocity of the particle normalised by the speed of light, $\mathrm{d}s = c\mathrm{d}t/\gamma$ is the spacetime interval, and $F^{\mu\nu}$ is the electromagnetic tensor. Landau and Lifshitz (1971) derived the expression of g^μ in the relativistic case:

$$g^\mu = \frac{2e^2}{3c}\left(\frac{\mathrm{d}^2u^\mu}{\mathrm{d}s^2} - u^\mu u^\nu \frac{\mathrm{d}^2u_\nu}{\mathrm{d}s^2}\right). \tag{3.91}$$

The expression of the second derivative can be written by extracting the first derivative from the relativistic equation of motion, supposing $g^\mu = 0$.

$$\frac{du^\mu}{\mathrm{d}s} = \frac{e}{mc^2}F^{\mu\nu}u_\nu \tag{3.92}$$

$$\frac{\mathrm{d}^2u^\mu}{\mathrm{d}s^2} = \frac{e}{mc^2}\frac{\partial F^{\mu\nu}}{\partial x^\lambda}u^\lambda u_\nu + \frac{e^2}{m^2c^4}F^{\mu\nu}F_{\nu\lambda}u^\lambda \tag{3.93}$$

Injecting the second derivative in Eq. (3.91) gives

$$g^\mu = \frac{2e^3}{3mc^3}\frac{\partial F^{\mu\nu}}{\partial x^\lambda}u^\lambda u_\nu - \frac{2e^4}{3m^2c^5}F^{\mu\lambda}F_{\lambda\nu}u^\nu + \frac{2e^4}{3m^2c^5}\left(F_{\nu\lambda}u^\lambda\right)\left(F^{\mu\kappa}u_\kappa\right) \tag{3.94}$$

In the standard 3-force formalism, the expression reads

$$\begin{aligned}\mathbf{g} =& \frac{2e^3}{3m_\mathrm{e}c^3}\gamma\left[\left(\partial_t + c\boldsymbol{\beta}\cdot\boldsymbol{\nabla}\right)\mathbf{E} + c\boldsymbol{\beta}\times\left(\partial_t + \boldsymbol{\beta}\cdot\boldsymbol{\nabla}\right)\mathbf{B}\right] + \frac{2}{3}r_\mathrm{e}^2\left[\left(\mathbf{E}+\boldsymbol{\beta}\times\mathbf{B}\right)\times\mathbf{B} + \left(\boldsymbol{\beta}\cdot\mathbf{E}\right)\mathbf{E}\right] \\ & - \frac{2}{3}r_\mathrm{e}^2\gamma^2\left[\left(\mathbf{E}+\boldsymbol{\beta}\times\mathbf{B}\right)^2 - \left(\boldsymbol{\beta}\cdot\mathbf{E}\right)^2\right]\boldsymbol{\beta}\end{aligned} \tag{3.95}$$

where $r_\mathrm{e} = e^2/m_\mathrm{e}c^2$ is the classical radius of the electron and $\boldsymbol{\beta}$ is the 3-velocity normalised to the speed of light c. The non-relativistic limit is recovered for $\beta \ll 1$.

Several numerical implementations do exist to take into account the radiation-reaction force. Here we describe the procedure used in ZELTRON from Tamburini et al. (2010), other implementations can be found in Sokolov et al. (2009), Capdessus et al. (2012). The new (discretised) equation of motion with both the Lorentz and radiation-reaction force is

$$\frac{\mathrm{d}\mathbf{u}}{\mathrm{d}t} = \frac{1}{m_\mathrm{s}c}\left(\mathbf{F}_\mathrm{L} + \mathbf{g}\right) \quad \Longleftrightarrow \quad \frac{\left(\mathbf{u}\right)^{n+1/2} - \left(\mathbf{u}\right)^{n-1/2}}{\Delta t} = \frac{1}{m_\mathrm{s}c}\left(\left(\mathbf{F}_\mathrm{L}\right)^n + \left(\mathbf{g}\right)^n\right) \tag{3.96}$$

where $\mathbf{F}_\mathrm{L}$ is the Lorentz force and $\mathbf{g}$ is still the radiation-reaction force, but where the first term of Eq. (3.95) is neglected. The radiation-reaction is important for ultra-relativistic particles $\gamma \gg 1$, meaning that the third term is dominant. The second term is kept in the radiation-reaction force to model the curvature radiation (Cerutti, Philippov, & Spitkovsky, 2016). In practice, the equation of motion is split in two to add the contribution of each force separately, before merging the effect of each force on the particle momentum. This gives a set of two equations

$$\frac{(\mathbf{u}_\mathrm{L})^{n+1/2} - (\mathbf{u}_\mathrm{L})^{n-1/2}}{\Delta t} = \frac{1}{m_\mathrm{s} c} (\mathbf{F}_\mathrm{L})^n \tag{3.97}$$

$$\frac{(\mathbf{u}_\mathrm{R})^{n+1/2} - (\mathbf{u}_\mathrm{R})^{n-1/2}}{\Delta t} = \frac{1}{m_\mathrm{s} c} (\mathbf{g})^n \tag{3.98}$$

where $\mathbf{u}_\mathrm{L}, \mathbf{u}_\mathrm{R}$ are two intermediate momenta. Next, we assume that $\mathbf{u}_\mathrm{L}^{n-1/2} = \mathbf{u}_\mathrm{R}^{n-1/2} = \mathbf{u}^{n-1/2}$, the value of $(\mathbf{g})^n$ required in Eq. (3.98) is still unknown. Combining the previous assumption and the above equation, we have

$$(\mathbf{u})^{n+1/2} = (\mathbf{u}_\mathrm{L})^{n+1/2} + (\mathbf{u}_\mathrm{R})^{n+1/2} - (\mathbf{u})^{n-1/2} \tag{3.99}$$

$$= (\mathbf{u}_\mathrm{L})^{n+1/2} + \frac{\Delta t}{m_\mathrm{s} c} (\mathbf{g})^n \tag{3.100}$$

This is where the independently computed impact of $\mathbf{F}_\mathrm{L}$ and $\mathbf{F}_\mathrm{R}$ comes in. The above equation closes the leapfrog step where we get $(\mathbf{u})^{n+1/2}$, similar to the classic Boris push. However, to compute it, we need to know $(\mathbf{g})^n$. The latter depends on the velocity at half a timestep $(\boldsymbol{\beta})^n$ (Eq. 3.95). The trick here is to have an approximation of $(\mathbf{u})^n$ to access it. This is done by doing the Boris push on the Lorentz force to have $(\mathbf{u}_\mathrm{L})^{n+1/2}$. This way the estimate becomes

$$(\mathbf{u})^n \approx \frac{(\mathbf{u}_\mathrm{L})^{n+1/2} + (\mathbf{u})^{n-1/2}}{2}; \qquad (\boldsymbol{\beta})^n \approx \frac{(\mathbf{u})^n}{(\gamma)^n} \tag{3.101}$$

where $(\gamma)^n = \sqrt{1 + \left((\mathbf{u})^n\right)^2}$. With the expression given by the equation above, $(\mathbf{g})^n$ can be computed easily. It allows next to fully compute $(\mathbf{u})^{n+1/2}$.

3.4 Limitations of force-free and PIC approaches

3.4.1 Strengths and weaknesses

We have described the force-free approach in Sect. 3.2 and the PIC method in Sect. 3.3. We will now discuss what are the benefits and disadvantages of each method.

- **Timestep cycle**: if we compare Figs. 3.7 and 3.8, the obvious difference is the number of steps required per timestep. The PIC method has three steps, whereas the force-free method only has two. This difference is caused by the particle approach, for which we need to evolve the particles in time. A possible conclusion coming from this crude comparison between the two methods is that the force-free approach is faster than the PIC approach because it requires one step less,
- **Current density computation**: in the force-free method, the current density requires the recentring of the electromagnetic field components. The associated complexity

is $\mathcal{O}_{\text{FFE}} = \mathcal{O}\left(N_g\right)$, where N_g is the number of grid points. For the PIC method, we need to deposit the current of each individual particle on the grid nodes with an interpolation. The complexity of the deposition is $\mathcal{O}\left(N\right)$, where N is the total number of macroparticles. Usually, we have at least two species composing the plasma in PIC simulations. This results in the general case to $N = \sum_s N_s$, where N_s is the number of macroparticles/species. Even in the extreme case of a single particle/species/cell, the final crude estimate of the PIC complexity is $\mathcal{O}_{\text{PIC}} = \mathcal{O}\left(2N_s\right)$, leading to $\mathcal{O}_{\text{PIC}} \geq \mathcal{O}_{\text{FFE}}$. Commonly, PIC simulations have a large number of particle/cell, $N_s \gg 1$. The computation in PIC is therefore more expensive than in force-free,

- **Shot noise**: because in the PIC method we have a finite number of discrete particles, PIC simulations suffer from what is called the shot noise. The sampling of the distribution function in phase-space is sensitive to the number of macroparticles (Eq. 3.49). This effect or shot noise impacts all quantities reconstructed from the macroparticles (e.g. $f, \mathbf{J}, \rho$). Two possible ways exist to counter the shot noise: (i) increase N the number of macroparticles as the signal-to-noise ratio is $\text{SNR} = N/\sqrt{N} = \sqrt{N}$; (ii) use a filtering procedure to remove the high-frequencies associated with the lack of macroparticles, this last solution usually requires multiple filter passes,

- **HPC constraints**: both PIC and force-free methods can be run on a relatively high number of CPUs (good scalability). In a force-free simulation as long as the number of cells/process is the same, the duration of a timestep (computing time) is constant. This is not the case in a PIC simulation where the duration of a timestep is constrained by the process hosting the largest number of particles. A simple illustration is if Proc. 1 has N particles to treat and Proc. 2 has $2N$ particles, Proc. 2 is the bottleneck as it will take twice as long to treat all particles. Physically speaking, this happens when an over-density develops in the simulation. A way of dealing with this issue is to implement a load-balancing algorithm in the code. This procedure modifies the subdomain of each process on-the-fly in order to have roughly the same amount of particles/process, see Beck et al. (2016) for an example of implementation. It is also possible to implement variable particle weights (Vranic et al., 2015),

- **Physical information**: this is the most important point of comparison. Depending on the method, the physical information captured does not have the same amount of details. In PIC, all the kinetic scales are modelled, therefore, a wide range of physics can be accessed. Examples are particle spectra, densities, Lorentz factors, non-thermal radiation, reconnection, dissipation, and fluid quantities ... (the list is not exhaustive). In force-free, we only have the macroscopic scales, not the kinetic ones. Consequently, this method is very useful if we want to study the global behaviour of a system and its response to a perturbation. The difference in the physical details comes from the ab-initio modelling done with the PIC method,

- **Scale separation issue**: this issue is only intrinsic to a specific type of simulation using the PIC approach. The scale separation issue arises when we try to model global systems in PIC. Because the particles are on the kinetic scale, global simulations need to cover the physics from this point up to the macroscopic scale. The difference between both scale is usually several orders of magnitude, especially in the context of relativistic magnetospheres. PIC simulations are, in principle, able to cover these orders of magnitudes. This would require extremely high spatial resolution and tens of millions of CPU-hours, which is not acceptable. In practice, the problem is scaled down in PIC simulations while maintaining the correct hierarchy of scales between the most fundamental ones, i.e., the plasma scales, and the macroscopic system.

The conclusions from this comparison are quite clear. The force-free approach is computationally cheaper, it does not require explicit load balancing, and simulations can reach macroscopic scales easily. However it does not give a wide range of information on the physics of the system. The PIC approach is expensive because of the number of particles used, it can suffer from uneven load balancing, but the method gives insights on all the kinetic scales. The main issue with the PIC method is the modification of the simulated scales, which impacts the physics. An example is for particle acceleration, where the maximum energy or Lorentz factor of particles suffers from the rescaling. The consequence of this is that PIC simulations cannot be directly compared to observations as the strength of the physical parameters or the system size are smaller. This aspect of PIC simulations is treated in the next chapter. Assuming that the assumption behind the rescaling is correct, results from PIC simulations can still be scaled up to realistic parameters to compare to observational data. In conclusion, we need to find ways of pushing the limit of our simulations to be closer to realistic parameters with the least assumptions possible.

3.4.2 Beyond stand-alone approaches

To get closer to real system sizes or to access the full physics of a system, state-of-the-art numerical codes are trying to mix different approaches together to develop what are called *hybrid* methods. Nowadays many *hybrid* methods exist, always pushing the limits and numerical barriers. We give in the following a brief overview of existing *hybrid* approaches.

Kinetic ions and fluid electrons: in this approach, the main point is to treat ions and electrons differently. Ions/protons are kinetic, while electrons are assumed massless and treated as a fluid. This difference allows to remove the electronic scales thus, the simulation only needs to resolve the ionic scale. The latter is a factor $\sqrt{m_\mathrm{p}/m_\mathrm{e}} = \sqrt{1836} \approx 42$ larger than the electronic scale. With this gain in scale, the system size can be larger with the same resolution. Various codes are available on the market such as dHybrid (Gargaté et al., 2007), Pegasus (Kunz et al., 2014) or H-VLPL (Tückmantel & Pukhov, 2014) and even a Python package (Li et al., 2024). For the ions, everything remains the same as in the PIC method, but not for the electrons. The set of equations is the same as for standard PIC method and is complemented by an Ohm's law with a pressure term

$$\mathbf{E} = -\mathbf{v}_\mathrm{e} \times \mathbf{B} - \frac{1}{en_e}\boldsymbol{\nabla} P_\mathrm{e} \tag{3.102}$$

$\mathbf{v}_\mathrm{e}$ and P_e are respectively the velocity and the pressure of the electrons, we note that a resistive term can also be added. Further details on this type of approach can be found in Winske et al. (2023). This approach is powerful for studying the acceleration of ions but is not suited for relativistic magnetospheres. In these environments, the electronic scale plays an important role in the description of the magnetosphere. For example, the current sheet is tearing unstable at the electronic scale. Pair production is also important in these environments and leads to a larger number of leptons than ions. Inside the magnetosphere, the leptons are not passive as they dictate some of the dynamics.

MHD-PIC: this method is similar to the previous one, meaning that we have a background plasma considered as a fluid, and kinetic particles. However, in this approach, MHD models the background plasma where electrons and ions are thermal. Only the non-thermal population of ions (low in number) is modelled via particles. This method has been implemented in the non-relativistic MHD regime. The application of such a method can be to study cosmic rays (Zachary & Cohen, 1986; Lucek & Bell, 2000; Bai et al., 2015; Makwana et al., 2018; Mignone et al., 2018; van Marle et al., 2018; Sun & Bai, 2023), but also to

model magnetic island coalescence by embedding a PIC box inside the MHD (Shou et al., 2021; Li et al., 2023), or even the Earth's magnetosphere (Daldorff et al., 2014). On the PIC side, the set of equation is the same as for the standard PIC algorithm. Compared to the previous method, here the MHD equations are solved (conservation of mass density, momentum density, magnetic field and energy density). Depending on the problem, feedback terms can be added as source terms in the equations. For a full description of the procedure needed to embed PIC regions in MHD, see Daldorff et al. (2014).

Force-free-GRMHD approach: this last method is probably the most interesting in the context of compact objects. The method proposed by Parfrey and Tchekhovskoy (2017, 2023) is applied to accreting pulsars, and works both in $2D$ and $3D$ in spherical coordinates. It combines in the same numerical framework two different fluid approaches: relativistic MHD and force-free. The MHD part models the accretion disc and material falling onto the pulsar, while the force-free handles the magnetosphere. This approach is very interesting if we want to look at the interaction between the magnetosphere and the accretion disc. However, it is not suited to study particle acceleration. The algorithm can adapt dynamically with the evolution of the solution, and regions are allowed to switch back and forth between the force-free and relativistic MHD descriptions. The force-free approach is used to model the magnetosphere, where the magnetisation is high $\sigma \gg 1$, and the MHD models the disc, where $\sigma \lesssim 1$. The approach solves the GRMHD equations

$$\nabla_\mu(\rho u^\mu) = 0 \qquad \nabla_\mu T^\mu_\nu = 0 \qquad \nabla_\mu F^{*\mu\nu} = 0 \tag{3.103}$$

where $T^{\mu\nu}$ is the total energy-momentum tensor, u^μ is the fluid 4-velocity and $F^{*\mu\nu}$ is the dual of the electromagnetic tensor. The coupling is done thanks to a blending function called $\mathcal{A} = 1 - \mathcal{F}\mathcal{P}$ where $\mathcal{F}$ is a passive scalar used to know if the region is force-free or MHD, and $\mathcal{P}$ is a restricting radial profile used on the force-free solution. $\mathcal{A} = 0$ means that the regime is force-free while $\mathcal{A} = 1$ is the full GRMHD regime, and, in between, the value of $\mathcal{A}$ is interpolated to produce a smooth transition. This method removes the issue encountered in regions where the magnetisation is too high for GRMHD simulations, caused by the floor in mass density. These peculiar regions are treated with the force-free approach.

3.5 Summary

In this chapter, we have detailed two numerical approaches used to model relativistic magnetospheres. Both the PIC and force-free method presented here rely on a Finite-Difference Time-Domain scheme, in which we use a Yee mesh (space) combined to a leapfrog algorithm (time). The force-free numerical scheme appears simpler than the PIC one. It does not account for particles which removes a step from the algorithm. However, the force-free scheme hosts a complex computation of the current density when we want to maintain the second-order accuracy. Therefore, some numerical treatments are done by hand to avoid some of the difficulties.
In the PIC method, the particle aspect forces us to do additional steps, like solving for the trajectories. The contribution to the current and to the charge density of each individual particle must be computed at each grid node, meaning that the more particle the simulation hosts the longer the computation takes. Despite this aspect, the PIC method is able to model the trajectory of particles but also to apply the radiation-reaction force to them.
However, whether the method is force-free or PIC, both have limitations. Either they are not able to account for dissipative effects but are cheap, or they can give insights of the microphysics but are expensive.

The community is now trying to by-pass some of these limitations by building *hybrid* methods. Such new methods are usually combining two approaches in order to describe two different behaviours of a system.

3.6 [Français] Points clés du chapitre

Dans ce chapitre, nous avons détaillé deux approches numériques utilisées pour modéliser les magnétosphères relativistes. Ces deux approches reposent sur la résolution des équations de Maxwell au cours du temps. Pour procéder à cette résolution, nous avons considéré la méthode des différences finies dans le domaine temporel (FDTD) à l'ordre 2. Pour cette méthode, il est nécessaire de discrétiser à la fois en espace et en temps notre problème. Ces deux discrétisations sont d'ordre 2 afin de conserver la précision du second ordre voulu pour la méthode FDTD. La discrétisation spatiale utilise la maille de Yee et la discrétisation temporelle repose sur la méthode du saute-mouton. Afin d'accélerer la résolution de notre problème, il est possible de paralléliser les tâches entre différents CPUs. Pour cela, il est nécessaire de communiquer des informations entre les différentes unités de calcul. On peut, par exemple, utiliser des communications directes entre les unités ou définir des cellules fantômes qui sont utilisées pour les échanges. La méthode FDTD n'est pas la seule possible, on peut aussi utiliser une méthode pseudo-spectrale pour modéliser une magnétosphère.

Les approches sans-force et PIC peuvent toutes deux utiliser la méthode FDTD. Dans un premier temps, nous appliquons la méthode FDTD dans le cas sans-force. Le schéma sans-force se divise en deux étapes : 1) calcul de la densité de courant, 2) résolution des équations de Maxwell. Le traitement de la densité de courant est assez complexe dans le cas sans-force lorsqu'on veut conserver la précision du second ordre, de nombreux termes liés à des opérateurs doivent être calculés ce qui est très coûteux. Une astuce consiste à calculer uniquement une partie du courant et d'appliquer un traitement numérique pour imiter les effets des parties non calculées. Une fois le courant calculé, il est naturel de l'injecter dans les équations de Maxwell afin de les résoudre et de faire évoluer la solution. L'approche PIC présente quelques différences avec l'approche sans-force, mais elle est très similaire lorsque l'on utilise la méthode FDTD. Cette approche est décomposée en trois étapes, soit une de plus que l'approche sans-force : 1) résolution de l'équation de Newton, 2) dépôt des courants et des charges, 3) résolution des équations de Maxwell. La première étape découle du caractère particulaire de la méthode PIC, car il est nécessaire de faire évoluer les particules dans le temps pour décrire la magnétosphère. Pour les courants et les charges, il faut déposer la contribution individuelle de chaque particule aux coins de la cellule dans laquelle la particule se trouve. Une méthode possible consiste à attribuer un poids à la contribution de la particule pour chacun des coins de sa cellule. La dernière étape est identique à l'approche sans-force, c'est-à-dire que la densité de courant est injectée dans les équations de Maxwell, qui sont ensuite résolues. Il est toutefois possible de modifier légèrement l'approche PIC pour tenir compte de la force de réaction au rayonnement, cette modification intervenant dans la résolution de l'équation de Newton.
Ces deux approches permettent donc de modéliser des magnétosphères relativistes, mais elles ne sont pas infaillibles. En effet, elles présentent toutes les deux des points forts, des points faibles et des limitations. L'approche sans-force est plus rapide car l'algorithme ne comporte que deux étapes et n'implique pas de particules et donc aucun traitement individuelle de ces dernières. Pour l'approche PIC, l'étape supplémentaire liée aux particules a un impact non négligeable sur le temps de calcul. Celui-ci est fortement lié au nombre de particules présentes dans la simulation. Il est possible de réduire cet effet en diminuant le nombre de particules, mais cette astuce introduit le problème du bruit de grenaille. En termes de physique, l'approche PIC est plus complète car elle permet d'accéder à différentes quantités soit directement depuis les particules, soit reconstruites à partir de celles-ci. Cependant, un problème très important fait partie intégrante du paysage PIC : celui de la séparation des échelles (discuté dans le prochain Chapitre).

La communauté cherche aujourd'hui à contourner certaines de ces limitations en élaborant des méthodes dites *hybrides*. Ces nouvelles méthodes combinent généralement deux approches ou deux traitements distincts afin de décrire deux comportements différents d'un système. Nous avons vu quelques exemples de couplage possible à la fin de ce chapitre, la liste n'est en aucun cas exhaustive.

CHAPTER 4

State-of-the-art relativistic magnetospheres and objectives of this thesis

Contents

We have seen in the previous chapters that in relativistic magnetospheres, a wide range of plasma processes can be triggered. Consequently, to model such an environment, numerical simulations should account for all of them. This aspect is rather complex to obtain, and some simplifications must be done. Nonetheless, current state-of-the-art simulations of relativistic magnetospheres bring a lot of potential explanations for the observed emissions. In Sect. 4.1, we will see the current state-of-the-art simulations of pulsar magnetospheres and the inherent issue of the scale separation. In Sect. 4.2, we will do the same exercise for black hole magnetospheres and we will see that the scale separation is still a problem. Finally, Sect. 4.3 will establish the different questions that I aim at answering with my thesis.

4.1 Pulsar magnetosphere simulations

4.1.1 State-of-the-art PIC simulations

In the past decade, the community has been developing a wide range of tools to have ab-initio simulations of pulsar magnetospheres. Within these tools, we can highlight force-free and PIC codes which were detailed in Chapt. 3. Nowadays, the community uses PIC simulations to try to explain the different observational signatures of pulsars by continuously adding more physics. These simulations allowed the community to study dissipation, particle acceleration and emission in pulsar magnetospheres. We can name a few PIC codes with which it is possible to model such magnetospheres: APERTURE (Chen & Beloborodov, 2017), C-3PA (Kalapotharakos et al., 2018), OSIRIS (Fonseca et al., 2002), TRISTAN-MP V2 (Hakobyan, Spitkovsky, et al., 2023), ZELTRON (Cerutti et al., 2013).

At the beginning of pulsar magnetosphere simulations, the configuration used was the aligned rotator. The first PIC study of this configuration was done by Philippov and Spitkovsky (2014) in $3D$ using Cartesian coordinates. In their simulations, they use a volumetric injection of plasma which is an idealised injection. However, this work showed that the magnetosphere could have different structures depending on the amount of plasma injected. For low injection, the magnetosphere is an electrosphere while for a high plasma supply, the magnetosphere reaches a force-free state. Following this work, several groups performed $2D$ spherical PIC simulations to study the injection parameter. The plasma injection mechanism took different forms: a simplified pair production model based on an energy threshold (Chen & Beloborodov, 2014), a reservoir of pairs at the stellar surface (Cerutti et al., 2015) or a criterion based on the parallel electric field (Belyaev, 2015). Independently of the injection prescription, all studies agreed that two regimes (and a transition) are reached depending on the amount of plasma injected. The simulation either ends up in a fully developed force-free-like magnetosphere when the plasma injection is large enough, or it reaches the electrosphere regime and an intermediate state in between. This conclusion is in agreement with the previous $3D$ Cartesian work. These $2D$ simulations were also used to study the acceleration of particles and the dissipation of electromagnetic energy, especially in the context of gamma-ray pulsars. To show some of these results, we will use one of the latest simulations of the aligned rotator. The results presented in Fig. 4.1 are taken from Hu and Beloborodov (2022). The simulation setup is almost identical to the one from Chen and Beloborodov (2014). In this study, the pair production is based on an energy threshold above which a lepton produces a photon. Inside the light-cylinder, the mean-free-path of the photon is rather short, $\lambda_{\rm mfp} = r_\star$, and it gets larger after the light-cylinder, with $\lambda_{\rm mfp} = R_{\rm LC}$. The photon-photon interaction and pair production is done via a Monte-Carlo approach. However, the two simulations differ on the grid resolution. The recent work has a grid resolution eight times larger in both directions than the first work. In terms of physics, this increase of resolution allowed them to have a larger potential drop. The latter results in a new maximum Lorentz factor at the polar cap, from $\gamma_{\rm pc} = 425$ to $\gamma_{\rm pc} = 10^4$. The current highest value of this parameter was set by Bransgrove et al. (2023) and reached $\gamma_{\rm pc} = 2 \times 10^4$, thanks to another increase of resolution up to $(8192)^2$. The value of $\gamma_{\rm pc}$ gets closer to realistic values, but it still remains far from the value of a true pulsar. For the Crab pulsar (J0534+2200), $P = 33.6$ ms and $B_\star \approx 8 \times 10^{12}$ G, leading to $\gamma_{\rm pc} \sim 10^{11}$.

The left panel of Fig. 4.1 shows that gamma-rays are mainly emitted by the current sheet, with a strong production around the Y-point. Some gamma-rays are also produced along the separatrix. As expected by the presence of a large number of gamma-ray photons, the current sheet is a great site for pair production (middle panel of Fig. 4.1). At the

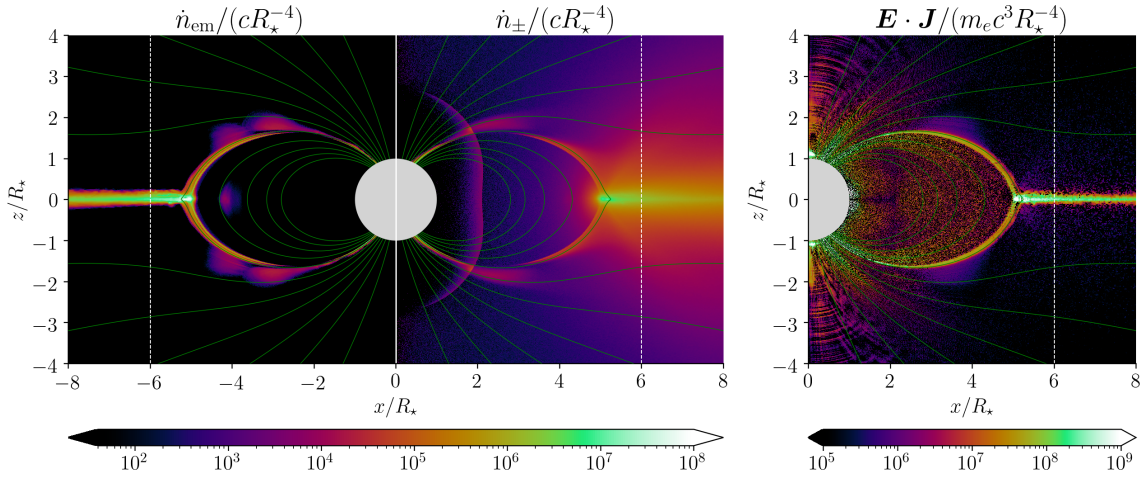

FIGURE 4.1: Left: emission rate of gamma-ray per unit volume. Middle: creation rate of electron-positron pairs per unit volume. Right: Map of $\mathbf{E}\cdot\mathbf{J}$ showing where dissipation occurs and its rate. Figures taken and adapted from Hu and Beloborodov (2022).

Y-point, pair production is the strongest and is correlated with the high number of gamma-ray photons present in a small volume around the Y-point. The right panel of Fig. 4.1 represents a map of $\mathbf{E}\cdot\mathbf{J}$. This quantity traces where the dissipation of electromagnetic energy occurs and at which rate. The Poynting flux dissipated is converted into particle energy via Poynting's theorem and particles are accelerated to high Lorentz factors. Unsurprisingly, the current sheet is the dominant site of dissipation. This conclusion is consistent with all previous work studying dissipation in pulsar magnetospheres (Belyaev, 2015; Cerutti et al., 2015). However, we can see that the separatrix is also dissipating energy. In their simulation, the authors also model ions with a mass ratio $m_{\rm i}/m_{\rm e} = 5$. The ratio is orders of magnitude below the realistic value $m_{\rm i}/m_{\rm e} = 1836$. In this setup, ions can almost be seen as non-radiating positrons. One of the highest mass ratios used for a pulsar magnetosphere simulation is $m_{\rm i}/m_{\rm e} = 18.36$ (Guépin et al., 2020), the true mass ratio is still waiting to be used.

Still with $2D$ simulations, it is possible to study the inclined rotator in its equatorial plane. Such study was performed by Cerutti and Philippov (2017). In this setup, pair production by photon-photon annihilation is not considered. The pairs are created and injected from the surface of the star. The results of this more realistic pulsar, in the sense that there is a misalignment between the spin axis and the magnetic axis, are shown in Figure 4.2.

In their work, the authors showed similar results to the one obtained in the $2D$ aligned rotator. However, in the equatorial setup and with an oblique rotator, two current sheets appear as Archimedean spirals and form a striped wind. The left panel of Fig. 4.2 shows the multiplicity of the plasma, indicating dense regions. Such regions appear to be the current sheet where particles are accelerated. The right panel of the same figure shows again the dissipation rate of electromagnetic energy. As for the aligned rotator, the current sheet is highlighted meaning that it dissipates energy and converts it into particle energy.

On the $3D$ side, the inclined rotator was modelled by Philippov et al. (2015) at first without radiative losses. The simulations were then upgraded to account for radiative processes and could also track photons (Cerutti, Philippov, & Spitkovsky, 2016; Philippov & Spitkovsky, 2018). Now that $3D$ simulations are able to model an inclined rotator with its associated emission, the community was able to produce light-curves and spectra.

Cerutti, Philippov, and Spitkovsky (2016) identified a caustic effect coming from the

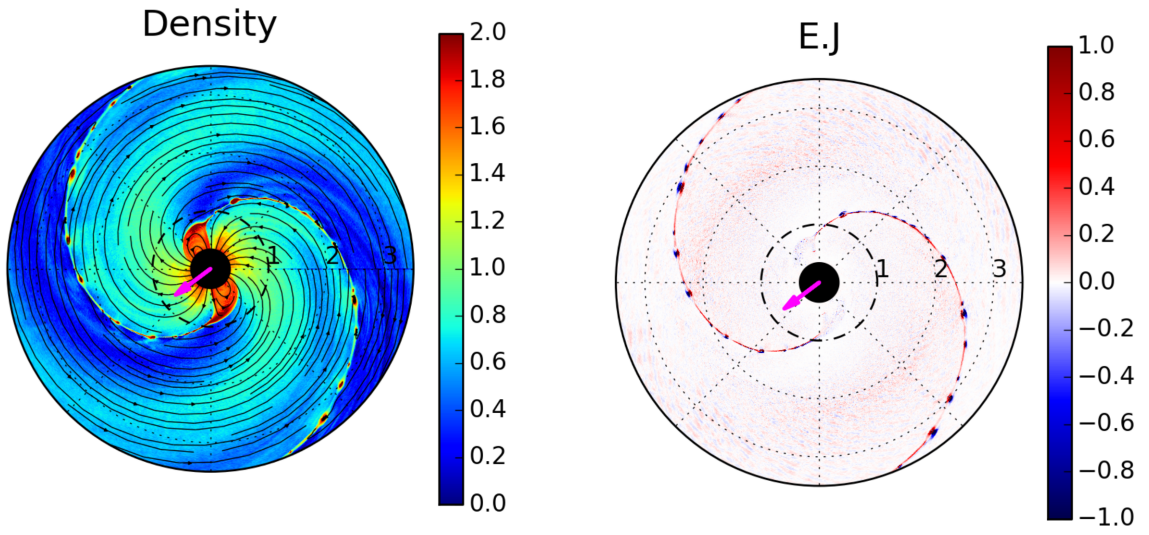

FIGURE 4.2: Left: map of the plasma multiplicity in log-scale. Right: $\mathbf{E} \cdot \mathbf{J}$ map showing the dissipation of electromagnetic energy, normalised by $\left(B_\star J_{\rm GJ}\right)\left(r_\star/r\right)^3$. Figures taken and adapted from Cerutti and Philippov (2017)

current sheet. This means that photons emitted at different places of the current sheet arrive in phase to the observer. The peaks observed are the result of the current sheet photons hitting the observer's screen at the same time. The latest $3D$ simulation of an inclined rotator was performed by Hakobyan, Philippov, et al. (2023) where they recovered a high density of pairs in the current sheet and a force-free state outside of it, see Fig. 4.3. In the $3D$ setup, the current sheet fragments in both the radial and the $\phi-$direction (the latter is dominant in the wind) and forms flux tubes. $3D$ simulations also allows to study the impact of the inclination angle on the electromagnetic dissipation. This was highlighted by Cerutti, Philippov, and Spitkovsky (2016) in their $3D$ study of the dissipation of the pulsar wind. They showed that when the inclination angle increases, the dissipation of electromagnetic energy drops significantly.

A global conclusion of these recent works is that in the regime of abundant pair supply, the force-free state is achieved almost everywhere in the magnetosphere, such that force-free simulations are sufficient for the majority of the magnetosphere. The only exception is the current sheet/separatrix where non-ideal fields develop. One way of illustrating this is to say that force-free simulation results are encapsulated in PIC results, when the latter consider a high supply of pairs.

Moreover, PIC simulations allow to study specific regions of the magnetosphere in details where the force-free assumptions break. This is the case if we want to study gap models and for example the polar cap gap. The most recent study on this gap was performed by Torres et al. (2024). In this work, the PIC simulation is able to capture the polar cap dynamics and the behaviour of the pair cascade. The latter could be responsible for the detected radio emission, see the review by Philippov and Kramer (2022).

4.1.2 PIC simulations in the scope of observations

Via PIC simulations, we can obtain the structure of the magnetosphere and have an ab-initio modelling of the plasma. However, these are not the only benefits. It is possible to derive synthetic observables (light curves, spectra, polarisation) from the simulations. We show some of these synthetics in Fig. 4.4, the list is not exhaustive.

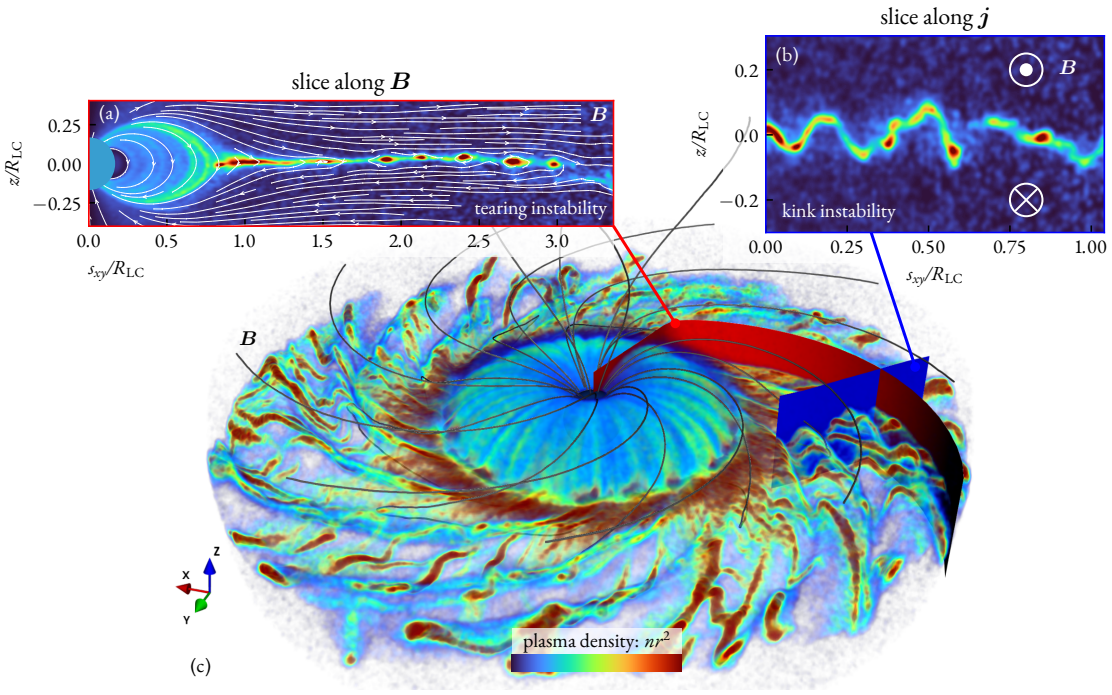

FIGURE 4.3: 3*D* rendering of the plasma density for an aligned rotator simulation, figure taken from Hakobyan, Philippov, et al. (2023). The upper left panel shows a slice along a magnetic field line, while the upper right panel is a slice perpendicular to the same field line.

These synthetic observables are crucial if we want to constrain the models. However, it is not possible to make a direct comparison between some of the synthetics and observations. This is the case for spectra. The top left panel of Fig. 4.4 shows a synthetic spectrum of particles. This is not directly a synthetic observable but the information inside it can be translated into a photon spectrum, which is observed. The latter would be compared to Fig. 4.5, where we show an observed spectrum in the gamma band. If we consider that photons are emitted via synchrotron radiation, we can compute the energy of the parent particle (Eq. 2.98). A photon of energy $\epsilon = 0.7\,\mathrm{GeV}$ radiated at the light-cylinder where $B_{\rm LC} \simeq 10^5$ Gauss would have been produced by a particle with a Lorentz factor of $\gamma = 7 \times 10^5$ or an energy $E = 4 \times 10^{11} = 400\,\mathrm{GeV}$. If we try to compare the two figures, we see that the particle spectra from the simulation extends up to tens of MeV. Such particles are thus producing gamma-rays, but are not able to cover the full range of observed energies. Therefore, it is impossible to compare the two results. This issue is currently inherent to global PIC simulations and is caused by the rescaling of the simulation.

4.1.3 Scale separation issue

When we model a global magnetosphere in PIC, we want to have the microscopic scales, i.e. kinetic scales, and the macroscopic scales. In this section, we consider a pulsar belonging to the canonical pulsar population. The latter is defined as an isolated, magnetised, rotating neutron star. For such a pulsar, we estimate that its mass is $M_\star \approx 1.44 M_\odot$, its magnetic field is $B_\star = 10^{12}$G and its spin period is $P = 100$ms. In a canonical pulsar, the smallest microscopic scale is set by the electron skin depth at the surface

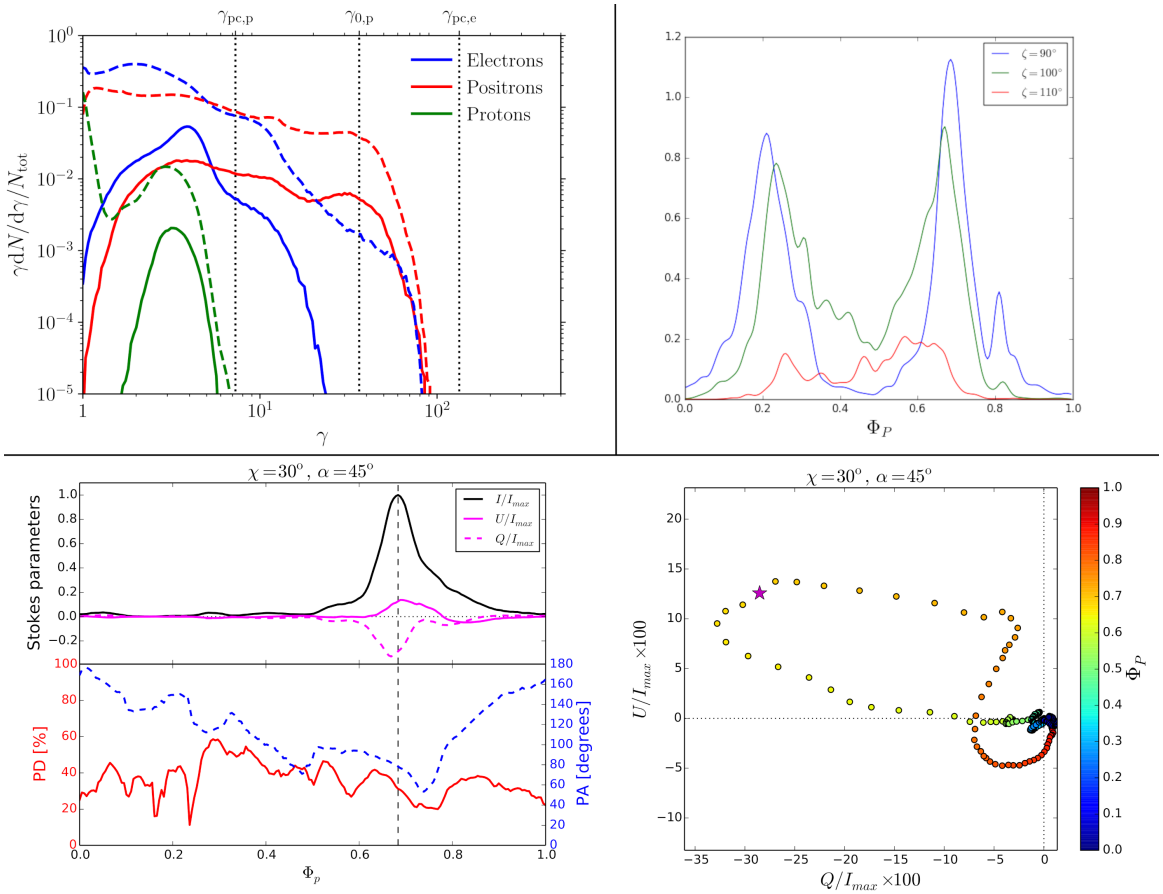

FIGURE 4.4: Classical synthetic observables obtained thanks to a PIC simulation. Top left: Spectra of pairs and ions taken from Guépin et al. (2020). Top right: Light curves obtained from a 3*D* simulation for three different viewing angles, figure taken from Philippov and Spitkovsky (2018). Bottom: Polarisation measurements from a 3*D* simulation, figure taken from Cerutti, Mortier, et al. (2016).

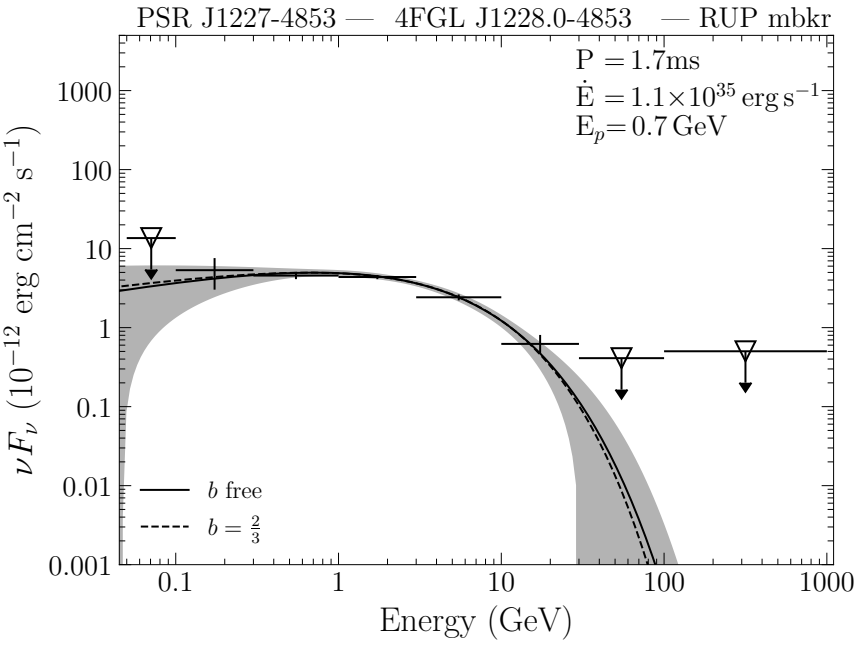

FIGURE 4.5: Gamma-ray spectral energy distribution of the millisecond pulsar PSR J1227-4853, figure taken from Smith et al. (2023).

$$d_{\rm e}^{\star} = \sqrt{\frac{\gamma m_{\rm e} c^2}{4\pi n_{\star} e^2}} \approx 6\times10^{-2}\left(\frac{\gamma}{10^0}\right)^{1/2}\left(\frac{\kappa}{10^2}\right)^{-1/2}\left(\frac{P}{100{\rm ms}}\right)^{1/2}\left(\frac{B_{\star}}{10^{12}{\rm G}}\right)^{-1/2}{\rm cm}, \tag{4.1}$$

while the macroscopic scale is set by the light-cylinder

$$R_{\rm LC} = \frac{cP}{2\pi} \approx 500 r_{\star}\left(\frac{P}{100{\rm ms}}\right) \approx 5000{\rm km}. \tag{4.2}$$

The resulting scale separation is **nine orders of magnitude**. Such scale separation would be achievable in a PIC simulation, but it would require a simulation with an extremely high resolution and thus many CPU hours. To explain why PIC simulations are not able to produce spectra with the right energy range, we need to look at the maximum energy of a particle. At the surface, the upper limit on the particle energy is set by

$$\gamma_{\rm pc} = \frac{e\Phi_{\rm pc}}{m_{\rm e}c^2} = \frac{eB_{\star}r_{\star}^3\Omega^2}{m_{\rm e}c^4} \approx 2.6\times10^9\left(\frac{B_{\star}}{10^{12}{\rm G}}\right)\left(\frac{P}{100{\rm ms}}\right)^{-2}. \tag{4.3}$$

To reduce the numerical cost of simulations, the size of the star and the strength of the magnetic field are reduced thus, lowering the maximum energy $(\propto B_{\star}r_{\star}^3)$. The scale separation of standard global PIC simulations of pulsar magnetospheres is of a few thousands. However, the rescaling is not done randomly, it must respect the hierarchy of scales. For pulsars, this hierarchy is based on three characteristic Lorentz factors

- polar cap $\gamma_{\rm pc}$
- pair production threshold $\gamma_{\rm th}$
- secondary pairs energy $\gamma_{\rm s}$

where they must respect

$$\gamma_{\rm s} \ll \gamma_{\rm th} \ll \gamma_{\rm pc} \tag{4.4}$$

to keep the physical ordering.

Another point is regarding the radiative losses. If the simulation does model the radiation-reaction force, the latter must also be modified, to account for the rescaling done on the magnetic field. The force has a new parameter $f_{\rm rad}$, which artificially enhances the strength of the magnetic field. This parameter reduces the synchrotron timescale so that energetic particles lose a significant fraction of their energy during a gyration time.

4.2 Black hole magnetospheres simulations

PIC or GRPIC simulations of black hole magnetospheres are still at an early stage. The first full kinetic simulation of such magnetospheres was performed a few years ago by Levinson and Cerutti (2018) in $1D$ and Parfrey et al. (2019) for $2D$ simulations. These simulations are a unique tool to understand what is happening in the close vicinity of the black hole and to try to explain what is causing the observed emission.

4.2.1 State-of-the-art GRPIC simulations

The black hole community is able to perform $2D$ and $3D$ global GRPIC simulations of the magnetosphere. In Fig. 4.6, we highlight some results of $2D$ and $3D$ simulations.

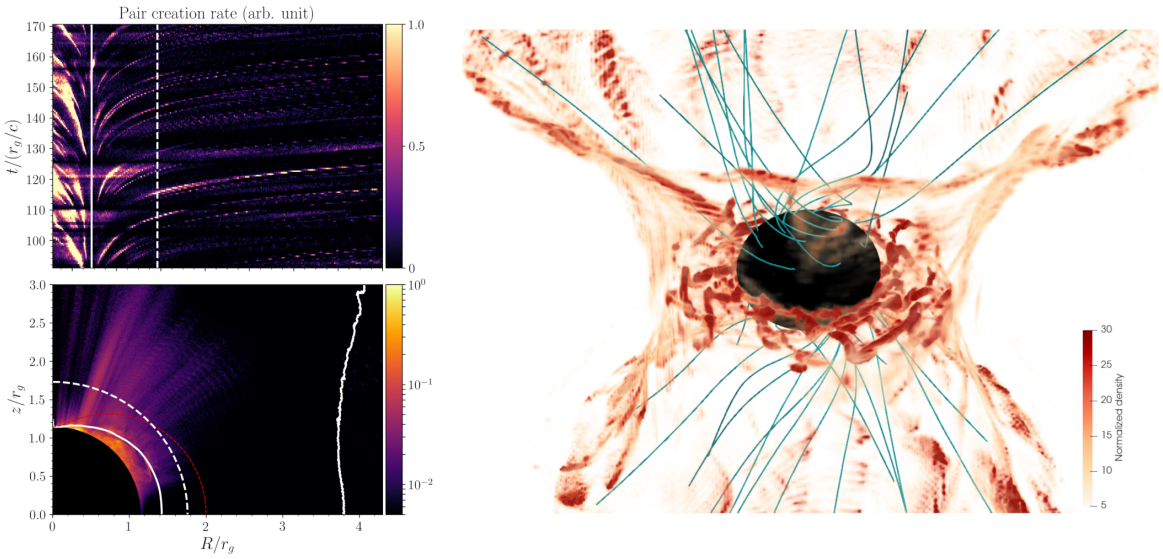

FIGURE 4.6: Left: Pair creation rate in a 2D GRPIC simulation, figure taken from Crinquand et al. (2020). The top panel shows a spacetime diagram of the pair production, while the bottom one shows where on average pairs are created. Right: 3D rendering of a GRPIC black hole magnetosphere, figure taken from Crinquand et al. (2022).

The right panel of Fig. 4.6 shows a 3D rendering of the number density inside the magnetosphere. In the equatorial plane, we can see the current sheet fragmenting into flux tubes with a high density. This is the sign of 3D magnetic reconnection and, thus, of particle acceleration. The left panel shows the pair creation rate. The spacetime diagram at the top left shows that pair creation is not continuous. The behaviour is identical to the polar cap gap for pulsars, where pair creation occurs while the density is below the Goldreich-Julian density. The lower left panel pictures where pair creation is occurring in the poloidal plane. The main mechanism for pair production close to the black hole is expected to be via Breit-Wheeler or photon-photon annihilation. Because photons are tracked in the simulation, this means that is possible to produce synthetic images to compare to observations.

4.2.2 GRPIC simulations in the scope of observations

Once simulations are performed, we need to compare or try to apply what is seen in them to astrophysical objects. Thanks to the EHT collaboration, the community has an image of the emission at the horizon scale for both M87* and SgrA*. They represent a valuable comparison for the models.

Figure 4.7 shows on the left side a synthetic image of a GRPIC simulation and on the right the image of M87*. The left panel was obtained from a simulation by using a ray-tracing method while the right one was constructed from observational data. Even if we cannot compare the two images in details, the comparison of the overall structure is important to build an intuition of what is happening. For example, the simulation recovers two features present in the observation: a side of the image is brighter (Doppler boosting) and the croissant shape of the brighter region. This emission is coming from synchrotron radiation for an optically thin regime.

4.2.3 Scale separation issue

The issue of the scale separation remains in GRPIC simulations. However, in this context, we define a new parameter $\widetilde{B}_0$ to measure the scale separation. The expression of $\widetilde{B}_0$ is

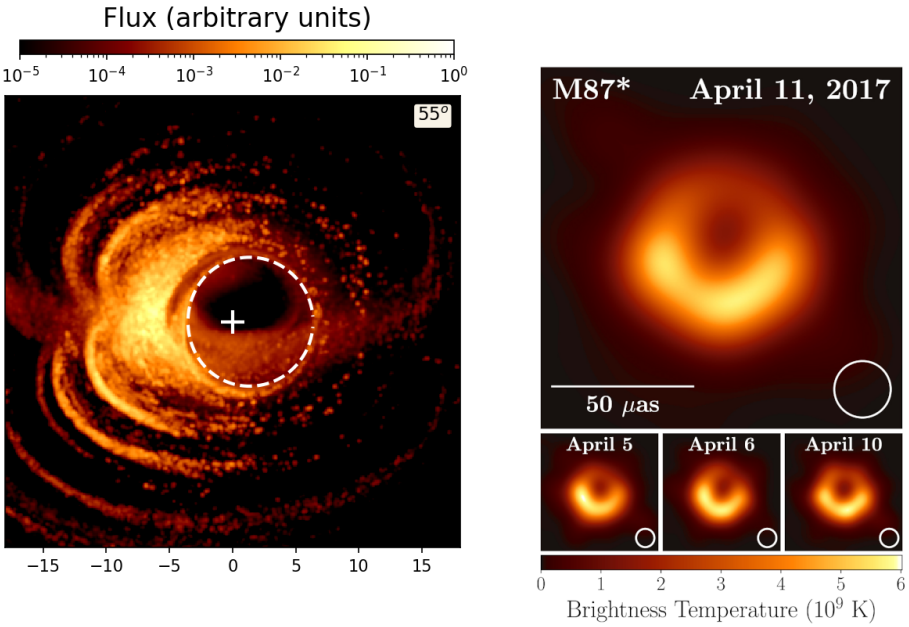

FIGURE 4.7: Left: Synthetic observables of synchrotron emission from a simulation, figure taken from El Mellah et al. (2022). Right: image obtained by the Event Horizon Telescope Collaboration et al. (2019).

$$\widetilde{B}_0 = \frac{eB_0 r_g}{m_e c^2} = \frac{r_g}{r_L}. \tag{4.5}$$

Its expression is directly related to the macroscopic and microscopic fiducial scales, respectively the gravitational radius and the Larmor radius of particles.

In black magnetospheres, the scale separation is similar to the one of pulsars. We can compute the value of $\widetilde{B}_0$ for M87* and SgrA* where the magnetic field at the horizon is between $1 - 100$ G. For these two supermassive black holes, the scale separation is

$$\widetilde{B}_{0,\mathrm{M87}^\star} \approx 10^{11-13} \qquad \widetilde{B}_{0,\mathrm{SgrA}^\star} \approx 10^{8-10} \tag{4.6}$$

These scales are not yet tractable to GRPIC simulations. Consequently, GRPIC simulations also perform a rescaling similar to the one of standard PIC simulations. Commonly, the scale separation of GRPIC simulations reaches $\widetilde{B}_0 \sim 10^6$ in $2D$ and 10^4 in $3D$. The gap between simulations and realistic systems is large and is waiting to be filled.

The conclusion of this section and the previous one is rather simple. If we want to rigorously confront our models to observations, we must increase the scale separation of (GR)PIC simulations. However, a few constraints do apply: (i) all the physics of relativistic magnetospheres must remain, (ii) simulations must have a reasonable cost in terms of computing hours.

4.3 Objectives of the thesis

In light of the scale separation issue that we highlighted previously, the main idea was to shift gears by trying a new method. We recall that relativistic magnetospheres are globally in the force-free regime, except the current sheet and separatrix. The idea behind the possible new approach is to have a force-free description, in regions where the force-free regime is valid, and a particle description, in regions where non-ideal fields and plasma processes are important. My thesis work is articulated as follows:

- Is it possible to develop a viable force-free-PIC approach?
- If so, could this force-free-PIC approach be used to model pulsar magnetospheres?
- With a working hybrid approach, what is the maximum reachable scale separation?
- Are PIC results holding strong for close to realistic scale separation?
- Without rescaling, what is the typical energy of particles and where does the acceleration occurs?
- Can this approach be translated from flat space to a curved spacetime to model black hole magnetospheres?

This manuscript is outlined as follows. In this Part I, I presented the observational, theoretical and numerical context as well as the state-of-the-art simulations of relativistic magnetospheres. In Part II, I describe the force-free-PIC approach with a first validation using the Michel monopole. Then, I use my method to model a weak millisecond pulsar for an aligned configuration. Finally, I summarise the main results of my thesis in Part III with a statement on the current development of the method in curved spacetime to model black hole magnetospheres.

4.4 [Français] Objectifs de la thèse

Dans ce chapitre, nous avons mis en avant différentes simulations de magnétosphères relativistes. Que ce soit pour les pulsars ou pour les trous noirs, ces simulations ont permis d'étudier le comportement du plasma autour de ces objets extrêmes. Elles permettent aussi de produire des observables synthétiques qui peuvent être utilisées pour tenter d'interpréter les diverses observations. Cependant, les simulations produisant ces observables utilisent principalement la méthode PIC et présentent donc une faille majeure. Celle-ci est liée à l'utilisation d'une méthode particulaire (échelle microscopique) pour décrire un système macroscopique. Pour les magnétosphères relativistes, ces deux échelles sont séparées par environ neuf ordres de grandeur. Cela implique donc d'utiliser des résolutions extrêmes pour capturer en totalité ces deux échelles simultanément ou de recourir à une procédure de rééchelonnement. C'est cette dernière méthode qui est généralement utilisée par la communauté. Cette procédure permet de réduire les écarts entre les différentes échelles tout en conservant la hiérarchie du système réel, mais elle introduit une faille dans les simulations. Les échelles étant réduites, cela impacte directement les énergies accessibles dans le système par les particules. De ce fait, la comparaison directe avec les observations devient impossible.

En raison de cette faille présente dans les simulations globales actuelles, nous avons décidé de changer de tactique en essayant une nouvelle méthode. Pour rappel, les magnétosphères relativistes sont globalement dans un régime physique dit sans-force, à l'exception de la nappe de courant et de la séparatrice. L'idée principale derrière cette tentaive de nouvelle approche est d'utiliser une description sans-force dans les régions où cette hypothèse est valide, et d'employer une description particulaire dans les régions où des champs non-idéaux se développent et où les processus plasmas sont importants. La liste suivante regourpe les différentes questions auxquelles je vais tenter d'apporter une réponse dans le cadre de mon travail de thèse :

- Est-il possible de mettre au point une approche sans-force-PIC viable ?
- Si tel est le cas, cette approche sans-force-PIC peut-elle être utilisée pour modéliser les magnétosphères de pulsars ?
- Avec une approche hybride fonctionnelle, quelle est la séparation d'échelle maximale que l'on peut atteindre ?
- Est-ce que les résultats obtenus avec la méthode PIC sont toujours valables pour une séparation d'échelle proche de la réalité ?
- Sans rééchelonnage, quelle est l'énergie typique des particules et où sont-elles accélérées ?
- Est-il possible de transposer cette approche en espace plat vers une approche en espace courbe pour modéliser les magnétosphères de trous noirs ?

Ce manuscrit s'articule de la façon suivante. Dans la Partie I, j'ai présenté les contextes observationnel, théorique, mais aussi numérique des objets compacts. J'ai également établi l'état de l'art actuel et soulevé des questions auxquelles je tenterais de répondre par la suite. Dans la Partie II, je décris l'approche sans-force-PIC et l'applique sur le cas analytique du monopole de Michel afin de valider l'approche. Ensuite, j'utilise cette méthode pour modéliser un rotateur dipolaire aligné correspondant à un pulsar faible. Enfin, je résume les principaux résultats de mon travail de thèse dans la Partie III et je présente aussi l'avancé actuelle de mes travaux sur le portage de ma méthode en espace courbe afin de modéliser les magnétosphères de trous noir.

Part II

Results

CHAPTER 5

Hybrid approach

Contents

In this chapter, I describe how I implemented my hybrid approach in the ZELTRON code. In Sect. 5.1, I present the procedure behind the implementation of the force-free module. In Sect. 5.2, I give all the details of the force-free-PIC approach (coupling, criterion, difficulties). In Sect. 5.3, I apply the new force-free-PIC method to the Michel monopole configuration. This solution is analytical and represents a valuable resource when doing numerical development on pulsar magnetospheres. Finally, I summarise the results in Sect. 5.4. This chapter is partly adapted from my paper "Scaling up global kinetic models of pulsar magnetospheres using a hybrid force-free-PIC numerical approach" accepted in *Astronomy & Astrophysics* (Soudais et al., 2024).

5.1 Force-free module in *Zeltron*

ZELTRON is a PIC code first introduced by Cerutti et al. (2013). It uses the FDTD method described in Sect. 3.1.1 to solve Maxwell's equations and the Boris push (Sect. 3.3.2) to solve the equation of motion. In the spherical version of the code, the Yee mesh is slightly modified to fit the geometry as shown in Fig. 5.1. This was the current state of the code when I started the project, an ab-initio PIC code solving global magnetospheric problems. To develop the hybrid coupling between the PIC and the force-free method, I had first to develop a new force-free module in ZELTRON from scratch.

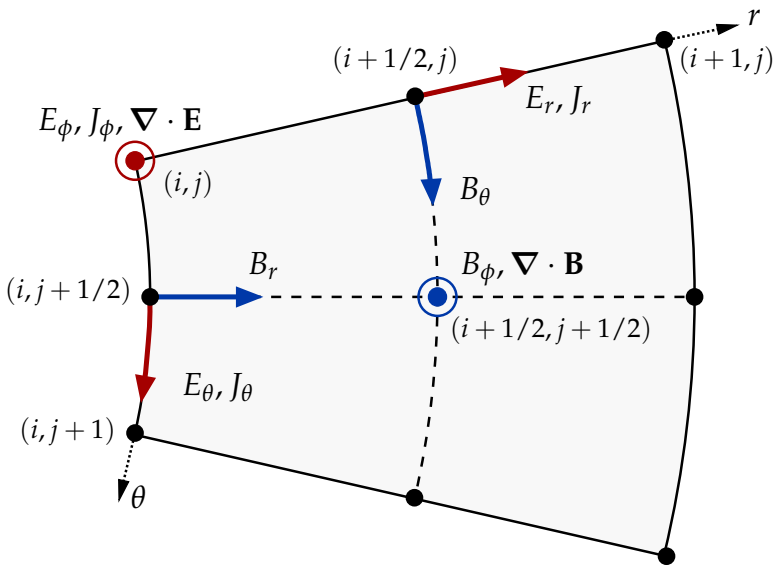

FIGURE 5.1: Spherical Yee mesh used in ZELTRON .

5.1.1 Impact on the code

The force-free method is encapsulated in a new module that contains all the tools needed. The core of the code was slightly modified to allow the use of the force-free module, with a switch to change from the PIC to the force-free approach. At this stage, this change is the only one which touches the spin of the code. The force-free method is not intrusive as it is only contained in one module and can run in parallel.

In a force-free code, we need to solve Maxwell's equations to evolve the electromagnetic field. This step is common in PIC and force-free thus, the Maxwell solver used in our force-free approach is the one used in the original PIC method. However, during the development of the module, I implemented a third-order Runge-Kutta scheme (RK3) for the time integrator. This scheme has a higher accuracy and was originally used by Spitkovsky (2006). Moreover, it allows to have the electric and magnetic fields centred on the same time. As a consequence, the current density computation is always correctly centred in time. This will become clearer in the next section. No differences were shown between the two schemes, and the RK3 scheme was left behind to favour the leapfrog scheme. Sticking to the original time integrator of ZELTRON was also a way of starting with solid foundations. This exact solver was already involved in previous works (Cerutti et al., 2015; Cerutti & Philippov, 2017; Guépin et al., 2020).

5.1.2 Current density computation

Even if the Maxwell solver is identical in PIC and force-free, there is a strong difference in the origin of the current density. In PIC, it comes directly from the individual contribution of particles. In force-free, there are no particles and the current density is only computed from the electromagnetic field. We recall the expression of the force-free current density

$$\mathbf{J} = \mathbf{J}_\perp + \mathbf{J}_\parallel \tag{5.1}$$

with

$$\mathbf{J}_\perp = c\frac{\boldsymbol{\nabla}\cdot\mathbf{E}}{4\pi}\left(\frac{\mathbf{E}\times\mathbf{B}}{B^2}\right) \qquad \mathbf{J}_\parallel = \frac{c}{4\pi}\Big(\mathbf{B}\cdot(\boldsymbol{\nabla}\times\mathbf{B}) - \mathbf{E}\cdot(\boldsymbol{\nabla}\times\mathbf{E})\Big)\frac{\mathbf{B}}{B^2}. \tag{5.2}$$

Computing these expressions in a temporally and spatially centred scheme is a difficult task. The computation uses all the components of **E** and **B**, which are staggered on the Yee mesh (Fig. 5.1). Therefore, computing the different components of the current density requires a proper re-centring. Each components of the electromagnetic field need to be computed at the exact location of J_r, J_θ, J_ϕ. In addition to the spatial misalignment, we recall that in the leapfrog scheme **B** and **J** are misaligned with respect to **E** by half a timestep. To have a clean estimate of the current density and to keep the second order accuracy, the current density must be computed at the right time. This introduces another extra centring step. If this procedure is not done properly in space and time, the second-order accuracy is lost, leading to the accumulation of small errors. With the current density being used in Maxwell's equations, the small errors will propagate in time and grow in amplitude. The simulation will result at best in the crash of the code if not worse, an unphysical solution. From a practical point of view, the first term $\mathbf{J}_\perp$ is relatively simple to centre in space and in time. However, the second term $\mathbf{J}_\parallel$is cumbersome to compute if we want to maintain the second-order accuracy in time and space. To avoid the computation of $\mathbf{J}_\parallel$, we apply the same method as Spitkovsky (2006) for the current density. This means that only the perpendicular component of the current density is computed and evolved in the loop in time. To simplify the computation of $\mathbf{J}_\perp$, all quantities from the Yee mesh are computed on the nodal grid. This grid differs from the Yee mesh, as the physical quantities are only known at the points (i, j). In this configuration, the current density is

$$(\mathbf{J}_\perp)_{i,j} = \frac{c}{4\pi}(\boldsymbol{\nabla}\cdot\mathbf{E})_{i,j}\left(\frac{(\mathbf{E})_{i,j}\times(\mathbf{B})_{i,j}}{(B_r)^2_{i,j} + (B_\theta)^2_{i,j} + (B_\phi)^2_{i,j}}\right) \tag{5.3}$$

where

$$(E_r)_{i,j} = \frac{(E_r)_{i+1/2,j}\sqrt{\gamma}_{i+1/2,j} + (E_r)_{i-1/2,j}\sqrt{\gamma}_{i-1/2,j}}{\sqrt{\gamma}_{i+1/2,j} + \sqrt{\gamma}_{i-1/2,j}} \tag{5.4}$$

$$(E_\theta)_{i,j} = \frac{(E_\theta)_{i,j+1/2}\sqrt{\gamma}_{i,j+1/2} + (E_\theta)_{i,j-1/2}\sqrt{\gamma}_{i,j-1/2}}{\sqrt{\gamma}_{i,j+1/2} + \sqrt{\gamma}_{i,j-1/2}} \tag{5.5}$$

$$(E_\phi)_{i,j} = (E_\phi)_{i,j} \tag{5.6}$$

$$(B_r)_{i,j} = \frac{(B_r)_{i,j+1/2}\sqrt{\gamma}_{i,j+1/2} + (B_r)_{i,j-1/2}\sqrt{\gamma}_{i,j-1/2}}{\sqrt{\gamma}_{i,j+1/2} + \sqrt{\gamma}_{i,j-1/2}} \tag{5.7}$$

$$(B_\theta)_{i,j} = \frac{(B_\theta)_{i+1/2,j}\sqrt{\gamma}_{i+1/2,j} + (B_\theta)_{i-1/2,j}\sqrt{\gamma}_{i-1/2,j}}{\sqrt{\gamma}_{i+1/2,j} + \sqrt{\gamma}_{i-1/2,j}} \tag{5.8}$$

$$\begin{aligned}(B_\phi)_{i,j} = &\Big[(B_\phi)_{i+1/2,j+1/2}\sqrt{\gamma}_{i+1/2,j+1/2} + (B_\phi)_{i+1/2,j-1/2}\sqrt{\gamma}_{i+1/2,j-1/2} \\ &+ (B_\phi)_{i-1/2,j-1/2}\sqrt{\gamma}_{i-1/2,j-1/2} + (B_\phi)_{i-1/2,j+1/2}\sqrt{\gamma}_{i-1/2,j+1/2}\Big] \\ &\times \frac{1}{\sqrt{\gamma}_{i+1/2,j+1/2} + \sqrt{\gamma}_{i-1/2,j+1/2} + \sqrt{\gamma}_{i-1/2,j-1/2} + \sqrt{\gamma}_{i+1/2,j-1/2}}\end{aligned} \tag{5.9}$$

$$\begin{aligned}(\boldsymbol{\nabla}\cdot\mathbf{E})_{i,j} = &\frac{3}{\Delta r_i^3}\left(r_{i+1/2}^2 (E_r)_{i+1/2,j} - r_{i-1/2}^2 (E_r)_{i-1/2,j}\right) \\ &+ \frac{3\Delta r_i^2}{2\Delta r_i^3 \Delta\mu_j}\left(\sin\theta_{j+1/2}(E_\theta)_{i,j+1/2} - \sin\theta_{j-1/2}(E_\theta)_{i,j-1/2}\right)\end{aligned} \tag{5.10}$$

where $\Delta r_i^3 = \left(r_{i+1/2}^3 - r_{i-1/2}^3\right)$, $\Delta r_i^2 = \left(r_{i+1/2}^2 - r_{i-1/2}^2\right)$ and $\Delta\mu_j = \left(\cos\theta_{j-1/2} - \cos\theta_{j+1/2}\right)$. The centring of each field component is done by taking the arithmetic average, in which $\sqrt{\gamma}_{i,j}$ is the determinant of the $2D$ spherical metric at the grid node (i,j),

$$\sqrt{\gamma}_{i,j} = r_i^2 \sin\theta_j. \tag{5.11}$$

This centring is heavy to write and needs to use several buffers for communications to work in parallel. This term is implemented in ZELTRON and works for highly parallelised simulations.

The current density from Eq. (5.1) has a second term, $\mathbf{J}_\parallel$. The difficulty with the parallel term comes from the centring of the two curls. Even if we use the nodal grid to compute $\mathbf{J}_\parallel$, we need to compute the three components of the two curls on the Yee mesh before computing them at each grid node. This manipulation adds truncation errors to the solution (coming from the order of the scheme) that spreads across multiple cells. Despite the cumbersomeness of the computation, the parallel current density is still implemented and parallelised in the force-free module. The reason behind this implementation is that the computation of $\mathbf{J}_\parallel$ is mandatory if we want to look at the current density or any quantity related to $\mathbf{J}$. In practice, $\mathbf{J}_\parallel$ is computed right before the output of the simulation to reconstructed the full current density. We performed a numerical experiment in which the parallel term was computed and evolved in order to have the true current density injected into Maxwell's equations. Surprisingly, the result of this experiment was not successful. The benefit of adding the $\mathbf{J}_\parallel$ term was not significant and even showed some failures. The

reason behind this is still unclear to this date. For this reason, only the perpendicular term is computed for the time evolution. Consequently, the numerical treatment given in Sect. 3.2.2 and detailed in Sect. 5.1.3 must be applied.

Once the current density is computed on the nodal grid, it is staggered on the Yee mesh using the same arithmetical average method.

$$(J_{r,\perp})_{i+1/2,j} = \frac{(J_{r,\perp})_{i+1,j}\sqrt{\gamma}_{i+1,j} + (J_{r,\perp})_{i,j}\sqrt{\gamma}_{i,j}}{\sqrt{\gamma}_{i+1,j} + \sqrt{\gamma}_{i,j}} \tag{5.12}$$

$$(J_{\theta,\perp})_{i,j+1/2} = \frac{(J_{\theta,\perp})_{i,j+1}\sqrt{\gamma}_{i,j+1} + (J_{\theta,\perp})_{i,j}\sqrt{\gamma}_{i,j}}{\sqrt{\gamma}_{i,j+1} + \sqrt{\gamma}_{i,j}} \tag{5.13}$$

$$(J_{\phi,\perp})_{i,j} = (J_{\phi,\perp})_{i,j} \tag{5.14}$$

The current density is now at the right spatial location, but its time centring needs to be done. We remind that in the FDTD method, the electric and magnetic fields are misaligned in time. The electric field is known at integer timestep $(\mathbf{E})^n$ and the magnetic field at half-timestep $(\mathbf{B})^{n+1/2}$. Just like for the magnetic field, the current density should be computed at half time step $(\mathbf{J})^{n+1/2}$ for the time evolution of $\mathbf{E}$ to be centred (Eq. 3.17). To maintain the second-order in time, the electric field is pushed in time by half a time step and a temporary variable is used $(\mathbf{E})^n \longrightarrow (\mathbf{E}_{\text{temp}})^{n+1/2}$. The current density used for the half push is computed from the misaligned field in time. A new current density is computed with $(\mathbf{E}_{\text{temp}})^{n+1/2}$ to maintain the time centring. Once this procedure is done, the correctly centred current density is injected to evolve $(\mathbf{E})^n \longrightarrow (\mathbf{E})^{n+1}$.

5.1.3 Rescaling

Because we do not use the parallel current density, we need to mimic its physical effect by hand. This term acts on the electric field to maintain $\mathbf{E}\cdot\mathbf{B} = 0$, to remove the parallel component. Physically speaking, particles would be accelerated by the spurious electric field to unrealistic velocities. The numerical way of mimicking the parallel current is to remove the parallel excess of the electric field after its time evolution. We use Eq. (3.45) from Sect. 3.2.2 for this purpose. As for the perpendicular current density, we use the nodal grid

$$\mathbf{E} = \mathbf{E} - \left(\frac{\mathbf{E}\cdot\mathbf{B}}{B^2}\right)\mathbf{B}$$

$$\begin{pmatrix} E_r \\ E_\theta \\ E_\phi \end{pmatrix}_{i,j} = \begin{pmatrix} E_r \\ E_\theta \\ E_\phi \end{pmatrix}_{i,j} - \frac{(E_r)_{i,j}(B_r)_{i,j} + (E_\theta)_{i,j}(B_\theta)_{i,j} + (E_\phi)_{i,j}(B_\phi)_{i,j}}{(B_r)^2_{i,j} + (B_\theta)^2_{i,j} + (B_\phi)^2_{i,j}} \begin{pmatrix} B_r \\ B_\theta \\ B_\phi \end{pmatrix}_{i,j} \tag{5.15}$$

While we have the electric field on the nodal grid, we also rescale it according to Eq. (3.46)

$$\mathbf{E} = \sqrt{\frac{B^2}{E^2}}\mathbf{E}$$
$$\begin{pmatrix} E_r \\ E_\theta \\ E_\phi \end{pmatrix}_{i,j} = \sqrt{\frac{(B_r)_{i,j}^2 + (B_\theta)_{i,j}^2 + (B_\phi)_{i,j}^2}{(E_r)_{i,j}^2 + (E_\theta)_{i,j}^2 + (E_\phi)_{i,j}^2}} \begin{pmatrix} E_r \\ E_\theta \\ E_\phi \end{pmatrix}_{i,j} \tag{5.16}$$

This rescaling ensures that the force-free condition $\mathbf{B}^2 - \mathbf{E}^2 > 0$ is verified in the whole domain. To preserve the time centring, the magnetic field is pushed by half a time step before removing the parallel component and rescaling the electric field. Once the two treatments are applied to the electric field, it is staggered back onto the Yee mesh with Eq. (5.1.2) where (J_r, J_θ, J_ϕ) is replaced by (E_r, E_θ, E_ϕ).

5.1.4 Time integration loop

We now have all the ingredients needed to describe explicitly how in practice the time integration loop works. In Fig. 5.2, we show the time scheme corresponding to the force-free implementation in the ZELTRON code.

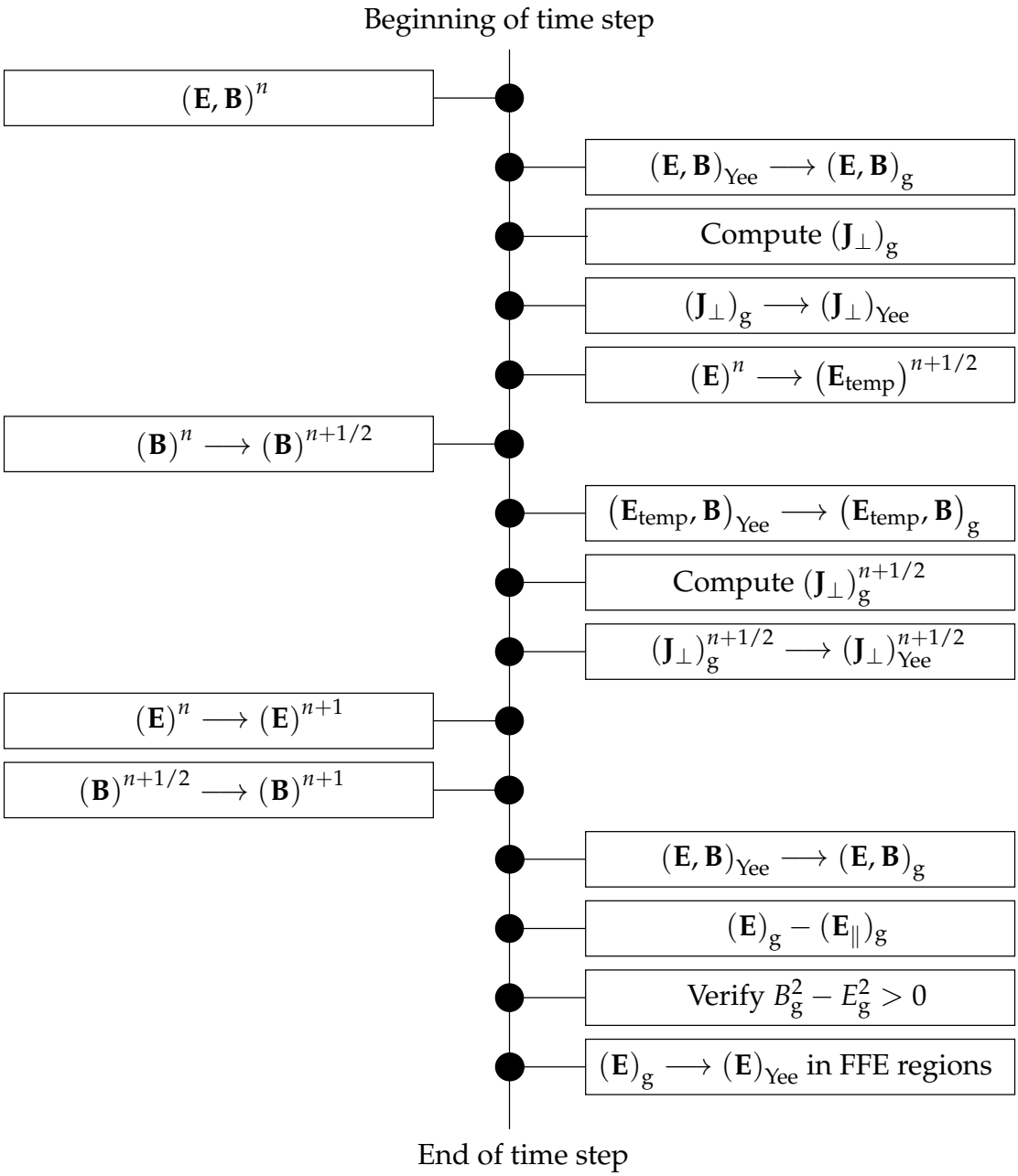

FIGURE 5.2: Force-free time integrator scheme. $(A)_{\text{g}}$ and $(A)_{\text{Yee}}$ denote respectively quantities on the nodal grid and on the Yee mesh. The left side corresponds to the evolution of the fields while the right one indicates the adjustments made in force-free.

5.2 Hybrid approach

Before diving into the full description of this new approach, we briefly recall the main aspects of each method.

5.2.1 Hybrid approach philosophy

In Fig. 5.3, we show side by side the main steps of the time loop of each method. Only two steps are needed in force-free: a first one to compute the current density and a second one to update the electric and magnetic field. In PIC, an extra step is needed due to the particle approach. This extra step allows to solve Newton's equation to update the positions and velocities of the particles in the simulation. Even if the PIC current density is obtained via current deposition on the nodal grid, it still remains a step where we compute the current density.

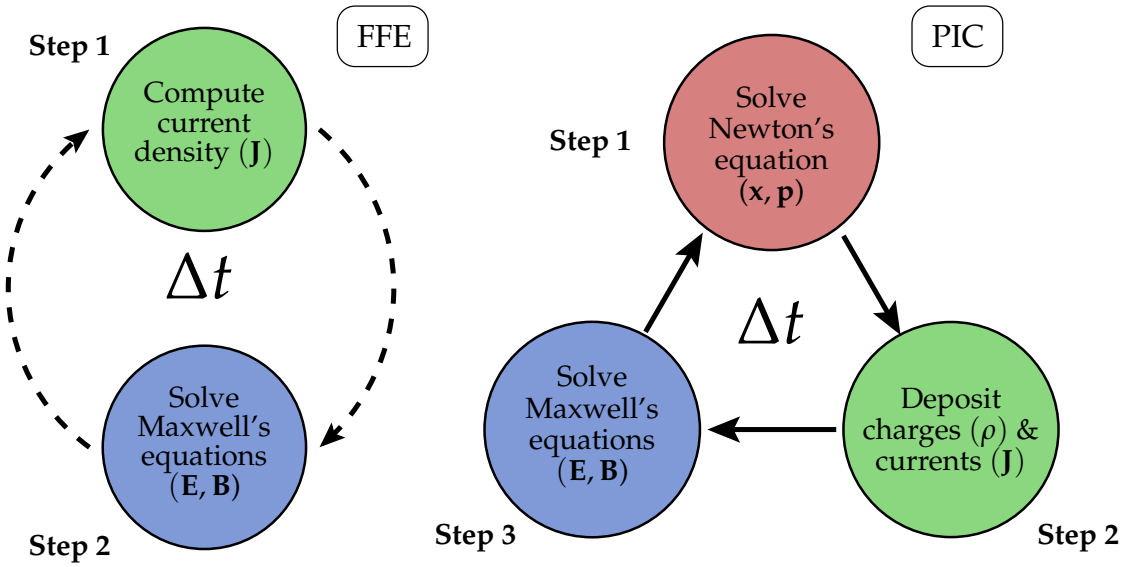

FIGURE 5.3: Comparison of the steps in the Particle-in-cell and force-free method.

With the hybrid approach, we wanted to do the lowest amount of modifications to the architecture of the code. With these constraints, the grid, Maxwell solver and particle pusher remained untouched. The modifications will impact the particle injection, especially where the particles are injected and allowed to exist and the current density. Even with this willingness, the hybrid approach still touches the core of the code.

5.2.2 Magnetic flux function

I will now elaborate on one of the crucial aspects of the method: which quantity do we use to distinguish if a region is force-free or PIC? We have seen in Sect. 2.1.2 that for the aligned rotator we have two main morphologies of field lines: closed or opened. To trace where magnetic field lines are, we can use the magnetic flux function Ψ, defined as

$$\Psi = \frac{1}{2\pi} \iint \mathbf{B} \cdot \mathrm{d}\mathbf{S} = \int_0^\theta B_r r^2 \sin\theta' \mathrm{d}\theta'. \tag{5.17}$$

We can use the isocontours of the magnetic flux function to obtain the magnetic field lines. In the context of axisymmetric pulsar magnetosphere, this choice is the most evident

one, as the field lines are anchored in the crust of the neutron star. In a simulation, the magnetosphere is a dynamic environment which never really reaches a steady-state but more of a quasi-steady state. As magnetic reconnection is occurring, some magnetic fields lines will close and produce plasmoids. Their shape and structure evolve with time during their advection outwards. To consider the behaviour of the magnetosphere in the simulation, the flux function must be computed at every time step of the loop in time to adapt to the solution. The parallel computation of Ψ is implemented in the code.

Coming back to the morphology of magnetic field lines, we have the specific case of the last closed field line connected to the current sheet. The separatrix and current sheet can also be localised thanks to the isocontours of Ψ. However, this configuration is the exact location where non-ideal fields develop and where magnetic reconnection occurs. If we have relativistic magnetic reconnection, we have the conversion of magnetic energy into particle acceleration. With this in mind, we see that particles must be present along the separatrix and must populate the current sheet. This specific region (separatrix + current sheet) is not described by the force-free approach but rather by the PIC approach.

5.2.3 Coupling

With the hybrid method heavily relying on the magnetic flux function to distinguish the topology of field lines, it is natural to base the coupling on this same function. In Fig. 5.3, we can note that the major difference between the PIC and force-free approach lies in the computation of the current density. Therefore, it appeared that coupling the two approaches through the current density might be the proper way of doing it.
Current from the PIC and the force-free parts are computed independently before being blended together into a unique current density. The resulting blended current is injected into Maxwell's equations to evolve the electromagnetic field in time. The Maxwell solver remains identical and conserves its original properties. The updated fields are unique across the simulation.

The equation performing the coupling between the force-free and the PIC region is the following

$$\mathbf{J} = \mathbf{J}_{\text{PIC}} \left(1 - f\left(\Psi\right)\right) + \mathbf{J}_{\text{FFE}} f\left(\Psi\right) \tag{5.18}$$

where $f\left(\Psi\right)$ is the blending function, $\mathbf{J}_{\text{PIC}}$ and $\mathbf{J}_{\text{FFE}}$ are respectively the PIC and force-free current densities. The profile of the blending function is shown in Fig. 5.4.

Its profile corresponds to three possible behaviours in the simulation.

$$f\left(\Psi\right) = \begin{cases} 1 & \text{force-free region} \\ \in]0,1[& \text{transition layer} \\ 0 & \text{PIC region} \end{cases} \tag{5.19}$$

The current density from Eq. (5.18) reduces to the force-free current when $f\left(\Psi\right) = 1$ and to the PIC current when $f\left(\Psi\right) = 0$. We set two pairs of critical values, namely Ψ_0, Ψ_1, Ψ_2 and Ψ_3. These values are used to define two transition layers, which are used to switch between the two numerical approaches. Inside the transition layers, the force-free and PIC currents are gradually mixed to smooth out the transition and avoid the propagation of numerical artefacts.

We give in Fig. 5.5 two azimuthal profiles of the radial current density. The results shown in this figure are purely to illustrate the impact of the transition layer. Both simulations are identical (setup and resolution), the only difference is the presence of a transition layer. The switch of method is set at $\theta = \pi/2$. When the transition layer is active, it is centred on $\theta = \pi/2$ and has a width of $\pm\epsilon$ (shaded region in Fig. 5.5). We can see a clear drop

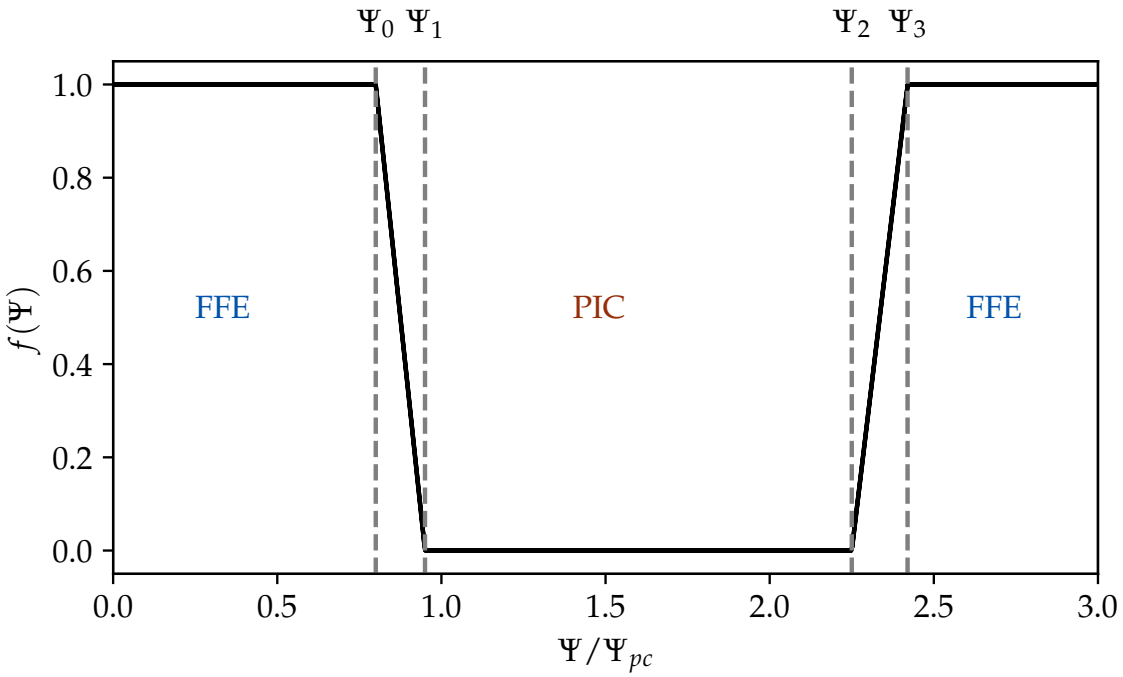

FIGURE 5.4: Blending function $f(\Psi)$. $\Psi_{0,1,2,3}$ correspond to the different critical field lines chosen by the user and are represented by the grey dashed lines.

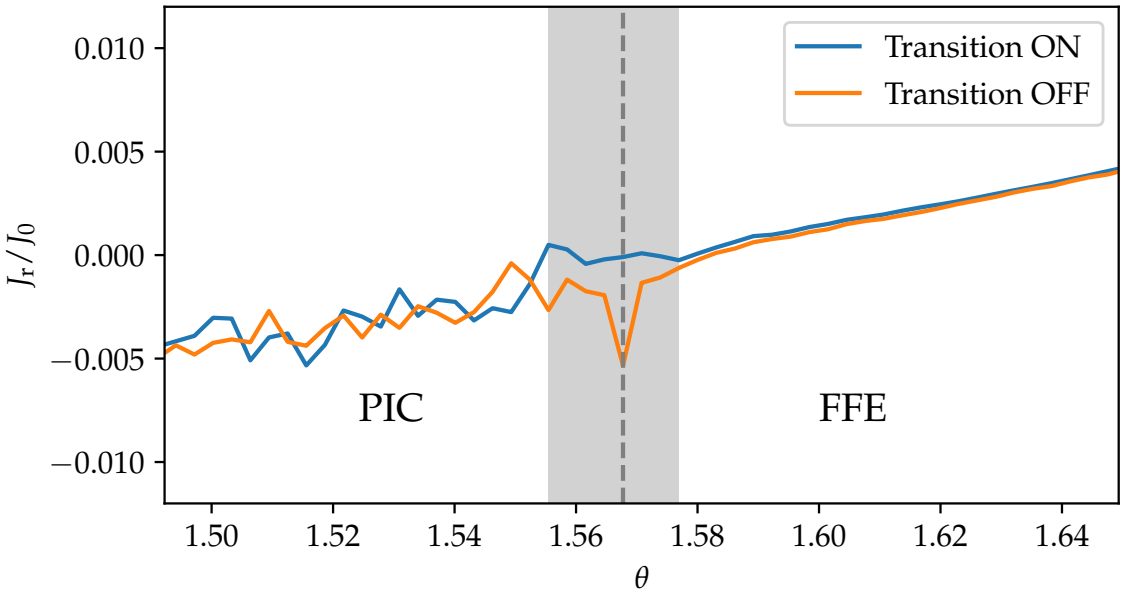

FIGURE 5.5: Zoom on the radial current density profile near the equator for a medium resolution simulation $(r, \theta) = (512 \times 1024)$. The shaded grey area shows where the transition layer is located, while the vertical dashed grey line is the location of the interface when the transition layer is removed.

in the profile when the transition layer is disabled. The second profile is smoother, and is the result of the active transition layer. This example illustrates the fact that the transition layer impacts the solution and eases the switch of approach.

We are now on track to perform the first test of the hybrid approach, but before that, we have a few constraints that we need to tackle. Two distinct treatments must be performed in each region. In the force-free region, we need to validate the force-free conditions. To this aim, Eqs. (5.15) and (5.16) are only applied in the force-free domain. The second treatment comes from the deposition scheme. Because of the non-charge-conserving deposition scheme used in ZELTRON , we must solve Poisson's equation

$$\nabla^2 \phi = 4\pi \rho_{\text{PIC}} \tag{5.20}$$

where ρ_{PIC} is the charge density of the PIC region. During a timestep, the electric field is modified at three different places: (i) Poisson's equation, (ii) first force-free condition, (iii) second force-free condition.

The final aspect of the coupling is regarding the particles. In the hybrid method, they are only allowed to evolve in the PIC regions and the transition layer. At every timestep, the position of each individual particle is compared to the position of the PIC boundary. If the particle is inside a PIC region, we keep it for the next timestep. However, if this particle crosses the boundary, we remove it from the simulation by setting its weight to zero. This treatment acts as a one way membrane, where particles can exit the PIC regions but never enter.

5.2.4 Hybrid time integrator

The hybrid scheme can be represented in a similar way to the PIC or force-free sequence. In Fig. 5.6, we show the hybrid scheme with the same representation used for the force-free and PIC methods.

Step 1 corresponds to the particle aspect with the evolution of the particle positions and velocities. In **Step 2**, the current of each numerical domain is computed independently before being blended during **Step 3**. **Step 4** is the common step where we solve Maxwell's equations. The fully detailed time integrator of the hybrid method is given in Fig. 5.7.

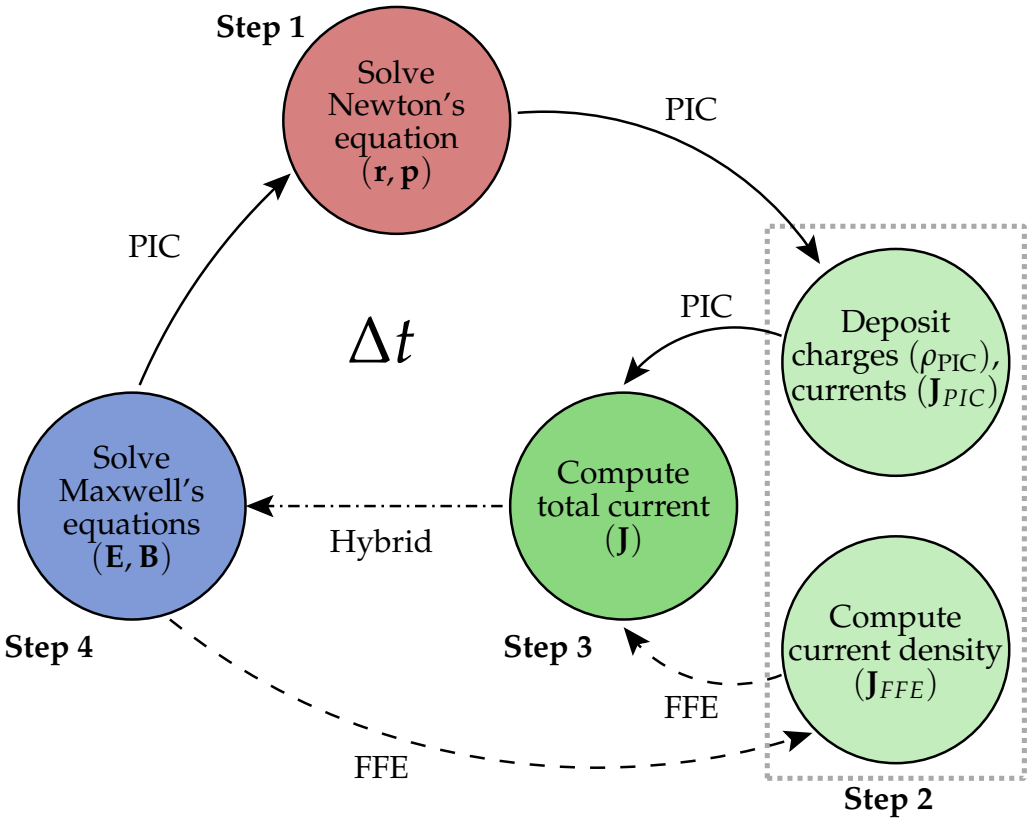

FIGURE 5.6: Diagram showing the construction of a hybrid timestep. PIC and FFE notation correspond respectively to Particle-in-cell and force-free regions of the simulation.

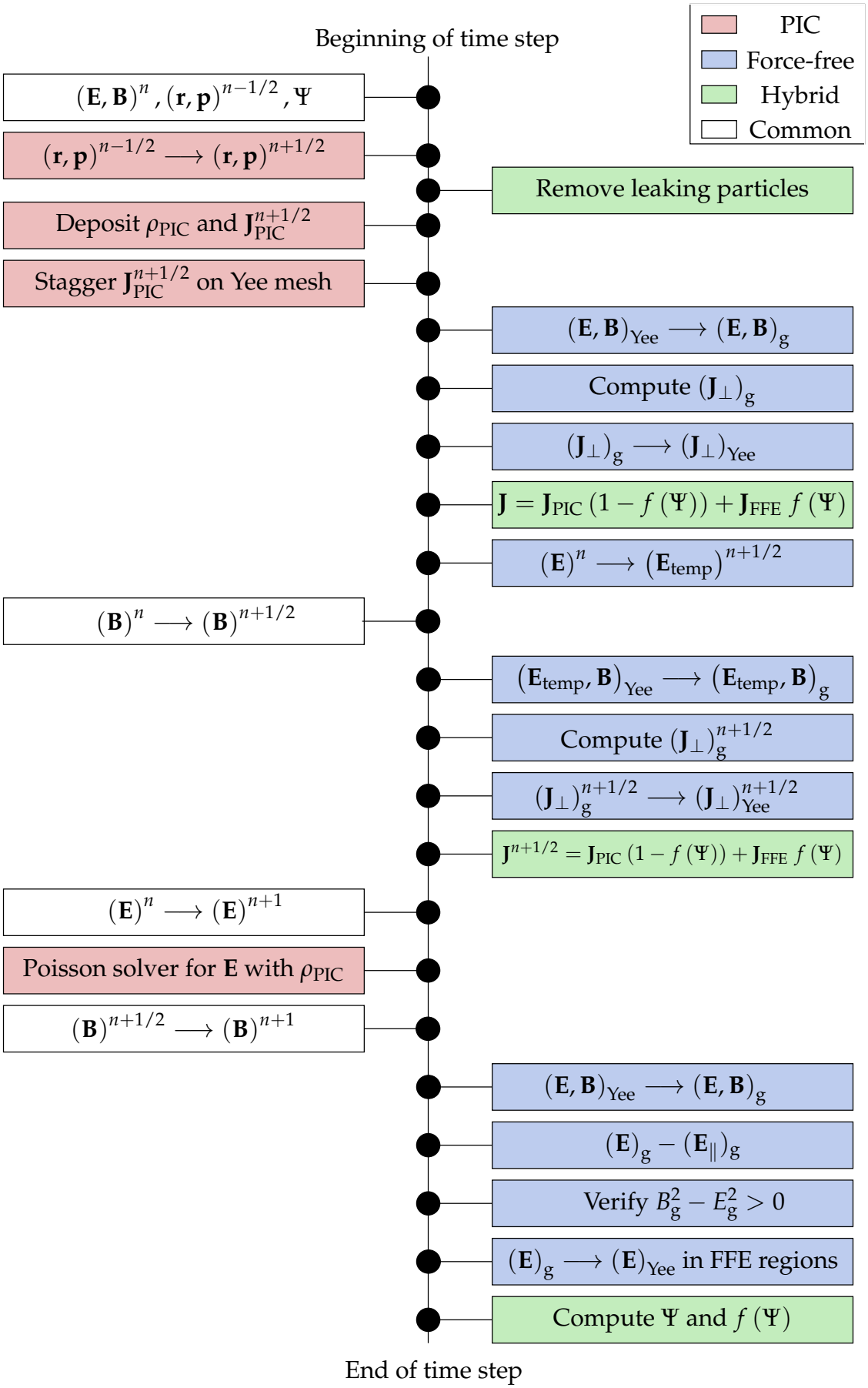

FIGURE 5.7: Hybrid time integrator details. $(\mathcal{A})_{\text{g}}$ denotes quantities on the nodal grid, while $(\mathcal{A})_{\text{Yee}}$ are quantities on the Yee mesh. Quantities from the PIC and force-free regions are respectively noted $(\mathcal{A})_{\text{PIC}}$ and $(\mathcal{A})_{\text{FFE}}$. The left side corresponds to a standard PIC scheme and the right side shows the force-free and hybrid steps.

5.3 Validation of the method

In this section, we put the new force-free-PIC method to the test against an exact solution of the pulsar equation.

5.3.1 Aide-mémoire for the Michel monopole

Regarding the magnetic configuration, we use the Michel monopole derived in Sect. 2.1.3. In this setup, the magnetic flux function is given by

$$\Psi_{\rm M}(\theta) = \Psi_\star (1 - \cos\theta), \tag{5.21}$$

where $\Psi_\star = B_\star r_\star^2$. From the magnetic flux function, we can express the magnetic and electric field components

$$\begin{aligned} B_r &= B_\star \left(\frac{r_\star}{r}\right)^2 & E_r &= 0 \\ B_\theta &= 0 & E_\theta &= B_\phi \\ B_\phi &= \mp B_\star \left(\frac{r_\star}{R_{\rm LC}}\right)\left(\frac{r_\star}{r}\right)\sin\theta & E_\phi &= 0 \end{aligned}$$

If $\boldsymbol{\Omega}\cdot\mathbf{B} > 0$, the sign of B_ϕ is negative, while it is positive for $\boldsymbol{\Omega}\cdot\mathbf{B} < 0$. This exact solution also allows us to compute the associated current density

$$\mathbf{J}_{\rm M} = \frac{c}{4\pi}\boldsymbol{\nabla}\times\mathbf{B} = -J^\star_{\rm GJ}\left(\frac{r_\star}{r}\right)^2 \cos\theta\,\mathbf{e}_{\rm r}, \tag{5.22}$$

where $J^\star_{\rm GJ} = \Omega B_\star/2\pi$ is the Golreich-Julian current density. The last characteristic quantity we can compute is the Poynting flux

$$L_{\rm M} = \frac{c}{4\pi}\iint (\mathbf{E}\times\mathbf{B})\cdot d\mathbf{S} = \frac{c}{2}\int_{-1}^{1} r^2 B_\phi^2 d\cos\theta = \frac{2\Psi_\star^2\Omega^2}{3c}. \tag{5.23}$$

The current density and the Poynting flux will play a crucial role in the validation of the method.

5.3.2 Numerical setup

We perform a set of three simulations with identical physical parameters. The only difference between each simulation is the resolution. This allows us to study the convergence of the method as well as the numerical dissipation of the algorithm. For each simulation, we prescribe the initial radial magnetic field in vacuum. We set the other components and the electric field to zero. At $t = 0$, we enforce the rotation of the star from $0 \longrightarrow \Omega$, this procedure is instantaneous. It is also possible to ramp up the angular velocity with time up to the wanted Ω. We chose the instantaneous maximal rotation to reduce the integration time of the simulation. The numerical setup corresponds to a millisecond pulsar ($P = 1$ms) with a magnetic field at the surface $B_\star = 5\times10^5$ G. The strength of the magnetic field does not fit within the range of magnetic field associated with pulsars, but is sufficient to reach a quasi-force-free regime. This is not an issue for this setup as we want to study the numerical side of the method and not its physical one. The full set of parameters is summarised in Table 5.1.

For these simulations, we use a logarithmic spacing in the radial direction and a linear one in the azimuthal direction. An example of such grid is shown in Fig. 5.8a. Regarding the boundary conditions, they are different for the fields and for the particles. At the inner

Physical parameters	Values
Neutron star radius	$r_\star = 10$ km
Spin period	$P = 1$ ms
Light cylinder radius	$R_{\rm LC} = 5r_\star$
Surface magnetic field	$B_\star = 5 \times 10^5$ G
Numerical parameters	**Values**
# grid cells (r, θ)	(1024×1024) , (2048×2048) , (4096×4096)
Radial log-grid	$r \in \left[r_\star, \frac{10}{3} R_{\rm LC}\right]$
Azimuthal linear-grid	$\theta \in [0, \pi]$
Absorbing layer radius	$r_{\rm abs} = 3R_{\rm LC}$
FFE-PIC domain boundary	$\Psi_0 = \Psi_\star$

TABLE 5.1: Physical and numerical parameters of the validation setup.

boundary, the magnetic field is set to the Michel solution and the electric field sets the corotation of the star with

$$\mathbf{E}_\star = -\frac{(\mathbf{\Omega} \times \mathbf{r}_\star) \times \mathbf{B}}{c}. \tag{5.24}$$

For this simulation, the inner boundary injects corotating electrons and positrons in the simulation. The momentum of the injected particles is set to zero in the poloidal direction. The inner boundary constantly supplies the Goldreich-Julian density for both leptons and the electric field dictates how many particles are injected in the simulation per timestep. At the outer boundary, we use a perfectly matched layer (PML) (see Fig. 5.8b) to mimic an opened boundary. The layer damps the fields to zero to avoid possible reflections at the edge of the box. Any particle entering this perfectly matched layer is deleted from the simulation. There is a small chance that when the particles are deleted, they leave behind a small fraction of their electric charge. This could add some small fluctuations on the pml boundary. The final boundary conditions are at the poles. There, we use a symmetrical conditions for the fields and a reflective condition for the particles. The latter are elastically reflected on the boundary.

For the hybrid part of the simulation, we need to define the various force-free and PIC regions. In this experiment, we cut the box at the equator for $\theta = \pi/2$. With this decomposition, we have one hemisphere described in PIC and the other one in force-free. We can thus, study the behaviour of the method in each individual domain or in its entirety. To have this transition, we define the magnetic flux boundary to be

$$\Psi_0 = \Psi_{\rm M}\left(\theta = \frac{\pi}{2}\right) = \Psi_\star \tag{5.25}$$

This setup does not contain a transition layer at the equator. As we will see in the next section, when the resolution increases we have smoother gradients between the cells. The direct consequence is a gradual adjustment of the solution at the interface, where the numerical discontinuity is located. For the PIC hemisphere, we continuously inject a plasma of electron-positron pairs from the neutron star surface. The multiplicity of the injected

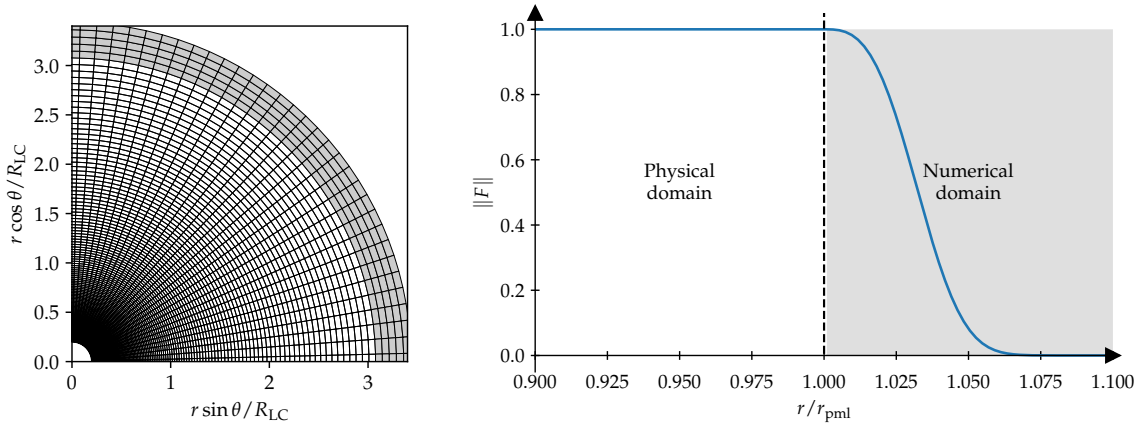

(A) (B)

FIGURE 5.8: A) Example of a spherical grid with a logarithmic spacing in r and constant in θ. The grey region indicates the perfectly matched layer. B) Perfectly matched layer applied on the field component F.

plasma is $\kappa_{inj} = 10$, this high multiplicity ensures that the force-free state is reached. This simulation does not consider pair creation or ions.

5.3.3 Validation of the simulation

To validate the FFE-PIC method, we must pass three checkpoints: (i) the structure of the magnetosphere is a monopole, (ii) the current density of the simulation matches the analytical expression, (iii) the Poynting flux of the simulation corresponds to the analytical Poynting flux.

Magnetospheric structure

For the moment, we only show results from the simulation with the highest resolution. The conclusions are the same for lower resolutions. In Fig. 5.9, we show the toroidal magnetic field after a time integration of about two periods.
We remind that this component is not present at the beginning of the simulation. It is being produced self-consistently by the electric field emerging from the rotation. We recover the analytical description of the toroidal component. The first step towards the validation of the method is passed.

Current density

The next checkpoint is the current density. In Michel's solution, the current is purely radial. A map of the radial component of the current density from the simulation is shown in Fig. 5.10.

The overall description of the current density corresponds to the expected one for a monopole. We recover two hemispheres of opposite signs. The current in the PIC domain is mainly carried by electrons with the presence of some positrons near the equator, while the force-free current which is reconstructed from the electromagnetic field has the opposite sign. Figure 5.10 presents the right overall description of the current density. Nonetheless, it is more accurate to compare cuts of the current density to the analytical expression from Eq. (5.22). In Fig. 5.11, we show the profile of the current density for the three resolutions. The profiles are taken at the middle of the physical box, $r = 1.5R_{LC}$.

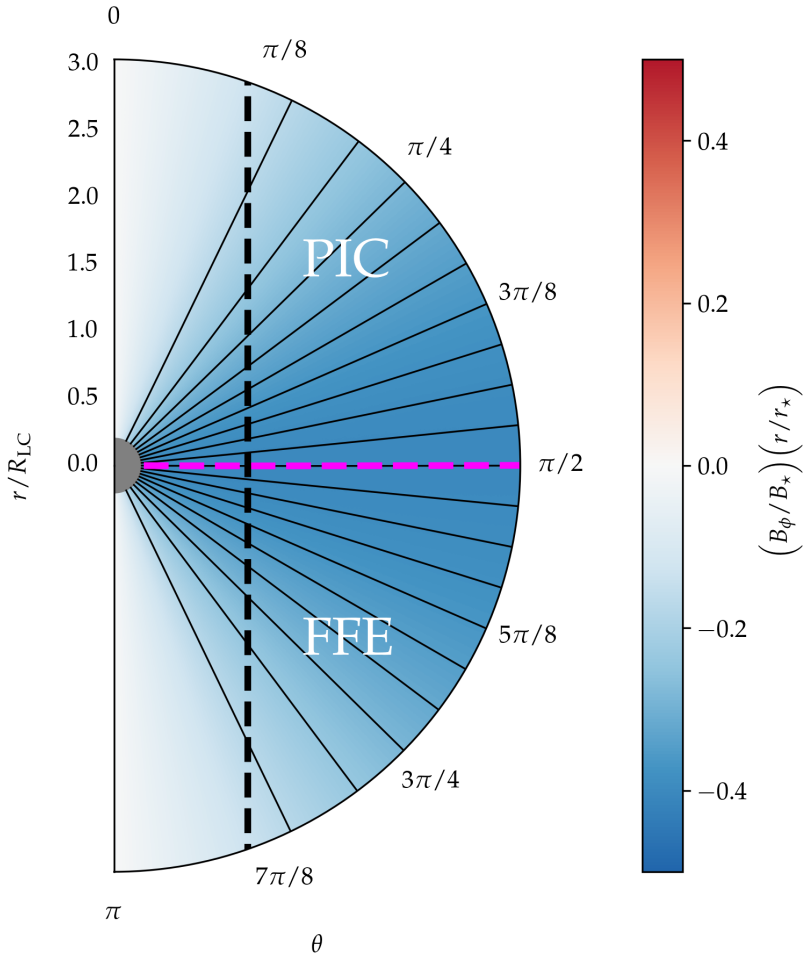

FIGURE 5.9: Map showing the toroidal component of the magnetic field. The black dashed line indicates the position of the light-cylinder, while the magenta dashed line shows the numerical domain separation.

Each profile is normalised by $J_{\rm GJ}$ and multiplied by $(r_\star/r)^2$, this procedure only keeps the cosine form (visual purpose).

The profile of each simulation matches with the predicted cosine evolution in both hemisphere. Regarding the absence of a transition layer, we note a small glitch for the lowest resolution. The match with the predicted evolution shows that the solution is well-balanced between both hemispheres. The magnetosphere as well as the interface does not show signs of net charge accumulation. The outgoing force-free current is perfectly balanced by the ingoing PIC current, no net current is present. The main difference between the PIC and force-free regions is regarding the small variations within the profiles. Contrary to force-free profiles, PIC profiles are noisy. This noise is coming from the shot noise from the finite number of particles and fast plasma oscillations.

Numerical dissipation

The last step that the simulation needs to pass is regarding the Poynting flux. A great benefit of using Michel's solution is the constant value of the Poynting flux. Since the solution is dissipation-free, any divergence from the analytical value corresponds to an estimation of the dissipation of the numerical scheme. This estimation is mostly true for the force-free domain as the PIC region can physically dissipate (e.g. gaps). In Fig. 5.12, we

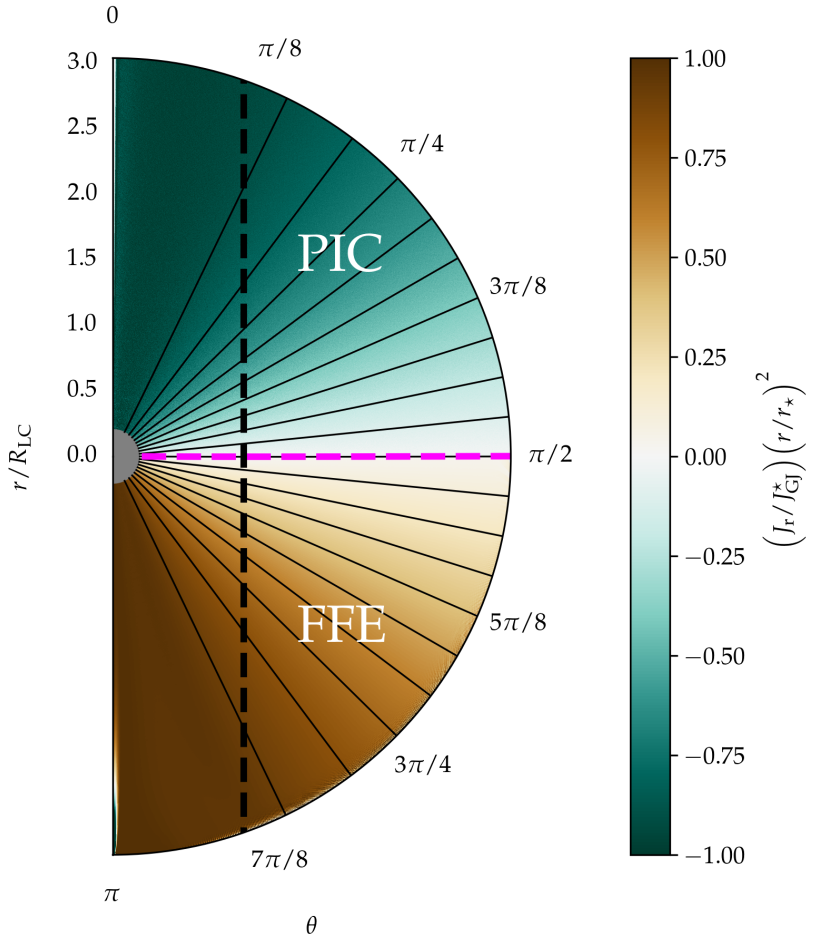

FIGURE 5.10: Spatial distribution of the hybrid radial current density normalised to the fiducial current density, $J^{\star}_{\rm GJ}$, and compensated by $(r/r_{\star})^2$ for visualisation purposes, for the 4096^2 cells run. The division between the force-free and the PIC domains is the equatorial plane (dashed magenta line). Solid lines show the poloidal magnetic field lines.

show the Poynting flux evaluated for the three resolutions. Each curve corresponds to the Poynting flux of the associated simulation which is averaged over one period ($t \in [2, 3]\, P$) when a steady state is achieved.

We see right away that the Poynting flux is not perfectly conserved for all radii but is still close to the analytical value. Thus, we can measure the amount of numerical dissipation of the method. The rate of dissipation is computed as

$$\epsilon_{\rm diss} = \frac{|L_{\rm in} - L_{\rm out}|}{L_{\rm out}} \tag{5.26}$$

where $L_{\rm in}$ is the Poynting flux averaged in the $r \in [r_{\star}, 2\,r_{\star}]$ interval, and $L_{\rm out}$ is averaged over the $r \in [2R_{\rm LC}, 3R_{\rm LC}]$ interval (grey intervals in Fig. 5.12). We observe numerical convergence with a numerical dissipation decreasing with increasing resolution. The error is always small and varies between $\epsilon_{\rm diss} < 1\%$, for the lowest resolution $(1024)^2$, and $\epsilon_{\rm diss} \sim 0.15\%$ for the highest resolution. We note that the main origin of the numerical dissipation is associated with the force-free hemisphere, this is shown in Fig. 5.13.

The deviation of the force-free hemisphere is stronger than for the PIC one. This indicates that the force-free scheme is numerically more dissipative. The conclusion from this

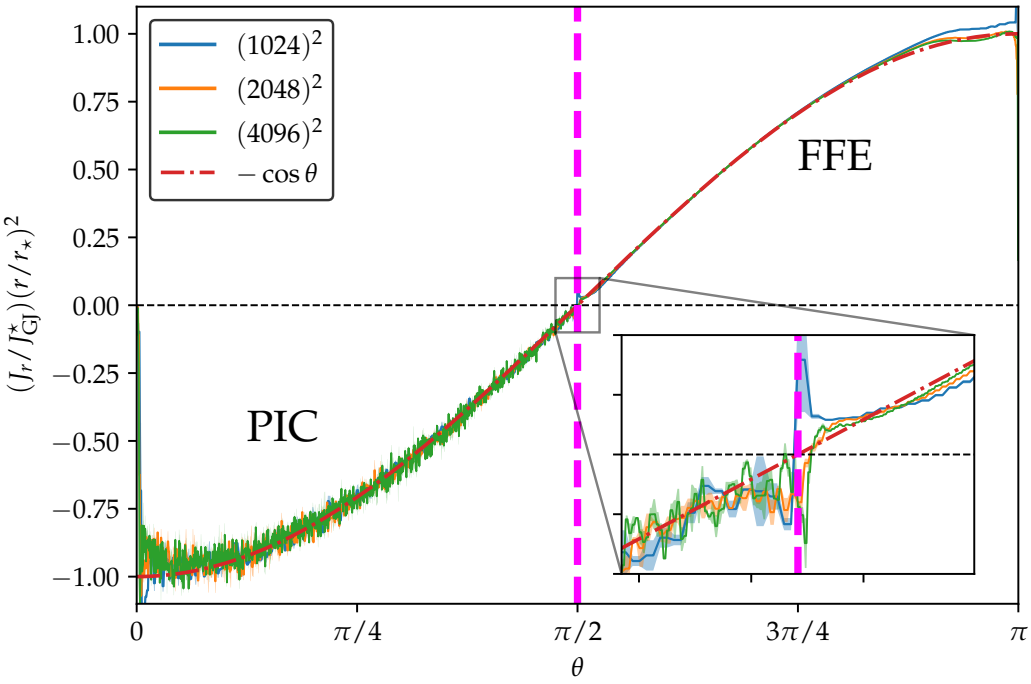

FIGURE 5.11: Cross-section of the hybrid current density profile at $r = 1.5R_{\rm LC}$ as a function of the numerical resolution, and comparison with the exact profile (red dashed-dotted line, Eq. 5.22). The dashed magenta line is the interface between force-free and PIC domains.

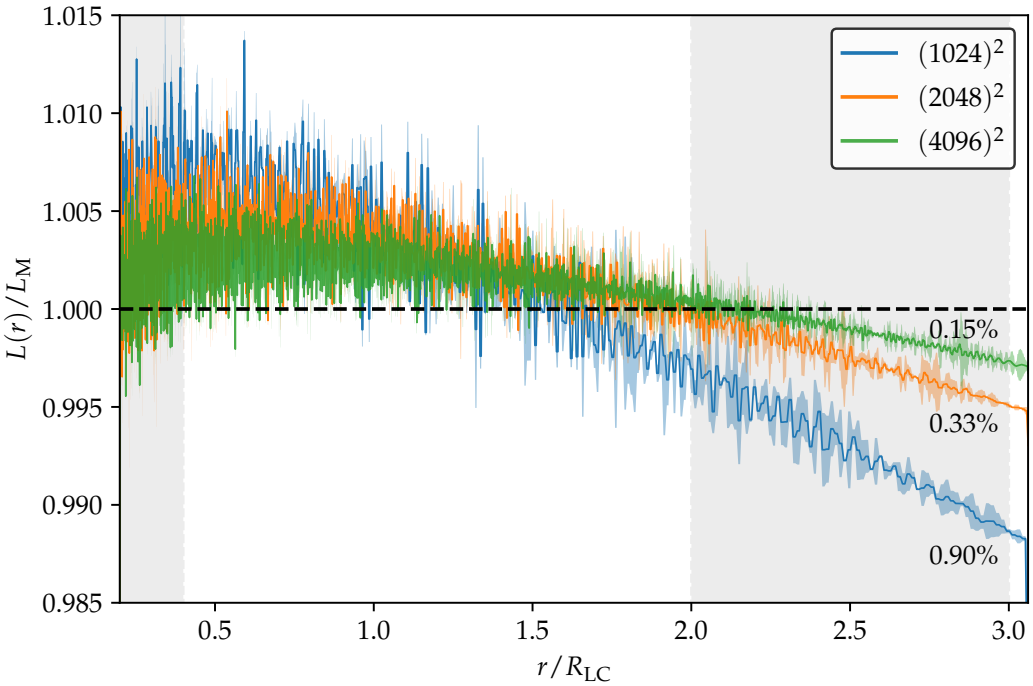

FIGURE 5.12: Radial profiles of the Poynting flux, $L(r)$, normalised to the monopole solution, $L_{\rm M}$ (Eq. 5.23), for all three resolutions. Percentages correspond to the amount of numerical dissipation for each run, computed between the flux averaged in the grey areas.

study on the numerical dissipation is that: the hybrid method suffers from small numerical dissipation, however, any dissipation larger than $\epsilon_{\rm diss}$ (for a given resolution) will have a

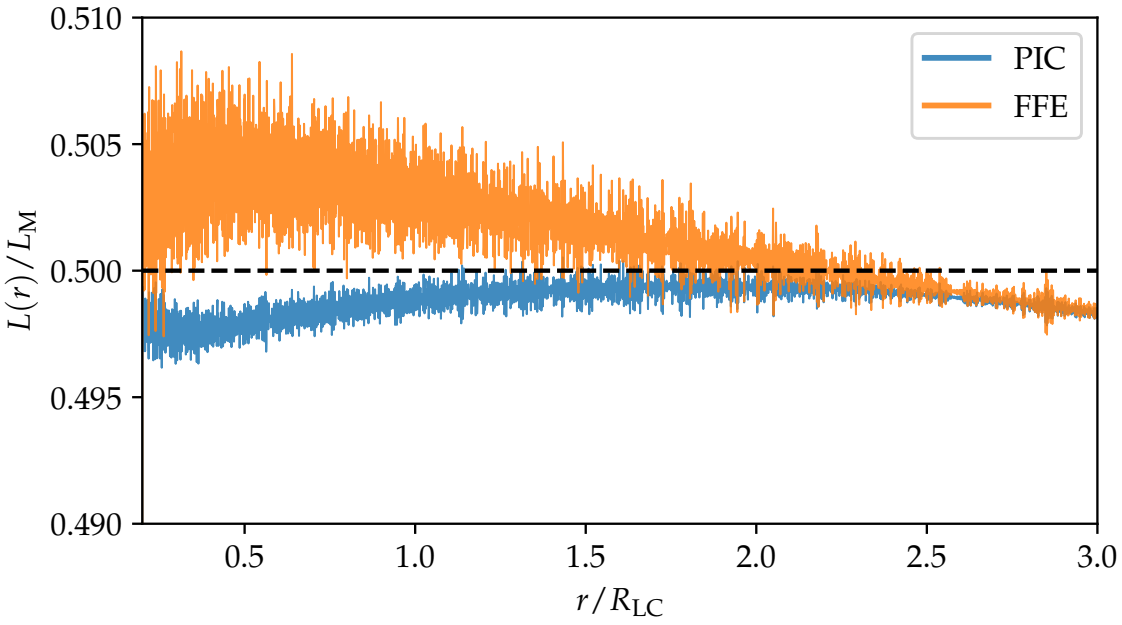

FIGURE 5.13: Radial Poynting flux of each hemisphere. The blue curve corresponds to the PIC hemisphere and the orange one to the force-free hemisphere for the $(4096)^2$ run.

physical origin.

5.4 Summary

In this chapter, I have described the full process behind the development of the force-free-PIC approach. The first step was to develop a new force-free module which could be used in the framework of the ZELTRON PIC code. Once the implementation was done, the force-free-PIC approach could start. During development of a hybrid approach, one has to answer two questions: How do I couple the two approaches? and What criterion do I use to distinguish which method needs to be used? In the force-free-PIC method, the coupling is done on the current density. Each numerical method computes its own current separately. Once this is done, the blending of the currents is performed by using a blending function. To build the latter, we must answer the second question. For pulsar magnetospheres, the easiest way was to use the magnetic flux function which isocontours highlight the magnetic field lines. The magnetic topology of these magnetospheres is well understood thanks to the previous studies. Therefore, we can use this topology at our advantage to build the blending function. The user decides at which field lines the change of numerical approach is done, and he must also give the thickness of the transition layer. It is imperative to consider this layer in the simulations so that the two methods can "speak" to each other and smoothly transition.

To validate the method, I performed a set of simulations of a Michel monopole. This solution is analytic and is a do or die test for the method. In these simulations, each hemisphere is modelled by one method and the transition between them occurs at the equator. This set of simulations uses different resolutions in order to make a convergence study on the method. As a result, I find that the azimuthal profile of the current density of the full set of simulations is in agreement with the analytic expression. The structure of the

magnetosphere is also coherent with the monopole magnetic configuration. The particularity of the Michel solution is that it is dissipation free, meaning that the Poynting flux is constant. With the convergence test, I estimated the amount of numerical dissipation from the method. The maximum dissipation observed is approximately 1% and decreases with a higher resolution, as expected. The force-free scheme occurs to have a numerical dissipation higher than the PIC method. This conclusion is based on the computation of the dissipation is each hemisphere and thus, corresponds to each method.

With all the above steps validated, we were confident enough to move to the application of the hybrid approach to a physical case: the aligned rotator.

5.5 [Français] Points clés du chapitre

Dans ce chapitre, j'ai décrit l'ensemble du processus de développement de l'approche sans-force-PIC. La première étape a consisté à développer un nouveau module sans-force qui pourrait être utilisé dans le cadre du code PIC ZELTRON . Une fois l'implémentation terminée, l'approche sans-force-PIC a pu être mise en œuvre. Lors du développement d'une approche hybride, il faut principalement répondre à deux questions : Comment coupler les deux approches ? et quel critère dois-je utiliser pour déterminer la méthode à appliquer dans une région donnée ? Dans la méthode sans-force-PIC, le couplage se fait via la densité de courant. Chaque méthode numérique calcule séparément sa propre densité de courant. Une fois cela fait, la fusion des courants est réalisée à l'aide d'une fonction de mélange. Pour construire cette dernière, nous devons répondre à la deuxième question. Pour les magnétosphères de pulsars, le plus simple était d'utiliser la fonction de flux magnétique, dont les isocontours mettent en évidence les lignes de champ magnétique. La topologie magnétique de ces magnétosphères étant bien comprise grâce aux études précédentes, nous pouvons donc utiliser cette topologie à notre avantage pour construire la fonction de mélange. L'utilisateur détermine à quelles lignes de champ le changement d'approche numérique s'effectue et il doit également définir l'épaisseur de la couche de transition. Il est impératif de prendre en compte cette couche dans les simulations afin que les deux méthodes puissent échanger les informations entre elles et que la transition se fasse en douceur.

Pour valider la méthode, j'ai effectué une série de simulations d'un monopôle de Michel. Cette solution est analytique et constitue un test important pour la méthode. Dans ces simulations, chaque hémisphère est modélisé par une méthode et la transition entre les deux méthodes s'effectue à l'équateur. Cette série de simulations utilise différentes résolutions afin d'étudier la convergence de la méthode. En conséquence, j'ai constaté que le profil azimutal de la densité de courant de l'ensemble des simulations est en accord avec l'expression analytique. La structure de la magnétosphère est également cohérente avec la configuration magnétique monopolaire. La particularité de la solution de Michel est qu'elle est exempte de dissipation, ce qui signifie que le flux de Poynting est constant. Grâce au test de convergence, j'ai pu estimer la quantité de dissipation numérique introduite par la méthode. La dissipation maximale observée est d'environ 1% et diminue avec une résolution plus élevée, comme attendu. Le schéma sans-force semble présenter une dissipation numérique plus élevée que la méthode PIC. Cette dernière conclusion est fondée sur le calcul de la dissipation dans chaque hémisphère, correspondant donc à chaque méthode.

Avec toutes les étapes ci-dessus validées, nous pouvons avoir suffisamment confiance en la méthode pour passer à l'application de l'approche hybride à un cas physique : le rotateur dipolaire aligné.

CHAPTER 6

Pulsar magnetosphere: Aligned rotator

Contents

The time has come to use the force-free-PIC approach in an astrophysical context. In this chapter, we aim at modelling a weak millisecond pulsar within the *Fermi*-LAT detection range, in order to produce the first realistic pulsar magnetosphere. In Sect. 6.1, we will compute the different scales that we need to reach for the targeted pulsar. In Sect. 6.2, we will give the numerical parameters of the fiducial simulation. Section 6.3 will provide the different results of the weak millisecond pulsar simulation. In Sect. 6.4, we will address the effect of rescaling PIC simulations to smaller system sizes. Finally, we will show in Sect. 6.5 that the simulations presented here have numerically converged before summarising the results in Sect. 6.6. This chapter is partly adapted from my paper "Scaling up global kinetic models of pulsar magnetospheres using a hybrid force-free-PIC numerical approach" accepted in *Astronomy & Astrophysics* (Soudais et al., 2024).

6.1 Scale separation

We presented the micro and macro-scales of the problem previously for a canonical pulsar, we will now translate these scales to our targeted pulsar. For the simulation, we set the two main pulsar parameters, P and $B_\star$, to $P = 1\,\mathrm{ms}$ and $B_\star = 10^7\,\mathrm{G}$. In terms of spindown power, this corresponds to

$$L_0 = \frac{\mu^2\Omega^4}{c^3} = 4.8\times10^{33}\,\mathrm{erg.s^{-1}}\left(\frac{B_\star}{10^7\,\mathrm{G}}\right)^2\left(\frac{P}{1\,\mathrm{ms}}\right)^{-4}. \tag{6.1}$$

This value corresponds to one of the weakest gamma-ray pulsar reported by the *Fermi*-LAT, see Fig. 1.8 from Chapt. 1. For the smallest scales, the relevant limit is set by the electronic skin depth at the stellar surface. With the previous parameters, the skin-depth is

$$\begin{aligned} d_\mathrm{e}^\star &= \sqrt{\frac{\gamma m_\mathrm{e}c^2}{4\pi n_\star e^2}} \\ &\approx 2\left(\frac{\gamma}{10^0}\right)^{1/2}\left(\frac{\kappa}{10^2}\right)^{-1/2}\left(\frac{P}{1\mathrm{ms}}\right)^{1/2}\left(\frac{B_\star}{10^7\mathrm{G}}\right)^{-1/2}\mathrm{cm}, \end{aligned} \tag{6.2}$$

where the number density of the plasma is $n_\star = \kappa n_\mathrm{GJ}^\star$. This density is proportional to the fiducial Goldreich-Julian density presented in Sect. 2.1.2. If we compare this scale to the star, we end up with $d_\mathrm{e}^\star/r_\star = 2\times10^{-6}$. This value is large even for the weakest pulsar considered here. However, as we introduced earlier, particles are not extracted from the crust of the star at rest. They have a non-zero Lorentz factor thanks to the parallel electric field at the surface. The maximum Lorentz factor a particle can reach, is given by the vacuum potential drop across the polar cap. We remind that such potential drop is expressed as

$$\Phi_\mathrm{pc} = \frac{\mu\Omega^2}{c^2}. \tag{6.3}$$

An electron experiencing this potential would acquire a Lorentz factor

$$\gamma_\mathrm{pc} = \frac{e\Phi_\mathrm{pc}}{m_\mathrm{e}c^2} \approx 2.6\times10^8\left(\frac{B_\star}{10^7\mathrm{G}}\right)\left(\frac{P}{1\mathrm{ms}}\right)^{-2}. \tag{6.4}$$

Therefore, we can compute an upper limit for the electronic skin depth,

$$d_\mathrm{e}^\star\left(\gamma_\mathrm{pc}\right) \approx 3\times10^4\left(\frac{\gamma}{\gamma_\mathrm{pc}}\right)^{1/2}\left(\frac{\kappa}{10^2}\right)^{-1/2}\left(\frac{P}{1\mathrm{ms}}\right)^{1/2}\left(\frac{B_\star}{10^7\mathrm{G}}\right)^{-1/2}\mathrm{cm}. \tag{6.5}$$

This value is attractive but it only represents an upper limit for the size of the skin depth. As we saw in Sect. 2.2.4, pair production is occurring close to the surface of the star. Therefore, a more realistic Lorentz factor to consider would be the energy of secondary leptons. The detailed mechanism for pair creation is given in Sect. 2.2.2. Assuming magnetic conversion, the pair production energy scales for our pulsar parameters are: the threshold Lorentz factor,

$$\gamma_\mathrm{th} = \sqrt{\frac{1}{15b^2}} \approx 10^6\left(\frac{B_\star}{10^7\mathrm{G}}\right)^{-1}, \tag{6.6}$$

and the secondary Lorentz factor,

$$\gamma_{\rm s} = \frac{1}{20b} \approx 2.2 \times 10^5 \left(\frac{B_\star}{10^7 {\rm G}}\right)^{-1}. \tag{6.7}$$

This last value for the Lorentz factor is more realistic for the bulk of the extracted particles than the polar cap one. The skin depth and scale separation then become

$$d_{\rm e}^\star(\gamma_{\rm s}) \approx 10^3 \left(\frac{\gamma}{\gamma_{\rm s}}\right)^{1/2} \left(\frac{\kappa}{10^2}\right)^{-1/2} \left(\frac{P}{1{\rm ms}}\right)^{1/2} \left(\frac{B_\star}{10^7 {\rm G}}\right)^{-1/2} {\rm cm} \tag{6.8}$$

$$\frac{d_{\rm e}^\star(\gamma_{\rm s})}{r_\star} \approx 10^{-3} \tag{6.9}$$

This scale separation directly appears more tractable if we assume that pair production is vigorous enough to fill the magnetosphere with a high multiplicity, $\kappa \gg 1$. Pair production via QED processes also put constraints on the magnetic field strength. In fact, we can derive the minimum magnetic field required to have pair production by equating Eq. (6.4) and (6.6). The lowest magnetic field is

$$B_\star = \sqrt{\frac{25}{\sqrt{15}} \frac{B_{\rm QED} m_{\rm e} c^2}{e r_\star}} \gtrsim 7 \times 10^5 \, {\rm G}. \tag{6.10}$$

Any pulsar with a surface magnetic field lower than the above value cannot develop a pair cascade. Below this value, the threshold for pair production becomes larger than the maximum Lorentz factor achievable at the surface. This is a hard floor as this is for an electron experiencing the full potential drop, which is rather exceptional.

Another scale appears more tractable if we go further from the star, and look at the light-cylinder. We presented in Sect. 2.2.5 the relativistic reconnection process. The thickness, δ, of the current sheet is set by the electronic skin depth at the light-cylinder, $d_{\rm e}^{\rm LC}$. However, during magnetic reconnection at the light-cylinder, particles are accelerated to Lorentz factors of values similar to the magnetisation. The magnetisation and thickness of the current are expressed as

$$\gamma_{\rm LC} \sim \sigma_{\rm LC} = \frac{B_{\rm LC}^2}{4\pi \Gamma_{\rm LC} \kappa n_{\rm GJ}^{\rm LC} m_{\rm e} c^2} = \frac{\gamma_{\rm pc}}{2\Gamma_{\rm LC}\kappa}, \tag{6.11}$$

$$\delta \sim d_{\rm e}^{\rm LC}(\gamma_{\rm LC}) = \sqrt{\frac{\gamma_{\rm LC} m_{\rm e} c^2}{4\pi\kappa\Gamma_{\rm LC} n_{\rm GJ}^{\rm LC} e^2}} = \frac{R_{\rm LC}}{2\Gamma_{\rm LC}\kappa}, \tag{6.12}$$

where $\Gamma_{\rm LC}$ is the bulk Lorentz factor of the pulsar wind. We remind that the strength of the magnetic field is evaluated at the light-cylinder as $B_{\rm LC} = B_\star \left(r_\star / R_{\rm LC}\right)^3$. In terms of values, the thickness of the current layer is

$$\delta \sim 2.4 \times 10^4 \left(\frac{\Gamma_{\rm LC}}{10^0}\right)^{-1} \left(\frac{\kappa}{10^2}\right)^{-1} \left(\frac{P}{1{\rm ms}}\right) {\rm cm}, \tag{6.13}$$

this corresponds to a scale separation of

$$\frac{\delta}{r_\star} \sim 2 \times 10^{-2} \qquad \frac{\delta}{R_{\rm LC}} \sim 5 \times 10^{-3}. \tag{6.14}$$

With these considerations, the scale separation of the current layer is an order of magnitude larger than the scale separation at stellar surface (Eq. 6.9). Therefore, the scale separation at the light-cylinder appears more tractable in terms of resolution with realistic

parameters. This region is the one of interest in this work because it is a great site of acceleration and thus, of gamma-ray emission.

The last technical part on the scale separation is regarding the radiative cooling, set by the radiation-reaction-force. From Sect. 3.3.5, we recall that this force acts as a continuous drag force to balance the accelerating electric force. Equation-wise, it translates in $eE_{\parallel} \sim F_{\rm rad}$. In the ultra-relativistic regime ($\gamma \gg 1$), the radiation-reaction-force from Eq. (3.95) can be approximated by

$$F_{\rm rad} \approx \frac{2}{3} r_{\rm e}^2 \gamma^2 B_{\perp}^2. \tag{6.15}$$

Thus, we can deduce the "radiation-reaction-limited" electron Lorentz factor,

$$\gamma_{\rm rad} = \sqrt{\frac{3eE_{\parallel}}{2r_{\rm e}^2 B_{\perp}^2}}. \tag{6.16}$$

The Lorentz factor values at the surface and light-cylinder are respectively

$$\gamma_{\rm rad} \approx 3 \times 10^4 \left(\frac{E_{\parallel}}{B_{\perp}}\right)^{1/2} \left(\frac{B_{\perp}}{10^7 \rm G}\right)^{-1/2} \qquad \gamma_{\rm rad}^{\rm LC} \approx 3.3 \times 10^5 \left(\frac{E_{\parallel}}{B_{\perp}}\right)^{1/2} \left(\frac{B_{\perp}}{B_{\rm LC}}\right)^{-1/2} \tag{6.17}$$

The radiation-reaction-limited Lorentz factor at the light-cylinder stands precisely between the secondary energy and the threshold energy. Physically speaking, the particles will accelerate up to $\gamma_{\rm rad}$. If the acceleration pushes the particles above this critical Lorentz factor, they will radiate their energy away and will never reach the pair creation threshold. However, the current sheet is able to break this behaviour and is an active site for pair production. In the current layer, the magnetic field goes to zero and the parallel electric field is strong. The radiation-reaction becomes weaker and particles are able to accelerate above $\gamma_{\rm rad}$ until they reach $\gamma_{\rm th}$ and pair production occurs.

We now have all the different physical and energetic scales to fully constrain our fiducial pulsar. We emphasise that the various energy and spatial scales are derived in the case of a weak millisecond pulsar, where $P = 1\,$ms and $B_\star = 10^7\,$G. Firstly, for the spatial scales

$$\frac{d_{\rm e}^{\rm s}}{r_\star} \sim 10^{-3} \ll \frac{\delta}{r_\star} \sim 2.5 \times 10^{-2} \ll 1 < \frac{R_{\rm LC}}{r_\star} = 5, \tag{6.18}$$

where all scales are normalised by the pulsar radius $r_\star$. Secondly, regarding the energy scales

$$\frac{\gamma_{\rm s}}{\gamma_{\rm pc}} \sim 8.5 \times 10^{-4} < \frac{\gamma_{\rm rad}^{\rm LC}}{\gamma_{\rm pc}} \sim 10^{-3} < \frac{\gamma_{\rm th}}{\gamma_{\rm pc}} \sim 4 \times 10^{-3} \ll 1, \tag{6.19}$$

where the energy scales are normalised by the full potential drop energy $\gamma_{\rm pc}$. The two scales derived above do not apply for all pulsar parameters. One should verify all these scales whenever one of the pulsar parameters is modified. One noticeable fact is that the gap between the spatial scale is roughly one or two orders of magnitude while the energy gaps are quite narrow in the pair cascade and cooling.

6.2 Numerical setup

6.2.1 Initial and boundary conditions

The simulation is initialised with a dipolar magnetic field in a box empty of plasma. The initial magnetic field is set by the magnetic flux function

$$\Psi_{\rm D} = \frac{\mu \sin^2\theta}{r}. \tag{6.20}$$

At the inner boundary, we have two constraints for the fields. First, the magnetic field verifies the dipolar field at the surface. Second, the star is put in corotation by setting the initial electric field

$$\mathbf{E}_\star = -\frac{(\mathbf{\Omega} \times \mathbf{r}_\star) \times \mathbf{B}}{c}. \tag{6.21}$$

Regarding the plasma inner boundary, the simulation is allowed to extract both electrons and ions. Injected particles are in corotation with the star, but do not have poloidal momentum. In the simulation, ions are actually protons as the mass-ratio is set to the full value, $m_{\rm p} = 1836 m_{\rm e}$. This is the first time that a global magnetosphere simulation uses the full mass ratio. All previous studies used a reduced mass ratio of at most $m_{\rm p} = 20 m_{\rm e}$. The number density available at the inner boundary for each species is always equal to the Goldreich-Julian number density, $n^\star_{\rm GJ}$. The number of particles injected from the surface at each timestep is set by the requirements given by the surface electric field. The latter extracts the different charges and accelerates them to high Lorentz factors. In a realistic system, the accelerated electrons can emit photons responsible for pair production. The simulation does consider the pair creation mechanism but with a highly simplified mechanism. We use the energy threshold from Eq. (6.6) above which a lepton is able to pair produce. We do not model photons in the simulation, we make the assumption that pair creation occurs on-the-spot where the parent lepton has reached an energy above the threshold. The created leptons have a momentum aligned with the parent's one and a Lorentz factor $\gamma_{\rm s}$. In the simulation, pair creation can occur anywhere in the magnetosphere. This is an important assumption which can have an impact on the description of the magnetosphere.

For the outer boundary, we perform again two treatments related to the physical nature of the incoming quantity. For fields, we use the same absorption layer described in Sect. 5.3.2. For particles, we set their weight to zero whenever they enter the numerical layer. The axial boundary conditions are also identical to the monopole simulation, reflective for particles and symmetric for the fields.

The last boundary conditions needed are related to the hybrid method itself. We need to place the PIC domain around the separatrix and current sheet. However, from the initial dipole state, we do not know precisely where the current sheet and separatrix will form. The hybrid boundaries locations are educated from previous studies in which we focused on the magnetic topology. Theoretically, the separatrix emerges at the polar cap angle-size $\theta_{\rm pc}$, see Sect. 2.2.1. At this angle, we can compute the theoretical polar cap magnetic flux function $\Psi_{\rm pc}$ associated to a dipole in vacuum. We use this specific scale as a reference in the method, which is a good approximation even for a force-free dipole. Based on a trials

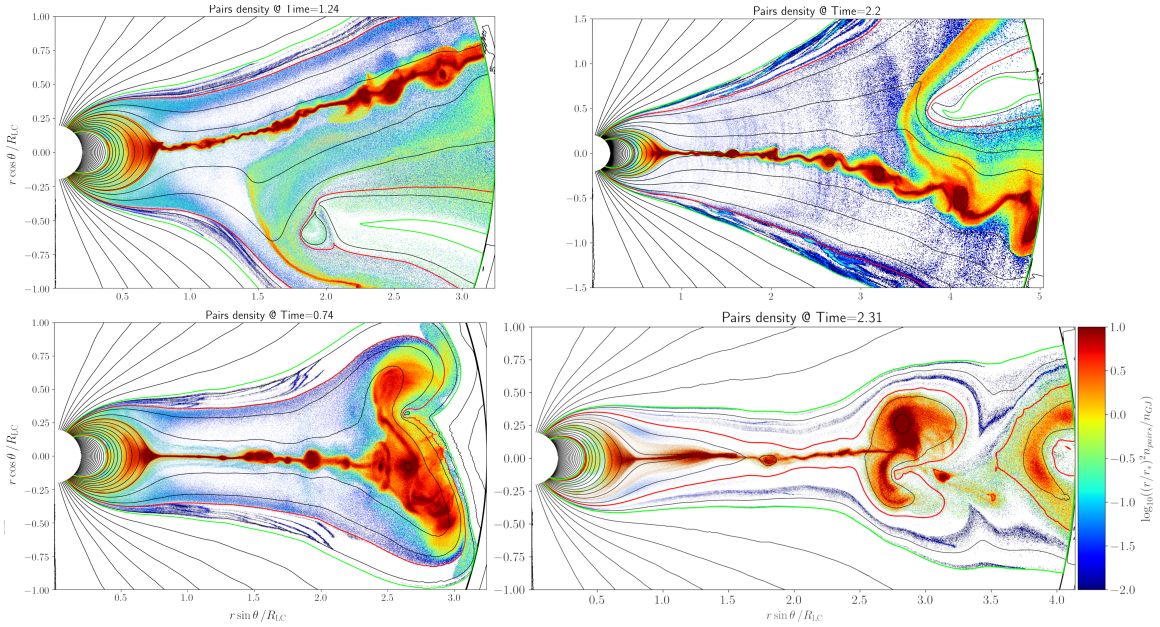

FIGURE 6.1: "Dead" simulations. The top row show the issue of the "force-free bubbles". The bottom left panel highlights the issue during the transient. Bottom right panel shows a simulation where the boundary in red reconnects.

and errors method, we ended with the following set of boundaries:

- $0 < \Psi < 0.9\Psi_{\rm pc}$: first force-free domain corresponding to the polar cap region
- $0.85\Psi_{\rm pc} < \Psi < 2.4\Psi_{\rm pc}$: PIC domain encapsulating the separatrix and current sheet
- $2.3\Psi_{\rm pc} < \Psi < \Psi_{\rm max}$: second force-free domain modelling the deep closed field line region inside the light-cylinder.

$\Psi_{\rm max} = \mu/r_\star$ is the maximum magnetic flux function. $\Psi_{\rm D}$ is maximum at the equator of the star surface, see Eq. (2.68). If the PIC domain is too large, then the method becomes useless in a sense. The simulation box will mainly contain particles and will be equivalent to a full PIC simulation. However, a too narrow PIC domain also represents an issue. If we do not give enough room to the PIC domain with respect to the separatrix, the result is a "dead" simulation. In this kind of simulation, the PIC region is not able to open the field lines completely and does not connect to the outer boundary. Even when the PIC domain extends from the pulsar surface all the way to the end of the box, it is still possible for the simulation to end in a dead regime. An example of such behaviour shown in the bottom right panel of Fig. 6.1. The particles are not able to break through the reconnected field line and are trapped in the simulation. In nature, the particles from the current sheet are advected outwards at relativistic speeds. If this does not occur in the simulation, it is a consequence of the hybrid approach, not a physical one.

The last crucial point of the hybrid boundary is its thickness. In the dipole case, the thickness of the layer appeared as a highly sensitive problem. While the inner transition layer inside the closed region always behaves as expected, it is not the case for the outer one in the wind zone. For low resolution simulations, the outer transition layer must exist to smooth out the transition. With the increase of resolution, we faced a rather disturbing conclusion. During the transient state of the simulation, the outer transition layer becomes

vertical and acts a "wall". Particles must push against this to break through the field lines. This leads to an accumulation of particles right behind the transition layer, see the bottom left panel of Fig. 6.1. Even if the particles manage to open the field lines and to connect to the PML, the simulation could end up in a dead state where "force-free bubbles" are trapped inside the PIC domain. They can also grow in size and completely disturb the magnetosphere, see the top row of Fig. 6.1. This technical issue prevented the field lines from the polar cap to open up correctly. Even with this numerical issue, the magnetosphere could sometimes achieve a quasi-steady-state but not consistently, only when the bubbles are advected outwards. The numerical issues during the transient were counterbalanced by removing the transition layer of high resolution simulations. The hybrid layer is reapplied once the opened field lines connect to the outer boundary. In the end, we found that a layer of thickness $\Delta\Psi = 0.1\Psi_{\rm pc}$ is optimum.

6.2.2 Resolution

We derived in Sect. 6.1 the various scales that must be resolved by the simulation. We fill the simulation box with 8192^2 cells, and use a logarithmic grid spacing in the radial direction and a constant one for the θ direction. The grid spans radially from $r_\star = 10^6$ cm up to $r_{\rm max} = (10/3)\, R_{\rm LC}$ where $R_{\rm LC} = 5 \times 10^6$ cm. The azimuthal grid spans from $\theta = 0$ up to $\theta = \pi$. With such grid and number of cells, the smallest cell is located at the surface of the star and has a resolution power of

$$\Delta r = 3.4 \times 10^2 \,\text{cm}. \tag{6.22}$$

We can compare this to the most constraining scale to see if it is sufficiently resolved. The comparison to the skin depth of secondary at the surface gives

$$\frac{d_{\rm e}^{\rm s}}{\Delta r} \approx 3. \tag{6.23}$$

This means that the skin depth of the secondary is captured by three cells in the simulation. More cells would be preferable to fully trust what is happening close to the surface, here we are touching the limits in terms of resolution. Given the CFL condition, the temporal resolution is fixed with the spatial resolution at a value

$$\Delta t = 4.3 \times 10^{-9} \,\text{s}. \tag{6.24}$$

We can do the same exercise as the one for the skin depth at the surface but for the electronic plasma frequency,

$$\frac{\omega_{\rm pe}^{-1}}{\Delta t} \approx 8. \tag{6.25}$$

The plasma frequency is better resolved than the skin depth at the surface but the most important fact is that both quantities are sufficiently resolved. The resolution constrains get softer as we go further from the star surface, resulting in well resolved scales after a few times the stellar radii.

With this high resolution, we also resolve the Larmor scales after the light-cylinder, especially in the equatorial current sheet. At the light-cylinder, the most constraining Larmor scales are for the secondary pairs as they have a Lorentz factor $\gamma_{\rm s}$. The Larmor radius and timescale are locally resolved by

$$\frac{r_{\rm L}}{\Delta R_{\rm LC}} = \frac{\gamma_{\rm s} m_{\rm e} c^2}{e B_{\rm LC}} \approx 3 \qquad \frac{r_{\rm L,s}}{c\Delta t} \approx 36 \tag{6.26}$$

where $\Delta R_{\rm LC} = \Delta r\, R_{\rm LC}/r_\star$ is the local spatial grid at the light-cylinder.

6.2.3 Cooling treatment

The simulation does consider cooling in the form synchrotron cooling. In the simulation, the synchrotron cooling time is well resolved with

$$t_{\rm sync}^{\rm LC} \sim \frac{3 m_{\rm e} c}{2 r_{\rm e}^2 \gamma_{\rm s} B_{\rm LC}^2} \approx 85 \Delta t. \tag{6.27}$$

However, close to the surface the cooling is stronger. This can represent a numerical issue for the particle integrator, where it cannot integrate the particle trajectory. To avoid this numerical effects near the surface, the particle pusher is modified to remove any particle momentum perpendicular to the magnetic field. This is applied at every timestep but only inside a thin shell of thickness $r_\star$. The particle pusher is not modified outside of this shell. Another manipulation is done on the cooling in the simulation to avoid the crash of the simulation. We need to reduce by hand the strength of the radiation-reaction force during the transient phase. We set the amplitude of the force to only 1% of its true value and apply it on particles during one period. During the second period, the force is slowly increased from 1% to 10%. The last step is to ramp up the force from 10% to 100% after the second period. Once the nominal force strength is reached and quasi-steady-state is achieved, the simulation becomes physically exploitable.

6.2.4 Simulation parameters

We summarise the numerical setup and different scales of the simulation in Table 6.1.

Compared to the current state-of-the-art simulation, the simulation presented here goes deeper in the physics modelled. First, the rescaling done in previous PIC studies is not applied. The size of the star and spin period are coherent with the one of neutron stars. The surface magnetic field is stronger than any previous studies. The radiation-reaction force is not modified/amplified to account for the rescaling of the magnetic field. We use protons with their real mass. The code uses cgs units and we put the true values of each parameters. The pair production threshold is based on QED estimations. This simulation is equal in terms of resolution to the work of Bransgrove et al. (2023). The scale separation modelled here is realistic for a weak millisecond pulsar.

Physical parameters	Values
Neutron star radius	$r_\star = 10$ km
Spin period	$P = 1$ ms
Surface magnetic field	$B_\star = 10^7$ G
Spindown power	$L_0 = 4.8 \times 10^{33}$erg/s
Polar cap energy	$\gamma_{\rm pc} = 2.6 \times 10^8$
Threshold energy	$\gamma_{\rm th} = 10^6$
Secondary pairs energy	$\gamma_{\rm s} = 2.2 \times 10^5$
Radiation-reaction energy	$\gamma_{\rm rad}^{\rm LC} = 3.3 \times 10^5$
Electron plasma skin depth	$d_{\rm e}^{\rm s} = 10^3$cm
Plasma timescale	$\omega_{\rm pe}^{-1} = 3.3 \times 10^{-8}$s
Synchrotron cooling time	$t_{\rm syn}^{\rm LC} = 3.6 \times 10^{-7}$s
Numerical parameters	**Values**
# grid cells (r, θ)	8192×8192
Proton to electron mass ratio	$m_{\rm p}/m_{\rm e} = 1836$
Time step	$\Delta t = 4.3 \times 10^{-9}$s
Highest spatial resolution	$\Delta r = 3.4 \times 10^2$cm
FFE domain I boundaries	$\Psi_{\rm min} = 0$, $\Psi_1 = 0.85\Psi_{\rm pc}$
PIC domain boundaries	$\Psi_0 = 0.85\Psi_{\rm pc}$, $\Psi_3 = 2.4\Psi_{\rm pc}$
FFE domain II boundaries	$\Psi_2 = 2.3\Psi_{\rm pc}$, $\Psi_{\rm max} = \mu/r_\star$

TABLE 6.1: Physical and numerical parameters for the reference weak gamma-ray pulsar hybrid force-free-PIC simulation. Energy scales refer to electron Lorentz factors.

6.3 Results

In this section, we present the result of the first simulation of a weak gamma-ray millisecond pulsar. Before giving the different results, I want to underline the fact that some features of the magnetosphere, mainly the closed region, are not fully relaxed yet. The steady-state picture of the magnetosphere could be slightly different than the one presented in the following.

6.3.1 Leptonic and proton density maps

The first result is shown in Fig. 6.3[1] and displays the pairs density. Several features are visible on the figure. Starting from the surface of the star, we see two prominent separatrices merging near the light-cylinder. The structure of the two branches between the last closed and first opened field lines is coherent with previous PIC studies, even though it might be slightly thicker in the hybrid simulation. This result should be taken with a grain of salt as the closed region still present some magnetic tension. This region is not yet in a steady-state, longer integration could show a different final state for the closed region and separatrix. However, this region is not the main focus of this work in which we focus on particle acceleration in the wind zone. The latter is physically relevant as the quasi-steady-state has been reached. At the beginning of the simulation (transient phase), the two branches of the separatrix forms a Y-point located well inside the light-cylinder. The Y-point forms at $r_Y \approx 0.6 R_{LC}$ and slowly migrates outwards, $r_Y \approx 0.95 R_{LC}$ at the final snapshot. We note that the Y-point keeps migrating radially towards the light-cylinder at the end of the simulation. The magnetic reconnection history of field lines is visible in the closed region. It is shown by the curved sawtooth pattern inside the thick separatrix, where the "tooth" are attached to reconnected field lines. Moving away from the closed region to the opened one, we enter in the wind zone. At first sight, the wind zone appears depleted of plasma outside of the equatorial plane. Some plasma depletion is expected in the region, however, our pair production model probably exaggerates this feature as photons do not have a mean-free-path. We believe that this aspect does not impact the high-energy emission of the magnetosphere. Focusing on the equatorial region, we can see a current layer emerging from the Y-point, which is where pair production starts to become efficient. The layer extends radially from the Y-point to the edge of the simulation box, it shows slight kinks and a plasmoid-chain. The kinked current sheet is a result of current-driven instabilities that were already presented in previous works (Belyaev, 2015; Cerutti et al., 2015). Near the light-cylinder, the layer is extremely thin with a thickness $\delta \sim 10^{-3} R_{LC}$. This extreme narrowest was not seen in previous PIC studies but is in agreement with the expected thickness computed in Sect. 6.1. We have reached the expected scale separation for the current sheet. To appreciate the narrowness of this layer, we give a zoomed-in view in Fig. 6.2.

The current layer does not only suffer from current-driven instabilities but also from the tearing instability. This instability leads to the formation of plasmoids. During the simulation, we observe the fragmentation of the current sheet into plasmoids of different sizes and also mergers of plasmoids. They grow from the microscopic scale up to the macroscopic one. Microscopic ($\sim$ layer-thickness) and macroscopic ($\sim$ star radius) plasmoids are showed in Fig. 6.3. These magnetic islands present internal structures in the form of concentric rings. The highest densities, with multiplicities of $\kappa \sim 10 - 100$, are at the core of the plasmoids while the rim of them shows the lowest density, with multiplicities of $\kappa \sim 1 - 10$. In Fig. 6.2, we show the bulk velocity map of electrons and positrons in the

[1] I encourage the reader to take a few minutes to look carefully at all the figures of this section to appreciate all the features captured by the high-resolution.

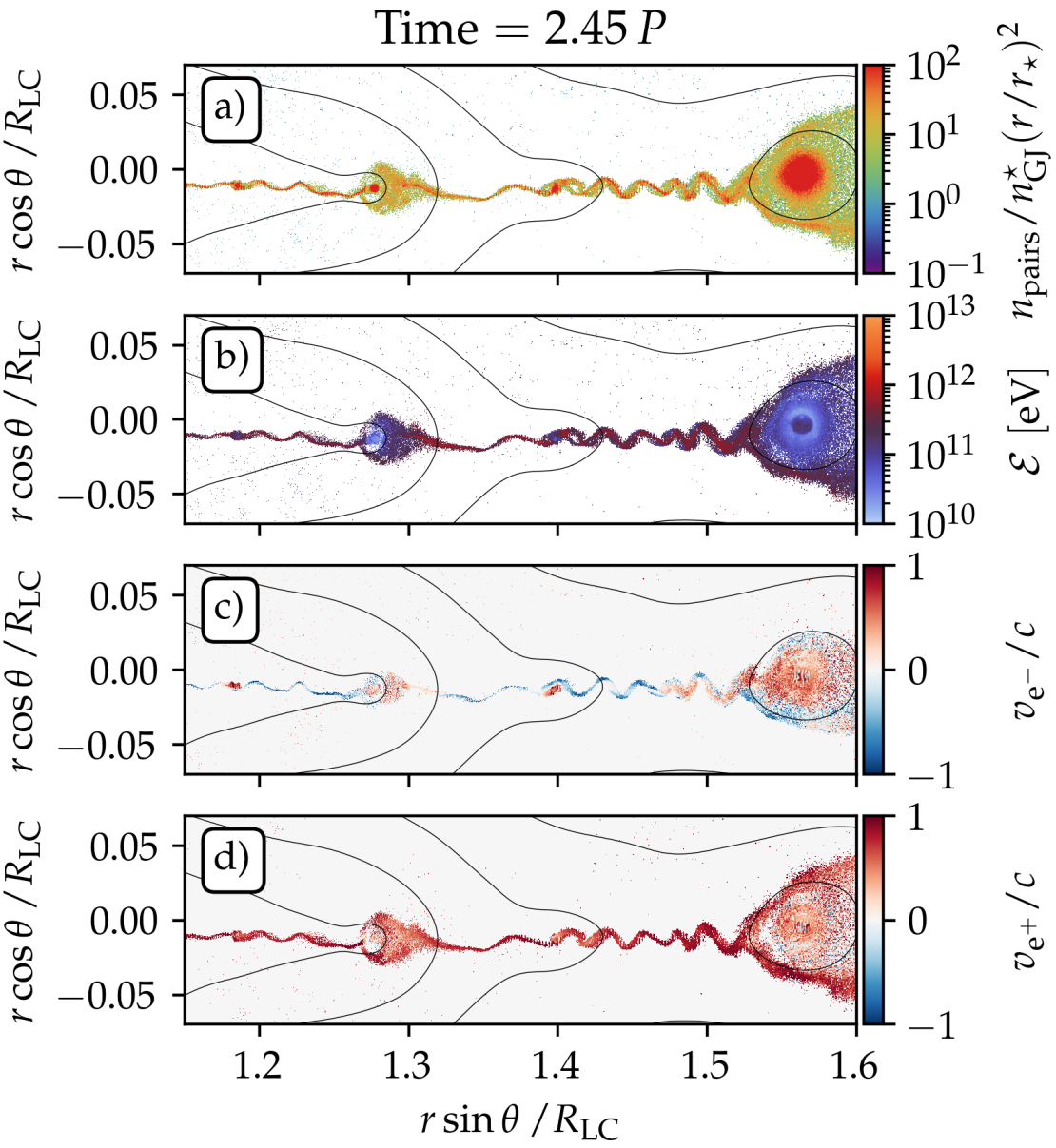

FIGURE 6.2: Zoomed-in view on the current layer. Panel *a*): Map of the pairs density to show the extreme thinness of the current layer. Panel *b*): Map of the pairs energy. Panel *c*): velocity map of electrons in the current layer. Panel *d*): velocity map of positrons in the current layer.

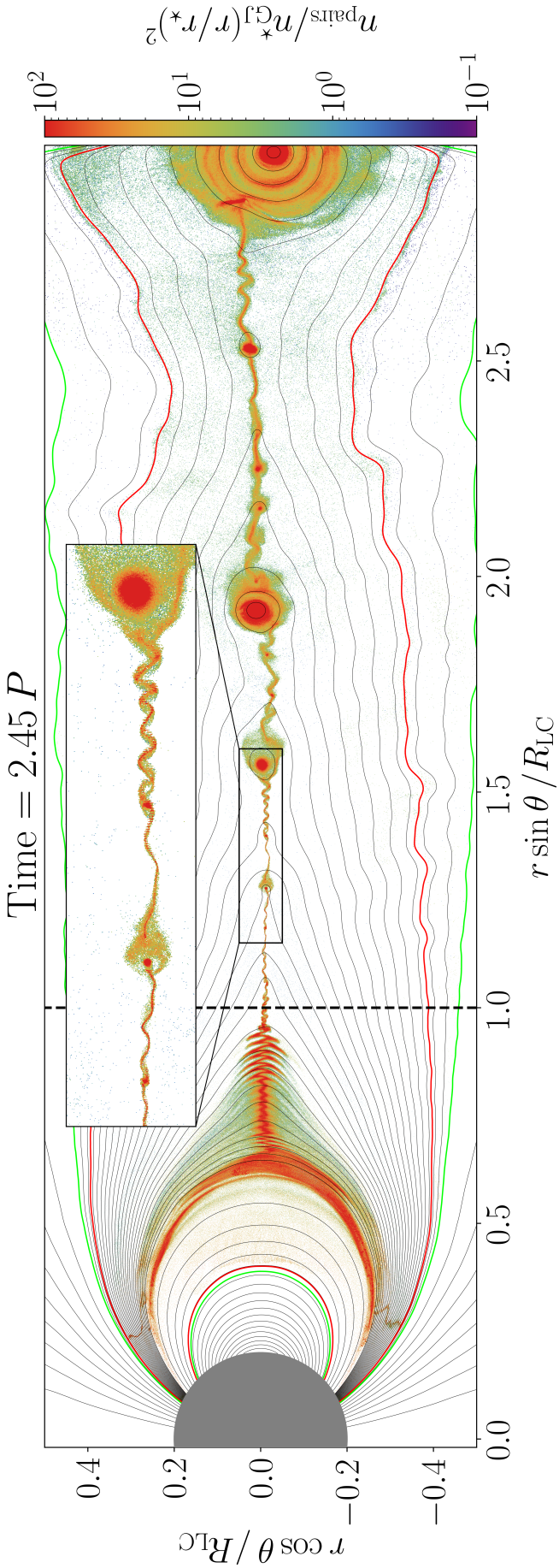

FIGURE 6.3: Snapshot of the aligned rotator using the hybrid approach at time $t/P = 3.01$. Solid black lines show the poloidal magnetic field lines, green and red solid lines show respectively the transition from region I to the PIC region and from the PIC region to region II. Map of the pairs density normalised by $n_{\rm GJ}$ and compensated by $(r/r_{\star})^2$. Light-cylinder shown by the vertical dashed black line.

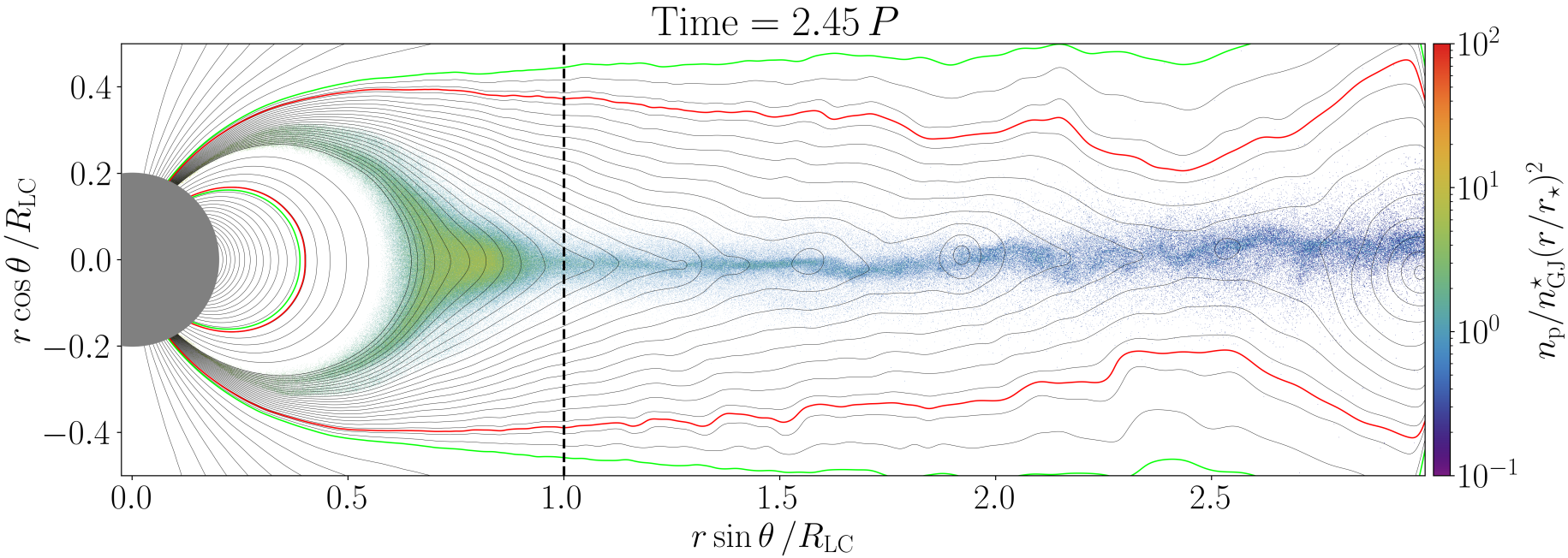

FIGURE 6.4: Snapshot of the aligned rotator using the hybrid approach at time $t/P = 3.01$. Solid black lines show the poloidal magnetic field lines, green and red solid lines show respectively the transition from region I to the PIC region and from the PIC region to region II. Map of the protons density normalised by $n_{\rm GJ}$ and compensated by $(r/r_\star)^2$. Light-cylinder shown by the vertical dashed black line.

current layer. This velocity corresponds to the reconstructed fluid velocity of each species. From this figure, we can conclude that we have two counter-streaming beams of electrons (inwards) and positrons (outwards) when magnetic reconnection is triggered at X-points. This aspect is needed to carry the return current necessary inside the magnetosphere. The counter-streaming is strong near the light-cylinder and diminishes radially. However, this is not the case for all electrons, especially those trapped in plasmoids. The latter form a "coherent" structure moving radially outwards, thus carrying electrons.

The simulation does also contain protons. In Fig. 6.4, we show the density of protons with the same normalisation and range of density as for the pairs, such that direct comparison can be made. Overall, the density of protons is at best of order unity which is low compared to the pairs density. In the closed region, protons are extracted from the surface and go along the separatrix. Then, they enter the current layer at the equator where only a small density is evacuated from the simulation. The proton beam has a thickness $\sim 0.1 R_{\rm LC}$ at the light-cylinder, which is much thicker than the current layer at the same position. Regarding the structure of the proton beam, it is not impacted by the presence of plasmoids, meaning that protons and pairs scales are perfectly decoupled. Finally, all the protons of the simulation have a positive radial velocity, they have a positron-like radial motion.

6.3.2 Particle energy maps

The main focus of this study is on particle acceleration. We want to know where particles are accelerated and the different energies probed in a magnetosphere. In Fig. 6.6, we show a map of the energy of pairs in the simulation, while in Fig. 6.7 we show the same map for protons. To allow a straightforward comparison, the same energy scale is used in both figures. In the case of pairs, the separatrix has pairs with energies around a few tens of GeV. However, when the pairs enter the current layer, they experience a strong parallel electric field. The latter accelerates pairs to high-energies around $\mathcal{E} = \gamma m_{\rm e} c^2 \sim 1$TeV. On the other end of the energy spectrum, we have plasmoids in which pairs have a low energy. The difference between the two behaviours rely on the cooling. Inside the current layer, the radiation-reaction is small because of the low strength of the perpendicular magnetic field. Therefore, pairs are able to accelerate above the radiation-reaction-limited energy $\mathcal{E}_{\rm rad} = \gamma_{\rm rad}^{\rm LC} m_{\rm e} c^2$. On the other hand, inside plasmoids, the perpendicular magnetic field is strong, meaning that pairs are cooled catastrophically. All their energy is radiated away in the form of synchrotron photons (Cerutti et al., 2013). This effect is visually impressive in Fig. 6.6 where we can see pairs accelerated deep inside the current layer losing all their energy when they enter a plasmoid. A zoomed-in view of this behaviour is shown in Fig. 6.2. Once pairs are cooled inside the plasmoid, they are not able to gain energy via plasmoid contraction or escape plasmoids to reaccelerate (Petropoulou & Sironi, 2018; Zhang et al., 2021). The acceleration timescale for a lepton corresponds to the timescale between the merge of two plasmoids.

For the protons, everything that we mentioned previously for pairs is irrelevant. They do not suffer from radiative losses, thus they are purely accelerated in the current layer as shown in Fig. 6.7. They are freely accelerated by the strong parallel electric field inside the current layer, with trajectories described by relativistic Speiser orbits. In the linear accelerator, i.e. the current sheet, protons reach energies of $\mathcal{E}_{\rm p} \approx 10$ TeV. This average energy corresponds to a significant fraction of the full polar-cap potential drop, and is in agreement with previous PIC studies (Philippov & Spitkovsky, 2018; Guépin et al., 2020). This fraction fits with the maximum energy reachable when the acceleration occurs via reconnection in a system-size limited accelerator. The typical energy for such mechanism is $\mathcal{E} \sim \beta_{\rm rec} e \Phi_{\rm pc} \approx \beta_{\rm rec} \times 130$ TeV, where the reconnection rate $\beta_{\rm rec}$ is between $10 - 20\%$.

6.3.3 High-energy signature

We have seen in Sect. 6.3.1 and 6.3.2 the global structure of the magnetosphere, the acceleration site as well as the energy dumping of plasmoids. Here, we describe the high-energy signature and emission of the magnetosphere.

Particle spectra

In a first step, we can compute the energy spectra of all particles. Useful information contained in the latter are the shape, the energy range and cut-off energy. The spectrum for each species is given in Fig. 6.5. To compute the spectrum, we only use the particles located after the Y-point and up to the outer boundary. This region has reached the wanted regime in terms of cooling and steady-state, while the region before still presents some signs of relaxation.

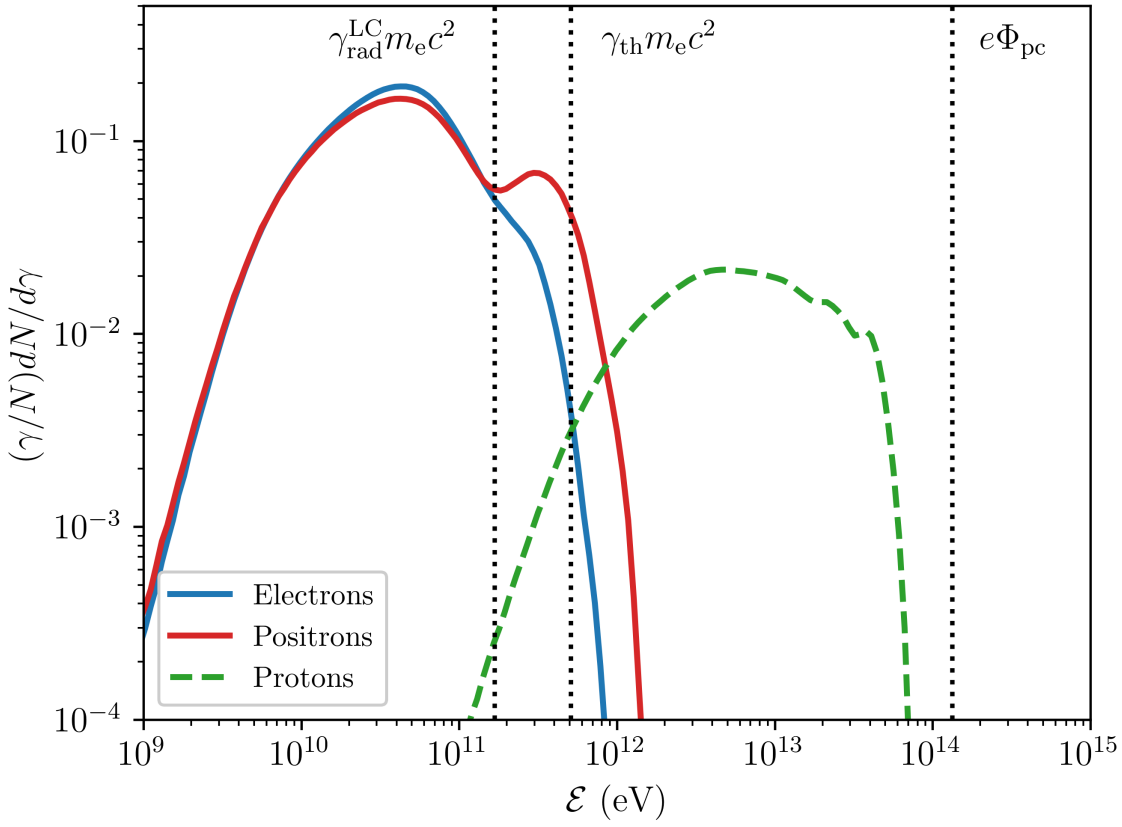

FIGURE 6.5: Energy spectra of electrons (solid blue), positrons (solid red) and protons (dashed green). From left to right, the vertical dashed lines correspond respectively to: the light-cylinder radiation-reaction-limited energy, $\gamma_{\rm rad}^{\rm LC} m_{\rm e} c^2 \approx 150\,{\rm GeV}$, the pair production energy threshold, $\gamma_{\rm th} m_{\rm e} c^2 \approx 500{\rm GeV}$, and the polar-cap potential drop energy, $e\Phi_{\rm pc} = 130{\rm TeV}$.

Electrons and positrons spectra have a similar shape below the radiation-reaction-limited energy, the two spectra are almost identical. However, above this energy, the spectra have two different shapes. The number of high-energy electrons diminishes while the positrons show an extra component. The latter is occurring between the radiation energy and the energy threshold for pair creation, and peaks at about $300 - 400{\rm GeV}$. Particles accelerated and thus energised at X-points typically reach this energy, see Fig. 6.6 and the zoomed-in view from Fig. 6.2. However, this difference in the spectral shape is expected

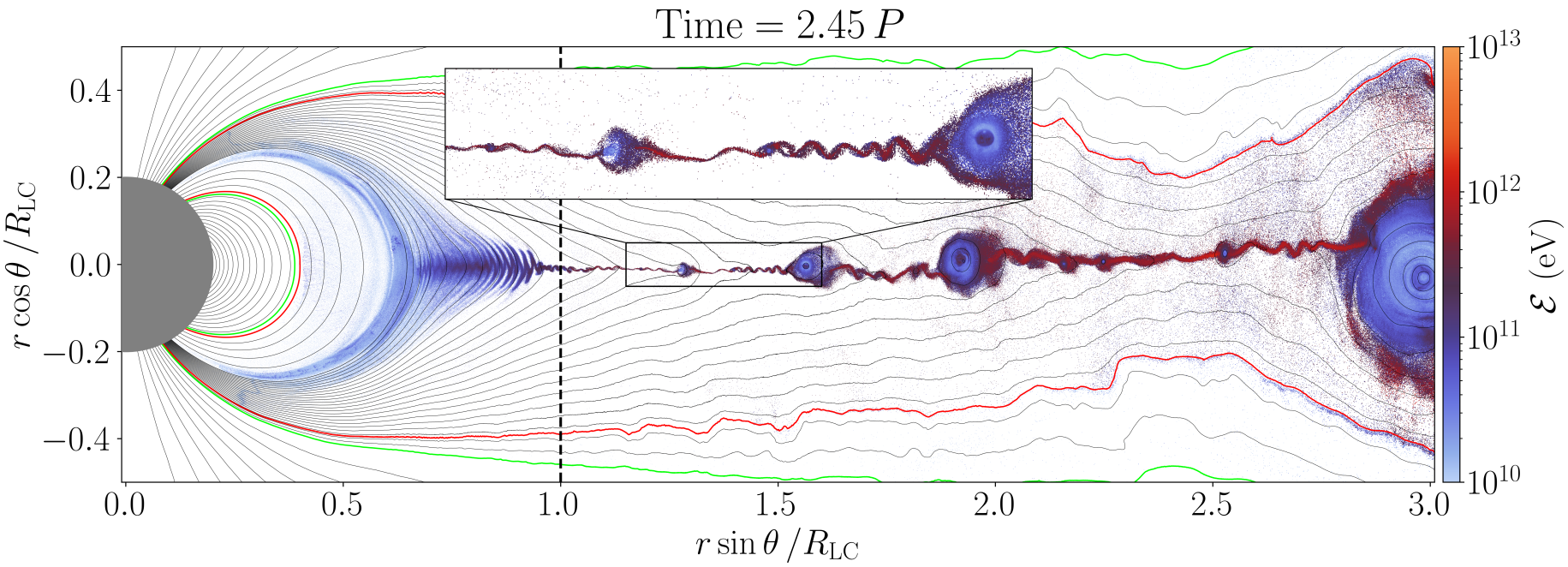

FIGURE 6.6: Snapshot of the aligned rotator using the hybrid approach at time $t/P = 3.01$. Solid black lines show the poloidal magnetic field lines, green and red solid lines show respectively the transition from region I to the PIC region and from the PIC region to region II. Map of the mean Lorentz factor of pairs. Light-cylinder shown by the vertical dashed black line.

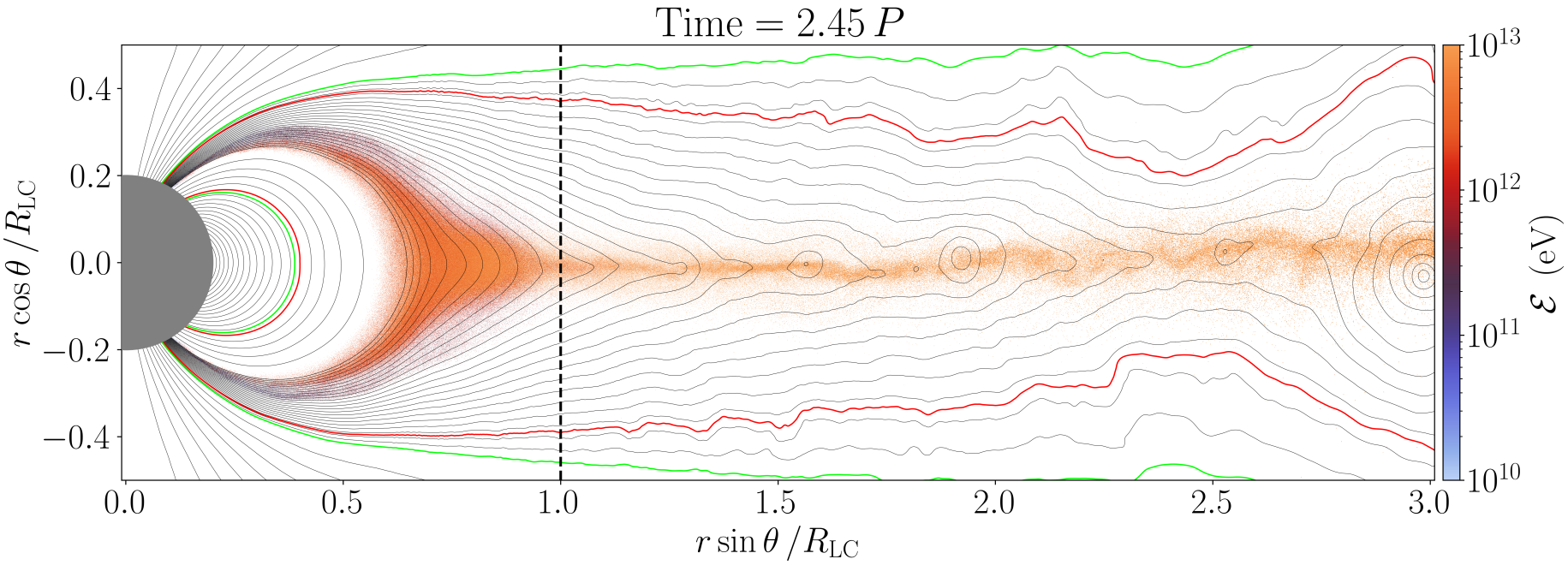

FIGURE 6.7: Snapshot of the aligned rotator using the hybrid approach at time $t/P = 3.01$. Solid black lines show the poloidal magnetic field lines, green and red solid lines show respectively the transition from region I to the PIC region and from the PIC region to region II. Map of the mean Lorentz factor of protons. Light-cylinder shown by the vertical dashed black line.

in the case where $\boldsymbol{\Omega} \cdot \boldsymbol{\mu} > 0$. In this configuration, the magnetosphere is electrically polarised and the equatorial regions possess a positive net charge. If we had a simulation with $\boldsymbol{\Omega} \cdot \boldsymbol{\mu} < 0$, the extra spectral component would be present in the electronic spectrum. The spectral shape difference at high-energy is enhanced by the aligned configuration. With an increasing inclination angle, the difference becomes smaller and vanishes in the orthogonal case (see Figure 6 of Philippov and Spitkovsky 2018). The overall conclusion for the leptons is that they have a narrow energy spectrum coming from the proximity of the different energy scales.

Moving on to the proton spectrum, we see that its probed energies are shifted by two orders of magnitudes to the highest energies compared to leptons, but they are also fewer in numbers by an order of magnitude. In terms of energies, the protons probe mostly energies of $1 - 30$TeV. As mentioned in the previous section, this represent approximately 10% of the maximum energy available in the system. If we fit a power-law on the proton spectrum, we find a power index $p \sim -1.5$. This is in qualitative agreement with works of local magnetic reconnection (Melzani et al., 2014; Werner et al., 2018).

However, we must be careful with the conclusions drawn from the spectral shape of each species. Since the pair production model is oversimplified, the spectral shapes are not exact and may differ when considering a more realistic pair production model. Despite this flaw, we believe that the different results on the energy budget, energy scales and width of the spectra are robust.

Synchrotron spectrum

From Fig. 6.5, we can see that leptons are accelerated to energies higher that the radiation-reaction-limited energy. Above this energy, pairs radiate their energy away in the form a synchrotron radiation. The latter is only relevant for pairs as protons do not radiate. In Fig. 6.8, we show the total synchrotron spectrum. We use the same procedure as for the particle spectra, meaning that the synchrotron spectrum is only the result of particles after the Y-point.

The energy range of the synchrotron spectrum spans from 0.1MeV to 1GeV. The synchrotron emission is not perfectly equal between electrons and positrons. This is a result of the positronic bump in the energy spectrum. Since observations cannot distinguish between the electronic and positronic signatures, we show in the same figure the total synchrotron spectrum. The latter shows a strong component above 100MeV which corresponds to the detection threshold of the *Fermi*-LAT. The synchrotron emission from our fiducial simulation would be visible by the satellite. We remind that the synchrotron emission is strongly beamed, see Sect. 2.2.2, meaning that this spectrum would be seen by an observer pointing directly at the equatorial plane. The synchrotron emission produced above 100MeV is emitted by the particles above the 100GeV band of the particle spectra. The latter is populated by particles accelerated at X-points which radiate. These particles, mostly positrons, produce synchrotron photons that are above the synchrotron burn-off limit defined by $\epsilon_{\rm rad} = (9/4)\,\beta_{\rm rec} m_{\rm e} c^2/\alpha_{\rm fs} \approx 160\,{\rm MeV}\beta_{\rm rec}$ (Uzdensky et al., 2011), where $\alpha_{\rm fs}$ is the fine structure constant. Above the burn-off limit, leptons cool off catastrophically via synchrotron. To estimate the power lost in the form of synchrotron, we need to integrate the spectrum over all frequencies. When doing so, we find that the synchrotron luminosity represents a significant fraction of the pulsar spindown power, about 18%. The latter is computed as the amount of Poynting flux that is dissipated in the magnetosphere in the current layer, from the Y-point up to a few light-cylinder. The dissipation of Poynting flux is dictated by the reconnection rate (Cerutti et al., 2020; Hakobyan, Philippov, et al., 2023). We argue that this dissipation is physical and not numerical as the numerical

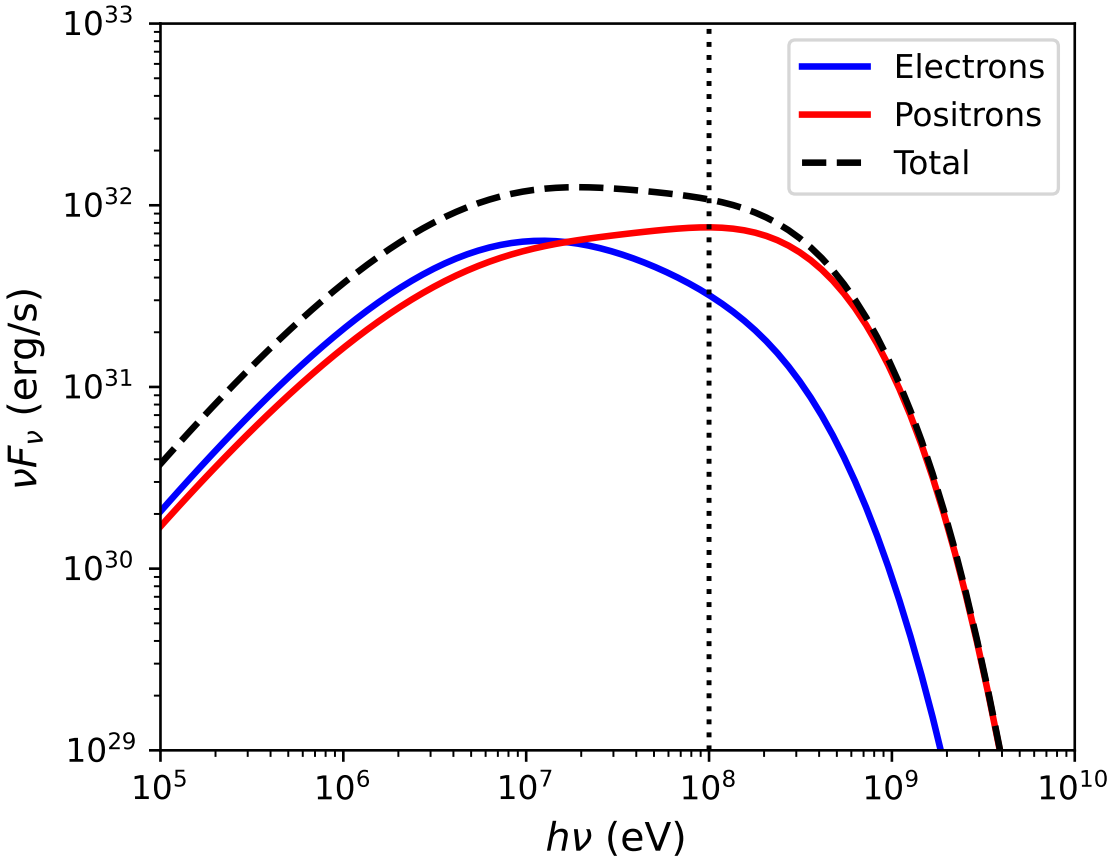

FIGURE 6.8: Synchrotron spectral energy distribution. The electronic contribution is in blue while the positronic one is in red. The black dashed line is the total synchrotron SED. The 100MeV energy threshold of the *Fermi*-LAT is indicated by the vertical dotted line.

dissipation given in Sect. 2.1.3 was way below 1% (Fig. 5.12). In our simulation, the dissipated energy is almost entirely channelled into non-thermal radiation. This conversion is possible in the simulation as a consequence of the strong cooling regime. If we look at the energy budget presented in Fig. 6.9, we see that the pairs are leaving the box with $\lesssim 1\%$ of the spindown power and protons leave with $\sim 2\%$ of it. Further from the star, these energy fractions would be greater as the acceleration and dissipation proceeds, as well as a more and more inefficient synchrotron cooling.

The final result on this simulation is to compare our pulsar to the *Fermi*-LAT gamma-ray pulsars. To do so, we integrate the obtained synchrotron spectrum above the energy detection threshold of the satellite. We give the direct comparison to the observed pulsars in Fig. 6.10. The simulation is shown in red with error bars coming from the variability of the spectrum within half a period. Our result is consistent with what is reported by the *Fermi* collaboration, where our gamma-ray efficiency is in the $1 - 10\%$ range (Smith et al., 2023).

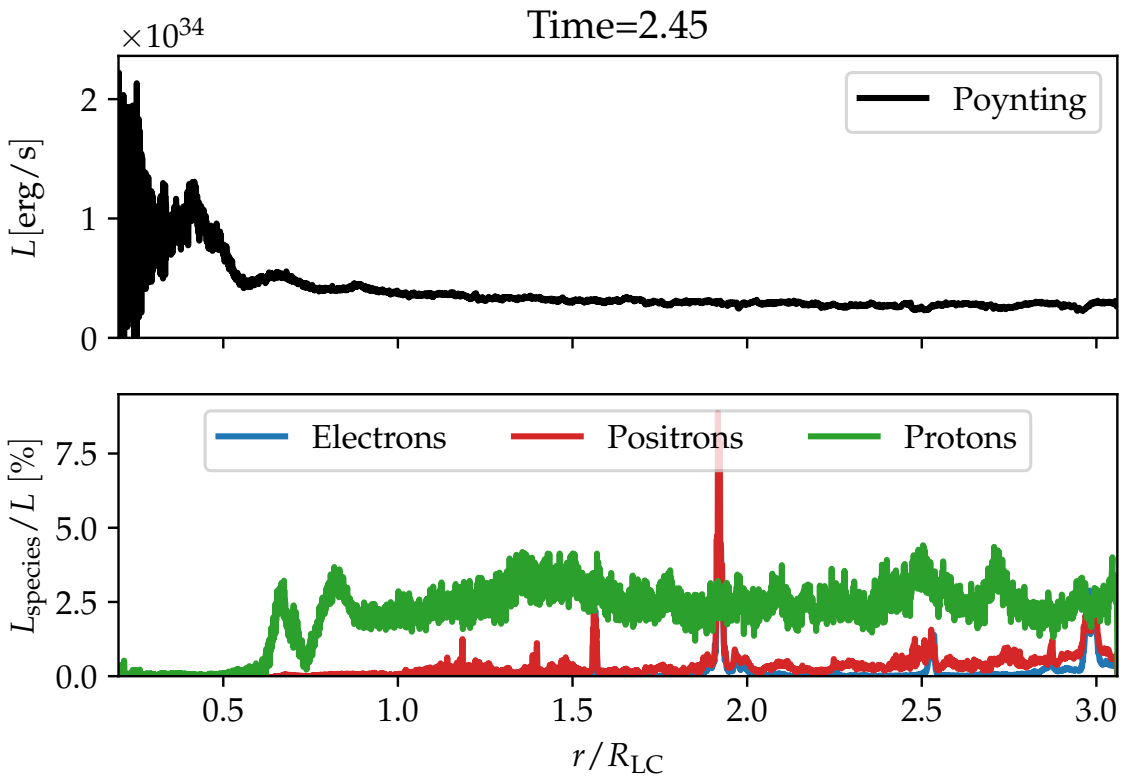

FIGURE 6.9: Energy budget of the simulation. The top panel shows the outgoing radial Poynting flux while the bottom panel shows the energy of electrons (blue), positrons (red), and protons (green) as a percentage of Poynting flux.

6.4 Effect of rescaling

6.4.1 Rescaling procedure

We, painfully but successfully, performed a simulation of an aligned rotator with realistic pulsar parameters. With this as our reference, we can now explore the following question: **How far from reality are we when we perform a rescaling in PIC?** To this end, we perform three additional simulations. They are identical to the fiducial run presented in the above section in terms of numerical parameters. However, we change the value of the surface magnetic field. This change of parameter impacts all the scales from the spatial one to the energetic ones including radiation. To have consistency between these runs and the fiducial one, and to test the rescaling performed by previous PIC studies, we keep the ratio of energies identical to the ones from Eq. (6.19):

$$\frac{\gamma_s}{\gamma_{pc}} \sim 8.5 \times 10^{-4} < \frac{\gamma_{rad}^{LC}}{\gamma_{pc}} \sim 10^{-3} < \frac{\gamma_{th}}{\gamma_{pc}} \sim 4 \times 10^{-3} \ll 1.$$

With this approach, we place ourselves in conditions where we model a rescaled version of our reference pulsar. To perform the rescaling of the radiation-reaction force, we artificially amplify its amplitude by a factor f_{rad}. The radiation-reaction-limited Lorentz factor is expressed as

$$\gamma_{rad} = \sqrt{\frac{3eE_{\parallel}}{2r_e^2 f_{rad} B_{\perp}^2}}. \tag{6.28}$$

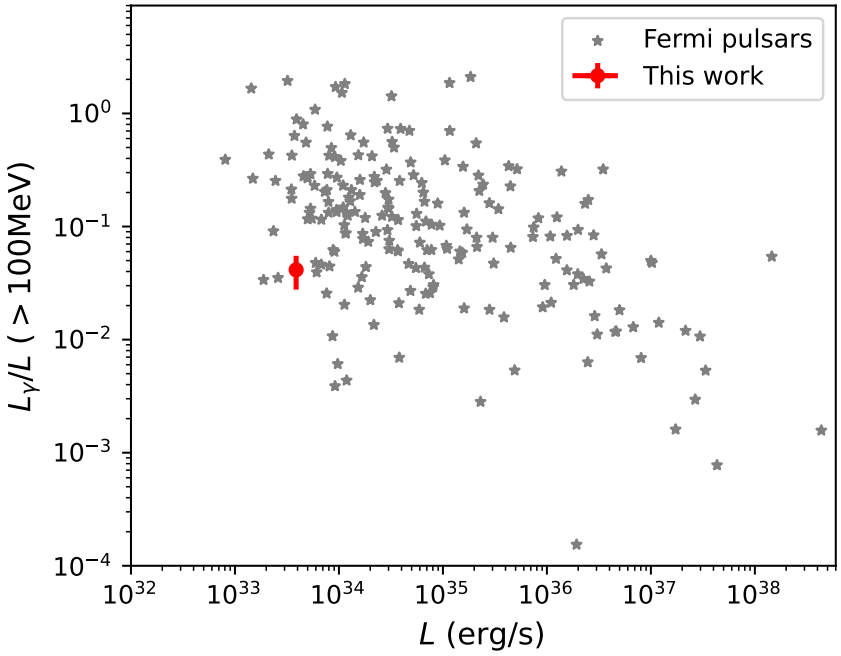

FIGURE 6.10: Gamma-ray efficiency of pulsar above 100MeV. The grey stars are from the third *Fermi*-LAT catalogue (Smith et al., 2023). The red dot corresponds to our simulation.

The artificial amplification is derived by equating the ratio $\gamma_{\rm rad}/\gamma_{\rm pc}$ between the fiducial simulation and the rescaled one.

$$\frac{\gamma^{\rm ref}_{\rm rad}}{\gamma^{\rm ref}_{\rm pc}} = \frac{\gamma'_{\rm rad}}{\gamma'_{\rm pc}} \Longrightarrow f_{\rm rad} = \left(\frac{E'_\parallel}{E^{\rm ref}_\parallel}\right)\left(\frac{B^{\rm ref}_\star}{B'_\star}\right)^2\left(\frac{B^{\rm ref}_\perp}{B'_\perp}\right)^2 . \tag{6.29}$$

where primed quantities are the parameters of the rescaled simulations, the other quantities correspond to the simulation with $B^{\rm ref}_\star = 10^7$G. If we assume that $E_\parallel \approx B_\perp \approx B_\star$ for the reference and rescaled simulations, the amplification is computed as

$$f_{\rm rad} = \left(\frac{B^{\rm ref}_\star}{B'_\star}\right)^3 . \tag{6.30}$$

We give the different rescaled magnetic field used in this experiment and values of $f_{\rm rad}$ in Table 6.2.

$B'_\star$	10^7	10^6	10^5	10^4
$f_{\rm rad}$	1	10^3	10^6	10^9

TABLE 6.2: Rescaling parameters.

6.4.2 Results

We do not seen major differences either in the global structure of the magnetosphere or the leptons parameters. However, we note that the protons are less prone to propagate in the magnetosphere for smaller magnetic fields. Their number density is reduced as a

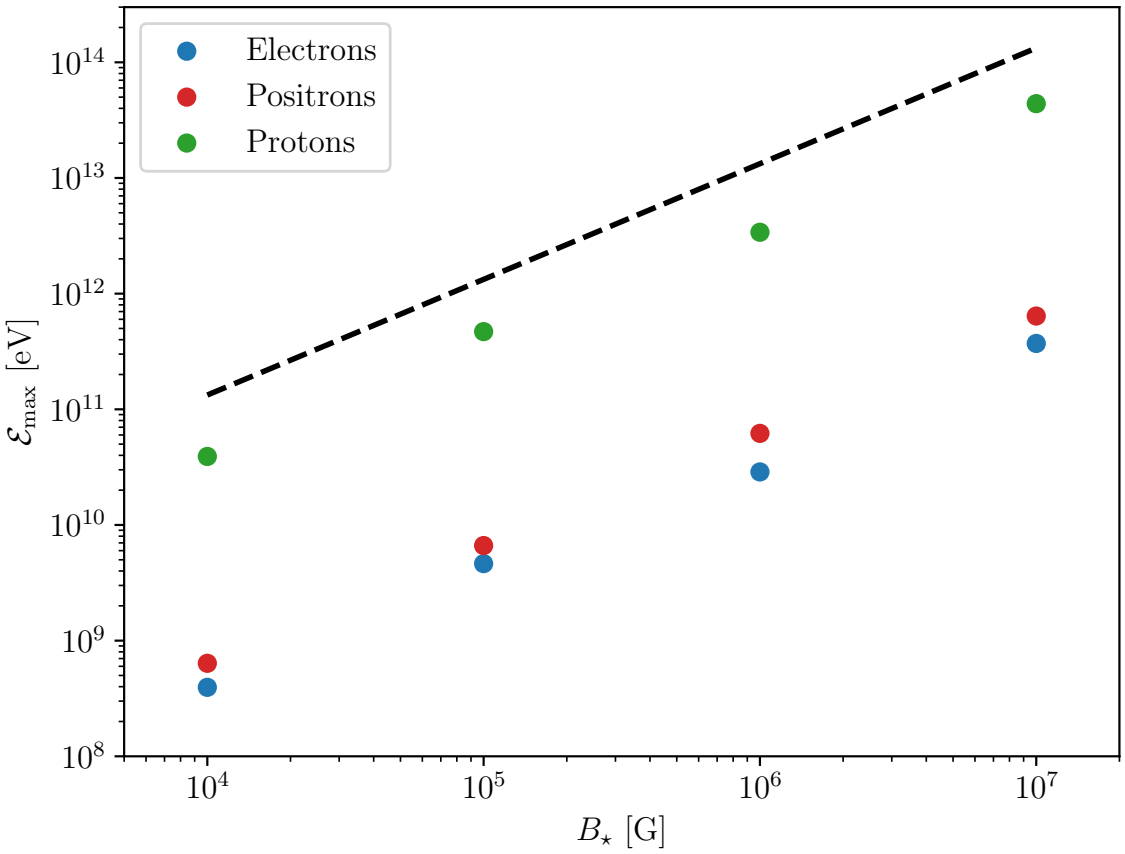

FIGURE 6.11: Spectral energy distribution peaks for various rescaled magnetic field strengths. The black dashed line shows the polar-cap potential drop as a function of the magnetic field.

consequence of a less efficient extraction. The magnetic field is weaker while the mass ratio stays the same. This indicates that during the rescaling of PIC simulations, we also need to rescale the mass of the protons accordingly. Another difference is on the energies probed by the simulation. The main result of this experiment is shown in Fig. 6.11.

The conclusion of our experiment is reassuring. We see a linear correlation between the strength of the magnetic field and the peak of the spectral energy distribution of each species. This result shows that, for a valid rescaling of a PIC simulation, we must keep the value of the different energy ratios identical to the one of the pulsar we want to model. If the hierarchy of scales of the realistic system is respected, the conclusions of a rescaled PIC simulation are legitimate.

6.5 Numerical convergence of the aligned rotator

To assess the validity of the method, we performed several tests where we focus on the global structure of the magnetosphere, the Poynting flux and the net charge. In the following, we consider a weaker and less resolved simulation compared to the fiducial simulation. The simulation setup for this aligned rotator consists of a 4096^2 cells grid, and a surface magnetic field $B_\star = 5.7 \times 10^5\,\mathrm{G}$. The modification of the magnetic field is necessary if we want to do a full PIC simulation. The parameters from the fiducial run are too extreme and a full PIC simulation would simply crash right away.

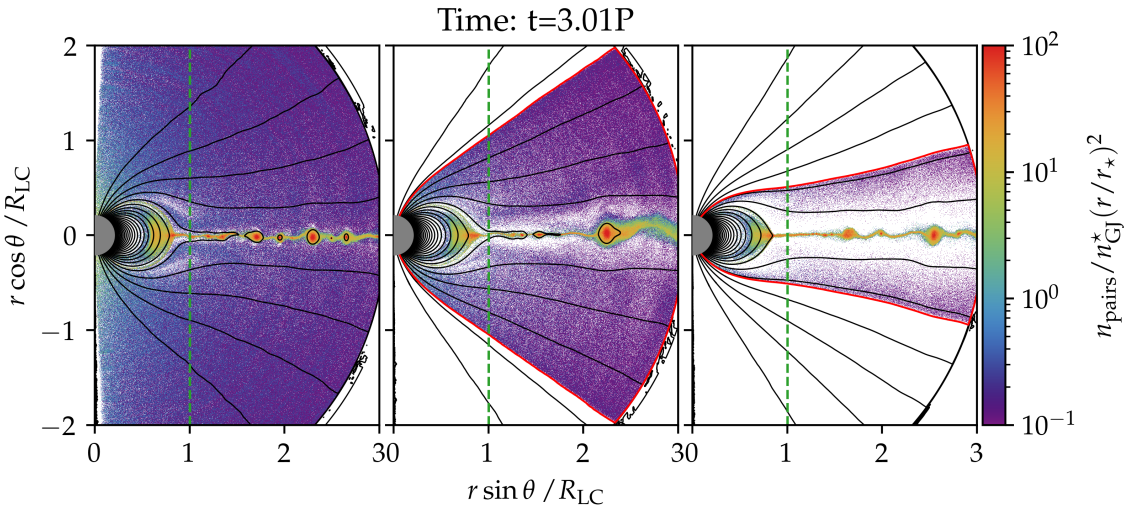

FIGURE 6.12: Comparison of the pairs density for three numerical configurations. Left: pure PIC simulation. Middle: wide hybrid simulation, the polar-cap is cut in half. Right: optimal hybrid simulation, narrow setup. The vertical green dashed line indicates the light-cylinder radius.

6.5.1 Sensitivity to the force-free-PIC boundary position

For this test, we perform a set of three simulations. They are identical regarding the physical and numerical parameters, the only difference lies in the outer force-free-PIC frontier. The inner hybrid boundary is kept identical. Our reference simulation corresponds to a full PIC simulation, where the outer hybrid boundary is removed. For the second simulation, we decided to cut the polar-cap in half. The upper half (close to the pole) is described in force-free, meaning that the other half is described by particles. We will refer to this simulation as the wide simulation. The final simulation corresponds to an optimal (narrow) hybrid decomposition where the hybrid frontier is set close to the separatrix, completely removing the particle description of the polar-cap. In terms of magnetic flux boundaries, the different simulation have

Simulation	Pure PIC	Hybrid wide	Hybrid narrow
Hybrid boundary $(\Psi_{\rm pc}$ units$)$	$\Psi = 0$	$\Psi = 0.4$	$\Psi = 0.85$

In Fig. 6.12, we show the last snapshot of each simulation at time $t = 3P$. At the equator, all simulations show a clear current layer within which plasmoids are visible, the separatrix is also present in all simulations. However, for the full PIC simulation, the separatrix appears more rounded. The location of the Y-points is roughly the same with $r_{\rm Y} \approx 0.85 R_{\rm LC}$. Regarding the densities in the current layer and separatrix, the same number density is reached. We note a difference in the plasma density around the current layer. In the full PIC simulation, the region around the current sheet is denser with a higher multiplicity. In the hybrid case, the depletion of plasma above and below the current sheet is significant and leaves a large gap. A possible reason behind this difference is regarding the plasma supply and pair production model. The magnetosphere is heavily impacted by the initial transient with a lot of movement along the field lines while they are opening up. During the full PIC transient, particles are injected along all field lines to fill the full magnetosphere. Therefore, these initial particles fall back near the equator during the transient and can play the role a seed particles for pair creation, populating regions close

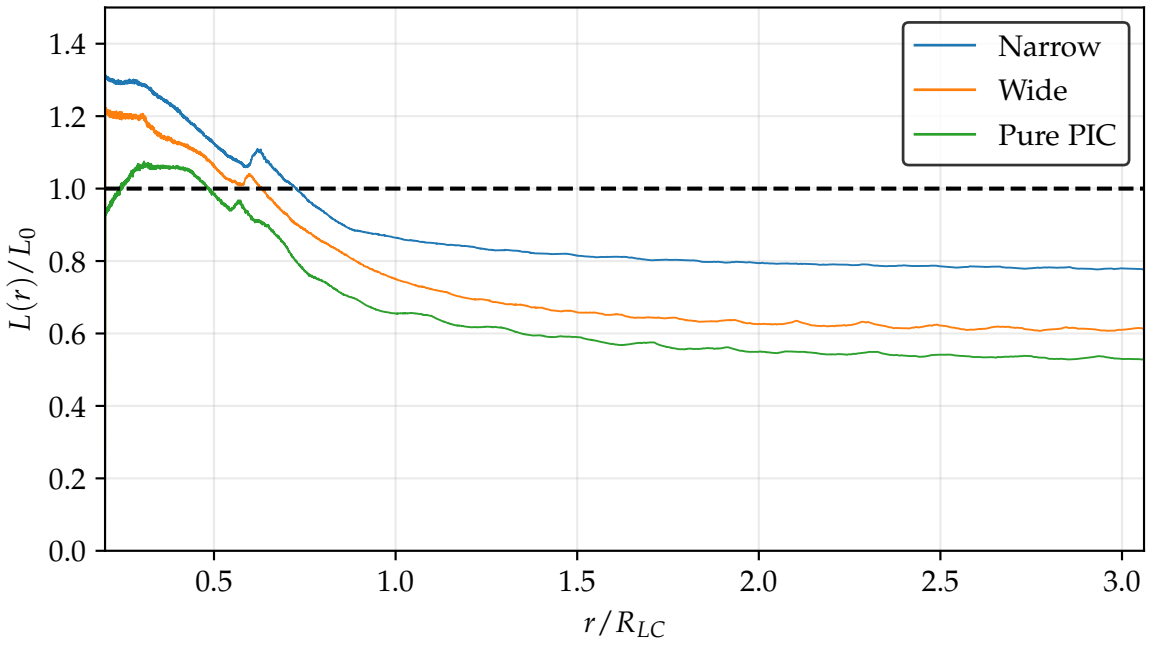

FIGURE 6.13: Outgoing radial Poynting flux for each simulation, averaged over one period.

to the current layer. In the hybrid run, the plasma supply is azimuthally limited to the PIC region. Therefore, it is impossible to have particles from the polar region falling back near the equator during the transient phase. The PIC boundary is set to be as close as possible to the separatrix, shortening out the particle supply. The intermediate run shows a slight depletion of density around the equatorial current sheet but is near the density reached in the full PIC simulation.

From this set of simulation, we can compute the radial Poynting flux. The latter is shown in Fig. 6.13, where the fluxes are averaged between $t = 2 - 3P$. Each Poynting flux is normalised by the expected force-free spindown power L_0 and is computed without the inner force-free region. The latter presents a high level of noise in the fields and does not participate in the dissipation process. From the figure, we can see that the spindown power of all simulations is not identical. The hybrid simulation tends to have a higher spindown power than the pure PIC one. This aspect is also seen in Fig. 6.12, where more field lines are opened in the hybrid run. However, if we look at the dissipation of Poynting flux from the light-cylinder to a few light-cylinder radii away, we see that the amount of dissipation is the same, around $\sim 15 - 20\%$. This dissipation corresponds to the fraction of spindown power converted into particle acceleration. The latter is the main focus of this work, thus having a hybrid dissipation equivalent to the PIC dissipation is a positive sign. The conclusions on the dissipation from the hybrid run are relevant.

6.5.2 Net charge

In this next test, we study the net charge of the simulation to see if we have some accumulation in the magnetosphere. This study allows us to see if the magnetosphere is properly screened and also to see when the steady-state is reached. The net charge is computed as

$$Q = \iint \mathbf{E} \cdot \mathrm{d}\mathbf{S} = \iint E_r r^2 \sin\theta \mathrm{d}\theta \mathrm{d}\phi. \tag{6.31}$$

At the surface of the star, the net charge is given by the Michel charge,

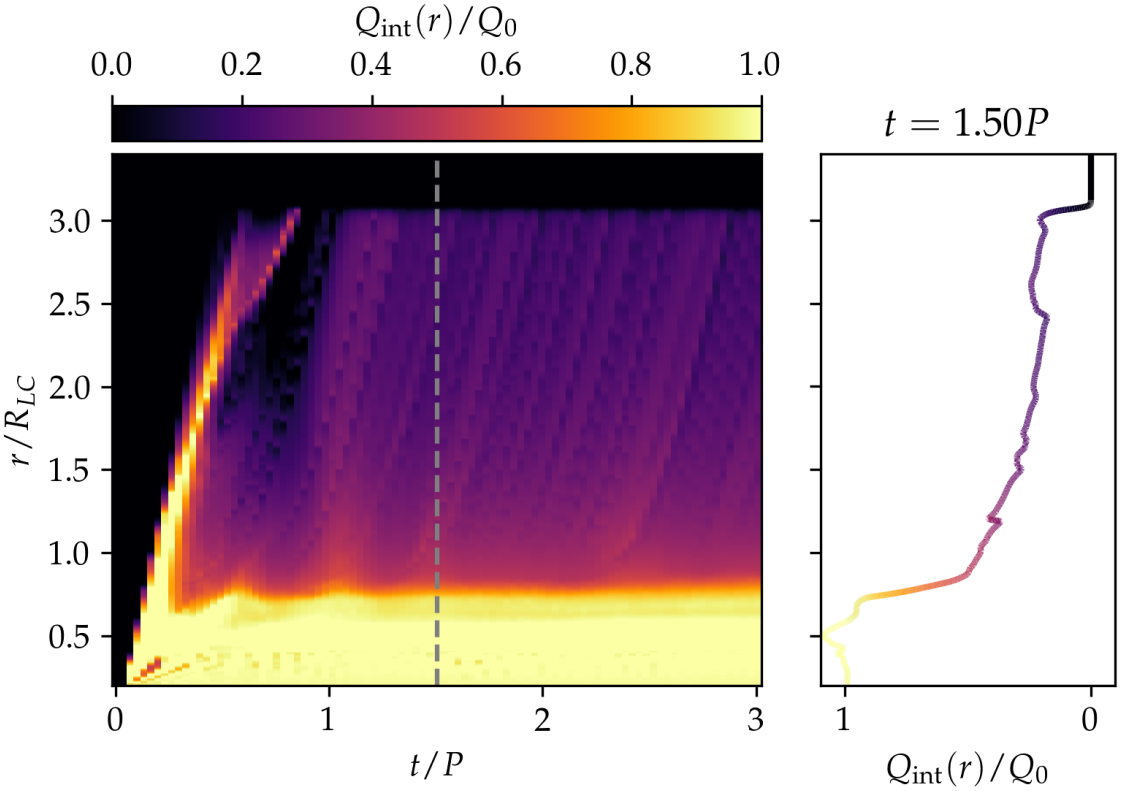

FIGURE 6.14: Spacetime diagram of the net charge for a force-free-PIC simulation of an aligned rotator, normalised to the net charge of the star. The right panel shows a cut of the diagram. The time of the profile is indicated by the grey dashed line.

$$Q_0 = \frac{2\mu\Omega}{3c} \tag{6.32}$$

In Fig. 6.14, we show a spacetime diagram of the net charge computed at every radii of the simulation over three spin periods. In this figure, we see a strong net charge for $t \leq 1P$. This net charge is a consequence of the initial transient when the magnetosphere is being filled with plasma. Once the transient is evacuated ($t > 1P$), we can see that the closed region (up to the Y-point) does present a net charge which is expected. This indicates that the magnetosphere has reached a steady-state after one spin period. The transition in the net charge value at $r \approx 0.75R_{\rm LC}$ corresponds to the location of the Y-point. Once the Y-point is passed, the net charge goes towards zero as we get further from the star. To better visualise this behaviour, we show the radial profile of the net charge at $t = 1.5P$ (right panel of Fig. 6.14). The various darker curves present in the spacetime diagram indicate the trajectory of the plasmoids inside the simulation. Their number at each time of the simulation can be estimated using this proxy.

6.5.3 Numerical benefits of the hybrid approach

Regarding the numerical aspects, the method shows interesting elements. The domain separation allows us to avoid particles in the polar cap regions and inner closed regions. In these regions, the plasma scales are smaller than at the light-cylinder. This is a direct consequence of the plasma being less relativistic at the poles. These scales are a bottleneck for full PIC simulations, in which the skin depth at the polar cap must be resolved. One

crucial point is that a full PIC simulation will not be able to handle the set of parameters of our fiducial pulsar.
By using the hybrid approach, the required memory is considerably reduced as well as the final data size. Thanks to the force-free treatment in some regions, we are able to have a quicker simulation. If we compare two identical simulations, one using the PIC description and the second using the force-free-PIC approach, we find a speed-up factor $\mathbf{f} = \Delta\mathbf{t}_{hybrid}/\Delta\mathbf{t}_{PIC} \approx 4-5$. The speed-up factor is not as large as what we expected, however it also depends on the CPU decomposition used. For instance, if a single CPU has to handle a large density of particles, it will slow down the simulation as the rest of the CPUs will be waiting for it to finish, i.e. race condition.

Finally, I want to give some estimation of the cost of such a new numerical method. In terms of computing time, the overall approach (from the start to the production runs included) required approximately 8 million CPU hours at the Très Grand Centre de Calcul (TGCC), and countless hours on my laptop. Developing new numerical methods costs a lot of time to be perfect but also has a carbon footprint which is often forgotten.

6.6 Summary

In this chapter, I presented the first application of the force-free-PIC method on a physical case. By using this method, I was able to produce the very first simulation of a weak millisecond pulsar, with a realistic set of parameters, cooling treatment and scale separation. The simulation has a surface magnetic field $B_\star = 10^7$G, a spin period $P = 1$ms corresponding to a spindown power $L = 4.8 \times 10^{33}$erg/s. Thanks to this simulation, I was able to highlight the fact that the current layer of pulsars is an efficient particle accelerator. Inside it, leptons can reach energies up to 1 TeV and protons are able to get up to ~ 10 TeV. The leptons in the simulation produce a synchrotron spectrum extending up to 1GeV which is above the detection threshold of the *Fermi*-LAT. The modelled pulsar presents an efficiency between $1-10\%$ which is in agreement with the gamma-ray millisecond pulsar population. Thanks to this new method, I was able to bridge the gap between global kinetic simulations of pulsar magnetospheres and observations of gamma-ray pulsars.

The hybrid approach also allowed me to validate the rescaling performed by previous PIC simulations. The maximum energy of the different species scales linearly with the strength of the surface magnetic field as long as the hierarchy of scales is respected. If this is the case, PIC results can be extrapolated to the targeted pulsar modelled.

I also carried out a convergence study on the method for the aligned rotator. The method recovers the proper description of the net charge inside the simulation. A comparison between two hybrid simulations and a full PIC simulation indicates that the method does not add dissipation to the system. This means that the dissipation measured in a hybrid simulation can be trusted.

6.7 [Français] Points clés du chapitre

Dans ce chapitre, j'ai présenté la première application de la méthode sans-force-PIC à un cas physique. En utilisant cette méthode, j'ai pu réaliser la toute première simulation d'un pulsar milliseconde faible, avec un ensemble réaliste de paramètres, allant du traitement du refroidissement à la séparation d'échelle. La simulation a un champ magnétique de surface $B_\star = 10^7$G, une période de rotation $P = 1$ms correspondant à une puissance de $L = 4.8 \times 10^{33}$erg/s. Grâce à cette simulation, j'ai mis en évidence le fait que la nappe de courant des pulsars est un accélérateur de particules efficace. À l'intérieur de celle-ci, les leptons peuvent atteindre des énergies allant jusqu'à 1 TeV et les protons jusqu'à ~ 10 TeV. Les leptons de la simulation produisent un spectre synchrotron s'étendant jusqu'à 1 GeV, ce qui dépasse le seuil de détection du *Fermi*-LAT. Le pulsar modélisé présente une efficacité comprise entre 1 et 10%, ce qui est en accord avec la population des pulsars millisecondes observée en rayons gamma. Grâce à cette nouvelle méthode, j'ai pu combler le fossé entre les simulations cinétiques globales de magnétosphères de pulsars et les observations des pulsars gamma.

L'approche hybride m'a également permis de valider le rééchelonnement effectué dans les simulations PIC précédentes. Ce résultat provient d'une série de simulations basées sur la simulation du pulsar réaliste (simulation fiduciaire). Dans cette série de simulations, seulement deux paramètres ont été modifiés : l'intensité du champ magnétique et celle de la force de réaction au rayonnement. Les rapports entre les différentes échelles d'énergie sont identiques à ceux de la simulation fiduciaire. La procédure suivie ici est quasiment identique à celle utilisée dans les simulations PIC antérieures. Cette série de simulation révèle un résultat important : l'énergie maximale des différentes espèces augmente linéairement avec l'intensité du champ magnétique de surface. Tant que la hiérarchie des échelles est respectée, cette conclusion reste valable et les résultats des simulations PIC peuvent être extrapolés au pulsar ciblé et modélisé.

J'ai également réalisé une étude de convergence sur la méthode appliquée au rotateur aligné. La méthode reconstruit correctement la distribution de la charge nette à l'intérieur de la simulation. On observe d'abord une charge nette proche de l'étoile à neutrons, qui tend vers zéro à mesure que l'on s'éloigne de l'étoile. Un dernier test pour valider la méthode a consisté à comparer deux simulations hybrides avec une simulation PIC complète. Les paramètres physiques et numériques sont identiques entre les trois simulations, seul l'emplacement de la transition sans-force-PIC est différente entre les deux simulations hybrides. Le calcul de la dissipation dans chacune des simulations hybrides montre que le taux de dissipation est cohérent avec celui de la simulation PIC. Ce test démontre que la méthode sans-force-PIC n'introduit pas de dissipation supplémentaire dans le système. Par conséquent, cela signifie que la dissipation mesurée dans une simulation hybride est fiable.

Part III

Conclusions & perspectives

CHAPTER 7

Conclusions & Perspectives

Pulsars and black holes are fascinating and terrifying objects. Close to them, the plasma is constantly oppressed by the strong magnetic- and gravitational fields. These extreme conditions could explain the production of high energy gamma-rays but also the high variability in the signals observed described in Chapt. 1. In this thesis, I focused on the development of a new numerical method to study the high-energy emission coming from relativistic magnetospheres.
The new method uses the Particle-in-cell and force-free framework simultaneously to describe the magnetosphere. The force-free approach is adapted to study the macroscopic scales. It cannot deal with the microphysics and non-ideal regions. The latter are not a problem for the PIC approach, in which we evolve individual particles. They can undergo acceleration, radiation processes during their evolution, and the observational signatures can be computed. The numerical aspect of each method is described in Chapt. 3. The first aspect of my work was to see if this kind of method could work and give a first proof-of-principle if it does. To this end, I first model a neutron star with a monopole magnetic field to test the method in Chapt. 5. With the test validated, it was time to modelled a more realistic solution: the aligned dipole. The simulation presented in Chapt. 6, is the first simulation of a pulsar within the detection range of observed *Fermi* pulsars. Finally, the moment arrives to translate the method from flat spacetime to curved spacetime. I am currently working on this last aspect at the moment of writing.

I will now summarise the different results obtained in this thesis, by answering the different questions raised in the introduction (Chapt. 4).

Is it possible to develop a viable force-free-PIC approach?

The quick answer is: yes it is! In Chapt. 5, I give the full details of the force-free-PIC method. The approach requires the implementation of both a force-free module and a PIC module in order to work. In the framework of a standard PIC code, the force-free module can easily be implemented by relying on the Maxwell solver already existing. The coupling between both methods is done via the current density, which is the main difference between the force-free and PIC numerical description. Once the current of both approaches is computed, it is assembled to create a unique current density. The latter is constructed thanks to a blending function built on the magnetic flux function. In the case of an axisymmetric pulsar, the magnetic flux function allows to establish where the magnetic field lines

are. With their footpoints anchored on the neutron stars, the field lines are a perfect proxy to know the regime in which the magnetosphere is. The choice of this proxy was picked based on previous PIC and force-free studies. The method on-boards a transition layer, which boundaries are set by hand by the user. This numerical layer is needed to avoid the development of numerical artefacts at the numerical transition, and to blend the two respective currents. Picking the right domain separation is one of the most difficult aspect of the method. It often relies on trials and errors.

If so, could this force-free-PIC approach be used to model pulsar magnetospheres?

For the first test of the method, I used a monopolar configuration for the magnetic field. This solution is not realistic but is the only analytical solution available in pulsar theory. The main idea with this test was to see how the method was performing physically and numerically. For the physics part, the magnetosphere has the right structure with radial field lines and the current density profile is in agreement with the analytical expression. Regarding the numerics, the method presents an intrinsic error below 1% for low resolutions. The error decreases with higher resolution as expected. My force-free-PIC method passes the monopole test.
The second test was get closer to a pulsar magnetosphere by modelling an aligned dipole. The idea was to recover the main results of a full PIC simulation with the hybrid method, and to check that the numerics was holding strong in this less friendly setup. Despite some differences in the solution, the hybrid method was able to recover the magnetospheric structure as well as the dissipation of electromagnetic energy. The net charge in the simulation is also coherent with what is expected. It is non-zero close to the star while it decays further away towards zero. This diagnosis allowed me to check that the simulation was not accumulating some net charge at the numerical boundary, between the force-free and PIC regions. Therefore, the method can be used to model pulsar magnetospheres.

Without rescaling, what is the typical energy of particles and where does the acceleration occurs?

This part was one of the real crux of my thesis work. In order to remove the various parameters, I had to proceed steps by steps. I started with a simple plasma of pairs and slowly added ions. Once the simulation was under control, I increased the mass of the ions to the real mass of protons. This step lifted for the first time the rescaling performed on ions by previous studies. The next step was to have a simple pair production mechanism, but where the threshold for pair creation was motivated by QED estimations. This step was only achieved when I slightly increased the magnetic field strength and resolution. The pair production was working but a new problem arrived. The results from the simulation were not consistent between each runs, and the method failed several times to model the magnetosphere. I dealt with these issues for a long time before discovering that the transition layer was causing the trouble. The layer was counter-productive during the initial transient of the simulation, and prevented the magnetosphere to reach a steady-state. The solution was to remove this layer during the initial transient, before putting it back. The last step was to remove the rescaling of the radiation-reaction force. This point appeared as an unbreakable wall for a long time. This last rampart was taken down by starting the simulation with a smaller radiation-reaction force and by ramping it up in time. When the strength of the radiation-reaction force reached its true value, the production run could be done.
The pulsar simulated without rescaling corresponds to a weak millisecond pulsar $\left(P = 1\text{ms}, B_\star = 10^7\text{G}\right)$ within the detection range of the *Fermi*-LAT. The estimated spin-down power of this pulsar is $4.8 \times 10^{33}\text{erg/s}$. My simulation indicates that:

- an aligned pulsar exhibits an extremely thin current sheet at the light-cylinder. The layer shows sign of the current driven instability and fragments into plasmoids (tearing instability). These magnetic islands of plasma do merge and have sizes ranging from the microscopic to the stellar radius scales,
- pair production occurs in the current layer where particles are accelerated by the non-ideal electric field. The acceleration happens deep inside the current sheet,
- protons are extracted from the pulsar surface and are insensitive to the dynamics of the leptons,
- acceleration is strong after the light-cylinder. Deep inside the current layer, leptons are accelerated up to 1 TeV, while those inside plasmoids radiated all their energy away and have energies of the order of 10-100 GeV,
- on the other hand, protons do not radiate. They see the current layer as a linear accelerator and reach the 10 TeV energy mark,
- the synchrotron spectrum is broad, and reach above the synchrotron burn-off limit. The spectrum extends from 0.1MeV to 1GeV,
- the efficiency of the simulated pulsar is consistent with the $1 - 10\%$ efficiency observed for millisecond gamma-ray pulsars.

As a general result, the current sheet in the magnetosphere of pulsars is able to accelerate particles to energies above the tera-electronvolt. With protons accelerated at least to 10TeV, pulsars could participate significantly to the production of Galactic cosmic rays.

This simulation is the **first global kinetic simulation to reach the realistic scales** of a pulsar magnetosphere. Therefore, the results of the simulation can directly be compared to the observations. We are finally able to bridge the gap between simulations and observations. This represents a considerable step towards understanding the high-energy emission of pulsars.

Are PIC results holding strong for close to realistic scale separation?

To address this question, I performed a series of simulations, in which I applied the traditional PIC rescaling for different magnetic fields. The weak millisecond pulsar simulation is used as a reference simulation. Downscaling this simulation to lower surface magnetic field strength implied to increase the radiation-reaction force strength. In this study, the energy hierarchy of scales is identical throughout the different simulations. This study allowed me to conclude that the rescaling done in PIC simulations was valid. The peak energy of the particle spectra shows a linear dependence with the surface magnetic field strength. The rescaling is valid as long as the simulation respects the realistic hierarchy of scales. The latter corresponds to the different scales of the targeted pulsar.

Can this approach be translated from flat space to a curved spacetime to model black hole magnetospheres?

For the moment, I cannot give a reliable answer as I am presently working on it. However, I can describe the on-going development of the method. To model black hole magnetosphere, we need to account for general relativistic effects. To this aim, a new version of ZELTRON has been developed, called GRZELTRON. The General Relativistic PIC (GRPIC) method is already implemented, and works on different setups including the monopole

and Wald configuration. The first goal was to add a new general relativistic force-free module to the code. This step is similar to the beginning of the method in flat space. However, the way the algorithm works in GR is very different than in flat space. It uses the 3+1 formalism from Komissarov (2011), meaning that four fields are now evaluated in the simulation. The next difference with the flat space code is the particle integration. The Boris push was originally designed to work in Cartesian coordinates but here we need to use it in a spherical curved spacetime. The code uses the concept of tetrads to perform this transformation, see Takahashi (2007) for the full explanations in Kerr-Schild coordinates.
After facing many issues, I finally managed to implement and fully parallelised the GR force-free module. To assess if it yields physical results, the first test I conducted was to consider a rapidly spinning black hole ($a = 0.99$) with a monopole magnetic field. This configuration corresponds to the analytical solution derived by Blandford and Znajek (1977) (BZ). For this test, I am able to recover the magnetic configuration, the angular velocity of the field lines, and to integrate for long timescales $\sim 10^3 r_g/c$. The power of the BZ jet is computed from the simulation and is in agreement with the analytical expression. This first test indicates that the force-free module implementation is correct and stable in time.
The targeted magnetic setup for this work is the Wald configuration. At the equator, a current layer is expected and implies that the force-free assumptions will not hold. For low enough resolutions, the effect of this layer should be weak. In my tests with the Wald setup, I find that the force-free method is having a lot of trouble with the ergo-region where the current sheet develops. The long time integration does not give clean results and get worst the longer the integration. Despite this issue, the point of the force-free-PIC method is to replace the regions where force-free fails with particles.
The next part of the approach is to couple the two methods in the same way as for the pulsar. Again, I am using the current density from both method and blending them inside a transition layer. The blending function is connected to the magnetic topology and relies on A_ϕ. The magnetic flux function is equal to the 4-potential. The coupling was comparatively more difficult than in flat space as a consequence of the GR algorithm. The real crux arrived with the first hybrid run. I took the monopole configuration in order to start with the only analytical solution. Even with this simple setup, the simulation did not behave properly and I was not able to recover the solution. The issue was numerical and came from the current density computation. I recall that the expression of the force-free current is not kind with codes using the FDTD scheme. The GR algorithm tends to break more easily than the flat space one, thus going back on forth between the nodal grid and the Yee mesh was introducing numerical artefacts. I had to implement some numerical manoeuvres to compute the right quantities on the right grid and at the right time to stabilise the scheme. This "trick" took me some time to master but it finally came out properly.
I am currently testing the new version of the approach with the monopole configuration. The decomposition between force-free and PIC is identical to the validation test case for a pulsar. The switch of method is set at the equator so that both hemispheres are numerically solved differently. Once this configuration is working efficiently and the BZ jet is recovered, I will move on to the force-free-PIC Wald simulation. The goal is to push the scale separation as far as possible with this method, to study particle acceleration near the horizon-scale. I will be able to give predictions of the particle and electromagnetic spectra. I will not tackle the issue of the plasma injection in this future work. For pulsars, the injection was straightforward as the neutron star possesses a surface. However, this is not the case for black holes where the plasma and magnetic field are external.

The force-free-PIC method is working but not to its full potential yet. For the moment, the method is setup-dependent and more efforts are needed to make it more general. From

this point several options are possible.
The first one is to extend the $2D$ method to $3D$. In this geometry, one can still use the current density to couple both approaches but the location of each of them will be more difficult. Indeed, if the axisymmetry is broken by the $3D$, the isocontours of the magnetic flux function do not represent the poloidal magnetic field lines any more. The quantity on which the method would rely in $3D$ is still unknown. It could very well be a combination of different criterion. One could potentially do a geometrical cut of the $3D$ space. It would be a great start to see the potential of the method, but the approach would become very stiff. If the method is portable in $3D$, we will be able to produce simulations with higher scale separation, getting closer and closer to realistic systems.
The second option is to move to a more dynamic approach by having an adaptive boundary between force-free and PIC regions. This modification would be similar in the spirit to what is done with the Adaptive Mesh Refinement. If we look at different domains of astrophysics, we can see that some communities have already started this process. The non-relativistic community already possesses codes where MHD and PIC are coupled with static PIC boxes. Last year, Chen et al. (2023) presented their method to have adaptive PIC boxes embedded in an MHD simulation. They managed to apply this method in the context of the Earth's magnetosphere. To my knowledge such codes do not exist in the relativistic community. Transposing this tool, or having one similar, to model relativistic magnetospheres would have a strong impact for the community. Therefore, I would like to upgrade the force-free-PIC method by finding a proxy in the force-free region that would allow me to turn a force-free region into a PIC region. The switch should produce the smallest numerical transient possible and properly describe the plasma. A starting point for this adaptive boundary could be magnetic reconnection simulations with a Harris sheet configuration.

One last possible extension of this thesis is regarding the pair production model used in the pulsar simulation. In the simulation, we use a very simple pair creation model. Tracking photons and treating pair production in a realistic way would bring us closer to the real physics happening in the magnetosphere. This would also increase the power of simulation to predict the shape of the particle spectrum, identify specific pair production regions and constrain the pair multiplicities.

As a final point, I want to say that we need to port our codes to GPUs. It will allow us to study systems at later stages, and also to probe parameters unachievable for the moment. One of the crux in the porting is the treatment of particles when multiple GPUs are used. We need to come up with clever ways of communicating the particles and their information.

The take away message of this manuscript is the following. I want to say that working on relativistic magnetospheres was a real pleasure but the high diversity of physical phenomenon can sometimes be overwhelming. The challenge of developing a new method is at the image of relativistic magnetospheres: both exiting and frightening.
The force-free-PIC method is working but is setup-dependent for the moment. This approach is not tender with the user as it is very fragile and can break at any time, until the right set of parameters is found. Thanks to this development, I was able to prove that the current sheet can be the locus of acceleration of particles to very high energies, and that the magnetosphere is able to produce the high-energy emission observed. My approach is new and offers a unique way of comparing simulations results to observations. We are getting closer and closer to realistic simulations, allowing us to unveil some mysteries of compact objects.

7.1 [Français] Conclusions et perspectives

Les pulsars et les trous noirs sont des objets à la fois fascinants et terrifiants. Près d'eux, le plasma est constamment soumis à de puissants champs magnétiques et gravitationnels. Ces conditions extrêmes pourraient expliquer la production de rayons gamma de haute énergie ainsi que la grande variabilité des signaux observés, décrite dans le Chapt. 1. Dans cette thèse, j'ai développé une nouvelle méthode numérique pour étudier l'émission à haute énergie provenant des magnétosphères relativistes.

Cette nouvelle méthode combine les approches « Particle-in-cell » (PIC) et sans-force pour modéliser la magnétosphère. L'approche sans-force est adaptée pour l'étude des échelles macroscopiques mais elle ne peut pas traiter la microphysique et les régions non idéales. Ces dernières ne représentent pas un problème pour l'approche PIC, dans laquelle les particules évoluent de manière individuelle. Les particules peuvent subir des processus d'accélération et de rayonnement au cours de leur évolution, et les signatures observationnelles peuvent être calculées. L'aspect numérique de chaque méthode est décrit dans le Chapt. 3. Le premier objectif de mon travail a été de voir si ce type de méthode pouvait fonctionner et de fournir une première preuve de concept si c'était le cas. Pour ce faire, j'ai commencé par modéliser une étoile à neutrons avec un champ magnétique monopolaire pour tester la méthode dans le Chapt. 5. Le test étant validé, il était temps de modéliser une solution plus réaliste : le dipôle aligné. La simulation présentée dans le Chapt. 6 est la première simulation d'un pulsar dans la gamme de détection des pulsars observés par *Fermi*. Enfin, le moment est venu de transposer la méthode d'un espace-temps plat à un espace-temps courbé. Je travaille actuellement sur ce dernier aspect au moment où j'écris ce manuscrit.

Je vais maintenant résumer les différents résultats obtenus dans cette thèse, en répondant aux différentes questions posées dans l'introduction (Chapt. 4).

Est-il possible de mettre au point une approche sans-force-PIC viable ?

La réponse brève est : oui, c'est possible ! Dans le Chap. 5, je donne tous les détails de la méthode sans-force-PIC. Cette nouvelle approche requiert l'implémentation dans le code à la fois d'un module sans-force et d'un module PIC pour pouvoir fonctionner. Dans le cadre d'un code PIC standard, le module sans-force peut facilement être implémenté en s'appuyant sur le solveur de Maxwell déjà existant. Le couplage entre les deux méthodes se fait par l'intermédiaire de la densité de courant, qui est la principale différence entre la description numérique sans-force et la description numérique PIC. Une fois que le courant des deux approches est calculé, il est assemblé pour créer une densité de courant unique. Cette dernière est construite grâce à une fonction de mélange. Cette fonction prend pour paramètre la valeur de la fonction de flux magnétique et permet d'attribuer un poids aux deux densités de courants pour les fusionner. Dans le cas d'un pulsar axisymétrique, la fonction de flux magnétique permet de connaître la position des lignes de champs magnétique. Ces dernières sont ancrées à la surface de l'étoile à neutrons et représentent un bon indicateur pour connaître le régime physique dans lequel se trouve la magnétosphère. Le choix de cette approximation a été fait sur la base d'études PIC et d'études sans-force antérieures. La méthode intègre une couche de transition, dont les limites sont fixées manuellement par l'utilisateur. Cette zone de transition est nécessaire afin de limiter le développement d'artefacts numériques à l'interface entre les deux méthodes, et pour mélanger les deux densités de courants. Le choix du positionnement de la zone de transition est l'un des aspects les plus complexes de la méthode. Cette partie se fait principalement par tâtonnement avec des essais répétitifs jusqu'à convergence.

Si tel est le cas, cette approche sans-force-PIC pourrait-elle être utilisée pour modéliser les magnétosphères de pulsars ?

Pour le premier test de la méthode, j'ai utilisé une configuration du champ magnétique dite monopolaire. Cette solution n'est pas réaliste mais elle correspond à la seule solution analytique disponible dans la théorie des pulsars. L'idée principale pour ce test était de voir le comportement à la fois physique mais aussi numérique de la méthode sans-force-PIC et d'étudier ses performances. Pour la partie physique, la magnétosphère répond aux différents critères avec des lignes de champs purement radiales ainsi que des profils de densité de courant en accord avec l'expression analytique. En ce qui concerne la partie numérique, la méthode présente une erreur intrinsèque inférieur à 1% pour des résolutions basses. Cette erreur décroît avec l'augmentation de la résolution comme attendu. Tous les voyants sont donc au vert pour affirmer que ma méthode sans-force-PIC passe le test du monopole.
Le deuxième test avait pour but de se rapprocher d'une magnétosphère de pulsar en modélisant un dipole aligné. L'idée était de retrouver les principaux résultats obtenus via une méthode entièrement PIC avec la méthode hybride, et de vérifier que la partie numérique était toujours robuste dans une configuration plus complexe. Malgré quelques différences dans la solution, la méthode hybride est capable de retrouver la bonne structure magnétosphérique ainsi que la quantité d'énergie électromagnétique dissipée. La charge nette de la simulation est aussi en accord avec ce qui est attendu pour un dipole. Une charge nette est présente à proximité de l'étoile et elle décroît vers zéro à mesure que l'on s'éloigne radialement. Ce diagnostic m'a aussi permis de vérifier qu'il n'y avait aucune accumulation de charge nette dans la simulation au niveau de la frontière numérique entre les régions décrites par le PIC et celles décrites par le sans-force. Pour toutes ces raisons, la méthode peut donc être utilisée pour modéliser les magnétosphères de pulsars.

Sans rééchelonnement, quelle est l'énergie typique des particules et où sont-elles accélérées ?

Cette parti a été l'une des plus problématique de mon travail de thèse. Le but était de retirer le plus de paramètres libres possible des simulations. Afin de pouvoir faire cela, j'ai dû procéder par étapes. J'ai tout d'abord commencé en injectant un plasma de paires avant d'ajouter des ions. Une fois la simulation sous contrôle, j'ai augmenté la masse des ions jusqu'à atteindre la masse réelle des protons. Cette étape m'a permis de supprimer pour la première fois le rééchelonnement qui était habituellement fait sur les ions dans les études antérieures. L'étape suivante était d'avoir un mécanisme simple pour la production de paires, tout en se basant sur les estimations données pour l'électrodynamique quantique. Cette étape n'a pu être réalisé qu'après l'utilisation d'un champ magnétique plus intense et d'une résolution numérique plus élevée. Le processus de production de paires était donc fonctionnel mais un nouveau problème de taille est apparue. Les résultats des simulations n'étaient pas cohérents d'une simulation à une autre, la méthode échouait plusieurs fois à modéliser la magnétosphère. J'ai fait face à ce problème pendant un long moment avant de découvrir que l'origine du problème était la couche de transition. Cette zone était contre-productive pendant la phase transitoire initiale de la simulation et empêchait la magnétopshère d'atteindre un régime (quasi)-stationnaire. La solution a été de supprimer cette zone pendant le transitoire initial avant de la réintroduire une fois le transitoire passé. La dernière étape a consisté à supprimer le rééchelonnement effectué sur la force de réaction au rayonnement. Dès les premiers tests, cette étape apparut comme un mur infranchissable. Ce dernier rempart fut brisé en démarrant la simulation avec une force de réaction au rayonnement faible puis d'augmenter son intensité au cours du temps. Quand l'amplitude de cette force atteint sa vraie valeur, la simulation peut être

utilisée comme simulation de production.

Le pulsar simulé sans rééchelonnement correspond à un pulsar milliseconde faible $\left(P = 1\text{ms}, B_\star = 10^7\text{G}\right)$ dans la gamma de détection du *Fermi*-LAT. La puissance de ce pulsar est estimée à $4.8 \times 10^{33}\text{erg/s}$. My simulation indicates that:

- un pulsar aligné présente une nappe de courant extrêmement fine au niveau du cylindre de lumière. Cette dernière montre des signes d'instabilité due au courant et se fragmente en plasmoïdes (instabilité de déchirement). Ces îlots magnétiques de plasma fusionnent et ont des tailles allant de l'échelle microscopique à l'échelle du rayon stellaire,
- la production de paires se produit essentiellement dans la nappe de courant où les particules sont accélérées par le champ électrique non idéal (profondément dans la nappe),
- les protons sont extraits de la surface du pulsar et sont insensibles à la dynamique des leptons,
- l'accélération est forte après le cylindre de lumière. Au plus profond de la couche de courant, les leptons sont accélérés jusqu'à 1 TeV, tandis que ceux qui se trouvent à l'intérieur des plasmoïdes ont rayonné toute leur énergie et ont des énergies de l'ordre de 10-100 GeV,
- en revanche, les protons ne rayonnent pas. Ils considèrent la couche de courant comme un accélérateur linéaire et atteignent une énergie de 10 TeV,
- le spectre synchrotron est large et dépasse la limite de « burn-off » du synchrotron. Le spectre s'étend de 0,1 MeV à 1 GeV,
- l'efficacité du pulsar simulé est cohérente avec l'efficacité de 1 à 10% observée pour les pulsars gamma millisecondes.

De manière générale, la nappe de courant dans la magnétosphère des pulsars est capable d'accélérer les particules à des énergies supérieures au téraélectronvolt. Avec des protons accélérés au moins à 10 TeV, les pulsars pourraient participer de manière significative à la production de rayons cosmiques galactiques.

Cette simulation est la **première simulation cinétique globale à atteindre les échelles réalistes** d'une magnétosphère de pulsars. Les résultats de la simulation peuvent donc être directement comparés aux observations. Nous sommes enfin en mesure de combler le fossé entre les simulations et les observations. Cela représente un pas en avant considérable pour la compréhension de l'émission à haute énergie des pulsars.

Est-ce que les résultats obtenus avec la méthode PIC sont toujours valables pour une séparation d'échelle proche de la réalité ?

Pour répondre à cette question, j'ai effectué une série de simulations dans lesquelles j'ai appliqué le rééchelonnement PIC traditionnel pour différents champs magnétiques. La simulation du pulsar milliseconde faible est utilisée comme simulation de référence dans cette série. La réduction d'échelle de cette simulation, pour une intensité de champ magnétique de surface plus faible, implique aussi l'augmentation de l'intensité de la force de réaction au rayonnement. Dans cette étude, la hiérarchie des échelles énergétiques est identique dans les différentes simulations. Cette étude m'a permis de conclure que le rééchelonnage

des simulations PIC était valide. L'énergie maxminale des spectres de particules montre une dépendance linéaire avec l'intensité du champ magnétique de surface. Le rééchelonnement est valable tant que la simulation respecte la hiérarchie réaliste des échelles. Cette dernière correspond aux différentes échelles du pulsar ciblé.

Est-il possible de transposer cette approche en espace plat vers une approche en espace courbe pour modéliser les magnétosphères de trous noirs ?

Pour l'instant, je ne peux pas donner de réponse fiable car je suis en train de travailler sur cette implémentation. Toutefois, je peux décrire le développement en cours de la méthode. Pour modéliser la magnétosphère d'un trou noir, nous devons tenir compte des effets produit par la relativité générale (RG). Pour cela, une nouvelle version de ZELTRON a été développée, appelée GRZELTRON. La méthode General Relativistic PIC (GRPIC) est déjà implémentée et fonctionne sur différentes configurations, y compris le monopôle et la configuration de Wald. Le premier objectif était d'ajouter un nouveau module sans-force tenant compte de la relativité générale au code. Cette étape est similaire au développement initial de la méthode en espace plat. Cependant, le fonctionnement de l'algorithme en RG est très différent de celui de l'espace plat. Il utilise le formalisme 3+1 de Komissarov (2011), ce qui signifie que quatre champs sont maintenant évalués dans la simulation. La différence suivante avec le code en espace plat est l'intégration des particules. Le pousseur de Boris a été conçue à l'origine pour fonctionner en coordonnées cartésiennes, mais ici nous devons l'utiliser dans un espace-temps sphérique courbé. Le code utilise le concept de tétrades pour effectuer cette transformation, voir Takahashi (2007) pour les explications complètes en coordonnées de Kerr-Schild.
Après avoir rencontré de nombreux problèmes, j'ai finalement réussi à implémenter et à entièrement paralléliser le module RG sans-force. Pour évaluer s'il fonctionnet et s'il produit des résultats physiques, le premier test que j'ai effectué a consisté à modéliser un trou noir en rotation rapide $(a = 0.99)$ avec un champ magnétique monopolaire. Cette configuration correspond à la solution analytique dérivée par Blandford and Znajek (1977) (BZ) et représente l'analogue du monopole du Michel pour les pulsars. Pour ce test, je suis capable de retrouver la configuration magnétique (lignes de champ radiales), la vitesse angulaire des lignes de champ, et d'intégrer pendant de longues échelles de temps $\sim 10^3 r_g/c$. La puissance du jet BZ est calculée à partir de la simulation et est en accord avec l'expression analytique. Ce premier test indique que l'implémentation du module sans-force est correcte et stable dans le temps. La configuration magnétique ciblée pour ce travail est la configuration de Wald. À l'équateur, une couche de courant est attendue ce qui implique que les hypothèses sur lesquelles reposent le régime sans-force ne seront plus valables. Pour des résolutions suffisamment basses, l'effet de cette nappe de courant devrait être faible. Dans mes tests avec la configuration de Wald, je trouve que la méthode sans-force a beaucoup de problèmes avec la région à l'intérieur de l'ergosphère où la nappe de courant se développe. L'intégration sur des échelles de temps long ne donne pas des résultats clairs et les résultats empirent à mesure que l'intégration est temporelle dure. Malgré ce problème, l'intérêt de la méthode sans-force-PIC est de remplacer les régions où la méthode sans-force échoue par des particules.
L'étape suivante pour l'approche consiste à coupler les deux méthodes de la même manière que pour le pulsar. Encore une fois, j'utilise la densité de courant des deux méthodes et je les mélange à l'intérieur d'une couche de transition. La fonction de mélange est liée à la topologie du champ magnétique et repose sur la quantité A_ϕ. La fonction de flux magnétique est égale au 4-potentiel. Le couplage était comparativement plus difficile que pour la version en espace plat, en raison de la relativité générale prise en compte par l'algorithme. Le véritable nœud du problème est apparu lors de la première

simulation hybride. Pour cette simulation, j'ai utilisé la configuration monopolaire afin de pouvoir comparer les résultats à la seule solution analytique disponible. Même avec cette configuration simple, la simulation ne s'est pas comportée correctement et je n'ai pas pu retrouver la solution. Le problème était numérique et provenait du calcul de la densité de courant. Je rappelle que l'expression de la densité de courant dans l'approximation sans-force n'est pas tendre avec les codes utilisant le schéma FDTD. De plus, l'algorithme en relativité générale a tendance à casser plus facilement que l'algorithme en espace plat. Les aller-retours entre les nœuds de la grille et la maille de Yee introduisaient des artefacts numériques qui étaient trop important pour l'algorithme. J'ai dû implémenter certaines manœuvres numériques pour calculer les bonnes quantités sur la bonne grille et au bon temps afin de stabiliser le schéma. Il m'a fallu du temps pour maîtriser cette « astuce », mais j'ai fini par aboutir à quelque chose de propre numériquement .
Je teste actuellement la nouvelle version de l'approche avec la configuration monopolaire. La décomposition entre le sans-force et le PIC est identique au cas de test pour un pulsar et permet de valider ou non la méthode. Le changement de méthode est fixé au niveau de l'équateur de sorte que les deux hémisphères sont résolus numériquement de deux manières différentes. Une fois que cette configuration fonctionnera parfaitement et que le jet BZ sera récupéré, je passerai à la simulation Wald utilisant la méthode sans-force-PIC. L'objectif est de pousser la séparation d'échelles aussi loin que possible avec cette méthode, afin d'étudier l'accélération de particules proche de l'horizon. Je serai en mesure de donner des prédictions sur les spectres de particules et électromagnétiques. Je n'aborderai pas la question de l'injection de plasma dans cette simulation. Pour les pulsars, l'injection de plasma est simple car l'étoile à neutrons possède une surface. Cependant, ce n'est pas le cas pour les trous noirs où le plasma et le champ magnétique sont externes.

La méthode sans-force-PIC fonctionne mais n'a pas encore atteint son plein potentiel. Pour l'instant, la méthode dépend de la configuration du problème et des efforts supplémentaires sont nécessaires pour la rendre plus générale. À partir de là, plusieurs options sont possibles.
La première consiste à étendre la méthode $2D$ à une méthode $3D$. Dans cette géométrie, on peut toujours utiliser la densité de courant pour coupler les deux approches, mais la séparation numérique entre les deux sera plus difficile. En effet, si l'axisymétrie est brisée par la $3D$, les isocontours de la fonction de flux magnétique ne représentent plus les lignes de champ magnétique poloïdal. La quantité sur laquelle la méthode s'appuierait en $3D$ est encore inconnue. Il pourrait très bien s'agir d'une combinaison de différents critères. On pourrait éventuellement faire une coupe géométrique de l'espace $3D$. Ce serait un bon début pour voir le potentiel de la méthode, mais l'approche deviendrait très rigide. Si la méthode est transposable en $3D$, nous serons en mesure de produire des simulations avec une séparation d'échelle plus importante, nous rapprochant de plus en plus des systèmes réalistes.
La deuxième option consiste à passer à une approche plus dynamique en ayant une frontière adaptative entre les régions sans-force et les régions PIC. Cette modification serait similaire dans l'esprit à ce qui est fait avec le raffinement adaptatif de maillage. Si nous regardons dans différents domaines de l'astrophysique, nous constatons que certaines communautés ont déjà entamé ce processus. La communauté non relativiste possède déjà des codes où la MHD et le PIC sont couplés avec des boîtes PIC statiques. L'année dernière, Chen et al. (2023) ont présenté leur méthode pour intégrer des boîtes PIC adaptatives dans une simulation MHD. Ils ont réussi à appliquer cette méthode dans le contexte de la magnétosphère terrestre. À ma connaissance, de tels codes n'existent pas encore dans la communauté relativiste. Transposer cet outil, ou en avoir un similaire, pour

modéliser les magnétosphères relativistes aurait un fort impact pour la communauté. Par conséquent, j'aimerais améliorer la méthode sans-force-PIC en trouvant un proxy dans la région sans-force qui me permettrait de transformer une région sans-force en une région PIC. Le changement devra produire le plus petit transitoire numérique possible et décrire correctement le plasma. Un point de départ pour cette frontière adaptative pourrait être les simulations de reconnexion magnétique avec une configuration de feuille de Harris.

Une dernière extension possible de cette thèse concerne le modèle de production de paires utilisé dans la simulation du pulsar. Dans la simulation, nous utilisons un modèle de création de paires très simple. Le suivi des photons et le traitement de la production de paires de manière réaliste nous rapprocheraient de la physique réelle qui se produit dans la magnétosphère. Cela augmenterait également la capacité de la simulation à prédire la forme du spectre de particules, à identifier des régions spécifiques de production de paires et à contraindre les multiplicités de paires.

Pour conclure, je voudrais dire que nous devons migrer nos codes d'une utilisation CPU pur à une utilisation basée sur les GPUs. Cela nous permettra d'étudier les systèmes à des stades plus avancés et de sonder des paramètres impossibles à atteindre pour le moment. L'un des points cruciaux du portage sur GPU est le traitement des particules lorsque plusieurs GPUs sont utilisés. Nous devons trouver des moyens astucieux de communiquer les particules et leurs informations.

Les message à retenir de ce manuscrit sont les suivants. Je tiens à dire que travailler sur les magnétosphères relativistes a été un réel plaisir, mais la grande diversité des phénomènes physiques peut parfois nous submerger. Le défi que représente le développement d'une nouvelle méthode est à l'image des magnétosphères relativistes : à la fois passionnant et effrayant.
La méthode sans-force-PIC fonctionne mais dépend pour l'instant de la configuration du problème. Cette approche n'est pas tendre avec l'utilisateur car elle est très fragile et peut se briser à tout moment, jusqu'à ce que le bon ensemble de paramètres soit trouvé. Grâce à ce développement, j'ai pu prouver que la nappe de courant peut être le lieu d'accélération de particules à de très hautes énergies, et que la magnétosphère est capable de produire l'émission à haute énergie observée. Mon approche est nouvelle et offre un moyen unique de comparer les résultats des simulations aux observations. Nous nous rapprochons de plus en plus de simulations réalistes, ce qui nous permettra de lever le voile sur certains mystères entourant les objets compacts.

Bibliography

Abdo, A. A., Ackermann, M., Ajello, M., Atwood, W. B., Axelsson, M., Baldini, L., Ballet, J., Barbiellini, G., Baring, M. G., Bastieri, D., Baughman, B. M., Bechtol, K., Bellazzini, R., Berenji, B., Blandford, R. D., Bloom, E. D., Bonamente, E., Borgland, A. W., Bregeon, J., … Ziegler, M. (2010). The First Fermi Large Area Telescope Catalog of Gamma-ray Pulsars. ApJS, *187*(2)arXiv 0910.1608, 460–494. https://doi.org/10.1088/0067-0049/187/2/460

Aharonian, F., Akhperjanian, A. G., Bazer-Bachi, A. R., Behera, B., Beilicke, M., Benbow, W., Berge, D., Bernlöhr, K., Boisson, C., Bolz, O., Borrel, V., Boutelier, T., Braun, I., Brion, E., Brown, A. M., Bühler, R., Büsching, I., Bulik, T., Carrigan, S., … Zdziarski, A. A. (2007). An Exceptional Very High Energy Gamma-Ray Flare of PKS 2155-304. ApJ, *664*(2)arXiv 0706.0797, L71–L74. https://doi.org/10.1086/520635

Aharonian, F., Akhperjanian, A. G., Bazer-Bachi, A. R., Beilicke, M., Benbow, W., Berge, D., Bernlöhr, K., Boisson, C., Bolz, O., Borrel, V., Braun, I., Brown, A. M., Bühler, R., Büsching, I., Carrigan, S., Chadwick, P. M., Chounet, L.-M., Coignet, G., Cornils, R., … Ward, M. (2006). Fast Variability of Tera-Electron Volt γ Rays from the Radio Galaxy M87. *Science*, *314*(5804)arXiv astro-ph/0612016, 1424–1427. https://doi.org/10.1126/science.1134408

Alpar, M. A., Cheng, A. F., Ruderman, M. A., & Shaham, J. (1982). A new class of radio pulsars. Nature, *300*(5894), 728–730. https://doi.org/10.1038/300728a0

Ansoldi, S., Antonelli, L. A., Antoranz, P., Babic, A., Bangale, P., Barres de Almeida, U., Barrio, J. A., Becerra González, J., Bednarek, W., Bernardini, E., Biasuzzi, B., Biland, A., Blanch, O., Bonnefoy, S., Bonnoli, G., Borracci, F., Bretz, T., Carmona, E., Carosi, A., … Zanin, R. (2016). Teraelectronvolt pulsed emission from the Crab Pulsar detected by MAGIC. A&A, *585*arXiv 1510.07048, A133. https://doi.org/10.1051/0004-6361/201526853

Arnowitt, R., Deser, S., & Misner, C. W. (1959). Dynamical Structure and Definition of Energy in General Relativity. *Physical Review*, *116*(5), 1322–1330. https://doi.org/10.1103/PhysRev.116.1322

Arons, J. (1983). Pair creation above pulsar polar caps : geometrical structure and energetics of slot gaps. ApJ, *266*, 215–241. https://doi.org/10.1086/160771

Arons, J., & Scharlemann, E. T. (1979). Pair formation above pulsar polar caps: structure of the low altitude acceleration zone. ApJ, *231*, 854–879. https://doi.org/10.1086/157250

Baade, W., & Zwicky, F. (1934). Remarks on Super-Novae and Cosmic Rays. *Physical Review*, *46*(1), 76–77. https://doi.org/10.1103/PhysRev.46.76.2

Babcock, H. W. (1953). The Possibility of Compensating Astronomical Seeing. PASP, *65*(386), 229. https://doi.org/10.1086/126606

Bacchini, F., Amaya, J., & Lapenta, G. (2019). The relativistic implicit Particle-in-Cell method, In *Journal of physics conference series*. https://doi.org/10.1088/1742-6596/1225/1/012011

Bai, X.-N., Caprioli, D., Sironi, L., & Spitkovsky, A. (2015). Magnetohydrodynamic-particle-in-cell Method for Coupling Cosmic Rays with a Thermal Plasma: Application to Non-relativistic Shocks. ApJ, *809*(1)arXiv 1412.1087, 55. https://doi.org/10.1088/0004-637X/809/1/55

Beck, A., Frederiksen, J. T., & Dérouillat, J. (2016). Load management strategy for Particle-In-Cell simulations in high energy particle acceleration. *Nuclear Instruments and Methods in Physics Research A*, *829*arXiv 1511.03878, 418–421. https://doi.org/10.1016/j.nima.2016.03.112

Begelman, M., & Rees, M. (2020). *Gravity's fatal attraction: Black holes in the universe* (3rd ed.). Cambridge University Press.

Belyaev, M. A. (2015). Dissipation, energy transfer, and spin-down luminosity in 2.5D PIC simulations of the pulsar magnetosphere. MNRAS, *449*(3)arXiv 1412.2819, 2759–2767. https://doi.org/10.1093/mnras/stv468

Beskin, V. S. (2010). *MHD Flows in Compact Astrophysical Objects*. https://doi.org/10.1007/978-3-642-01290-7

Birdsall, C. K., & Langdon, A. B. (1991). *Plasma Physics via Computer Simulation*.

Blandford, R. D., & Znajek, R. L. (1977). Electromagnetic extraction of energy from Kerr black holes. MNRAS, *179*, 433–456. https://doi.org/10.1093/mnras/179.3.433

Blandford, R., Meier, D., & Readhead, A. (2019). Relativistic Jets from Active Galactic Nuclei. ARA&A, *57*arXiv 1812.06025, 467–509. https://doi.org/10.1146/annurev-astro-081817-051948

Blandford, R. D. (2002). To the Lighthouse (M. Gilfanov, R. Sunyeav, & E. Churazov, Eds.). In M. Gilfanov, R. Sunyeav, & E. Churazov (Eds.), *Lighthouses of the universe: The most luminous celestial objects and their use for cosmology*. https://doi.org/10.1007/10856495_59

Blumenthal, G. R., & Gould, R. J. (1970). Bremsstrahlung, Synchrotron Radiation, and Compton Scattering of High-Energy Electrons Traversing Dilute Gases. *Reviews of Modern Physics*, *42*(2), 237–271. https://doi.org/10.1103/RevModPhys.42.237

Bogovalov, S. V. (1999). On the physics of cold MHD winds from oblique rotators. A&A, *349*arXiv astro-ph/9907051, 1017–1026. https://doi.org/10.48550/arXiv.astro-ph/9907051

Boris, J. P. (1970). Proceedings: Fourth Conference on Numerical Simulation of Plasmas, November 2, 3, 1970.

Bransgrove, A., Beloborodov, A. M., & Levin, Y. (2023). Radio Emission and Electric Gaps in Pulsar Magnetospheres. ApJ, *958*(1)arXiv 2209.11362, L9. https://doi.org/10.3847/2041-8213/ad0556

Browning, R., Ramsden, D., & Wright, P. J. (1971). Detection of Pulsed Gamma Radiation from the Crab Nebula. *Nature Physical Science*, *232*(31), 99–101. https://doi.org/10.1038/physci232099a0

Bühler, R., & Blandford, R. (2014). The surprising Crab pulsar and its nebula: a review. *Reports on Progress in Physics*, *77*(6)arXiv 1309.7046, 066901. https://doi.org/10.1088/0034-4885/77/6/066901

Capdessus, R., d'Humières, E., & Tikhonchuk, V. T. (2012). Modeling of radiation losses in ultrahigh power laser-matter interaction. Phys. Rev. E, *86*(3), 036401. https://doi.org/10.1103/PhysRevE.86.036401

Cerutti, B., & Philippov, A. A. (2017). Dissipation of the striped pulsar wind. A&A, *607*arXiv 1710.07320, A134. https://doi.org/10.1051/0004-6361/201731680

Cerutti, B., Werner, G. R., Uzdensky, D. A., & Begelman, M. C. (2012). Beaming and Rapid Variability of High-energy Radiation from Relativistic Pair Plasma Reconnection. ApJ, *754*(2)arXiv 1205.3210, L33. https://doi.org/10.1088/2041-8205/754/2/L33

Cerutti, B., Werner, G. R., Uzdensky, D. A., & Begelman, M. C. (2013). Simulations of Particle Acceleration beyond the Classical Synchrotron Burnoff Limit in Magnetic Reconnection: An Explanation of the Crab Flares. ApJ, *770*(2)arXiv 1302.6247, 147. https://doi.org/10.1088/0004-637X/770/2/147

Cerutti, B., & Beloborodov, A. M. (2017). Electrodynamics of Pulsar Magnetospheres. Space Sci. Rev., *207*(1-4)arXiv 1611.04331, 111–136. https://doi.org/10.1007/s11214-016-0315-7

Cerutti, B., Mortier, J., & Philippov, A. A. (2016). Polarized synchrotron emission from the equatorial current sheet in gamma-ray pulsars. MNRAS, *463*(1)arXiv 1609.00021, L89–L93. https://doi.org/10.1093/mnrasl/slw162

Cerutti, B., Philippov, A., Parfrey, K., & Spitkovsky, A. (2015). Particle acceleration in axisymmetric pulsar current sheets. MNRAS, *448*(1)arXiv 1410.3757, 606–619. https://doi.org/10.1093/mnras/stv042

Cerutti, B., Philippov, A. A., & Dubus, G. (2020). Dissipation of the striped pulsar wind and non-thermal particle acceleration: 3D PIC simulations. A&A, *642*arXiv 2008.11462, A204. https://doi.org/10.1051/0004-6361/202038618

Cerutti, B., Philippov, A. A., & Spitkovsky, A. (2016). Modelling high-energy pulsar light curves from first principles. MNRAS, *457*(3)arXiv 1511.01785, 2401–2414. https://doi.org/10.1093/mnras/stw124

Chadwick, J. (1932). Possible Existence of a Neutron. Nature, *129*(3252), 312. https://doi.org/10.1038/129312a0

Chandrasekhar, S. (1935). The highly collapsed configurations of a stellar mass (Second paper). MNRAS, *95*, 207–225. https://doi.org/10.1093/mnras/95.3.207

Chen, A. Y., & Beloborodov, A. M. (2014). Electrodynamics of Axisymmetric Pulsar Magnetosphere with Electron-Positron Discharge: A Numerical Experiment. ApJ, *795*(1)arXiv 1406.7834, L22. https://doi.org/10.1088/2041-8205/795/1/L22

Chen, A. Y., & Beloborodov, A. M. (2017). Particle-in-Cell Simulations of the Twisted Magnetospheres of Magnetars. I. ApJ, *844*(2)arXiv 1610.10036, 133. https://doi.org/10.3847/1538-4357/aa7a57

Chen, Y., Tóth, G., Zhou, H., & Wang, X. (2023). FLEKS: A flexible particle-in-cell code for multi-scale plasma simulations. *Computer Physics Communications*, *287*, 108714. https://doi.org/10.1016/j.cpc.2023.108714

Cheng, K. S., Ho, C., & Ruderman, M. (1986). Energetic Radiation from Rapidly Spinning Pulsars. I. Outer Magnetosphere Gaps. ApJ, *300*, 500. https://doi.org/10.1086/163829

Contopoulos, I., Kazanas, D., & Fendt, C. (1999). The Axisymmetric Pulsar Magnetosphere. ApJ, *511*(1)arXiv astro-ph/9903049, 351–358. https://doi.org/10.1086/306652

Courant, R., Friedrichs, K., & Lewy, H. (1928). Über die partiellen Differenzengleichungen der mathematischen Physik. *Mathematische Annalen*, *100*, 32–74. https://doi.org/10.1007/BF01448839

Crinquand, B., Cerutti, B., Dubus, G., Parfrey, K., & Philippov, A. (2022). Synthetic Images of Magnetospheric Reconnection-Powered Radiation around Supermassive Black Holes. Phys. Rev. Lett., *129*(20)arXiv 2202.04472, 205101. https://doi.org/10.1103/PhysRevLett.129.205101

Crinquand, B., Cerutti, B., Philippov, A., Parfrey, K., & Dubus, G. (2020). Multidimensional Simulations of Ergospheric Pair Discharges around Black Holes. Phys. Rev. Lett., *124*(14)arXiv 2003.03548, 145101. https://doi.org/10.1103/PhysRevLett.124.145101

Daldorff, L. K. S., Tóth, G., Gombosi, T. I., Lapenta, G., Amaya, J., Markidis, S., & Brackbill, J. U. (2014). Two-way coupling of a global Hall magnetohydrodynamics model with a local implicit particle-in-cell model. *Journal of Computational Physics*, *268*, 236–254. https://doi.org/10.1016/j.jcp.2014.03.009

Daugherty, J. K., & Harding, A. K. (1983). Pair production in superstrong magnetic fields. ApJ, *273*, 761–773. https://doi.org/10.1086/161411

Deutsch, A. J. (1955). The electromagnetic field of an idealized star in rigid rotation in vacuo. *Annales d'Astrophysique*, *18*, 1.

Djannati-Ataï, A. (2022). H.E.S.S. discovery of 20 TeV gamma-ray pulsations from the Vela pulsar, In *31st texas symposium on relativistic astrophysics*.

Eckart, A., Baganoff, F. K., Schödel, R., Morris, M., Genzel, R., Bower, G. C., Marrone, D., Moran, J. M., Viehmann, T., Bautz, M. W., Brandt, W. N., Garmire, G. P., Ott, T., Trippe, S., Ricker, G. R., Straubmeier, C., Roberts, D. A., Yusef-Zadeh, F., Zhao, J. H., & Rao, R. (2006). The flare activity of Sagittarius A*. New coordinated mm to X-ray observations. A&A, *450*(2)arXiv astro-ph/0512440, 535–555. https://doi.org/10.1051/0004-6361:20054418

El Mellah, I., Cerutti, B., Crinquand, B., & Parfrey, K. (2022). Spinning black holes magnetically connected to a Keplerian disk. Magnetosphere, reconnection sheet, particle acceleration, and coronal heating. A&A, *663*arXiv 2112.03933, A169. https://doi.org/10.1051/0004-6361/202142847

Erber, T. (1966). High-Energy Electromagnetic Conversion Processes in Intense Magnetic Fields. *Reviews of Modern Physics*, *38*(4), 626–659. https://doi.org/10.1103/RevModPhys.38.626

Esirkepov, T. Z. (2001). Exact charge conservation scheme for Particle-in-Cell simulation with an arbitrary form-factor. *Computer Physics Communications*, *135*(2), 144–153. https://doi.org/10.1016/S0010-4655(00)00228-9

Event Horizon Telescope Collaboration, Akiyama, K., Alberdi, A., Alef, W., Algaba, J. C., Anantua, R., Asada, K., Azulay, R., Bach, U., Baczko, A.-K., Ball, D., Baloković, M., Barrett, J., Bauböck, M., Benson, B. A., Bintley, D., Blackburn, L., Blundell, R., Bouman, K. L., … White, C. (2022). First Sagittarius A* Event Horizon Telescope Results. V. Testing Astrophysical Models of the Galactic Center Black Hole. ApJ, *930*(2), L16. https://doi.org/10.3847/2041-8213/ac6672

Event Horizon Telescope Collaboration, Akiyama, K., Alberdi, A., Alef, W., Asada, K., Azulay, R., Baczko, A.-K., Ball, D., Baloković, M., Barrett, J., Bintley, D., Blackburn, L., Boland, W., Bouman, K. L., Bower, G. C., Bremer, M., Brinkerink, C. D., Brissenden, R., Britzen, S., … Ziurys, L. (2019). First M87 Event Horizon Telescope Results. I. The Shadow of the Supermassive Black Hole. ApJ, *875*(1)arXiv 1906.11238, L1. https://doi.org/10.3847/2041-8213/ab0ec7

Event Horizon Telescope Collaboration, Akiyama, K., Algaba, J. C., Alberdi, A., Alef, W., Anantua, R., Asada, K., Azulay, R., Baczko, A.-K., Ball, D., Baloković, M., Barrett, J., Benson, B. A., Bintley, D., Blackburn, L., Blundell, R., Boland, W., Bouman, K. L., Bower, G. C., … Zhao, S.-S. (2021). First M87 Event Horizon Telescope Results. VIII. Magnetic Field Structure near The Event Horizon. ApJ, *910*(1)arXiv 2105.01173, L13. https://doi.org/10.3847/2041-8213/abe4de

Falcke, H., Melia, F., & Agol, E. (2000). Viewing the Shadow of the Black Hole at the Galactic Center. ApJ, *528*(1)arXiv astro-ph/9912263, L13–L16. https://doi.org/10.1086/312423

Ferraro, V. C. A. (1937). The non-uniform rotation of the Sun and its magnetic field. MNRAS, *97*, 458. https://doi.org/10.1093/mnras/97.6.458

Fonseca, R. A., Silva, L. O., Tsung, F. S., Decyk, V. K., Lu, W., Ren, C., Mori, W. B., Deng, S., Lee, S., Katsouleas, T., & Adam, J. C. (2002). Osiris: A three-dimensional, fully

relativistic particle in cell code for modeling plasma based accelerators (P. M. A. Sloot, A. G. Hoekstra, C. J. K. Tan, & J. J. Dongarra, Eds.). In P. M. A. Sloot, A. G. Hoekstra, C. J. K. Tan, & J. J. Dongarra (Eds.), *Computational science — iccs 2002*, Berlin, Heidelberg, Springer Berlin Heidelberg.

Ganse, U., Koskela, T., Battarbee, M., Pfau-Kempf, Y., Papadakis, K., Alho, M., Bussov, M., Cozzani, G., Dubart, M., George, H., Gordeev, E., Grandin, M., Horaites, K., Suni, J., Tarvus, V., Kebede, F. T., Turc, L., Zhou, H., & Palmroth, M. (2023). Enabling technology for global 3D + 3V hybrid-Vlasov simulations of near-Earth space. *Physics of Plasmas*, *30*(4), 042902. https://doi.org/10.1063/5.0134387

Gargaté, L., Bingham, R., Fonseca, R. A., & Silva, L. O. (2007). dHybrid: A massively parallel code for hybrid simulations of space plasmas. *Computer Physics Communications*, *176*(6)arXiv physics/0611174, 419–425. https://doi.org/10.1016/j.cpc.2006.11.013

Gillessen, S., Eisenhauer, F., Trippe, S., Alexander, T., Genzel, R., Martins, F., & Ott, T. (2009). Monitoring Stellar Orbits Around the Massive Black Hole in the Galactic Center. ApJ, *692*(2)arXiv 0810.4674, 1075–1109. https://doi.org/10.1088/0004-637X/692/2/1075

Gold, T. (1968). Rotating Neutron Stars as the Origin of the Pulsating Radio Sources. Nature, *218*(5143), 731–732. https://doi.org/10.1038/218731a0

Goldreich, P., & Julian, W. H. (1969). Pulsar Electrodynamics. ApJ, *157*, 869. https://doi.org/10.1086/150119

GRAVITY Collaboration, Abuter, R., Amorim, A., Bauböck, M., Berger, J. P., Bonnet, H., Brandner, W., Cardoso, V., Clénet, Y., de Zeeuw, P. T., Dexter, J., Eckart, A., Eisenhauer, F., Förster Schreiber, N. M., Garcia, P., Gao, F., Gendron, E., Genzel, R., Gillessen, S., … Zins, G. (2020). Detection of the Schwarzschild precession in the orbit of the star S2 near the Galactic centre massive black hole. A&A, *636*arXiv 2004.07187, L5. https://doi.org/10.1051/0004-6361/202037813

GRAVITY Collaboration, Abuter, R., Amorim, A., Bauböck, M., Berger, J. P., Bonnet, H., Brandner, W., Clénet, Y., Coudé du Foresto, V., de Zeeuw, P. T., Deen, C., Dexter, J., Duvert, G., Eckart, A., Eisenhauer, F., Förster Schreiber, N. M., Garcia, P., Gao, F., Gendron, E., … Yazici, S. (2018). Detection of orbital motions near the last stable circular orbit of the massive black hole SgrA*. A&A, *618*arXiv 1810.12641, L10. https://doi.org/10.1051/0004-6361/201834294

Gruzinov, A. (1999). Stability in Force-Free Electrodynamics. *arXiv e-prints*arXiv astro-ph/9902288, astro–ph/9902288. https://doi.org/10.48550/arXiv.astro-ph/9902288

Gruzinov, A. (2005). Power of an Axisymmetric Pulsar. Phys. Rev. Lett., *94*(2)arXiv astro-ph/0407279, 021101. https://doi.org/10.1103/PhysRevLett.94.021101

Guépin, C., Cerutti, B., & Kotera, K. (2020). Proton acceleration in pulsar magnetospheres. A&A, *635*arXiv 1910.11387, A138. https://doi.org/10.1051/0004-6361/201936816

Guo, F., Li, H., Daughton, W., & Liu, Y.-H. (2014). Formation of Hard Power Laws in the Energetic Particle Spectra Resulting from Relativistic Magnetic Reconnection. Phys. Rev. Lett., *113*(15)arXiv 1405.4040, 155005. https://doi.org/10.1103/PhysRevLett.113.155005

H. E. S. S. Collaboration, Aharonian, F., Ait Benkhali, F., Aschersleben, J., Ashkar, H., Backes, M., Barbosa Martins, V., Batzofin, R., Becherini, Y., Berge, D., Bernlöhr, K., Bi, B., Böttcher, M., Boisson, C., Bolmont, J., de Bony de Lavergne, M., Borowska, J., Bradascio, F., Breuhaus, M., … Smith, D. A. (2023). Discovery of a radiation component from the Vela pulsar reaching 20 teraelectronvolts. *Nature Astronomy*, *7*arXiv 2310.06181, 1341–1350. https://doi.org/10.1038/s41550-023-02052-3

Hakobyan, H., Philippov, A., & Spitkovsky, A. (2019). Effects of Synchrotron Cooling and Pair Production on Collisionless Relativistic Reconnection. ApJ, *877*(1)arXiv 1809.10772, 53. https://doi.org/10.3847/1538-4357/ab191b

Hakobyan, H., Philippov, A., & Spitkovsky, A. (2023). Magnetic Energy Dissipation and γ-Ray Emission in Energetic Pulsars. ApJ, *943*(2)arXiv 2209.02121, 105. https://doi.org/10.3847/1538-4357/acab05

Hakobyan, H., Spitkovsky, A., Chernoglazov, A., Philippov, A., Groselj, D., & Mahlmann, J. (2023). *PrincetonUniversity/tristan-mp-v2: v2.6* (Version v2.6). Zenodo. https://doi.org/10.5281/zenodo.7566725

Harding, A. K., & Lai, D. (2006). Physics of strongly magnetized neutron stars. *Reports on Progress in Physics*, *69*(9)arXiv astro-ph/0606674, 2631–2708. https://doi.org/10.1088/0034-4885/69/9/R03

Hewish, A., Bell, S. J., Pilkington, J. D. H., Scott, P. F., & Collins, R. A. (1968). Observation of a Rapidly Pulsating Radio Source. Nature, *217*(5130), 709–713. https://doi.org/10.1038/217709a0

Hoyle, F., Narlikar, J. V., & Wheeler, J. A. (1964). Electromagnetic Waves from Very Dense Stars. Nature, *203*(4948), 914–916. https://doi.org/10.1038/203914a0

Hu, R., & Beloborodov, A. M. (2022). Axisymmetric Pulsar Magnetosphere Revisited. ApJ, *939*(1)arXiv 2109.03935, 42. https://doi.org/10.3847/1538-4357/ac961d

Jennison, R. C., & Das Gupta, M. K. (1953). Fine Structure of the Extra-terrestrial Radio Source Cygnus I. Nature, *172*(4387), 996–997. https://doi.org/10.1038/172996a0

Kalapotharakos, C., & Contopoulos, I. (2009). Three-dimensional numerical simulations of the pulsar magnetosphere: preliminary results. A&A, *496*(2)arXiv 0811.2863, 495–502. https://doi.org/10.1051/0004-6361:200810281

Kalapotharakos, C., Brambilla, G., Timokhin, A., Harding, A. K., & Kazanas, D. (2018). Three-dimensional Kinetic Pulsar Magnetosphere Models: Connecting to Gamma-Ray Observations. ApJ, *857*(1)arXiv 1710.03170, 44. https://doi.org/10.3847/1538-4357/aab550

Kerr, R. P. (1963). Gravitational Field of a Spinning Mass as an Example of Algebraically Special Metrics. Phys. Rev. Lett., *11*(5), 237–238. https://doi.org/10.1103/PhysRevLett.11.237

Kirk, J. G. (2004). Particle Acceleration in Relativistic Current Sheets. Phys. Rev. Lett., *92*(18)arXiv astro-ph/0403516, 181101. https://doi.org/10.1103/PhysRevLett.92.181101

Komissarov, S. S. (2004). Electrodynamics of black hole magnetospheres. MNRAS, *350*(2), 427–448. https://doi.org/10.1111/j.1365-2966.2004.07598.x

Komissarov, S. S. (2006). Simulations of the axisymmetric magnetospheres of neutron stars. MNRAS, *367*(1)arXiv astro-ph/0510310, 19–31. https://doi.org/10.1111/j.1365-2966.2005.09932.x

Komissarov, S. S. (2011). 3+1 magnetodynamics. MNRAS, *418*(1)arXiv 1108.3511, L94–L98. https://doi.org/10.1111/j.1745-3933.2011.01150.x

Krause-Polstorff, J., & Michel, F. C. (1985). Electrosphere of an aligned magnetized neutron star. MNRAS, *213*, 43. https://doi.org/10.1093/mnras/213.1.43P

Kunz, M. W., Stone, J. M., & Bai, X.-N. (2014). Pegasus: A new hybrid-kinetic particle-in-cell code for astrophysical plasma dynamics. *Journal of Computational Physics*, *259*arXiv 1311.4865, 154–174. https://doi.org/10.1016/j.jcp.2013.11.035

Landau, L. D., & Lifshitz, E. M. (1971). *The classical theory of fields* (Landau, L. D. & Lifshitz, E. M., Ed.).

Laplace, P. S. (1799). Beweis des Satzes, dass die anziehende Kraft bey einem Weltkörper so groß seyn könne, dass das Licht davon nicht ausströmen kann. *Allgemeine Geographische Ephemeriden*, *4*(1), 1–6.

Levinson, A., & Cerutti, B. (2018). Particle-in-cell simulations of pair discharges in a starved magnetosphere of a Kerr black hole. A&A, *616*arXiv 1803.04427, A184. https://doi.org/10.1051/0004-6361/201832915

Li, D., Chen, Y., Dong, C., Wang, L., & Toth, G. (2023). Numerical study of magnetic island coalescence using magnetohydrodynamics with adaptively embedded particle-in-cell model. *AIP Advances*, *13*(1)arXiv 2212.07980, 015126. https://doi.org/10.1063/5.0122087

Li, J., Spitkovsky, A., & Tchekhovskoy, A. (2012). Resistive Solutions for Pulsar Magnetospheres. ApJ, *746*(1)arXiv 1107.0979, 60. https://doi.org/10.1088/0004-637X/746/1/60

Li, Y., Campos Pinto, M., Holderied, F., Possanner, S., & Sonnendrücker, E. (2024). Geometric Particle-In-Cell discretizations of a plasma hybrid model with kinetic ions and mass-less fluid electrons. *Journal of Computational Physics*, *498*arXiv 2304.01891, 112671. https://doi.org/10.1016/j.jcp.2023.112671

Lovelace, R. V. E., Sutton, J. M., & Craft, H. D. (1968). Pulsar NP 0532 Near Crab Nebula. IAU Circ., *2113*, 1.

Lucek, S. G., & Bell, A. R. (2000). Non-linear amplification of a magnetic field driven by cosmic ray streaming. MNRAS, *314*(1), 65–74. https://doi.org/10.1046/j.1365-8711.2000.03363.x

Luminet, J. .-P. (1979). Image of a spherical black hole with thin accretion disk. A&A, *75*, 228–235.

Lyubarskii, Y. E. (1990). Equilibrium of the Return Current Sheet and the Structure of the Pulsar Magnetosphere. *Soviet Astronomy Letters*, *16*, 16.

Lyubarskii, Y. E. (1996). A model for the energetic emission from pulsars. A&A, *311*, 172–178.

Lyutikov, M. (2003). Explosive reconnection in magnetars. MNRAS, *346*(2)arXiv astro-ph/0303384, 540–554. https://doi.org/10.1046/j.1365-2966.2003.07110.x

Lyutikov, M., & Uzdensky, D. (2003). Dynamics of Relativistic Reconnection. ApJ, *589*(2)arXiv astro-ph/0210206, 893–901. https://doi.org/10.1086/374808

Mahlmann, J. F., & Aloy, M. A. (2022). Diffusivity in force-free simulations of global magnetospheres. MNRAS, *509*(1)arXiv 2109.13936, 1504–1520. https://doi.org/10.1093/mnras/stab2830

Mahlmann, J. F., Aloy, M. A., Mewes, V., & Cerdá-Durán, P. (2021). Computational general relativistic force-free electrodynamics. II. Characterization of numerical diffusivity. A&A, *647*arXiv 2007.06599, A58. https://doi.org/10.1051/0004-6361/202038908

Makwana, K., Keppens, R., & Lapenta, G. (2018). Two-way coupled MHD-PIC simulations of magnetic reconnection in magnetic island coalescence, In *Journal of physics conference series*. https://doi.org/10.1088/1742-6596/1031/1/012019

Manchester, R. N., Hobbs, G. B., Teoh, A., & Hobbs, M. (2005). The Australia Telescope National Facility Pulsar Catalogue. AJ, *129*(4)arXiv astro-ph/0412641, 1993–2006. https://doi.org/10.1086/428488

McKinney, J. C. (2006). General relativistic force-free electrodynamics: a new code and applications to black hole magnetospheres. MNRAS, *367*(4)arXiv astro-ph/0601410, 1797–1807. https://doi.org/10.1111/j.1365-2966.2006.10087.x

Melzani, M., Walder, R., Folini, D., Winisdoerffer, C., & Favre, J. M. (2014). The energetics of relativistic magnetic reconnection: ion-electron repartition and particle distribution hardness. A&A, *570*arXiv 1405.2938, A112. https://doi.org/10.1051/0004-6361/201424193

Michel, F. C. (1979). Vacuum gaps in pulsar magnetospheres. ApJ, *227*, 579–589. https://doi.org/10.1086/156768

Michel, F. C., & Li, H. (1999). Electrodynamics of neutron stars. Phys. Rep., *318*(6), 227–297. https://doi.org/10.1016/S0370-1573(99)00002-2

Michel, F. C., & Smith, I. A. (2001). Axisymmetric Rotator Models as Pulsars: Abject Failure, In *Revista mexicana de astronomia y astrofisica conference series*.

Michel, F. C. (1973). Rotating Magnetospheres: an Exact 3-D Solution. ApJ, *180*, L133. https://doi.org/10.1086/181169

Michell, J. (1784). On the Means of Discovering the Distance, Magnitude, &c. of the Fixed Stars, in Consequence of the Diminution of the Velocity of Their Light, in Case Such a Diminution Should be Found to Take Place in any of Them, and Such Other Data Should be Procured from Observations, as Would be Farther Necessary for That Purpose. By the Rev. John Michell, B. D. F. R. S. In a Letter to Henry Cavendish, Esq. F. R. S. and A. S. *Philosophical Transactions of the Royal Society of London Series I*, *74*, 35–57.

Mignone, A., Bodo, G., Vaidya, B., & Mattia, G. (2018). A Particle Module for the PLUTO Code. I. An Implementation of the MHD-PIC Equations. ApJ, *859*(1)arXiv 1804.01946, 13. https://doi.org/10.3847/1538-4357/aabccd

Miller-Jones, J. C. A., Bahramian, A., Orosz, J. A., Mandel, I., Gou, L., Maccarone, T. J., Neijssel, C. J., Zhao, X., Ziółkowski, J., Reid, M. J., Uttley, P., Zheng, X., Byun, D.-Y., Dodson, R., Grinberg, V., Jung, T., Kim, J.-S., Marcote, B., Markoff, S., … Wilms, J. (2021). Cygnus X-1 contains a 21-solar mass black hole—Implications for massive star winds. *Science*, *371*(6533)arXiv 2102.09091, 1046–1049. https://doi.org/10.1126/science.abb3363

Moffett, D. A., & Hankins, T. H. (1996). Multifrequency Radio Observations of the Crab Pulsar. ApJ, *468*arXiv astro-ph/9604163, 779. https://doi.org/10.1086/177734

Muslimov, A. G., & Harding, A. K. (2003). Extended Acceleration in Slot Gaps and Pulsar High-Energy Emission. ApJ, *588*(1)arXiv astro-ph/0301023, 430–440. https://doi.org/10.1086/368162

Muslimov, A. G., & Harding, A. K. (2004). High-Altitude Particle Acceleration and Radiation in Pulsar Slot Gaps. ApJ, *606*(2)arXiv astro-ph/0402462, 1143–1153. https://doi.org/10.1086/383079

Nalewajko, K., Uzdensky, D. A., Cerutti, B., Werner, G. R., & Begelman, M. C. (2015). On the Distribution of Particle Acceleration Sites in Plasmoid-dominated Relativistic Magnetic Reconnection. ApJ, *815*(2)arXiv 1508.02392, 101. https://doi.org/10.1088/0004-637X/815/2/101

Narayan, R., Johnson, M. D., & Gammie, C. F. (2019). The Shadow of a Spherically Accreting Black Hole. ApJ, *885*(2)arXiv 1910.02957, L33. https://doi.org/10.3847/2041-8213/ab518c

Oppenheimer, J. R., & Volkoff, G. M. (1939). On Massive Neutron Cores. *Physical Review*, *55*(4), 374–381. https://doi.org/10.1103/PhysRev.55.374

Ostriker, J. P., & Gunn, J. E. (1969). On the Nature of Pulsars. I. Theory. ApJ, *157*, 1395. https://doi.org/10.1086/150160

Özel, F., & Freire, P. (2016). Masses, Radii, and the Equation of State of Neutron Stars. ARA&A, *54*arXiv 1603.02698, 401–440. https://doi.org/10.1146/annurev-astro-081915-023322

Pacini, F. (1967). Energy Emission from a Neutron Star. Nature, *216*(5115), 567–568. https://doi.org/10.1038/216567a0

Pacini, F. (1968). Rotating Neutron Stars, Pulsars and Supernova Remnants. Nature, *219*(5150), 145–146. https://doi.org/10.1038/219145a0

Paczynski, B. (1974). Mass of Cygnus X-1. A&A, *34*, 161–162.

Palmroth, M., Honkonen, I., Sandroos, A., Kempf, Y., von Alfthan, S., & Pokhotelov, D. (2013). Preliminary testing of global hybrid-Vlasov simulation: Magnetosheath and

cusps under northward interplanetary magnetic field. *Journal of Atmospheric and Solar-Terrestrial Physics*, *99*, 41–46. https://doi.org/10.1016/j.jastp.2012.09.013

Palmroth, M., Ganse, U., Pfau-Kempf, Y., Battarbee, M., Turc, L., Brito, T., Grandin, M., Hoilijoki, S., Sandroos, A., & von Alfthan, S. (2018). Vlasov methods in space physics and astrophysics. *Living Reviews in Computational Astrophysics*, *4*(1)arXiv 1808.05885, 1. https://doi.org/10.1007/s41115-018-0003-2

Panuzzo, P., Mazeh, T., Arenou, F., Holl, B., Caffau, E., Jorissen, A., Babusiaux, C., Gavras, P., Sahlmann, J., Bastian, U., Wyrzykowski, Ł., Eyer, L., Leclerc, N., Bauchet, N., Bombrun, A., Mowlavi, N., Seabroke, G., Teyssier, D., Balbinot, E., … Zwitter, T. (2024). Discovery of a dormant 33 solar-mass black hole in pre-release Gaia astrometry. *arXiv e-prints*arXiv 2404.10486, arXiv:2404.10486. https://doi.org/10.48550/arXiv.2404.10486

Parfrey, K., Beloborodov, A. M., & Hui, L. (2012). Introducing PHAEDRA: a new spectral code for simulations of relativistic magnetospheres. MNRAS, *423*(2)arXiv 1110.6669, 1416–1436. https://doi.org/10.1111/j.1365-2966.2012.20969.x

Parfrey, K., Philippov, A., & Cerutti, B. (2019). First-Principles Plasma Simulations of Black-Hole Jet Launching. Phys. Rev. Lett., *122*(3)arXiv 1810.03613, 035101. https://doi.org/10.1103/PhysRevLett.122.035101

Parfrey, K., Spitkovsky, A., & Beloborodov, A. M. (2017). Simulations of the magnetospheres of accreting millisecond pulsars. MNRAS, *469*(3)arXiv 1608.04159, 3656–3669. https://doi.org/10.1093/mnras/stx950

Parfrey, K., & Tchekhovskoy, A. (2017). General-relativistic Simulations of Four States of Accretion onto Millisecond Pulsars. ApJ, *851*(2)arXiv 1708.06362, L34. https://doi.org/10.3847/2041-8213/aa9c85

Parfrey, K., & Tchekhovskoy, A. (2023). Accreting Neutron Stars in 3D GRMHD Simulations: Jets, Magnetic Polarity, and the Interchange Slingshot. *arXiv e-prints*arXiv 2311.04291, arXiv:2311.04291. https://doi.org/10.48550/arXiv.2311.04291

Parker, E. N. (1957). Sweet's Mechanism for Merging Magnetic Fields in Conducting Fluids. J. Geophys. Res., *62*(4), 509–520. https://doi.org/10.1029/JZ062i004p00509

Pétri, J. (2012). The pulsar force-free magnetosphere linked to its striped wind: time-dependent pseudo-spectral simulations. MNRAS, *424*(1)arXiv 1205.0889, 605–619. https://doi.org/10.1111/j.1365-2966.2012.21238.x

Petropoulou, M., & Sironi, L. (2018). The steady growth of the high-energy spectral cut-off in relativistic magnetic reconnection. MNRAS, *481*(4)arXiv 1808.00966, 5687–5701. https://doi.org/10.1093/mnras/sty2702

Philippov, A., & Kramer, M. (2022). Pulsar Magnetospheres and Their Radiation. ARA&A, *60*, 495–558. https://doi.org/10.1146/annurev-astro-052920-112338

Philippov, A. A., & Spitkovsky, A. (2014). Ab Initio Pulsar Magnetosphere: Three-dimensional Particle-in-cell Simulations of Axisymmetric Pulsars. ApJ, *785*(2)arXiv 1312.4970, L33. https://doi.org/10.1088/2041-8205/785/2/L33

Philippov, A. A., & Spitkovsky, A. (2018). Ab-initio Pulsar Magnetosphere: Particle Acceleration in Oblique Rotators and High-energy Emission Modeling. ApJ, *855*(2)arXiv 1707.04323, 94. https://doi.org/10.3847/1538-4357/aaabbc

Philippov, A. A., Spitkovsky, A., & Cerutti, B. (2015). Ab Initio Pulsar Magnetosphere: Three-dimensional Particle-in-cell Simulations of Oblique Pulsars. ApJ, *801*(1)arXiv 1412.0673, L19. https://doi.org/10.1088/2041-8205/801/1/L19

Press, W. H., Teukolsky, S. A., Vetterling, W. T., & Flannery, B. P. (2007). *Numerical recipes 3rd edition: The art of scientific computing*. Cambridge university press.

Qin, H., Zhang, S., Xiao, J., Liu, J., Sun, Y., & Tang, W. M. (2013). Why is Boris algorithm so good? *Physics of Plasmas*, *20*(8), 084503. https://doi.org/10.1063/1.4818428

Ramachandran, O. H., Kempel, L. C., Luginsland, J., & Shanker, B. (2023). A Charge Conserving Exponential Predictor Corrector FEMPIC Formulation for Relativistic Particle Simulations. *IEEE Transactions on Plasma Science*, *51*(4)arXiv 2303.08037, 987–997. https://doi.org/10.1109/TPS.2023.3244030

Rhoades, C. E., & Ruffini, R. (1974). Maximum Mass of a Neutron Star. Phys. Rev. Lett., *32*(6), 324–327. https://doi.org/10.1103/PhysRevLett.32.324

Ruderman, M. A., & Sutherland, P. G. (1975). Theory of pulsars: polar gaps, sparks, and coherent microwave radiation. ApJ, *196*, 51–72. https://doi.org/10.1086/153393

Salpeter, E. E. (1964). Accretion of Interstellar Matter by Massive Objects. ApJ, *140*, 796–800. https://doi.org/10.1086/147973

Scharlemann, E. T., & Wagoner, R. V. (1973). Aligned Rotating Magnetospheres. General Analysis. ApJ, *182*, 951–960. https://doi.org/10.1086/152195

Schwarzschild, K. (1916). Über das Gravitationsfeld eines Massenpunktes nach der Einsteinschen Theorie. *Sitzungsberichte der Königlich Preussischen Akademie der Wissenschaften*, 189–196.

Shou, Y., Tenishev, V., Chen, Y., Toth, G., & Ganushkina, N. (2021). Magnetohydrodynamic with Adaptively Embedded Particle-in-Cell model: MHD-AEPIC. *Journal of Computational Physics*, *446*arXiv 2108.05425, 110656. https://doi.org/10.1016/j.jcp.2021.110656

Sironi, L., & Cerutti, B. (2017). Particle Acceleration in Pulsar Wind Nebulae: PIC Modelling (D. F. Torres, Ed.). In D. F. Torres (Ed.), *Modelling pulsar wind nebulae*. https://doi.org/10.1007/978-3-319-63031-1_11

Sironi, L., & Spitkovsky, A. (2014). Relativistic Reconnection: An Efficient Source of Nonthermal Particles. ApJ, *783*(1)arXiv 1401.5471, L21. https://doi.org/10.1088/2041-8205/783/1/L21

Smith, D. A., Abdollahi, S., Ajello, M., Bailes, M., Baldini, L., Ballet, J., Baring, M. G., Bassa, C., Becerra Gonzalez, J., Bellazzini, R., Berretta, A., Bhattacharyya, B., Bissaldi, E., Bonino, R., Bottacini, E., Bregeon, J., Bruel, P., Burgay, M., Burnett, T. H., … Zhu, W. (2023). The Third Fermi Large Area Telescope Catalog of Gamma-Ray Pulsars. ApJ, *958*(2)arXiv 2307.11132, 191. https://doi.org/10.3847/1538-4357/acee67

Sokolov, I. V., Naumova, N. M., Nees, J. A., Mourou, G. A., & Yanovsky, V. P. (2009). Dynamics of emitting electrons in strong laser fields. *Physics of Plasmas*, *16*(9)arXiv 0904.0405, 093115. https://doi.org/10.1063/1.3236748

Soudais, A., Cerutti, B., & Contopoulos, I. (2024). Scaling up global kinetic models of pulsar magnetospheres using a hybrid force-free-PIC numerical approach. *arXiv e-prints*arXiv 2406.14512, arXiv:2406.14512. https://doi.org/10.48550/arXiv.2406.14512

Spitkovsky, A. (2006). Time-dependent Force-free Pulsar Magnetospheres: Axisymmetric and Oblique Rotators. ApJ, *648*(1)arXiv astro-ph/0603147, L51–L54. https://doi.org/10.1086/507518

Staelin, D. H., & Reifenstein, I., Edward C. (1968). Pulsating Radio Sources near the Crab Nebula. *Science*, *162*(3861), 1481–1483. https://doi.org/10.1126/science.162.3861.1481

Sturrock, P. A. (1971). A Model of Pulsars. ApJ, *164*, 529. https://doi.org/10.1086/150865

Sun, X., & Bai, X.-N. (2023). The magnetohydrodynamic-particle-in-cell module in ATHENA++: implementation and code tests. MNRAS, *523*(3)arXiv 2304.10568, 3328–3347. https://doi.org/10.1093/mnras/stad1548

Sweet, P. A. (1958). The Neutral Point Theory of Solar Flares (B. Lehnert, Ed.). In B. Lehnert (Ed.), *Electromagnetic phenomena in cosmical physics*.

Takahashi, R. (2007). Horizon-penetrating transonic accretion discs around rotating black holes. MNRAS, *382*(2)arXiv 0705.0048, 567–593. https://doi.org/10.1111/j.1365-2966.2007.11877.x

Tamburini, M., Pegoraro, F., Piazza, A. D., Keitel, C. H., & Macchi, A. (2010). Radiation reaction effects on radiation pressure acceleration. *New Journal of Physics*, *12*(12), 123005. https://doi.org/10.1088/1367-2630/12/12/123005

Tchekhovskoy, A., Spitkovsky, A., & Li, J. G. (2013). Time-dependent 3D magnetohydrodynamic pulsar magnetospheres: oblique rotators. MNRAS, *435*arXiv 1211.2803, L1–L5. https://doi.org/10.1093/mnrasl/slt076

The Event Horizon Telescope Collaboration. (2023). First Sagittarius A* Event Horizon Telescope Results. I. The Shadow of the Supermassive Black Hole in the Center of the Milky Way. *arXiv e-prints*arXiv 2311.08680, arXiv:2311.08680. https://doi.org/10.48550/arXiv.2311.08680

Thompson, D. J. (2004). Gamma Ray Pulsars (K. S. Cheng & G. E. Romero, Eds.). In K. S. Cheng & G. E. Romero (Eds.), *Cosmic gamma-ray sources*. https://doi.org/10.1007/978-1-4020-2256-2_7

Thorne, K. S., & MacDonald, D. (1982). Electrodynamics in Curved Spacetime - 3+1 Formulation. MNRAS, *198*, 339. https://doi.org/10.1093/mnras/198.2.339

Timokhin, A. N. (2006). On the force-free magnetosphere of an aligned rotator. MNRAS, *368*(3)arXiv astro-ph/0511817, 1055–1072. https://doi.org/10.1111/j.1365-2966.2006.10192.x

Torres, R., Grismayer, T., Cruz, F., Fonseca, R. A., & Silva, L. O. (2024). OSIRIS-GR: General relativistic activation of the polar cap of a compact neutron star. *arXiv e-prints*arXiv 2401.02908, arXiv:2401.02908.

Tückmantel, T., & Pukhov, A. (2014). H-VLPL: A three-dimensional relativistic PIC/fluid hybrid code. *Journal of Computational Physics*, *269*, 168–180. https://doi.org/10.1016/j.jcp.2014.03.019

Uchida, T. (1997). Theory of force-free electromagnetic fields. I. General theory. Phys. Rev. E, *56*(2), 2181–2197. https://doi.org/10.1103/PhysRevE.56.2181

Uzdensky, D. A., Loureiro, N. F., & Schekochihin, A. A. (2010). Fast Magnetic Reconnection in the Plasmoid-Dominated Regime. Phys. Rev. Lett., *105*(23)arXiv 1008.3330, 235002. https://doi.org/10.1103/PhysRevLett.105.235002

Uzdensky, D. A., Cerutti, B., & Begelman, M. C. (2011). Reconnection-powered Linear Accelerator and Gamma-Ray Flares in the Crab Nebula. ApJ, *737*(2)arXiv 1105.0942, L40. https://doi.org/10.1088/2041-8205/737/2/L40

van Marle, A. J., Casse, F., & Marcowith, A. (2018). On magnetic field amplification and particle acceleration near non-relativistic astrophysical shocks: particles in MHD cells simulations. MNRAS, *473*(3)arXiv 1709.08482, 3394–3409. https://doi.org/10.1093/mnras/stx2509

Villasenor, J., & Buneman, O. (1992). Rigorous charge conservation for local electromagnetic field solvers. *Computer Physics Communications*, *69*(2-3), 306–316. https://doi.org/10.1016/0010-4655(92)90169-Y

Vlasov, A. A. (1967). The vibrational properties of an electron gas. *Usp. Fiz. Nauk*, *93*(11), 444–470. https://doi.org/10.3367/UFNr.0093.196711f.0444

Vranic, M., Grismayer, T., Martins, J. L., Fonseca, R. A., & Silva, L. O. (2015). Particle merging algorithm for PIC codes. *Computer Physics Communications*, *191*arXiv 1411.2248, 65–73. https://doi.org/10.1016/j.cpc.2015.01.020

Wald, R. M. (1974). Black hole in a uniform magnetic field. Phys. Rev. D, *10*(6), 1680–1685. https://doi.org/10.1103/PhysRevD.10.1680

Weisskopf, M. C., Hester, J. J., Tennant, A. F., Elsner, R. F., Schulz, N. S., Marshall, H. L., Karovska, M., Nichols, J. S., Swartz, D. A., Kolodziejczak, J. J., & O'Dell, S. L. (2000).

Discovery of Spatial and Spectral Structure in the X-Ray Emission from the Crab Nebula. ApJ, *536*(2)arXiv astro-ph/0003216, L81–L84. https://doi.org/10.1086/312733

Werner, G. R., Uzdensky, D. A., Begelman, M. C., Cerutti, B., & Nalewajko, K. (2018). Non-thermal particle acceleration in collisionless relativistic electron-proton reconnection. MNRAS, *473*(4)arXiv 1612.04493, 4840–4861. https://doi.org/10.1093/mnras/stx2530

Werner, G. R., Uzdensky, D. A., Cerutti, B., Nalewajko, K., & Begelman, M. C. (2016). The Extent of Power-law Energy Spectra in Collisionless Relativistic Magnetic Reconnection in Pair Plasmas. ApJ, *816*(1)arXiv 1409.8262, L8. https://doi.org/10.3847/2041-8205/816/1/L8

Winske, D., Karimabadi, H., Le, A. Y., Omidi, N. N., Roytershteyn, V., & Stanier, A. J. (2023). Hybrid-Kinetic Approach: Massless Electrons. In *Space and astrophysical plasma simulation. methods* (pp. 63–91). https://doi.org/10.1007/978-3-031-11870-8_3

Yee, K. (1966). Numerical solution of initial boundary value problems involving maxwell's equations in isotropic media. *IEEE Transactions on Antennas and Propagation*, *14*(3), 302–307. https://doi.org/10.1109/TAP.1966.1138693

Zachary, A. L., & Cohen, B. I. (1986). An orbit-averaged DARWIN quasi-neutral hybrid code. *Journal of Computational Physics*, *66*, 469–480. https://doi.org/10.1016/0021-9991(86)90076-8

Zel'dovich, Y. B. (1964). The Fate of a Star and the Evolution of Gravitational Energy Upon Accretion. *Soviet Physics Doklady*, *9*, 195.

Zenitani, S., & Hoshino, M. (2001). The Generation of Nonthermal Particles in the Relativistic Magnetic Reconnection of Pair Plasmas. ApJ, *562*(1)arXiv 1402.7139, L63–L66. https://doi.org/10.1086/337972

Zhang, B., Harding, A. K., & Muslimov, A. G. (2000). Radio Pulsar Death Line Revisited: Is PSR J2144-3933 Anomalous? ApJ, *531*(2)arXiv astro-ph/0001341, L135–L138. https://doi.org/10.1086/312542

Zhang, H., Sironi, L., & Giannios, D. (2021). Fast Particle Acceleration in Three-dimensional Relativistic Reconnection. ApJ, *922*(2)arXiv 2105.00009, 261. https://doi.org/10.3847/1538-4357/ac2e08

Znajek, R. L. (1977). Black hole electrodynamics and the Carter tetrad. MNRAS, *179*, 457–472. https://doi.org/10.1093/mnras/179.3.457